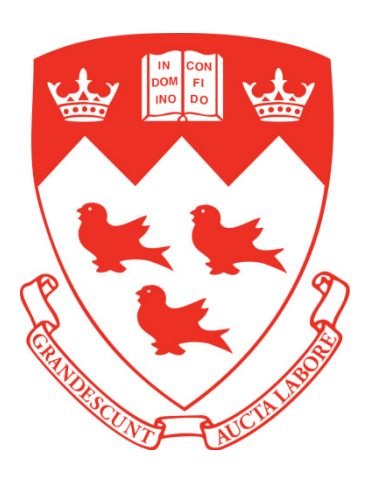
Application of Material Constitutive Models and Split-Hopkinson Pressure Bar Technique to Two Aerospace Alloys: IN718 & 300M Steel

Jessa Andrea A. Cañaveral



Department of Mining and Materials Engineering McGill University, Montreal Quebec, Canada

November 2016

A thesis submitted to McGill University in partial fulfillment of the requirements of the degree of Master of Engineering

Abstract

In an effort to optimize the machining process of aerospace components such as landing gears and engine rotors, aerospace companies are utilizing Finite Element Modelling (FEM) intensively to avoid trial and error processing. To guarantee the reliability of the FE analysis, a correct material constitutive model must be identified and used. The model must describe the dynamic behavior of the work piece material under machining conditions, must describe the physical process occurring during the machining operation, and must incorporate the appropriate material parameters. Therefore, a correct stress-strain relationship which can generalize the response of the material at high strain rates and high temperature condition is very important for a valid material modelling. In this study, the dynamic behavior of two aerospace materials, Inconel 718 (IN718) and 300M steel, were investigated.

To characterize the high strain rates and high temperature behaviors of the IN718 and 300M steel, compressive Split-Hopkinson Pressure Bar (SHPB) tests were performed over a large range of strain rates and temperatures. For the IN718 material, the experiments were carried out at strain rates from 300 s⁻¹ to 3,500 s⁻¹ and at temperatures from room (22°C) to 500°C. For the 300M steel material on the other hand, the experiments were carried out at strain rates from 300 s⁻¹ to 1,900 s⁻¹ and at temperature conditions similar to that of the IN718 material. Also as part of this work, the evaluation of an appropriate pulse shaper material to lessen the "ring-up period" during the tests was also done.

The compressive experiments showed that both IN718 and 300M steel have significant strain rate sensitivity. The flow stress of each material increased with an increase in the strain rate and decrease in the temperature. The 300M steel showed flow stress saturation on all deformation temperatures before failure. A clear thermal softening of the material due to the applied deformation temperatures was also observed.

The experimental stress-strain data of IN718 and 300M steel were used to obtain the material parameters of the Johnson-Cook and modified Johnson-Cook with Cowper-Symonds function models. The models were then evaluated by numerically predicting the results of the compressive experiments. The Johnson-Cook model has very low strain rate sensitivity and thus, was unable accurately to predict the dynamic behavior of the materials. The model follows a log-linear stress-strain rate relationship while experimental data showed that the behavior of the materials differs at strain rates of $10^2 \, \text{s}^{-1}$ and $10^3 \, \text{s}^{-1}$. On the other hand, the modified Johnson-Cook with Cowper-Symonds function model has a high strain rate sensitivity due to its power law relation. It fit the experimental data better and was able to predict the dynamic behavior of the materials well.

Résumé

En vue d'optimiser le procédé d'usinage de composantes aérospatiales tels les trains d'atterrissage et les rotors de réacteurs, plusieurs entreprises aérospatiales emploient la modélisation par éléments finis (FEM) de manière intensive afin d'éviter le traitement par essais et erreurs. Pour assurer la fiabilité de l'analyse FEM, un modèle constitutif juste doit être choisi et appliqué. Le modèle doit décrire le comportement dynamique du matériau de la pièce sous les conditions d'usinage, doit décrire le procédé physique se produisant durant l'usinage et doit comprendre les paramètres appropriés du matériau. Donc, il est de première importance pour une modélisation valide de la matière que la relation contrainte-déformation puisse généraliser de manière juste la réponse du matériau à des taux de déformation importants et à des températures élevées. Cette étude évalue le comportement dynamique de deux alliages aérospatiaux, soit l'Inconel 718 (IN718) et 300M steel.

Afin de caractériser les taux de déformation importants et les comportements à température élevée de l'IN718 et de l'acier 300M, des essais de barres d'Hopkinson divisées (SHPB) ont été effectuées sur un domaine de taux de déformations et de températures. Pour l'IN718, les expériences ont été réalisées à des taux allant de 300 s⁻¹ à 3500 s⁻¹, entre la température ambiante (22°C) et 500°C. Pour l'acier 300M, les expériences ont été réalisées entre 300 s⁻¹ et 1900 s⁻¹ à des températures comparables à celles de l'IN718. De plus, cet ouvrage comprend l'évaluation d'un matériau approprié pour la mise en forme de l'impulsion et pour diminuer la période d'équilibration des contraintes dynamiques.

Les essais compressifs ont démontré que l'IN718 ainsi que l'acier 300M sont appréciablement sensibles au taux de déformation. Les contraintes d'écoulement des matériaux ont augmenté avec les taux de déformations croissants et avec les températures décroissantes. L'acier 300M a démontré une contrainte d'écoulement avant de défaillir, et ce pour toutes les températures appliquées.

La courbe contrainte-déformation expérimentale de l'IN718 et de l'acier 300M ont servi à obtenir les paramètres constitutifs des modèles Johnson-Cook et Johnson-Cook modifié avec fonction Cowper-Symonds. Les modèles ont ensuite été évalués en prévoyant numériquement les résultats des essais en compression. Le modèle Johnson-Cook, étant très peu sensible au taux de déformation, n'a pu prévoir les comportements dynamiques des matériaux. Le modèle décrit une relation contrainte-déformation log-linéaire qui se trouve en désaccord avec les données expérimentales pour des taux de déformation de 10² s-1 et 10³ s-1. Toutefois, le modèle Johnson-Cook modifié avec fonction Cowper-Symonds est très sensible au taux de déformation dû à son expression en loi de puissance. Celle-ci s'accorde mieux aux données expérimentales et a permis de bien prévoir les comportements dynamiques des matériaux.

ACKNOWLEDGEMENTS

I would like to express my sincerest gratitude to my supervisor, Prof. Richard R. Chromik, for giving me the opportunity to pursue my Master's degree at McGill University and for his constant trust and unwavering support throughout the many challenges of this research. His guidance, counsel, patience, and financial support made this research possible. I would like to thank my co-supervisor, Prof. Mohammad Jahazi of École de Technologie Supérieure (ETS), for imparting his expertise and technical insights on the research topic.

I also offer my sincere gratefulness to Dr. Huseyin Aydin for his technical assistance and training on the Split-Hopkinson Pressure Bar Apparatus. My appreciation extends to the research associate of the MANU510 Project, Dr. Walid Jomaa, for machining my samples and providing technical guidance on the material modelling.

Many thanks are expressed to my colleagues in the project, Hamid Javadi, Jihane Ajaja, Morteza Sadeghifar, Paul Provencher, Heithem Touazine, and Hongyan Miao, for their constructive criticism, fruitful technical discussion, and encouragement. Special thanks to Paul Provencher for his help on the French translation of the abstract.

I wish to recognize the industrial partners, Pratt & Whitney Canada and Héroux Devtek, and the funding agencies, CRIAQ (Consortium for Research and Innovation in Aerospace in Quebec) and NSERC (Natural Sciences and Engineering Research Council of Canada) for their financial support which facilitated this project.

I would like to acknowledge all the administrative staff in the Department of Mining and Materials Engineering especially Ms. Barbara Hanley for her kind assistance with administrative matters. I extend my sincere thanks to the members of the McGill Hot Deformation Group for their assistance in the laboratory.

Last but not the least; I would like to thank my Mama and Papa, my brothers and my sister, for always being there for me and for supporting me throughout my studies. Finally and most importantly, I would like to express my heartfelt gratitude to my husband, Dr.

Clodualdo Aranas Jr., for his unconditional love, limitless moral support, and immense patience. His tolerance of my occasional whiny and depressed mood throughout my studies and thesis is a testament of his unyielding love and devotion. His encouragements inspired me to never quit and do better every day.

To all the people who helped me in one way or another, Maraming Salamat! (Thank you very much!)

Table of Contents

Abs	tract			i
Rés	umé			iii
Ack	nowle	dgeme	ents	v
Tab	le of Co	ontent	S	vii
List	of Figu	ıres		xi
List	of Tab	les		xix
Cha	pter 1:	Intro	duction	1
1.1	Backgr	ound		1
	1.1.1	High	Strain Rate Behavior of Material	2
1.2	Scope	of the S	Study	5
Cha	pter 2:	Litera	ature Review	6
2.1	High S	trength	n Aerospace Materials	6
	2.1.1	IN718	8	6
	2	2.1.1.1	High Strain Rate Properties of IN718	7
	2.1.2	300M	1 Steel	12
	2	.1.2.1	High Strain Rate Properties of 300M Steel	12
2.2	Turnin	ıg Proce	ess	14
2.3	Split-H	lopkins	son Pressure Bar (SHPB)	15
	2.3.1	Histo	ory of the Apparatus	15
	2.3.2		amentals of the Apparatus	
	2	.3.2.1	Parts of Split-Hopkinson Pressure Bar System	
	2	2.3.2.2	Design Parameters of Split-Hopkinson Pressure Bar System	

		2.3.2.3	High Temperature Split-Hopkinson Pressure Bar Test	21
	2.3.3	Stress	s, Strain, and Strain Rate Equations	21
	2.3.4	Pulse	Shaping in Split-Hopkinson Pressure Bar	24
		2.3.4.1	Striker Bar Geometry	25
		2.3.4.2	Three-Bar Technique	26
		2.3.4.3	Pulse Shaper or "Tip Material"	28
		2.3.4.4	Dual Pulse Shaper	29
2.4	The C	oncept o	f Material Constitutive Modelling	30
2.5	Mater	rial Const	titutive Models for Describing the Deformation Behavior of Metals	31
2.6	Flow	Stress M	odels	32
	2.6.1	Johns	on-Cook Model	32
		2.6.1.1	Results of Different Johnson-Cook Model Fitting	34
	2.6.2	Cowp	er-Symonds Model	40
		2.6.2.1	Results of Different Cowper-Symonds Model Fitting	40
	2.6.3	Modif	ied Johnson-Cook Models	43
	2.6.4	Zerilli	-Armstrong Model	45
		2.6.4.1	Results of Different Zerilli-Armstrong Model Fitting	47
	2.6.5	Modif	ied Zerilli-Armstrong Model	49
2.7	Sumn	nary		50
Cha	pter 3	: Exper	imental Set-up and Procedures	52
3.1	Mater	rials and	Experimental Conditions	52
	3.1.1	Incon	el 718 (IN718)	52
	3.1.2	300M	Steel	53
3.2	Comp	ressive S	Split-Hopkinson Pressure Bar Test	54
	3.2.1	Room	Temperature Split-Hopkinson Pressure Bar Test	55
	3.2.2	High '	Геmperature Split-Hopkinson Pressure Bar Test	58
	3.2.3	Data A	Acquisition and Processing	61
Cha	pter 4	: Pulse	Shaping Results	64

4.1	Evalu	ation o	f Pulse Shaper Material	64
	4.1.1	Effec	t of Pulse Shaper Thickness	66
	4.1.2	Effec	t of Pulse Shaper Diameter	67
Cha	pter 5:	Exper	imental Results and Discussion	71
5.1	Actual	and No	minal Strain Rate	71
5.2	Flow St	tress of	IN718	73
	5.2.1	Effec	t of Strain Rate on the Flow Stress of IN718	74
	5.2.2	Effec	t of Temperature on the Flow Stress of IN718	79
5.3	Flow St	tress of	300M Steel	83
	5.3.1	Effec	t of Strain Rate on the Flow Stress of IN718	83
	5.3.2	Effec	t of Temperature on the Flow Stress of IN718	87
Cha	pter 6:	Mater	ial Constitutive Model Fitting for IN718	90
6.1	Johnso	n-Cook	Constitutive Model for IN718	90
	6.1.1	Deter	mination of the Yield A, Strain Hardening Modulus B,	and Strain
		Harde	ening Exponent n	90
	6	1.1.1	Linear Regression Analysis	91
	6	.1.1.2	Non-Linear Regression Analysis	93
	6	.1.1.3	Comparison of Constants A, B, and n (Linear vs. Non-Linear	Regression
			Analysis	95
	6.1.2	Deter	mination of the Strain Rate Sensitivity Parameter C	96
	6.1.3	Deter	mination of the Thermal Softening Coefficient m	99
6.2	Cowpe	r-Symo	onds (Modified Johnson-Cook) Model for IN718	101
	6.2.1	Deter	mination of the Cowper-Symonds Coefficients D and p	102
6.3	Compa	rison o	f the Constitutive Model Fits for IN718	104
	6.3.1	Strair	Rate Sensitivity of the Johnson-Cook vs. Cowper Symond	s (Modified
		Johns	on-Cook) Model for IN718	105
	6.3.2	Temp	erature Sensitivity of the Johnson-Cook vs. Cowper Symono	ls (Modified
		Johns	on-Cook) Model for IN718	112
6.4	Compa	rison v	vith IN718 Johnson-Cook Model Parameters in Literature	118

Cha	pter 7:	Mater	rial Constitutive Model Fitting for 300M Steel	121
7.1	Johnso	on-Cook	Constitutive Model for 300M Steel	121
	7.1.1	Deter	rmination of the Yield A, Strain Hardening Modulus	B, and Strain
		Hard	ening Exponent n	121
	7	7.1.1.1	Linear Regression Analysis	121
	7	7.1.1.2	Non-Linear Regression Analysis	122
	7	7.1.1.3	Comparison Constants A, B, and n (Linear vs. Non-Line	ar Regression
			Analysis	123
	7.1.2	Deter	mination of the Strain Rate Sensitivity Parameter C	124
	7.1.3	Deter	mination of the Thermal Softening Coefficient m	126
7.2	Cowpe	er-Symo	onds (Modified Johnson-Cook) Model for 300M Steel	126
	7.2.1	Deter	rmination of the Cowper-Symonds Coefficients D and q	128
7.3	Compa	arison o	of the Constitutive Model Fits for 300M Steel	130
	7.3.1	Strair	n Rate Sensitivity of the Johnson-Cook vs. Cowper Symo	nds (Modified
		Johns	son-Cook) Model for 300M Steel	131
	7.3.2	Temp	perature Sensitivity of the Johnson-Cook vs. Cowper Symo	nds (Modified
		Johns	son-Cook) Model for 300M Steel	137
Cha	pter 8:	Concl	usions and Future Work	142
8.1	Conclu	ısions		142
8.2	Future	e Work.		145
Cha	nter 9:	Refer	ences	147

List of Figures

Figure 1.1 Lower yield stress vs. log of strain sate for En3B steel showing three regions of
strain rate sensitivity behavior at different testing method via shear (0), tension (X) and
punch (+) ⁹ 3
Figure 1.2 Strain rate regimes and associated instruments and experimental
conditions ¹⁴ 4
Figure 1.3 Strain vs. strain rate for various metal working operations ¹⁵ 4
Figure 2.1 True stress-strain curves of IN718 (AISI A2 Grade) under different strain rates and
temperatures ²³ 8
Figure 2.2 Stress vs. strain curve at different strain rates with initial temperature of (a) 20°C, (b)
500°C, and (c) 800°C ²⁴ 9
Figure 2.3 Variation of strain rate sensitivity β for IN718 with temperature as a function
of true strain and strain rate ²³ 10
Figure 2.4 Variation of flow stress with temperature as a function of strain rate and true
strain ^{23,25}
Figure 2.5 Engineering stress-strain curves as a function of temperature and driving
pressure (strain rate) ²⁸ 13
Figure 2.6 Schematic illustration of turning operation ²⁹
Figure 2.7 Cutting speed, feed, and depth of cut for a turning operation ²⁹ 14
Figure 2.8 Orthogonal cutting with a well-defined shear plane, also known as the Merchant
model ³¹ 15
Figure 2.9 Shear triangle used to derive the strain rate equation from chip formation
depicted as a series of parallel plates sliding relative to each other ³¹ 15
Figure 2.10 Apparatus developed by Bertram Hopkinson in 1914 for the pressure
measurement produced by gun cotton detonation: (A) explosive, (B) rod, (C) pellet, (D)
ballistic Pendulum ³⁴ 16
Figure 2.11 Schematic of Davies' apparatus ³⁵ developed in 194817
Figure 2.12 Schematic of Kolsky's apparatus ³⁴ developed in 194917
Figure 2.13 Schematic illustration of the Split-Hopkinson Pressure Bar (SHPB)
system ³⁸ 18

Figure 2.14 Schematic of compressive SHPB system and the <i>x-t</i> diagram of stress waves
propagation in the SHPB ³⁹ 19
Figure 2.15 Typical voltage history of SHPB compression test
Figure 2.16 Schematic of specimen sandwiched between two bars ⁴⁴ 23
Figure 2.17 (A) Schematic of the conical striker bar and (B) incident pulses produced by
varying the area ratio between the cylinder and the cone 43,55
Figure 2.18 Schematic of the three-bar pulse shaping technique ⁵⁹ 27
Figure 2.19 Strain pulses produced by the three-bar pulse shaping technique ⁵⁹ 27
Figure 2.20 Schematic of pulse shaping technique using a pulse shaper or "tip
material" ⁴³
Figure 2.21 Profile of different loading pulses produced by using a pulse shaper
$material ^{61}28$
Figure 2.22 Schematic of the dual pulse shaper technique ⁴³
Figure 2.23 Multiscale material mechanics ⁶⁵ 30
$\textbf{Figure 2.24} \ Comparison of experimental and Johnson-Cook simulated results of IN718 in the control of the control o$
annealed and precipitation hardened conditions at (a) typical quasi-static tests and (b)
typical high strain rate tests ⁷¹ 35
Figure 2.25 Comparison of experimental values and predicted values by Johnson-Cook
$model^{72}\ under\ different\ deformation\ rates:\ (a)\ 0.0015\ s^{\text{-}1}\text{,}\ (b)\ 0.005\ s^{\text{-}1}\text{,}\ (c)\ 0.015\ s^{\text{-}1}\text{36}$
Figure 2.26 Comparison of 6061 Al alloy experimental values and predicted values by
Johnson-Cook equation ⁵⁰ 37
Figure 2.27 Comparison of the experimental and predicted values by Johnson-Cook model
for (a) austenitic steel and (b) high-speed steel showing a better fit data for high-speed
steel ⁴⁷
Figure 2.28 Comparison between experimental data and Johnson-Cook model for 603
Armor steel under dynamic loading ²⁶ 39
Figure 2.29 Mild steel E185 simulated plastic flow stress curves for different strain rates
using the Cowper-Symonds model ⁷⁸ 41
Figure 2.30 Yield stress fitting by Cowper-Symonds model at room temperature and
increasing strain rates for (a) copper and (b) steel 79 41

Figure 2.31 Yield stress fitting by Johnson-Cook model at room temperature and
increasing strain rates for (a) copper and (b) steel ⁷⁹ 42
Figure 2.32 Cowper-Symonds fit on the true stress vs. true plastic strain of AZ31B-O under
tension loading along the rolling direction at different strain rates and temperatures (a)
room temperature, (b) 150°C, (c) 200°C, and (d) 250°C ⁸⁰
Figure 2.33 Comparison of theoretical and experimental stress-strain curves of 6061-T6
specimen at temperatures of (a) 100° C, (b) 200° C, (c) 350° C ⁹¹ 47
Figure 2.34 Variation of square root of dislocation density and true stress with strain rate
as a function of temperature 92
Figure 2.35 Variation of flow stress with square root of dislocation density given constant
true strain of 0.3^{92} 49
Figure 3.1 Schematic diagram of the SHPB set-up
Figure 3.2 McGill Split-Hopkinson Pressure Bar apparatus set-up56
Figure 3.3 Illustration of strain gage attached on the SHPB bar57
Figure 3.4 Half-Wheatstone bridge configuration in each Hopkinson bar58
Figure 3.5 Split-Hopkinson Pressure Bar oscilloscope set-up58
Figure 3.6 McGill Split-Hopkinson Pressure Bar high temperature test set-up59
Figure 3.7 Thermal gradient in the transmitted bar at 500°C deformation
temperature60
Figure 3.8 Sample output signal from compressive SHPB test61
Figure 3.9 Strain rate and true stress time history of a compressive SHPB test63
Figure 3.10 True strain time history of a compressive SHPB test63
Figure 4.1 Pulse shaping technique using a "tip material" or pulse shaper65
Figure 4.2 A typical ramp shaped incident pulse consisting of four regions: (1), (2), (3), and
(4) ⁵³ 65
Figure 4.3 Profile of incident pulse using 5.6 mm \varnothing Al6061 and Cu110 pulse shaper with
0.5 mm and 1.00 mm thickness
Figure 4.4 Profile of incident pulse using 3.175 mm \varnothing Al6061 and Cu110 pulse shaper with
0.5 mm and 1.00 mm thickness67
Figure 4.5 Profile of the incident pulse using 0.5 mm thick Al6061 and Cu110 pulse shaper
with 5.6 mm and 3.175 mm Ø68

$\textbf{Figure 4.6} \ \ \textbf{Profile of the incident pulse using 1} \ \ \textbf{mm thick Al6061} \ \ \textbf{and Cu110} \ \ \textbf{pulse shaper}$
with 5.6 mm and 3.175 mm ∅69
Figure 5.1 True stress and strain rate vs. true strain plot for IN718 6 mm \times 6 mm sample
(500°C, 220 psi)72
Figure 5.2 True stress and strain rate vs. true strain plot for IN718 4 mm \times 4 mm sample
(22°C, 180 psi)72
Figure 5.3 IN718 true stress vs. true strain plot at 500°C and nominal strain rates of 700,
1,000, 1,300, 2,200, 2,800, and 3,500 $s^{\text{-}1}\!.$ (X mark on the stress-strain curve at 3,500 $s^{\text{-}1}\!.$
denotes fractured specimen)
Figure 5.4 IN718 true stress vs. true strain plot at 350°C and nominal strain rates of 500,
700, 800, 2,200, 2,400, and 3,300 s ⁻¹ 75
Figure 5.5 IN718 true stress vs. true strain plot at 250°C and nominal strain rates of 500,
800, 900, and 2,200 s ⁻ 1
Figure 5.6 IN718 true stress vs. true strain plot at 22°C and nominal strain rates of 300,
500, 800, 2,000, 2,200, and 2,600 s ⁻¹ 76
Figure 5.7 Deformed 4 mm \times 4 mm IN718 samples tested at a temperature and strain rate
of (a) 22°C and 2,600 s ⁻¹ (b) 350°C and 3,300 s ⁻¹ , and (c) 500°C and 3,500 s ⁻¹ 77
Figure 5.8 Variation of IN718 work hardening rate with temperature as a function of strain
rate (500, 800 and 2,200 s ⁻¹) and true strain (ϵ = 0.04 and ϵ = 0.07)78
Figure 5.9 Variation of IN718 deformation-induced temperature rise ΔT with true strain as
a function of strain rate (800 and 2,200 s $^{\text{-}1}$) and temperature (22, 350 and 500°C)79
Figure 5.10 IN718 true stress vs. true strain at nominal strain rate of $2,200~\text{s}^{-1}$ and
temperatures of 22, 250, 350, and 500°C80
Figure 5.11 IN718 true stress vs. true strain at nominal strain rate of $800~s^{-1}$ and
temperatures of 22, 250, and 350°C81
Figure 5.12 IN718 true stress vs. true strain at nominal strain rate of $500 s^{-1}$ and
temperatures of 22, 250, and 350°C81
Figure 5.13 Variation of IN718 flow stress with temperature as a function of true strain (ϵ
= 0.04) and strain rate (500, 800, 2,200 s ⁻¹)82
Figure 5.14 Variation of IN718 flow stress with temperature as a function of true strain (ϵ
= 0.07) and strain rate (500, 800, 2,200 s $^{-1}$)82

Figure 5.15 300M steel true stress vs. true strain at 500° C and nominal strain rates of 600 ,
800, 1,300, 1,400, and 1,900 s $^{-1}$ (X mark on the stress-strain curve at 1,300, 1,400, and
1,900 s ⁻¹ denotes fractured specimen)84
Figure 5.16 300M steel true stress vs. true strain at 350° C and nominal strain rates of 300 ,
400 , 500 , 800 , $1,300$, and $1,500~{ m s}^{\text{-}1}$ (X mark on the stress-strain curve at $1,300~{ m and}~1,500~{ m s}^{\text{-}1}$
denotes fractured specimen)85
Figure 5.17 300M steel true stress vs. true strain at 22°C and nominal strain rates of 500,
800, 1,300, and 1,900 $\mathrm{s}^{\text{-}1}$ (X mark on the stress-strain curve at 1,900 $\mathrm{s}^{\text{-}1}$ denotes fractured
specimen)85
Figure 5.18 Fractured 4 mm $ imes$ 4 mm 300M steel samples tested at a temperature and
strain rate of (a) 22°C and $1900 \text{ s}^{\text{-}1}$ and (b) 500°C and $1900 \text{ s}^{\text{-}1}$ 86
Figure 5.19 300M steel True stress vs. true strain at a nominal strain rate of 800 s ⁻¹ and
temperatures of 22, 350, and 500°C87
Figure 5.20 300M steel true stress vs. true strain at a nominal strain rate of 1,300 s ⁻¹ and
temperatures of 22, 350, and 500°C (X mark on the stress-strain curve at 350 and 500°C
denotes fractured specimen)88
Figure 5.21 Variation of 300M steel flow stress with temperature as a function of true
strain (ϵ = 0.04) and strain rate (800 and 1,300 s ⁻¹)89
Figure 5.22 Variation of 300M steel flow stress with temperature as a function of true
strain (ϵ = 0.07) and strain rate (800 and 1,300 s ⁻¹)89
Figure 6.1 Illustration of yield stress determination for IN718 quasi-static stress-strain
curve92
Figure 6.2 Linear fit on the plastic region of IN71893
Figure 6.3 Non-linear curve fit on the plastic region of IN71894
Figure 6.4 IN718 experimental vs. Johnson-Cook approximated stress-strain curves using
linear vs. non-linear regression analysis method96
Figure 6.5 Illustration of static strain determination from the Johnson-Cook fit curve vs.
the experimental quasi-static stress-strain curve97
Figure 6.6 IN718 plot of dynamic to static stress ratio vs. ln $(\dot{\epsilon}/\dot{\epsilon}_o)$ 99
Figure 6.7 IN718 plot of $log\left(1-\left(\sigma/\sigma_{dynamic(RT)}\right)\right)$ vs. $log(T^*)$ for 2200 s ⁻¹ 101

Figure 6.8 Evaluation of the initial (lower and upper strain rate ranges) and final Cowper-
Symonds coefficients of IN718
Figure 6.9 Predicted curves for IN718 at room temperature with increasing strain rates
using the Johnson-Cook model
Figure 6.10 Comparison of experimental and Johnson-Cook model predicted flow stress
curves of IN718 at room temperature with increasing strain rate107
Figure 6.11 Johnson-Cook fit on the experimental data of IN718 at strain rates of $10^2 s^{-1}$
(300, 500, and 800 s ⁻¹) at room temperature107
Figure 6.12 Strain rate sensitivity of Johnson-Cook model for IN718 at room temperature
(true stress vs. log strain rate plot at 0.04 and 0.07 strain)108
Figure 6.13 Predicted curves for IN718 at room temperature with increasing strain rates
using Cowper-Symonds (modified Johnson-Cook) model109
Figure 6.14 Comparison of experimental and Cowper-Symonds (modified Johnson-Cook)
model predicted flow stress curves of IN718 at room temperature with increasing strain
rate110
Figure 6.15 Strain rate sensitivity of Cowper-Symonds (modified Johnson-Cook) model for
IN718 at room temperature (true stress vs. log strain rate plot at 0.04 and 0.07 strain)
110
Figure 6.16 Comparison of the strain rate sensitivity of the constitutive fits of Johnson-
Cook vs. Cowper-Symonds (modified Johnson-Cook) model for IN718 at 0.04 strain at room
temperature112
Figure 6.17 Johnson-Cook fit on the experimental data of IN718 at 500 s ⁻¹ with increasing
temperatures of 22°C, 250°C, and 350°C113
Figure 6.18 Johnson-Cook fit on the experimental data of IN718 at 800 s ⁻¹ with increasing
temperatures of 22°C, 250°C, and 350°C113
Figure 6.19 Johnson-Cook fit on the experimental data of IN718 at 2,200 s ⁻¹ with
increasing temperatures of 22°C, 250°C, 350°C, and 500°C
Figure 6.20 Cowper-Symonds (modified Johnson-Cook) fit on the experimental data of
IN718 at 500 s $^{\text{-}1}$ with increasing temperatures of 22°C, 250°C, and 350°C115
Figure 6.21 Cowper-Symonds (modified Johnson-Cook) fit on the experimental data of
IN718 at 800 s ⁻¹ with increasing temperatures of 22°C, 250°C, and 350°C115

Figure 6.22 Cowper-Symonds (modified Johnson-Cook) fit on the experimental data of
IN 718 at 2200 s $^{\text{-}1}$ with increasing temperatures of 22°C, 250°C, 350°C, and 500°C116
Figure 6.23 Experimental stress-strain curves vs. predicted stress-strain curves using
Wang's 24 , Demange's 71 , and Pereira's 105 Johnson-Cook parameters at room temperature
and 0.003, 800, and 2,200 s ⁻¹ strain rates119
Figure 6.24 Experimental stress-strain curves vs. predicted stress-strain curves using
Wang's 24 , Demange's 71 , and Pereira's 105 Johnson-Cook parameters at 2,200 s $^{\text{-}1}$ and 250 and
500°C temperatures120
Figure 7.1 Linear fit on the plastic region of 300M steel
Figure 7.2 Non-linear curve fit on the plastic zone of 300M steel123
Figure 7.3 300M steel experimental vs. Johnson-Cook approximated stress-strain curves
using linear vs. noon-linear regression analysis method124
Figure 7.4 Plot of 300M steel quasi-static stress vs. dynamic stress at room temperature
showing the strain of 0.0179125
Figure 7.5 300M steel plot of dynamic to static stress ratio vs. ln ($\dot{\epsilon}/\dot{\epsilon}_{o}$)126
Figure 7.6 300M steel plot of $\log \left(1 - \left(\sigma/\sigma_{\text{dynamic}(RT)}\right)\right)$ vs. $\log(T^*)$ for 800 s ⁻¹ 127
Figure 7.7 300M steel Plot of $log (1 - (\sigma/\sigma_{dynamic(RT)}))$ vs. $log(T^*)$ for 1300 s ⁻¹ 127
Figure 7.8 Evaluation of the initial (lower and upper strain rate ranges) and final Cowper-
Symonds coefficients of 300M steel129
Figure 7.9 Predicted curves for 300M steel at room temperature with increasing strain
rates using the Johnson-Cook model131
Figure 7.10 Comparison of experimental and Johnson-Cook model predicted flow stress
curves of 300M steel at room temperature with increasing strain rate132
Figure 7.11 Zoom-in of Johnson-Cook fit for 300M steel at room temperature starting at a
true stress 2000 MPa132
Figure 7.12 Strain rate sensitivity of Johnson-Cook fit for 300M steel at room temperature
133
Figure 7.13 Predicted curves for IN718 at room temperature with increasing strain rates
using Cowper-Symonds (modified Johnson-Cook) model134

Figure 7.14 Comparison of experimental and Cowper-Symonds (modified Johnson-Cook)
model flow stress curves of 300M steel at room temperature with increasing strain
rate135
Figure 7.15 Strain rate sensitivity of Cowper Symonds (modified Johnson-Cook) model for
$300\mbox{M}$ steel at room temperature (true stress vs. log strain rate plot at 0.04 and 0.07
strain)
Figure 7.16 Comparison of the strain rate sensitivity of the constitutive fits of Johnson
Cook vs. Cowper Symonds (modified Johnson-Cook) model for 300M steel at 0.04 strain at
room temperature
Figure 7.17 Johnson-Cook fit on the experimental data of 300M steel at 800 $\ensuremath{s^{\text{-1}}}$ with
increasing temperatures of 22°C, 350°C, and 500°C138
Figure 7.18 Johnson-Cook fit on the experimental data of 300M steel at 1300 $\ensuremath{\text{s}}^{\text{-1}}$ with
increasing temperatures of 22°C, 350°C, and 500°C138
Figure 7.19 Cowper-Symonds (modified Johnson-Cook) fit on the experimental data of
300M steel at $800s^{-1}$ with increasing temperatures of 22° C, 350° C, and 500° C139
Figure 7.20 Cowper-Symonds (modified Johnson-Cook) fit on the experimental data of
300M steel at 1300 s $^{-1}$ with increasing temperatures of 22°C, 350°C, and 500°C139

List of Tables

Table 3.1 Chemical composition of IN718 from manufacturing specification (AMS)
5662)52
Table 3.2 IN718 test matrix showing the number of tests done at room temperature53
Table 3.3 IN718 test matrix showing the number of tests done at elevated
temperatures53
Table 3.4 Chemical composition of 300M steel from manufacturing specification (AMS
6257E)53
Table 3.5 300M steel test matrix showing the number of tests done at room
temperature54
Table 3.6 300M steel test matrix showing the number of tests done at elevated
temperatures54
Table 3.7 Properties of VascoMax C350 maraging steel 55
Table 4.1 Test matrix for the Al6061 and Cu110 pulse shaper selection
Table 5.1 Test condition matrix and strain rates of 6 mm × 6 mm IN718 samples73
Table 5.2 Test condition matrix and strain rates of 4 mm × 4 mm IN718 samples74
Table 5.3 Test condition matrix and strain rates of 6 mm × 6 mm 300M steel samples83
Table 5.4 Test condition matrix and strain rates of 4 mm \times 4 mm 300M steel samples83
Table 6.1 Summary of strain hardening material constant values for IN718 (linear
regression analysis)92
Table 6.2 Summary of strain hardening material constant values for IN718 (non-linear
curve fitting)93
Table 6.3 Summary of the static strain and static stress values for IN71897
Table 6.4 Summary of Johnson-Cook parameters for IN718 101
Table 6.5 IN718 Cowper-Symonds coefficients D and p at strain rate ranges of 300-800 s ⁻¹
and 800-2,600 s ⁻¹
Table 6.6 Identified Johnson-Cook model parameters for IN718104
Table 6.7 Identified Cowper-Symonds (modified Johnson-Cook) model parameters for
IN718

Table 6.8 Summary of the statistical parameters representing the goodness of fit of the
models to IN718 experimental data at room temperature and varying strain rates111
Table 6.9 Summary of parameters representing the goodness of fit of the models to IN718
experimental data at $500~s^{\text{-}1}$ and increasing temperature116
Table 6.10 Summary of parameters representing the goodness of fit of the models to
IN718 experimental data at 800 s $^{\text{-}1}$ and increasing temperature117
Table 6.11 Summary of parameters representing the goodness of fit of the models to
IN718 experimental data at 2,200 s $^{\text{-}1}$ and increasing temperature117
Table 6.12 Johnson-Cook parameters of IN718 published in the literature118
Table 7.1 Summary of strain hardening material constant values for 300M steel (linear
regression analysis)122
Table 7.2 Summary of strain hardening material constant values for 300M steel (non-
linear curve fitting)
Table 7.3 Summary of Johnson-Cook parameters for 300M steel 128
Table 7.4 300M steel Cowper-Symonds coefficients D and p at strain rate ranges of 500-
800s ⁻¹ and 800-1,900 s ⁻¹ 129
Table 7.5 Identified Johnson-Cook model parameters for 300M steel130
Table 7.6 Identified Cowper-Symonds (modified Johnson-Cook) model parameters for
300M steel130
Table 7.7 Summary of the statistical parameters representing the goodness of fit of the
models to 300M steel experimental data at room temperature and varying strain
rates136
Table 7.8 Summary of parameters representing the goodness of fit of the models to 300M
steel experimental data at $800\ s^{-1}$ and increasing temperature140
Table 7.9 Summary of parameters representing the goodness of fit of the models to 300M
steel experimental data at 1,300 s $^{-1}$ and increasing temperature141

Chapter 1: Introduction

1.1 Background

The demand for aerospace components to build new aircraft has been increasing steadily over the last five years as global passenger traffic increased sharply by 8% to 10% year-on-year since 2011.¹ Boeing commercial airplanes for instance was expected to produce 900 aircrafts in 2015 compared to the 723 airliners built in 2014 vs. 648 in 2013 and, 601 in 2012.² For their 737 MAX Jet alone, they plan to boost its production by 47/month in 2017, 52/month in 2018, and 57/month in 2019.³ These large production volumes prompted the aerospace manufacturers to develop optimized and efficient manufacturing methods to avoid backlog of orders, scrap parts, and capacity constraints. This circumstance also caused the growing competitive pressure in the aerospace industry to address the technical demands for material performance in aerospace applications. Therefore, the choice of material to be used for components such as engine rotors and landing gears, and the improvement of the manufacturing process taking into account both the component function and its manufacturing requirement are presently the focus of aerospace research.

To meet the demand for better material performance, heat-resistant superalloys including nickel alloys such as IN718 and ultra-high strength low-alloy steel such as 300M steel are now being brought into the list of material selection. IN718 is widely used in the hot section of the aircraft jet engines due to its high temperature strength, high temperature stability, and good corrosion and oxidation resistance. 4,5 300M steel on the other hand is mostly used for landing gears and airframe parts due to its high strength properties which can withstand the severe deformation when the parts are in operation. 6 These materials are primarily manufactured via forging, casting, and rolling. The aerospace components are secondarily manufactured from these materials by machining, specifically via turning process.

One of the main goals of the aerospace industry is to develop efficient machining processes with high-productivity and low cost without sacrificing the quality and

performance of the machined part. One method is to select optimized machining parameters, which can be done by trial and error. To reduce experimental approaches that have high cost and process development time, the aerospace industry has increasingly moved towards Finite Element Modelling (FEM) to simulate and predict the performance of a particular machining operation and minimize its experimental trials. In order to accurately model the machining process, the workpiece material behavior under high rates of deformation and elevated temperature, which are representative of the machining conditions must be known. The material behavior is translated into material models that are used as an input in the finite element simulation.⁷ The material models define the relationship among variables such as stress, strain, strain rate, and temperature. They must be based on a correct stress-strain relationship which can generalize the mechanical response of the material under machining conditions.8 The accuracy and the reliability of the simulation results rely heavily on the material model suitable to the application to correctly describe the material behavior. Therefore, it is important to study and be able to predict the high strain rate and temperature behavior of IN718 and 300M steel to support the formulation of the material model that will serve as input data in the FEM of the machining process.

1.1.1 High Strain Rate Material Behavior

The plastic behavior of metallic materials is generally found to be sensitive to the deformation rate. For most metals, it has been observed that the flow stress is dependent on the logarithm of strain rate⁹ as illustrated in Figure 1.1. Different mechanisms govern the plastic flow of metals within the three strain rate behavior regimes.¹⁰ In Region I from strain rates of 10^{-5} s⁻¹ to 10^{-1} s⁻¹, the dislocation motion is based on the thermally activated slip mechanism and the dislocation generation occurs by Frank-Read source.¹¹ At strain rates from 10^2 s⁻¹ to 10^3 s⁻¹ in Region II, the controlling mechanism is related to the conventional slip mechanics of dislocations¹², while Region III is believed to be governed by drag mechanisms and relativistic effects.¹³

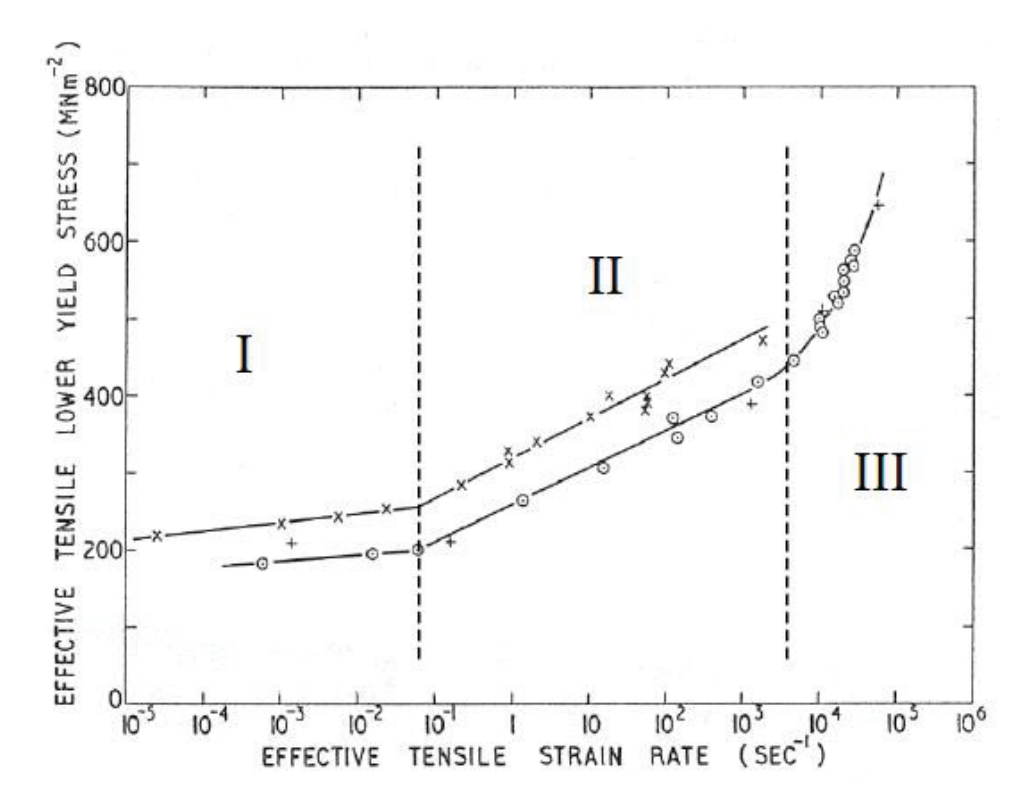


Figure 1.1. Lower yield stress vs. log of strain sate for En3B steel showing three regions of strain rate sensitivity behavior at different testing method via shear (0), tension (X) and, punch $(+)^9$

When strain rate is considered as a parameter in mechanical testing, identifying the loading method is essential to achieve the desired magnitude of the strain rate. Figure 1.2 shows the entire range of strain rate, the corresponding loading method for each strain rate regime, and the deformation conditions in each dynamic testing method.¹⁴

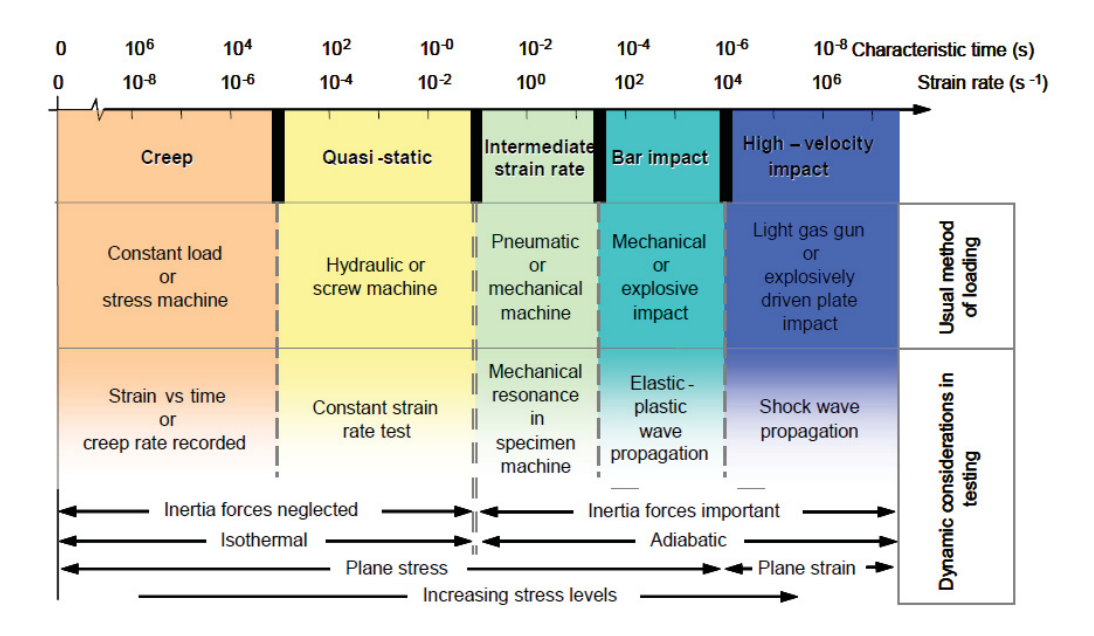


Figure 1.2. Strain rate regimes and associated instruments and experimental conditions¹⁴

Mechanical testing used to characterize the base metal plastic behavior representative of the turning conditions is considered to be at the high strain rate regime¹⁵ (strain rate of 10³ s-1 or higher) as shown in Figure 1.3. The deformation of the specimen at this regime is achieved by means of impact sources. One method that was developed to acquire and analyse data at high strain rate of loading is the Split Hopkinson Pressure Bar.¹⁶

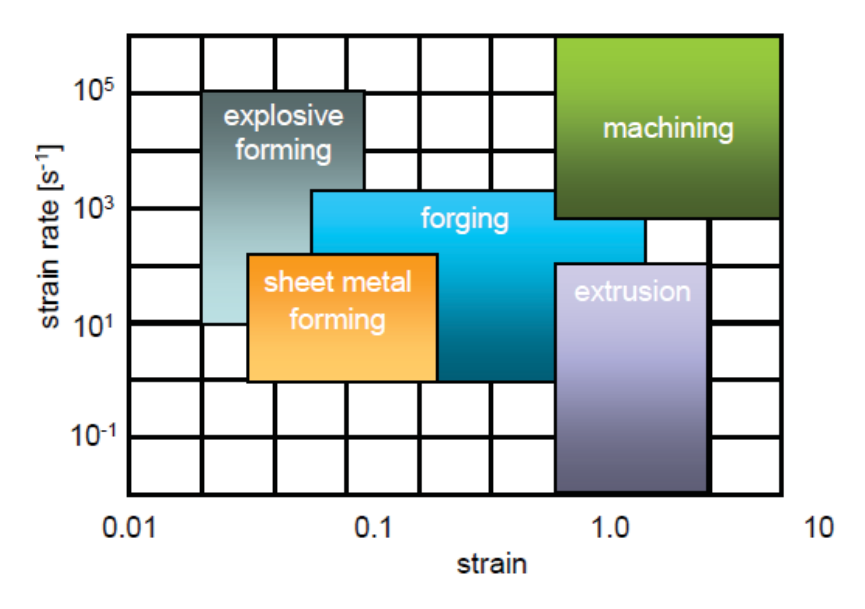


Figure 1.3. Strain vs. strain rate for various metal working operations¹⁵

1.2 Scope of the Study

The goals of the research in this thesis were to determine the high strain rate and high temperature behavior of IN718 and 300M steel and identify the Johnson-Cook and Cowper-Symonds parameters of the materials. Dynamic tests using compressive Split-Hopkinson Pressure Bar apparatus were performed at strain rates from 300 s⁻¹ to 3,500 s⁻¹ for IN718 material, strain rates from 300 s⁻¹ to 1,900 s⁻¹ for 300M steel material, at temperatures from room temperature (22°C) to 500°C for both materials. Quasi-static results from the tensile tests at room temperature were performed at a strain rate of 0.003 s⁻¹ for IN718 and 8.3X10⁻⁵ s⁻¹ for 300M steel.

The parameters of the Johnson-Cook and Cowper-Symonds models were identified from the quasi-static, high strain rate, and elevated temperature stress-strain results of the materials. The simulated curves using the Johnson-Cook and Cowper-Symonds models were fitted to the experimental results for both the IN718 and 300M steel. These material models are commonly used to describe the flow stress of material due to its simplicity and small number of material constants that can be determined from empirical results.

Chapter 2: Literature Review

This chapter presents a review of the literature pertinent to this research. This includes a review of the characteristics and properties of IN718 and 300M steel and their high strain rate behavior, the basics of the turning process, the fundamentals and theory of the Split-Hopkinson Pressure Bar apparatus, and the material constitutive models used in the literature to describe the deformation of metals, focusing on the Johnson-Cook and Cowper-Symonds model.

2.1 High Strength Aerospace Materials

2.1.1 Inconel 718

Superalloys are metallic alloys that were developed for elevated temperature applications, usually subjected at higher fraction, often in excess of 0.7 of their absolute melting temperature.^{17,18} Superalloys are usually based on group VIIIA elements and are divided into three classes based on their chemical composition. They can be classified as Nickel-based, Cobalt-based or Nickel-Iron based superalloys.¹⁸

Inconel 718 is a Nickel-based superalloy that was developed by H.L. Eiselstein of the International Nickel Company in the late 1950's mainly for gas turbine applications. 19 It is now most widely used for high temperature applications with temperatures above 500° C such as on aircraft engine compressor, engine rotors, and gas turbines. It has excellent properties in terms of strength, ductility, and toughness throughout the temperature range of -250 to 700° C. 4,20

The main strengthening mechanism of this superalloy that allows for its high temperature properties is based on precipitation hardening. The γ nickel matrix of IN718 is an *fcc* phase containing of a high fraction of alloying elements such as Cr, Mo, Nb, Ti, and Al.^{20,21} The major intermetallic phases are the γ' and γ'' metastable stable phases, and the δ equilibrium phase.^{20,21} Up to 60% volume fraction of γ' is present in the superalloy. The γ' phase has a cubic structure and composition of Ni₃Al or Ni₃Ti. The γ'' is the primary

strengthening phase with a body-centered tetragonal structure, a composition of Ni₃Nb and a volume fraction of 15-20%. It precipitates coherently as ellipsoidal, disk-shaped particles on {100} planes of the *fcc* matrix and thus believed to be the reason for the strengthening effects in the superalloy.²¹ The δ equilibrium phase on the other hand represents the thermodynamically stable form of the metastable γ " phase. It has an ordered orthorhombic phase and has a composition of Ni₃Nb similar to that of the γ " phase.²¹

The main reason for the degradation in strength of IN718 at temperatures above 650°C is due to the loss in stability of the γ'' strengthening phase. The γ'' particles coarsens after exposure to temperatures above 650°C . The morphology and precipitation kinetics of the δ phase also changes at high temperatures. Its rate of formation is typically somewhat slow below 700°C but accelerates significantly above 700°C and is accompanied by the rapid coarsening of the γ'' phase up to 885°C , which is above where the resolutioning of the γ'' occurs. 21

2.1.1.1 High Strain Rate Properties of IN718

The dynamic deformation data on IN718 were gathered by conducting tests on the material via Split-Hopkinson Pressure Bar in compression, tension or torsion. IN718 has been generally considered to be a strain rate sensitive material. Its mechanical behavior in terms of the true stress (at different initial temperatures) vs. true strain (at different strain rates) showed that the flow stress increases with increasing strain rate. This flow stress dependency in strain rate could be attributed to the increasing effect of dislocation drag mechanism at higher strain rate.²² Studies on the dynamic behavior of IN718 using compressive SHPB by Lee et al.²³ and Wang et al.²⁴ exhibits this trend as shown in Figures 2.1 and 2.2.

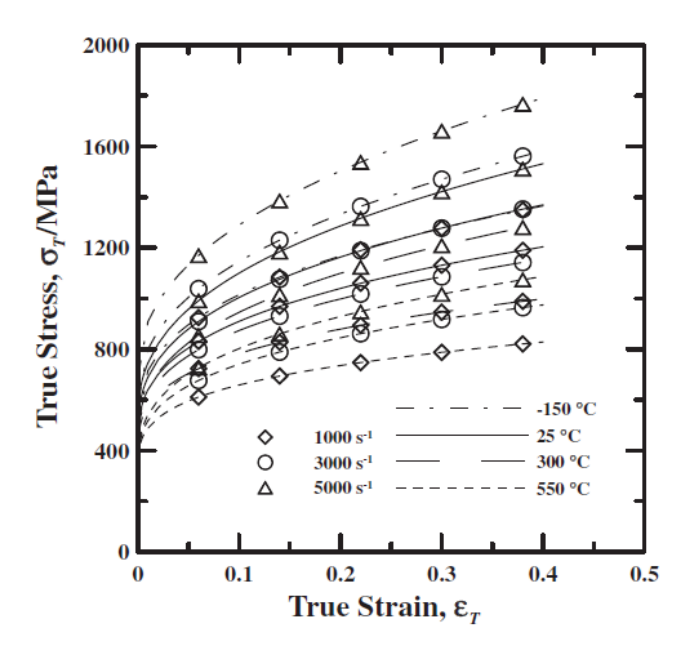
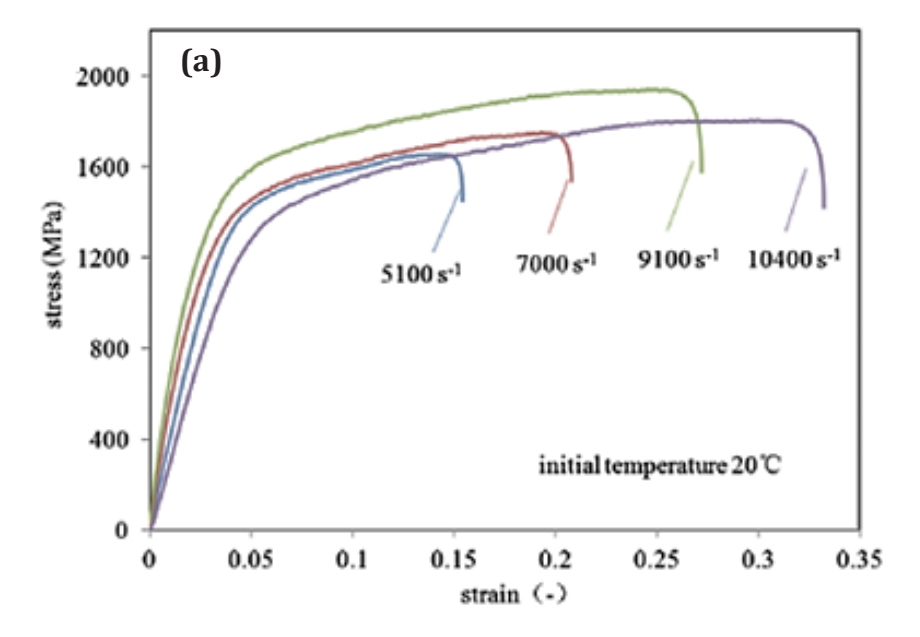


Figure 2.1. True stress-strain curves of IN718 (AISI A2 Grade) under different strain rates and temperatures 23



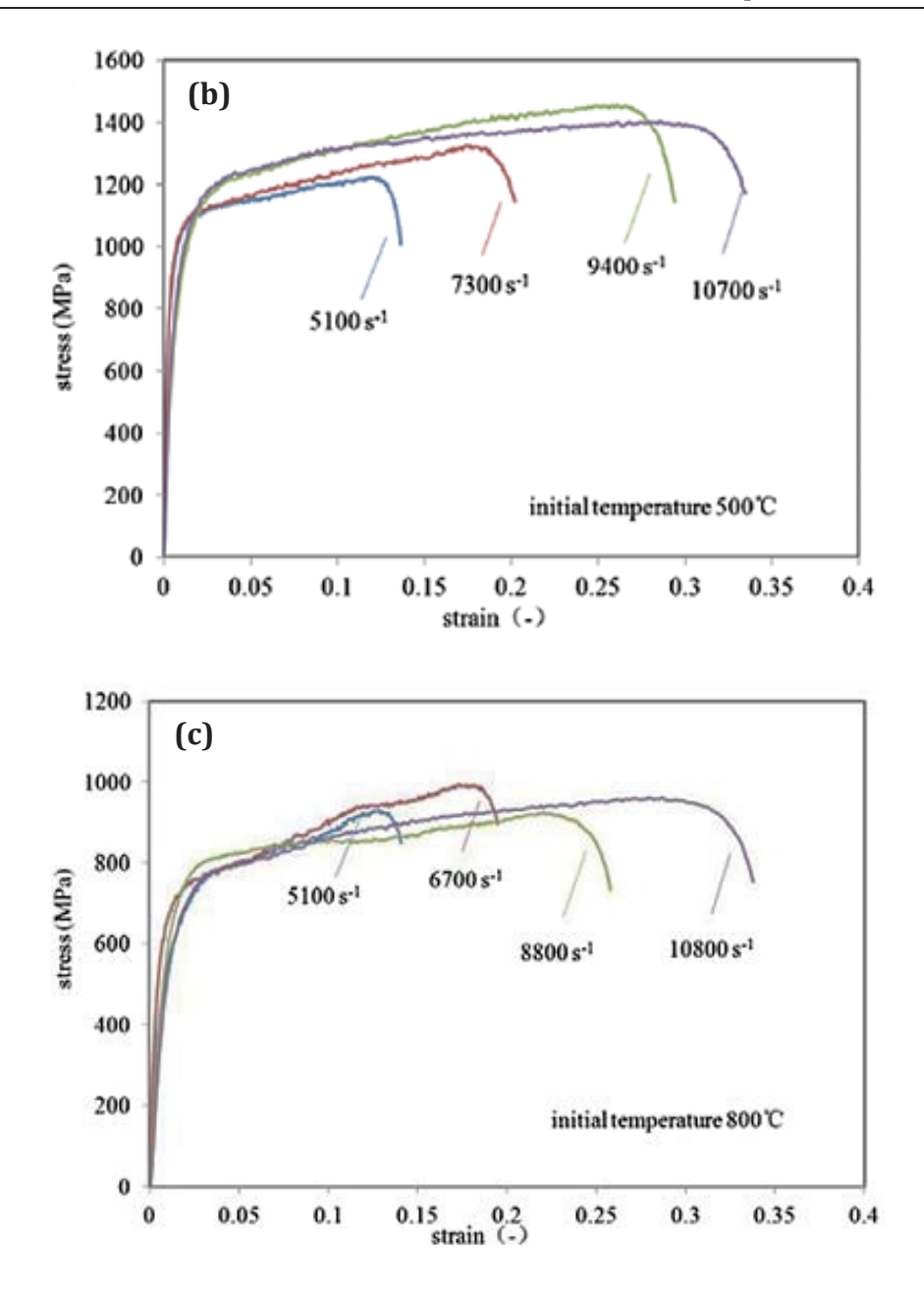


Figure 2.2. Stress vs. strain curve at different strain rates with initial temperature of (a) 20° C, (b) 500° C, and (c) 800° C²⁴

The microstructural observation for IN718 from the study of Wang et al.²⁴ showed that dislocation cell structures are formed at higher strain rates due to excessive cross slip. "The cross slip tangled dislocation features restrain subsequent dislocation motion",²⁵ thus the flow stress increases. However, the strain rate has a weaker effect on the flow stress as

compared with temperature represented by the strain rate sensitivity parameter β , defined as:

$$\beta = \frac{\sigma_2 - \sigma_1}{\ln(\dot{\varepsilon}_2 - \dot{\varepsilon}_1)} \tag{2.1}$$

where σ_1 and σ_2 are the flow stresses at a given plastic strain and temperature for strain rates $\dot{\epsilon}_1$ and $\dot{\epsilon}_2$, respectively. The value of β is largest when the strain rates are at the highest but it drops rapidly with temperature. This can be observed in IN718²³ as shown in Figure 2.3 The strain rate sensitivity increases with increasing strain rate but decreases with increasing temperature. This suggests that "at higher temperature, the diminishment of strain rate dependency of β indicates that the competition between the effects of strain rate hardening and thermal softening yields the final level of flow stress". When the temperature is at the maximum, the thermal softening effect overwhelms the strain rate strengthening effect and dominates the process of plastic deformation.

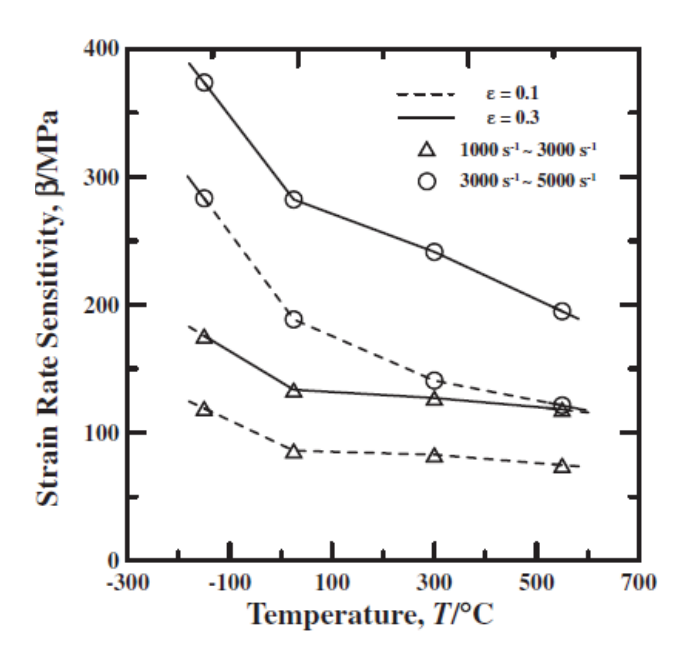


Figure 2.3. Variation of strain rate sensitivity β for IN718 with temperature as a function of true strain and strain rate²³

In the study of Lee et al.^{23,25} the behavior of IN718 also showed that at a higher temperature, the strain rate sensitivity is reduced. The strain rate strengthening effect is

restrained by the thermal softening effect at higher temperatures. Figure 2.4 shows that the stress decreases at increasing temperature at all values of strain and strain rate. This suggests that higher temperature prompts the annihilation of the dislocations as supported by microstructural observations showing lower dislocation density.

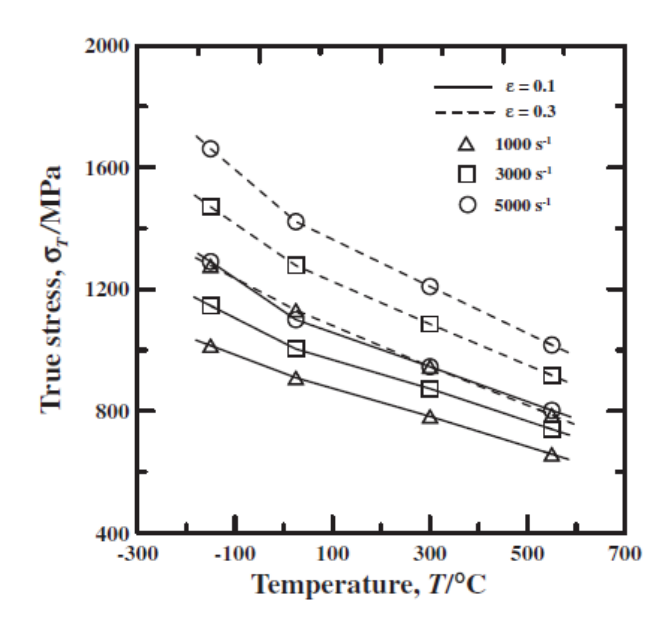


Figure 2.4. Variation of flow stress with temperature as a function of strain rate and true strain^{23,25}

A study by Wang et al.²⁴ showed that there is not only a strain rate hardening effect but also a strain rate softening effect. This was concluded from the observation that as strain rate is increased, the flow stress also increased at first and then decreased, but when the strain rate kept on rising, the flow stress increased again. The reason for this may be attributed to the stress-induced phase transformation which caused the strain rate softening effect. Microstructural observation showed that the dispersed phase disappeared when the strain rate is increased from 9000 s⁻¹ to 11,000 s⁻¹. The strain hardening effect results from dislocation pile up at high strain rates and strain softening effect results from dislocation annihilation when the density dislocation is high enough at higher strain rates. Additionally, the softening effect could be due to an increase in dislocation motion resulting from concentrated temperature rise at higher strain rates. Thus, the shift between the strain rate hardening and softening effect is temperature dependent.

2.1.2 300M Steel

Ultra-high strength steels are iron alloys that possess superior strength and toughness relative to other steel materials. Their high strength properties are derived from their dislocated martensitic structure with fine precipitates from intermetallic compounds.²⁷ They can be classified into low-alloy steels, maraging steels, precipitation hardened stainless steels, and alloyed secondary hardening steels.²⁷ Because of their relatively expensive cost, they are primarily used in applications where their high cost can be justified such as in aircraft parts. Some of their uses in aircrafts include landing gears, jet engine shafts, and fasteners.⁶

300M steel falls on the low-alloy steel category. It is a modified 4340 steel with an addition of 1.6 wt% silicon. The modification also includes the addition of Molybdenum and Carbon, plus a small addition of Vanadium. The addition of Silicon increases the yield strength and allows the steel to have higher tempering temperatures, higher than 200°C, without the degradation in yield strength and toughness as observed in 4340 steel when tempered at 250-300°C range.^{6,27} Furthermore, the tempering temperature for tempered-martensite embrittlement (so-called 260°C embrittlement) is displaced to higher temperatures above 316°C.^{6,27}

300M steel is normally produced by vacuum induction melting but for aerospace applications that require optimum properties, vacuum arc remelting is used. An oil quenched and tempered (~316°C) material that provides a very good combination of ductility and toughness at tensile strengths of 1860 – 2100 MPa (270-305 ksi) is generally used.^{6,27} It is normally not recommended for use at >316°C temperatures.⁶ It is highly susceptible to decarburization at elevated temperatures, which is unfavourable to its mechanical properties, predominantly to its fatigue resistance.^{6,27}

2.1.2.1 High Strain Rate Properties of 300M Steel

The plastic deformation of 300M steel at high strain rates has not been intensively explored yet. Thus, there are no published data available in the literature for its dynamic

behavior. However, the plastic deformation of 4340 steel, the material on which 300M steel was modified from has already been investigated.

A study of Lee and Yeh²⁸ on the deformation behavior of 4340 steel via compressive Split-Hopkinson Pressure Bar tests showed that flow stress increases with an increase in strain rate or with a decrease in the deformation temperature. The samples were subjected to high strain rates of loading from 500-3300 s⁻¹ and deformation temperatures in the range of 25-1100°C. The resulting engineering stress-strain curves from the tests are shown in Figure 2.5.

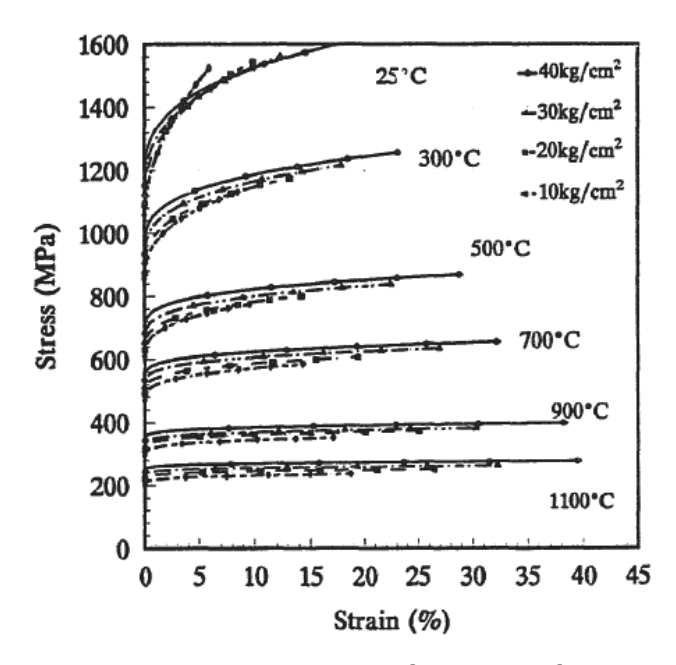


Figure 2.5. Engineering stress-strain curves as a function of temperature and driving pressure (strain rate)²⁸

The pronounced influence of the strain rate as represented by the driving pressure and temperature are evident on the plot. The flow stress decreases with temperature and it can be noted that a nearly horizontal stress curve is observed at 900°C, which suggests that the rate of thermal softening is balancing the rate of strain hardening. At a higher temperature of 1100°C the deformation of the material is under a nearly constant stress. The microstructural observation on the tested 300M materials showed that the dislocations and precipitates features depended strongly on the applied strain rate and temperature during the test.

2.2 Turning Process

Turning is one of the most important machining operations. In this operation, excess materials from the surface of a rotating cylindrical work piece are removed by using a single point cutting tool as illustrated in Figure 2.6.²⁹ The rotation of the work piece defines the primary motion of cutting while the secondary motion of cutting is given by the feed motion. The principal parameters that define the cutting conditions in turning operation are the cutting speed v, feed f, and depths of cut d as shown in Figure 2.7.²⁹ These parameters determine the deformation and temperature rise experienced by the work piece during the operation.

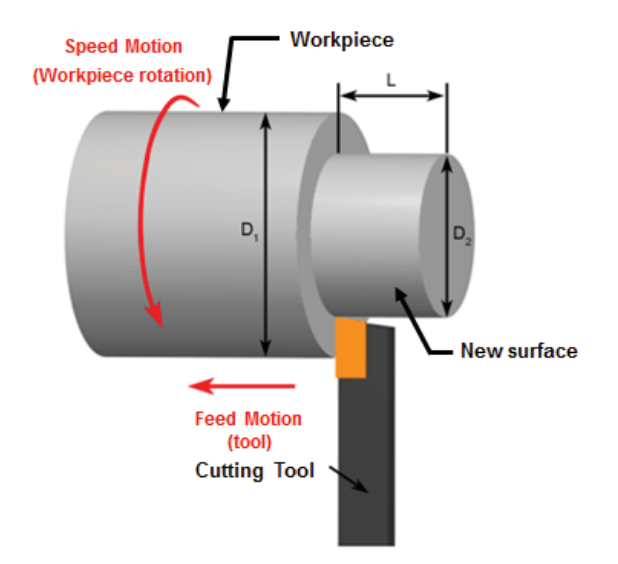


Figure 2.6. Schematic illustration of turning operation²⁹

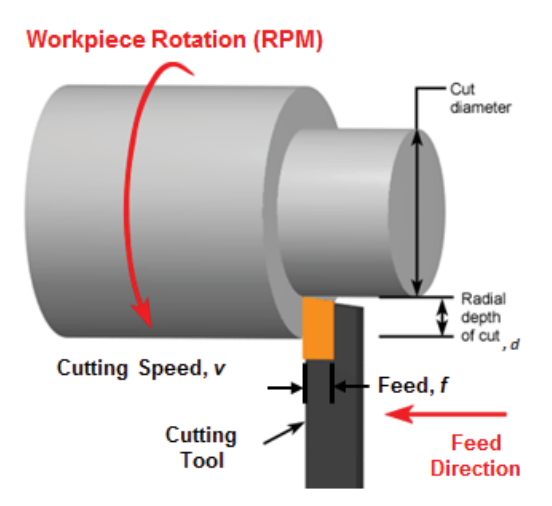


Figure 2.7. Cutting speed, feed, and depth of cut for a turning operation²⁹

The severe deformation (high strain) takes place at high temperatures and high strain rates in a very small area (primary and secondary deformation zones) which makes it hard for the actual measurement of the strain rate during turning. Ernst and Merchant³⁰ developed a shear plane model for orthogonal cutting as shown in Figure 2.8^{31} based on the assumption that shear deformation will occur on a shear plane angle φ which will reduce the cutting work to a minimum. Based from the relationships derived from this work, the mean strain rate $\dot{\epsilon}$ in the shear zone can be determined. It is a function of the cutting speed V, tool rake angle φ , shear angle φ , and thickness of the shear zone Δy , which is determined

experimentally.^{32,33} Figure 2.9 shows the schematic illustration of the geometrical basis for calculating the mean strain rate.³¹ The mean strain rate $\dot{\epsilon}$ is given by the equation:

$$\dot{\varepsilon} = \left[\frac{V \cos \alpha}{\cos(\phi - \alpha)} \right] \frac{1}{\Delta y} \tag{2.2}$$

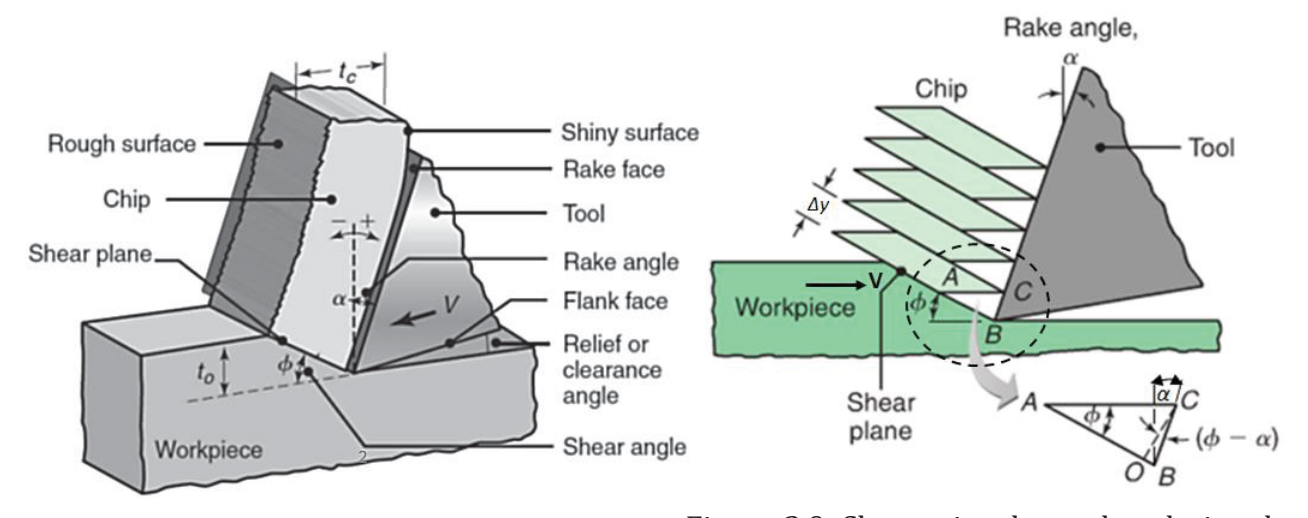


Figure 2.8. Orthogonal cutting with a well-defined shear plane, also known as the Merchant model 31

Figure 2.9. Shear triangle used to derive the strain rate equation from chip formation depicted as a series of parallel plates sliding relative to each other³¹

2.3 Split-Hopkinson Pressure Bar (SHPB)

2.3.1 History of the Apparatus

The pioneering work of Bertram Hopkinson³⁴ in 1914 started the history of experimental techniques using the Hopkinson Bars for high velocity impact tests and dynamic characterization of materials. He developed an apparatus and experimental method for the measurement of the pressure produced by an impact of a bullet or by detonation by gun cotton, which is well-known as the *Hopkinson Pressure Bar* technique. The apparatus consisted of a round bar, a small pellet, and a ballistic pendulum as shown in Figure 2.10.

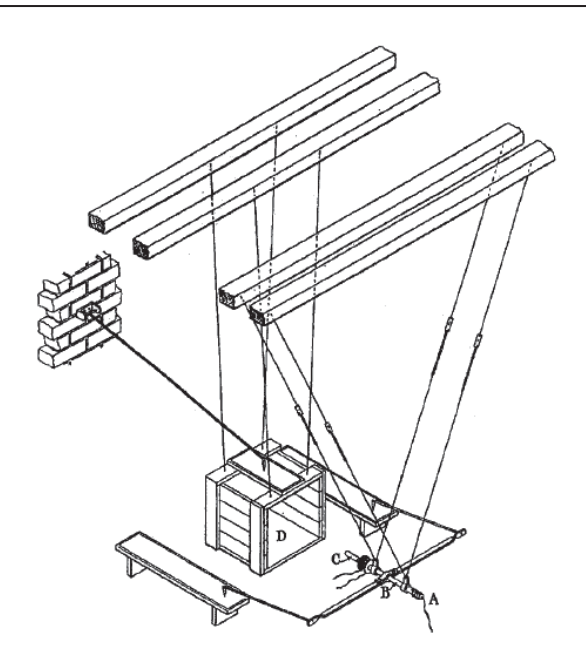


Figure 2.10. Apparatus developed by Bertram Hopkinson in 1914 for the pressure measurement produced by gun cotton detonation: (A) explosive, (B) rod, (C) pellet, (D) ballistic Pendulum³⁴

The pellet is made of the same material and has the same cross sectional dimension as the bar and is initially in contact with it. The pellet and explosive are placed at each end of the bar. The measurement of the pressure was based on his observation that when a rifle bullet is fired against the end of a cylindrical steel rod, the explosive (A) creates a compressive pulse that propagates along the bar (B). There is a definite pressure applied on the end of the rod at each instant of time during the period of impact, forming a pressure pulse. When the pulse reaches the pellet (C), part of it enters the pellet causing the pellet to fly off the pressure bar and trap part of the momentum generated by the detonation. The momentum of the pellet was measured by the ballistic pendulum (D). B. Hopkinson used different sizes of pellets to measure the pressure-time relationship of the compressive pulse generated by the detonation.³⁴

This work was followed by RM Davies³⁵ who in 1948 introduced the measurement technique (dynamic axial and radial strain measurement) and discussed the limitations of the Hopkinson Pressure Bar experiments and measurements. His experimental apparatus

which consists of a parallel plate and cylindrical condensers in conjunction with a double beam cathode-ray oscillograph is shown in Figure 2.11.

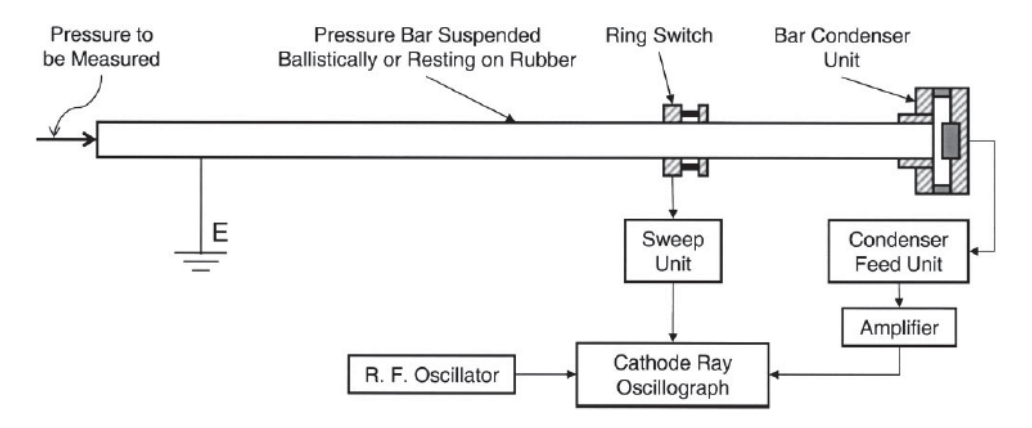


Figure 2.11. Schematic of Davies' apparatus³⁵ developed in 1948

H. Kolsky¹⁶ in 1949 modified the work of B. Hopkinson³⁴ and introduced the Split-Hopkinson Bar (SHPB) apparatus to measure the mechanical properties of several different materials (polythene, rubber, PMMA, copper, and lead) at high rates of loading. His design of the apparatus shown in Figure 2.12 is similar to that described by RM Davies³⁵ except the bar is in two parts, with the addition of the *extension bar* that can be coupled with a brass collar.

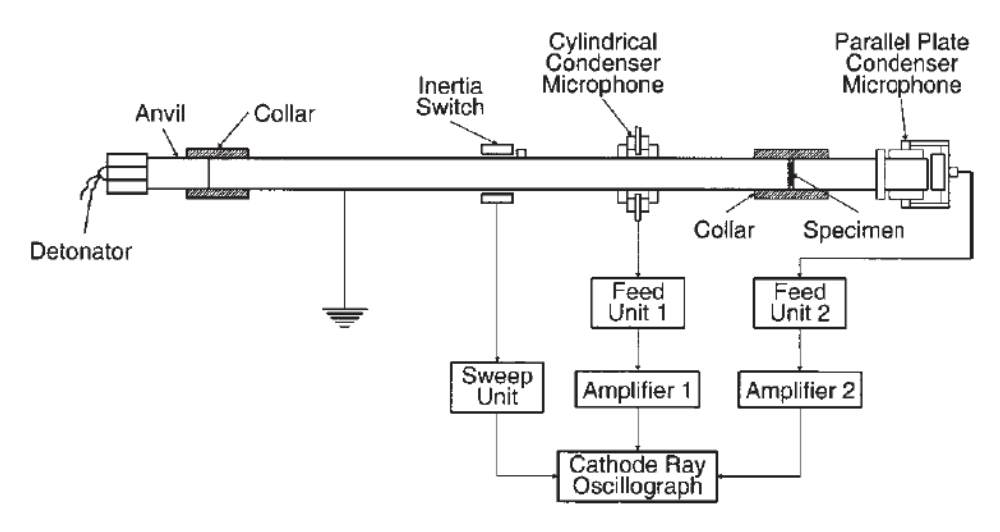


Figure 2.12. Schematic of Kolsky's apparatus¹⁶ developed in 1949

The two pressure bars are of similar material (silver steel) and cross section, and the material tested which is in form of thin disks is placed between the flat faces of the two cylindrical bars. Kolsky¹⁶ used explosives to create a compressive pulse and used similar parallel plates and cylindrical condenser microphones as Davies³⁵ to measure the stress waves in each bar. By working under the assumption that the bars remain elastic during the test, he directly related the stress waves to the displacement of the bars. The dynamic data is collected through a cathode-ray oscillograph.

2.3.2 Fundamentals of the Apparatus

The compression Kolsky bar or Split-Hopkinson Pressure Bar (SHPB) apparatus¹⁶ developed in 1949 has been widely modified such that the pulse is created by a striker bar propelled by a gas gun and the pulse propagation through the bars is recorded by strain gages and stored in an oscilloscope.

It is used extensively to determine the dynamic mechanical behavior of materials at high strain rate. It can conduct compression tests at strain rates ranging from 50 to 10^4 s⁻¹ depending on the design of the SHPB system. ^{14,36,37,38} The schematic illustration of the conventional SHPB system is shown in Figure 2.13.

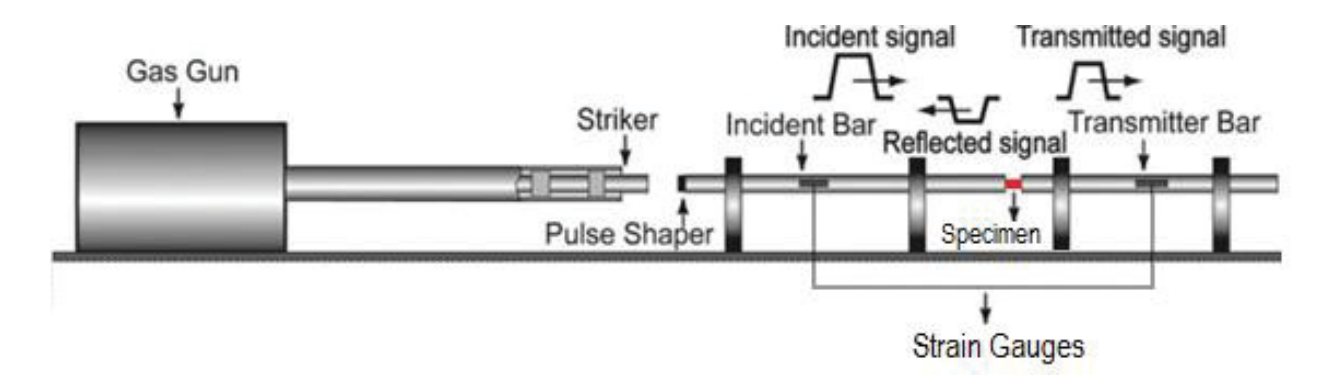


Figure 2.13. Schematic illustration of the Split-Hopkinson Pressure Bar (SHPB) system³⁸

2.3.2.1 Parts of Split-Hopkinson Pressure Bar System

The SHPB system is composed of an incident bar, a transmitter bar, a striker bar, and a gas gun. The incident and transmitter bars are typically made of high-strength steel with a very high yield stress and toughness that are designed to remain elastic throughout the test.^{37,39} A short cylindrical specimen is sandwiched between these two elastic bars. In the operation of the SHPB, a gas gun launches the striker bar that impacts on one end of the incident bar. A compressive stress wave (incident pulse, ε_i) is generated that travels down the incident bar and loads the specimen. When the stress wave reached the specimen-bar interface, part of it is reflected back (reflected pulse, ε_r) into the incident bar and part of it is transmitted (transmitted pulse, ε_t) through the specimen and through the transmitter bar depending on the impedance mismatch between the specimen and the bars.⁴⁰ A distance-time (x-t) diagram illustrating the stress waves propagation in a compressive Split-Hopkinson Pressure Bar is shown in Figure 2.14.

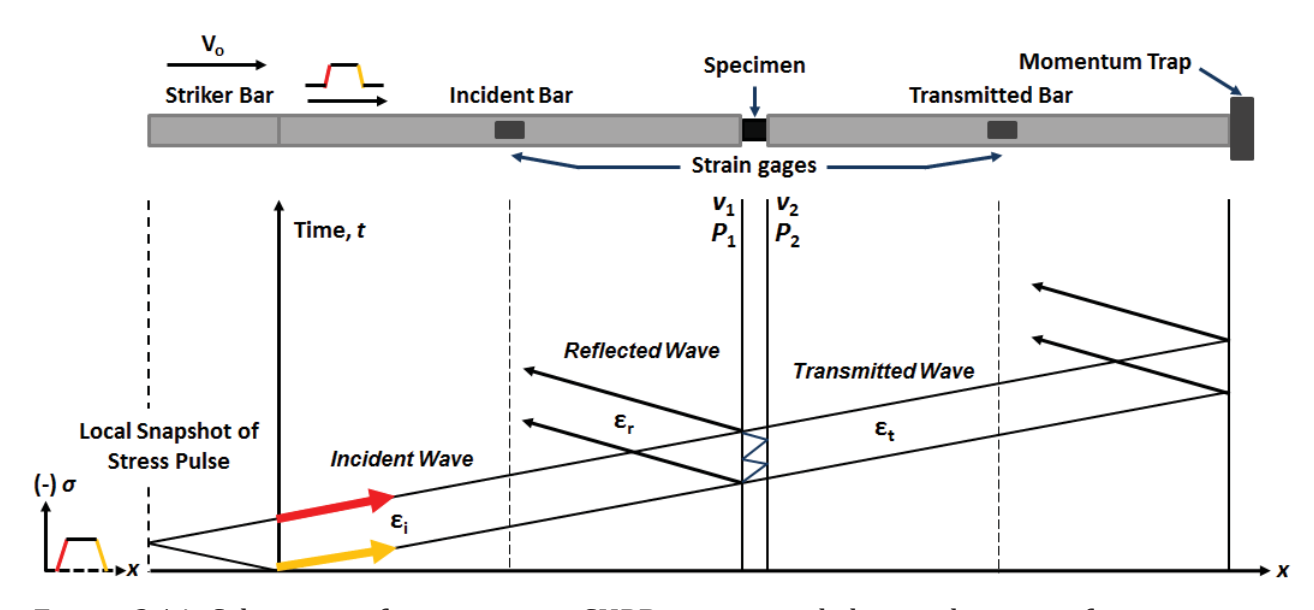


Figure 2.14. Schematic of compressive SHPB system and the x-t diagram of stress waves propagation in the SHPB³⁹

The amplitude of the incident and reflected pulses are recorded by the strain gages in the middle of incident bar, while the amplitude of the transmitted pulse is recorded by the strain gage in the middle of the transmitter bar. The locations of the strain gages are ideally such that the incident and reflected pulses do not overlap.³⁷

The strain gages then translate the stress waves into an analog voltage signal that are proportional to the elastic deformations. The resistance measured by the strain gages changes when deformation occurs. The change is detected by the Wheatstone bridge and is recorded as a voltage signal in the oscilloscope. The voltage signals are analyzed to obtain a dynamic stress-strain curve for the test specimen based on one dimensional wave propagation theory which states that the system of bars are linear and dispersion free thus stress equilibrium in the specimen exists.⁴¹ A typical wave produced from SHPB testing is illustrated in Figure 2.15.

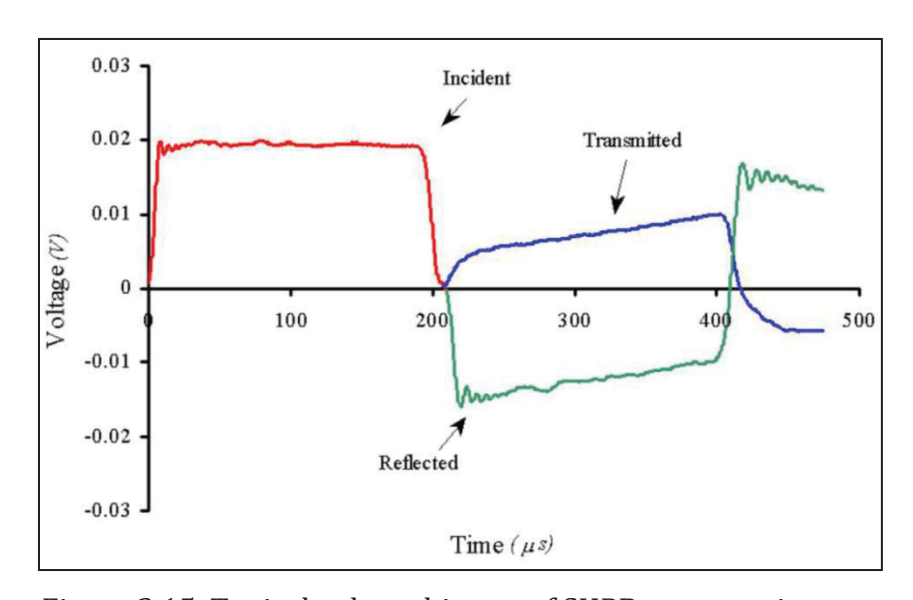


Figure 2.15. Typical voltage history of SHPB compression test

2.3.2.2 Design Parameters of Split-Hopkinson Pressure Bar System

The most important design parameters in the SHPB system are three ratios: L/D, D/d_o , and l_o/d_o where L and D are the Hopkinson bar's (incident and transmitter bar) length and diameter while l_o and d_o are the specimen's initial length and diameter.³⁷ To maintain a uniform axial stress distribution over the entire cross section of the bars⁴², L/D^{37} is typically of order 100 and must be >20.³⁵ In order for the specimen to be under uniaxial

stress, its length to diameter ratio l_0/d_0 must be less than or equal to unity³⁷, typically 0.6 to 1.0. The D/d_0 ratio³⁷ on the other hand is of order 2 to 4.

Proper lubrication of the specimen-bar interfaces is also essential to reduce the effects of interfacial friction. Inadequate lubrication may restrict the lateral expansion of the specimen resulting to non-uniform deformation.^{43,44} This friction effect may increase the axial flow stress wherein the measured flow stress can be higher than that of a uniform deformation and can be mistaken for a strain rate effect.^{43,44} Some common lubricants that can be used are high vacuum grease, petroleum jelly, polytetrafluoroethylene (PTFE), and molybdenum disulphide (MoS₂).⁴⁵

2.3.2.3 High Temperature Split-Hopkinson Pressure Bar Test

The Split-Hopkinson Pressure Bar can also be used for testing at high temperatures. Different kinds of heating systems can be incorporated into the SHPB system to achieve the temperature of choice which includes the use of clam-shell radiant heating furnace, 23,46 induction coil,47,48 infrared spot heater,39 and Electro-thermal cells furnace.26 The most common approach is to heat the specimen while in contact with the incident and transmission bars49 but this results to a strong temperature gradient in the bars. In order to avoid this problem, Li et al.38 developed an improved technique for high temperature and high strain rate test where the heating system (tube furnace) can pre-heat the specimen independently and after the desired specimen temperature is achieved, the bars are brought into contact with the specimen by the synchronically assembled system just before the stress waves reaches the interface between the incident bar and the specimen. This same technique was also utilized by Fan et al.50 and Wang et al.24 in their studies.

2.3.3 Stress, Strain, and Strain Rate Equations

The Hopkinson bar theory is based on the propagation of elastic waves in a cylindrical bar. A detailed analysis of this theory was discussed by Gray III.⁵¹ The characteristic relationship associated with the one dimensional elastic wave propagation in the bar

suggests that the velocities at the input bar/specimen interface (ν_1) and specimen/output bar interface (ν_2) are given by equations (2.3) and (2.4)

$$v_1 = c_o(\varepsilon_i - \varepsilon_r) \tag{2.3}$$

$$v_2 = c_o(\varepsilon_t) \tag{2.4}$$

where $c_o = \sqrt{\frac{E}{\rho}}$ is the phase velocity of the wave in the Hopkinson bars with E and ρ being the Young's modulus and density of the Hopkinson bars. On the other hand, the applied forces on each face of the specimen, P_1 and P_2 , are given by equations (2.5) and (2.6) where A_o is the cross sectional area of the bar.

$$P_1 = EA_o(\varepsilon_i + \varepsilon_r) \tag{2.5}$$

$$P_2 = EA_o(\varepsilon_t) \tag{2.6}$$

Taking a short specimen sandwiched between the two long Hopkinson bars, the displacements of the contact faces of the incident and transmitter bars, μ_1 and μ_2 , as shown in Figure 2.16 can be obtained in terms of the incident, reflected and transmitted strains. The displacement of the incident bar face (μ_1) and transmitter bar face are given by equations (2.7) and (2.8) where t is the time.

$$\mu_1 = c_o \int_0^t \varepsilon_i dt + (-c_o) \int_0^t \varepsilon_r dt = c_o \int_0^t (\varepsilon_i - \varepsilon_r) dt$$
 (2.7)

$$\mu_2 = c_o \int_0^t \varepsilon_t dt \tag{2.8}$$

The displacement of the incident bar face μ_1 is the result of both the incident and reflected travelling pulses where t = 0 corresponds to the primary arrival of the incident wave at the interface.⁴⁵

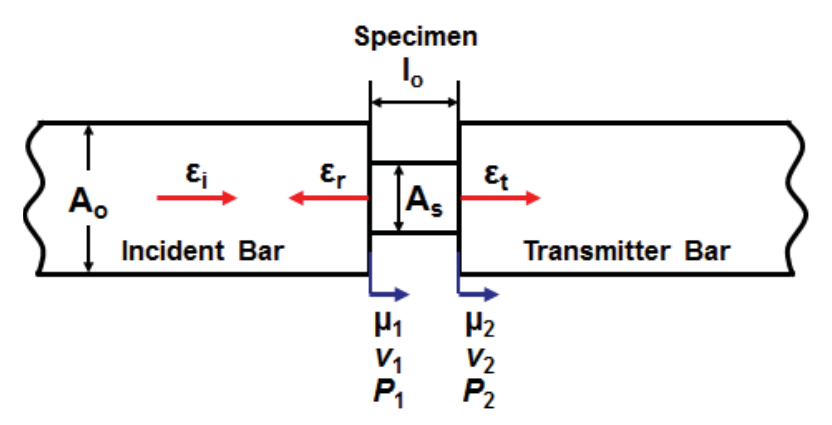


Figure 2.16. Schematic of specimen sandwiched between two bars⁴⁴

The average stress σ , strain ε , and strain rate $\dot{\varepsilon}$ in the specimen are obtained using equations (2.9) to (2.11) assuming that the stress across the short specimen is constant and A_o is the cross sectional area of the bar, l_o is the undeformed length of the specimen and A_s is the initial cross sectional area of the specimen.

The average stress σ is given by:

$$\sigma = \frac{P_1 + P_2}{2A_s} = \frac{1}{2} \frac{EA_o(\varepsilon_i + \varepsilon_r + \varepsilon_t)}{A_s}$$
 (2.9)

The average strain in the specimen ε is calculated as:

$$\varepsilon = \frac{\mu_1 - \mu_2}{l_o} = \frac{c_o}{l_o} \int_0^t (\varepsilon_i - \varepsilon_r - \varepsilon_t) dt$$
 (2.10)

and the average strain rate $\dot{\epsilon}$ is determined as:

$$\dot{\varepsilon} = \frac{\nu_1 - \nu_2}{l_o} = \frac{c_o \left(\varepsilon_{i} - \varepsilon_{r} - \varepsilon_{t}\right)}{l_o} \tag{2.11}$$

From one dimensional wave propagation theory, it is assumed that stress equilibrium exists in the specimen thus $P_1 \cong P_2$ or $\varepsilon_r = \varepsilon_t - \varepsilon_i$ thus the equations (2.9) to (2.11) can be transformed into:

$$\sigma = E\left(\frac{A_o}{A_S}\right) \, \varepsilon_{\mathsf{t}} \tag{2.12}$$

$$\varepsilon = -\frac{2c_o}{l_o} \int_0^t \varepsilon_r \, dt \tag{2.13}$$

$$\dot{\varepsilon} = \frac{2c_o}{l_o} \varepsilon_{\rm r} \tag{2.14}$$

The strain rate that the SHPB system can achieve is determined by the driving pressure, impact velocity, lengths of the incident and transmitter bars, and specimen dimensions.⁵¹ The maximum allowable impact velocity is given equation (2.15) where σ_Y is the yield stress of the pressure bar

$$v_{o,max} = \frac{2c_0\sigma_Y}{E} \tag{2.15}$$

On the other hand, the maximum strain ϵ in the specimen, at a constant strain rate, is directly proportional to the length of the striker bar L_s^{44}

$$\varepsilon = 2\dot{\varepsilon} \, \frac{L_s}{c_o} \tag{2.16}$$

Also, "strains exceeding 100% can be achieved with the Hopkinson bar method. The maximum strain rate that can be attained in a Hopkinson bar varies inversely with the length of the specimen",⁵¹ while the maximum attainable stress in the specimen is limited by the elastic limit of the bar material.⁴²

2.3.4 Pulse Shaping in Split-Hopkinson Pressure Bar

The analysis of the Split-Hopkinson Pressure Bar results was based on the assumption that the specimen is at equilibrium during the experiment.⁴¹ However, wave propagation through the specimen must still be considered to improve the accuracy of the analysis as stress equilibrium is a prerequisite for a valid SHPB test.

The loading pulse in a conventional SHPB system has an approximately trapezoidal shape accompanied by high level of oscillations. The sharp rising portion of the incident wave induces oscillations that results in the difficulty in achieving dynamic stress equilibrium state or constant strain rate⁵² specially in samples with considerable work

hardening or brittle materials with linear stress-strain behavior.⁵³ Aside from this, Davies and Hunter⁵⁴ estimated that π reverberations of the stress waves in the specimen are needed to reach a uniform state stress. The loading stress wave would take 3-4 rounds to travel in the specimen before a stress equilibrium state is achieved.⁵² The "ring-up time" t_e before equilibrium is attained is given by equation $(2.17)^{42,54}$ where ρ_s and ρ_s are the density and length of the specimen, and ρ_s is slope of the true stress-strain curve of the tested material.

$$t_e = \sqrt{\frac{\pi^2 \rho_s L_s^2}{\frac{d\sigma}{d\varepsilon}}}$$
 (2.17)

The "ring-up time" present in the experimental data makes it difficult to determine the elastic behavior of the specimen and its yield strength. The ring-up time can be lessened by reducing the size of the specimen, as its length is proportional to the ring-up time¹⁰ or increasing the rise time of the incident pulse.

The shape of the incident pulse specifically the rise time controls the loading of the specimen. The loading must be slow enough so that a quasi-static load is essentially being applied to the specimen resulting to a uniform deformation.⁵² A technique that is used to modify the shape of the incident pulse is called Pulse Shaping. The main objective of this technique is produce a slowly rising, ramp incident pulse as it is the preferred and more appropriate shape of the pulse to achieve dynamic stress equilibrium and constant strain rate in the sample and minimize the dispersion effect.⁵² Several pulse shaping methods such as shaping the striker bar, utilizing a preloading bar and using a tip material have been discussed in the literature.

2.3.4.1 Striker Bar Geometry

A different geometry of the striker bar can change the shape and slow down the rising or increase the rise time of the incident pulse. Christensen et al.⁵⁵ used striker bars with a truncated-cone on the impact end as shown in Figure 10 to partially achieve a ramp-like

incident loading pulse. Varying the area ratio of the cylinder and the cone can modify the profile of the loading pulse over a considerable range⁵⁵ as seen in Figure 2.17.

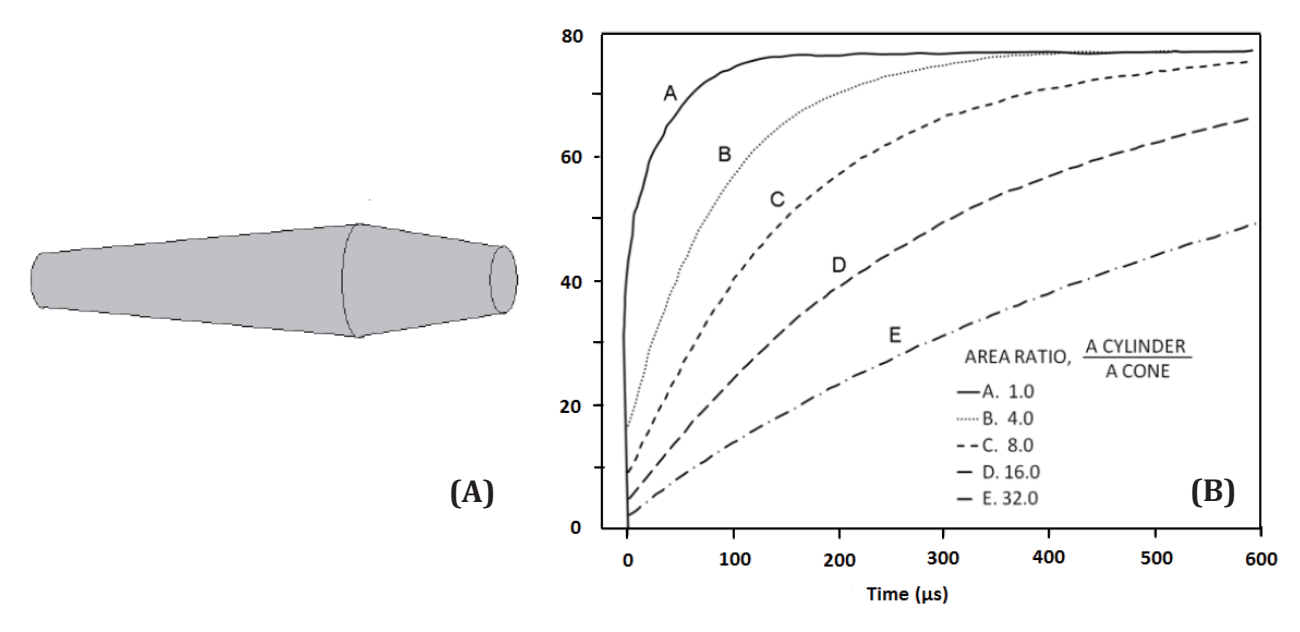


Figure 2.17. (A) Schematic of the conical striker bar and (B) incident pulses produced by varying the area ratio between the cylinder and the cone^{43,55}

A striker bar with a large radius on the impact face was used by Frantz et al.⁵⁶ to generate a slowly rising incident pulse while a tapered or cone-shaped striker bar was utilized by Li at al.⁵⁷ and Zhou et al.⁵⁸ in testing a rock sample to generate an approximately half-sine loading waveform and achieve dynamic stress equilibrium and constant strain rate.

2.3.4.2 Three-Bar Technique

Ellwood et al.⁵⁹ created a modified version of the SHPB system to alter the flattopped, short rise time incident pulse that results to a high initial and lower subsequent strain rate. The modified system consists of an additional pressure bar (pre-loading bar) and a dummy specimen that is placed before the incident bar as illustrated in Figure 2.18.

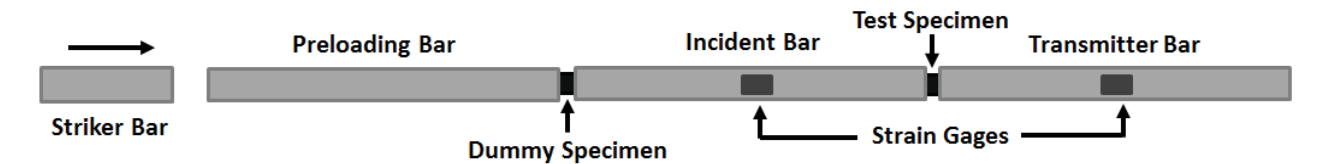


Figure 2.18. Schematic of the three-bar pulse shaping technique⁵⁹

The pre-loading bar is made of the same material as the incident and transmitted bar while the dummy specimen is recommended to be made of the same material as the specimen to be tested. The pulse transmitted through the dummy specimen becomes the actual loading incident pulse for the real specimen.^{43,59} With the three-bar technique configuration, the profile of the incident pulse is identical to that of the transmitted pulse measured behind the tested specimen as seen in Figure 2.19. ^{43,59} The shape of the incident pulse is dictated by the dummy specimen's elastic plastic response. ⁴³

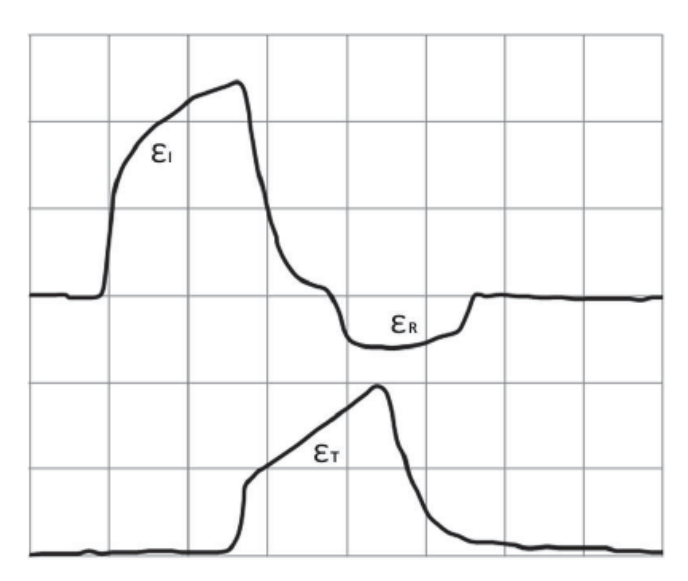


Figure 2.19. Strain pulses produced by the three-bar pulse shaping technique⁵⁹

Parry et al.⁶⁰ used a preloading bar with a lower-strength bar to minimize the dispersion in the stress wave. The length of the pre-loading bar dictates the magnitude of wave dispersion. The use of a longer pre-loading bar was observed to minimize the wave dispersion more efficiently.

2.3.4.3 Pulse Shaper or "Tip Material"

The simplest way to modify the profile of the incident pulse is by using a "tip" material placed between the striker and incident bar, on the impact end of the incident bar, as illustrated in Figure 2.20.⁴³ The "tip" material is usually a thin disk, with thickness from 0.1 mm to 2 mm, and diameter slightly smaller than the Hopkinson bars, and is made of soft materials such as copper, aluminum, brass, mild steel, etc.^{43,52} It is not necessarily the same as the specimen being tested.

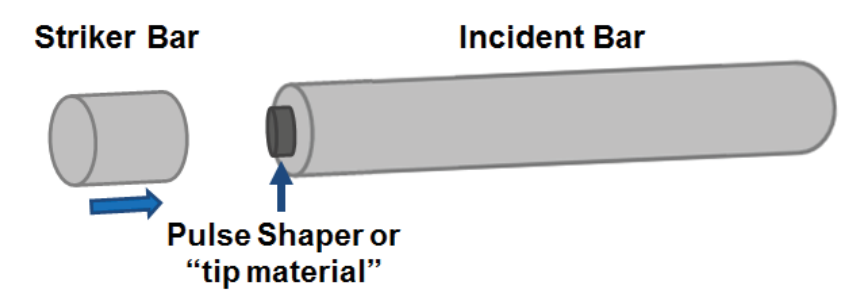


Figure 2.20. Schematic of pulse shaping technique using a pulse shaper or "tip material" 43

The pulse shaper is impacted by the striker bar before the incident bar, thus generating a non-dispersive ramp incident pulse. The rise time of the incident pulse can be modified by varying the diameter, thickness, and material of the pulse shaper.⁵³ Different loading pulses produced by using varied materials with different thickness are shown in Figure 2.21.⁶¹

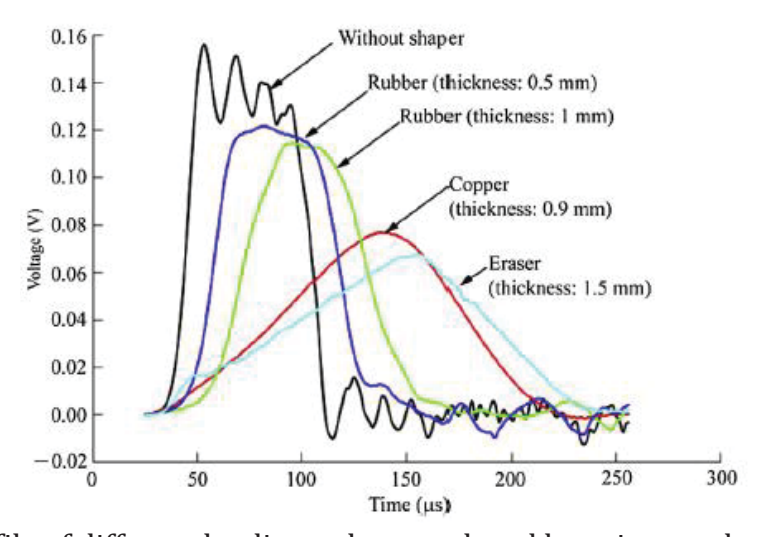


Figure 2.21. Profile of different loading pulses produced by using a pulse shaper material⁶¹

2.3.4.4 Dual Pulse Shaper

For the SHPB test of high-energy and high-strength elastic-plastic materials, using a soft pulse shaper material may not result to the desired profile of the incident pulse due to its low yield strength, thus the use of a harder pulse shaper is necessary. However, a high rate of loading even during the initial loading stage is generated by a harder pulse shaper which is not preferred for attaining early stress equilibrium.⁴³ A dual pulse shaper is therefore employed in this case.

A dual pulse shaper is a stack of a soft (such as copper) and hard (such as steel) pulse shapers as illustrated in Figure 2.22.⁶² A rigid platen with a large diameter is sometimes placed between the soft and hard pulse shapers to allow the soft pulse shaper to deform to larger strains. This is for the reason that during the initial compression, the deformation of the soft pulse shaper is much greater than that of the hard pulse shaper.⁴³

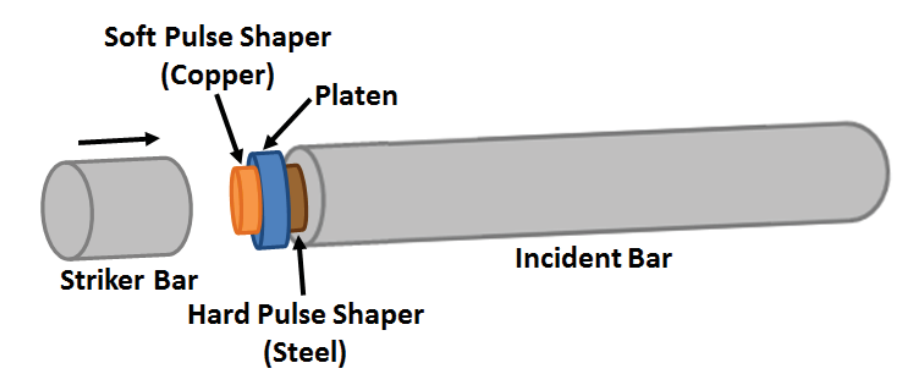


Figure 2.22. Schematic of the dual pulse shaper technique⁴³

The soft pulse shaper's main role is to produce a relatively low initial rate of loading to achieve stress equilibrium early in the test. As the soft pulse shaper is compressed to a very large strain, it eventually reaches its compressible limit. From this instant, the hard pulse shaper starts to dominate the shape of the incident pulse. The majority of the incident pulse is generated by the hard pulse shaper to achieve a constant strain rate.⁴³ Frew et al.⁶² used a stack of C-11000 copper disk and 1046 mild-steel disk dual pulse shaper for the dynamic test of a mild-steel specimen. Using the dual pulse shaper resulted to a nearly constant strain rate in the elastic and early yield response regions.⁶²

2.4 The Concept of Material Constitutive Modelling

The basic concept of materials science and engineering tells us that the performance and properties of an engineering material is a function of its structure and processing.⁶³ The processing of a material to a desired application involves a sequence of specific thermal and mechanical operations to which correspond a number of physical phenomena resulting in a material microstructure.⁶⁴ According to Willam,⁶⁵ the material behavior can be studied on four different scales as shown in Figure 2.23.

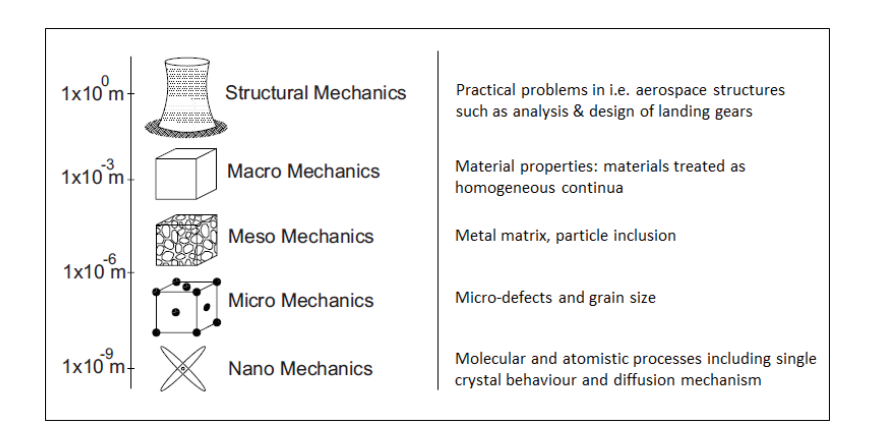


Figure 2.23. Multiscale material mechanics⁶⁵

The plastic deformation of a material on a microscopic level is influenced by the grain size, distribution of grain orientations, crystallographic texture, number of available slip systems which determines the nature of deformation mechanism, and sometimes second-phase grains or particles which are incorporated in the material by design to control either the microstructure or mechanical properties.⁶⁴ On the other hand, the macroscopic observations in plasticity includes the dependency of the flow stress on the testing temperature and strain rate and the occurrence of solid state transformations due to an applied stress.⁶⁴ The role of the constitutive relations is to quantify the performance and behavior of the material in structural components that would link the state of stress and strain.^{7,65} In view of the discussion above, it is impossible to derive a universal or exact material model applicable to all engineering materials used in various possible conditions that can capture all the macroscopic and microscopic phenomena involved in plastic deformation.^{7,64,65} Therefore, a change of material for a certain process or application

requires one to develop an appropriate model that would predict the material behavior for the specific application conditions. In addition, materials should be modelled in different ways depending on the purpose or application and the required precision of the model predictions.⁷

2.5 Material Constitutive Models for Describing the Deformation Behavior of Metals

A material constitutive model describes the stress-strain behavior of a material at low to high strain rate and temperature conditions. These models can be divided into three categories.⁶⁶ The first category is the phenomenological-based or empirical model based on the results of the mechanical tests (i.e. tensile test, compression test, shear test) done on the material. This model is usually characterized by material constants such as the strain rate constant and thermal softening coefficient. It is widely used due to its simple form (i.e. effect of strain, strain rate, and temperature are uncoupled).²⁶ Also, the material parameters in this model can be easily understood as they represent actual physical behavior.²⁶ The second category is the semi-empirical model. This model incorporates minimum physical phenomenon and still retains its simple form. In this model, the athermal and thermal part are additively separated with the thermal part making reference to thermally activated phenomena.⁶⁶ The last category is the physically-based model which is based on the physical state of the material (i.e. grain size, dislocation density, phase, texture, etc.) This is used to represent both the microscopic phenomena (microstructure evolution, recrystallization, twinning deformation) and macroscopic mechanical behavior (creep, relaxation, solid state transformation) on a material scale. This model explains a phenomenon based on the physics of the deformation processes, and thus is more complex to use.66

Gronostajski⁶⁷ reviewed the material models for calculating the changes in flow stress depending on the deformation conditions and divided them into two groups. In the first group of models, the changes in the flow stress of the materials are directly described as a function of temperature and rate of deformation. These models describe the flow stress correctly when strain hardening is the dominant factor which determines the state of

materials. They give erroneous results when there is a significant effect from thermally activated softening processes.⁶⁷ The second group of models considers the deformation history as a factor affecting the internal state of the material in which the response of the material to the deformation conditions is a function of its internal state.⁶⁷

2.6 Flow Stress Models

The model of the material behavior usually described as flow stress and defined by specific deformation conditions is one of the most essential elements for developing a Finite Element Simulation. The mathematical structure of the model along with the proper determination of the material parameters dictates the accuracy of the material model. The mathematical structure should therefore take into account the physical phenomena that occur in the material.⁶⁷

The characteristics of an engineering material are determined by its microstructure, all the way down to its atomic arrangement.⁷ Thus ideally, it is the theoretical constitutive relationships "derived from the physical processes at microstructure level that should be used to describe the macroscopic flow behavior of the material".⁶⁸ However, a study by Shi and Liu⁸ showed that the microstructure effect on the flow stress is difficult to generalize. Therefore, empirical model such as the Johnson-Cook model and Cowper-Symonds model and semi-empirical model such as the Zerilli-Armstrong model are commonly used to describe the material constitutive behavior due to their simple forms and small number of required constants. The focus of this section will be on these 3 models. Various modified Johnson-Cook models that are also commonly used in the open literature⁶⁸ will be discussed.

2.6.1 Johnson-Cook Model

The Johnson-Cook^{69,70} material model is an empirical model introduced in 1983 which is used to describe the thermo-visco-plastic hardening behavior of a material. It expresses the equivalent Von Mises flow stress as a function of plastic strain, strain rate,

and temperature that are multiplicatively decomposed into three separate functions. The equation for the Johnson-Cook model is of the form:

$$\sigma = [A + B\varepsilon^{n}][1 + C\ln\dot{\varepsilon}^{*}][1 - T^{*m}]$$
(2.18)

where σ is the equivalent Von Mises flow stress, ϵ is the equivalent plastic strain, $\dot{\epsilon}^* = \dot{\epsilon}/\dot{\epsilon}_0$ is the dimensionless plastic strain given by the test strain rate, $\dot{\epsilon}$ over the reference strain rate, $\dot{\epsilon}_0$ with values of 0.001 s⁻¹ to 1 s⁻¹, T*= (T-T₀)/(T_m-T₀) is the homologous temperature given by the ratio of the current temperature T to the melting temperature T_m and T₀ is the reference temperature which is typically the room temperature. The Johnson-Cook equation can then be expressed as:

$$\sigma = \left[A + B \left(\varepsilon^{n} \right) \right] \left[1 + C \ln \left(\frac{\dot{\varepsilon}}{\dot{\varepsilon}_{o}} \right) \right] \left[1 - \left(\frac{T - T_{o}}{T_{m} - T_{o}} \right)^{m} \right]$$
 (2.19)

The A, B, C, n, and m are material constants that are determined through experimental data fitting. The parameter A is the initial yield strength of the material at reference temperature, T_0 and reference strain rate, $\dot{\epsilon}_0$ while the parameters B and n represent the strain hardening effect, parameter m represents the thermal softening effect and parameter C is the strain rate constant. The model has three factors that are expressed in each bracket. The first bracket represents strain hardening expressed in terms of stress as a function of strain for $\dot{\epsilon}^* = 1.0$ and $T^*=0$. The second and third brackets represent strain-rate hardening and thermal softening, respectively. The Johnson-Cook model assumes that the three factors have independent effects on the slope of the flow stress curve. One of the problems with this model is that the strain rate and temperature effects on the flow stress are uncoupled which implies that the strain rate sensitivity is independent of the temperature, which is not the case for most metals.

Johnson-Cook model⁷⁰ also includes a cumulative-damage fracture model that expresses the equivalent plastic strain at the onset of damage (strain to fracture) as a function of the strain rate, temperature, and pressure. The strain at fracture is given by:

$$\varepsilon_{f} = [D_{1} + D_{2} \exp(D_{3}\sigma^{*})][1 + D_{4}\ln(\dot{\varepsilon}^{*})][1 - D_{5}T^{*}]$$
 (2.20)

where σ^* is the ratio of pressure divided by effective stress $\sigma^* = p / \sigma$, and D1, D2, D3, D4, and D5 are damage models parameters. The fracture occurs when the damage parameter D as in equation (2.21) reaches the value of 1.0. The term $\Delta\epsilon$ is the increment of equivalent plastic strain which occurs during an integration cycle.

$$D = \sum \frac{\Delta \varepsilon}{\varepsilon^{f}}$$
 (2.21)

2.6.1.1 Results of Different Johnson Cook Model Fitting

The Johnson-Cook model has been the material constitutive law of choice in many studies to predict the flow stress behavior of material over a wide range of temperature and strain rates. This section briefly discusses the results of fitting the Johnson-Cook model to the obtained experimental data from different mechanical testing over a wide range of temperature and strain rate conditions. The limitations of the model to predict the flow stress behavior will be also discussed in this section.

DeMange et al.⁷¹ investigated the dynamic material response of different heat treatments (annealed and precipitation hardened) of IN718. The Johnson-Cook parameters were determined from high rate compression Split-Hopkinson Pressure Bar tests. The results of fitting on the experimental data as shown in Figure 2.24 (a) and (b) showed that the Johnson-Cook equation provided an excellent fit to the quasi-static data but slightly over-predicts the flow stress response of both annealed and precipitation hardened IN718 at high strain rates.

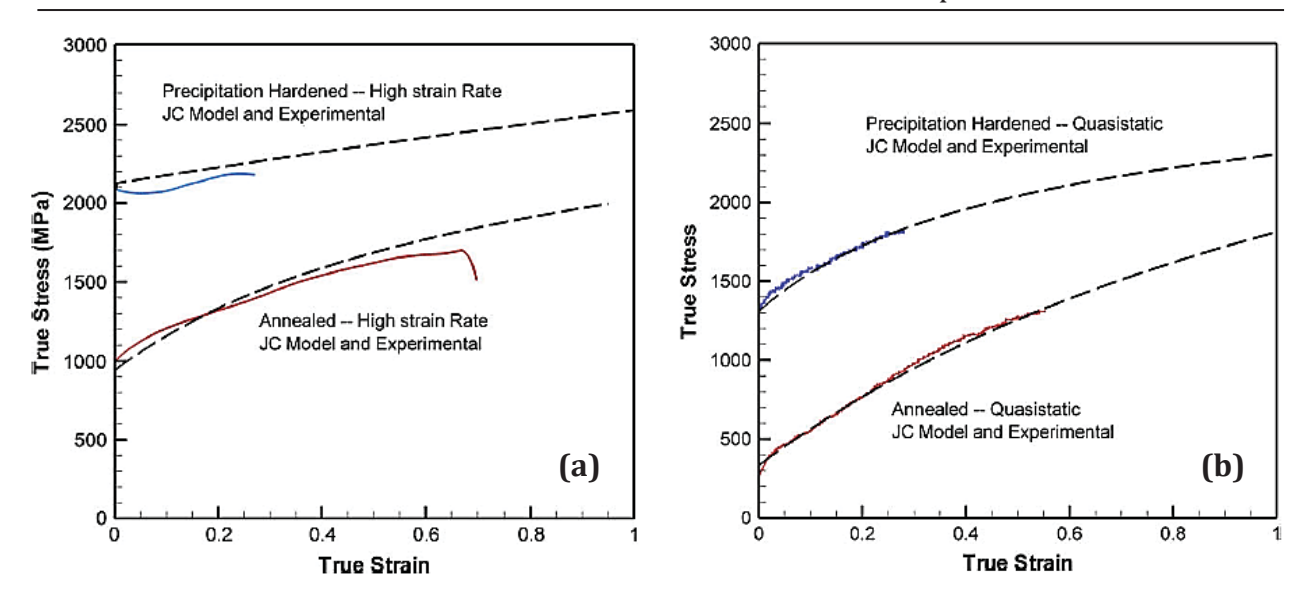


Figure 2.24. Comparison of experimental and Johnson-Cook simulated results of IN718 in annealed and precipitation hardened conditions at (a) typical quasi-static tests and (b) typical high strain rate tests⁷¹

This discrepancy is due to the constant value of the strain hardening exponent n in the Johnson-Cook model at all levels of plastic strains for all strain rates. A strain rate effect on the strain hardening parameter is clearly evident on the experimental results but was not captured in the model.⁷¹ Also, experimental results indicated a saturation level in the flow stress but this is not accommodated in the Johnson-Cook model framework.

In the study of He et al.⁷² on the high temperature and low strain rate flow stress in 20CrMo alloy steel, the comparison between the experimental values and predicted values using the Johnson cook model showed a large deviation. An acceptable correlation was only seen on the predicted values under or close to the reference deformation conditions of temperature, T = 1173K and strain rate, $\dot{\epsilon} = 0.005 \text{ s}^{-1}$ (Figure 2.25) This result was due to the assumption in the Johnson Cook model that the influences of the strain rate and deformation temperature on the flow stress are mutually independent, and thus the model is not applicable at high temperature or high strain rate.

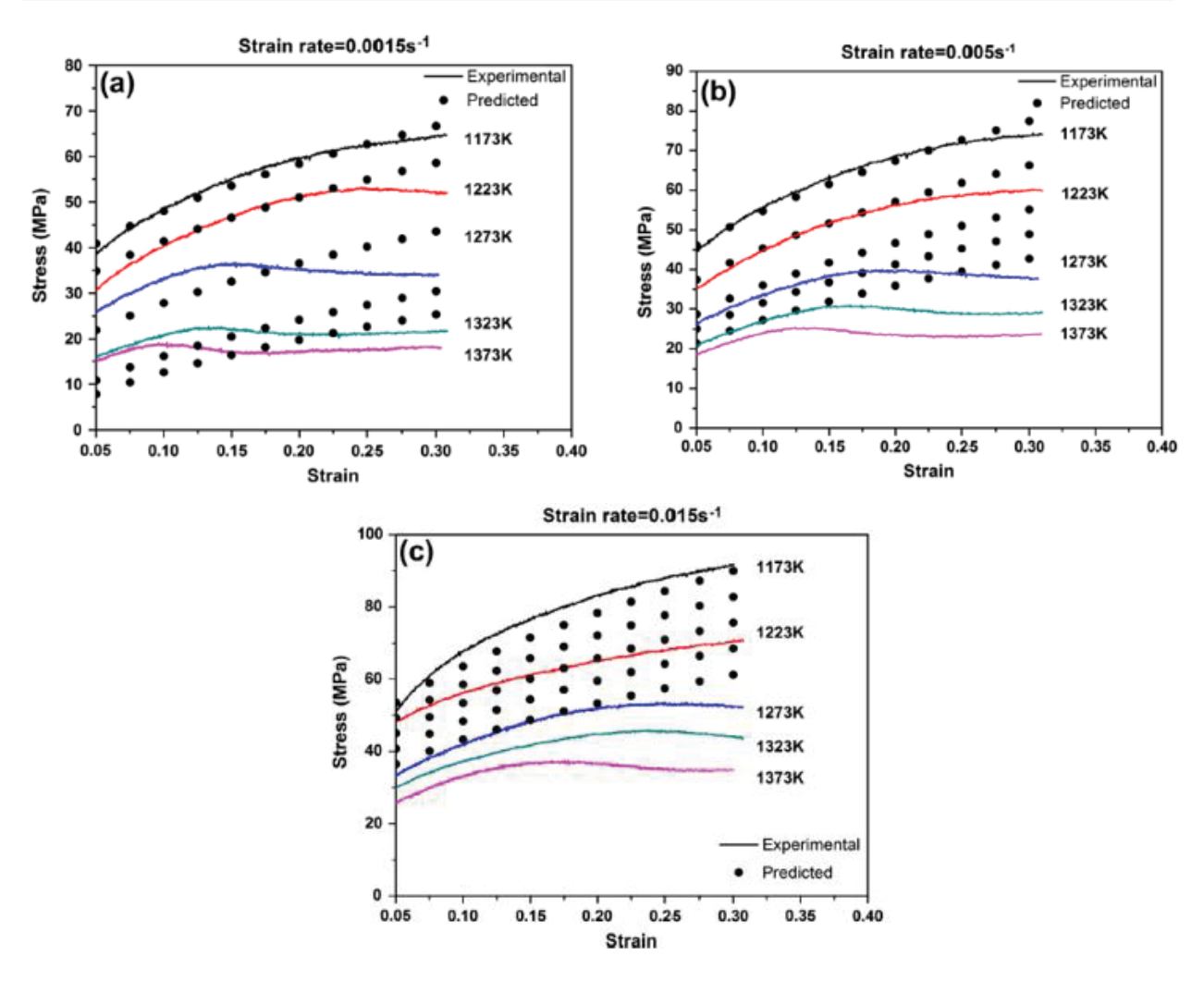


Figure 2.25. Comparison of experimental values and predicted values by Johnson-Cook model⁷² under different deformation rates: (a) $0.0015 \, \text{s}^{-1}$, (b) $0.005 \, \text{s}^{-1}$, (c) $0.015 \, \text{s}^{-1}$

Fan et al.⁵⁰ observed that the difference between the experimental and predicted data for 6061 Al alloy is minimal at room temperature, but the difference increases as the deformation temperature is increased (Figure 2.26). The possible explanations for this phenomenon are: (1) the temperature sensitivity of the alloy increases dramatically as the temperature is increased and (2) the Johnson Cook model is empirical and the temperature provides only a reversible effect on the plastic deformation via thermal activation of dislocation glide and climb but does not take into account the temperature effects on the microstructural changes involving: "(i) irreversible decrease in the dislocation density due to the operation of annealing/recrystallization processes; (ii) increase in grain-size due to high temperature exposure; and (iii) dynamic recrystallization induced grain

refinement".⁵⁰ The failure of the Johnson Cook model to predict the correct stress-strain relationship at high temperatures is due to the unavoidable microstructural variation which is not accounted for in the model.

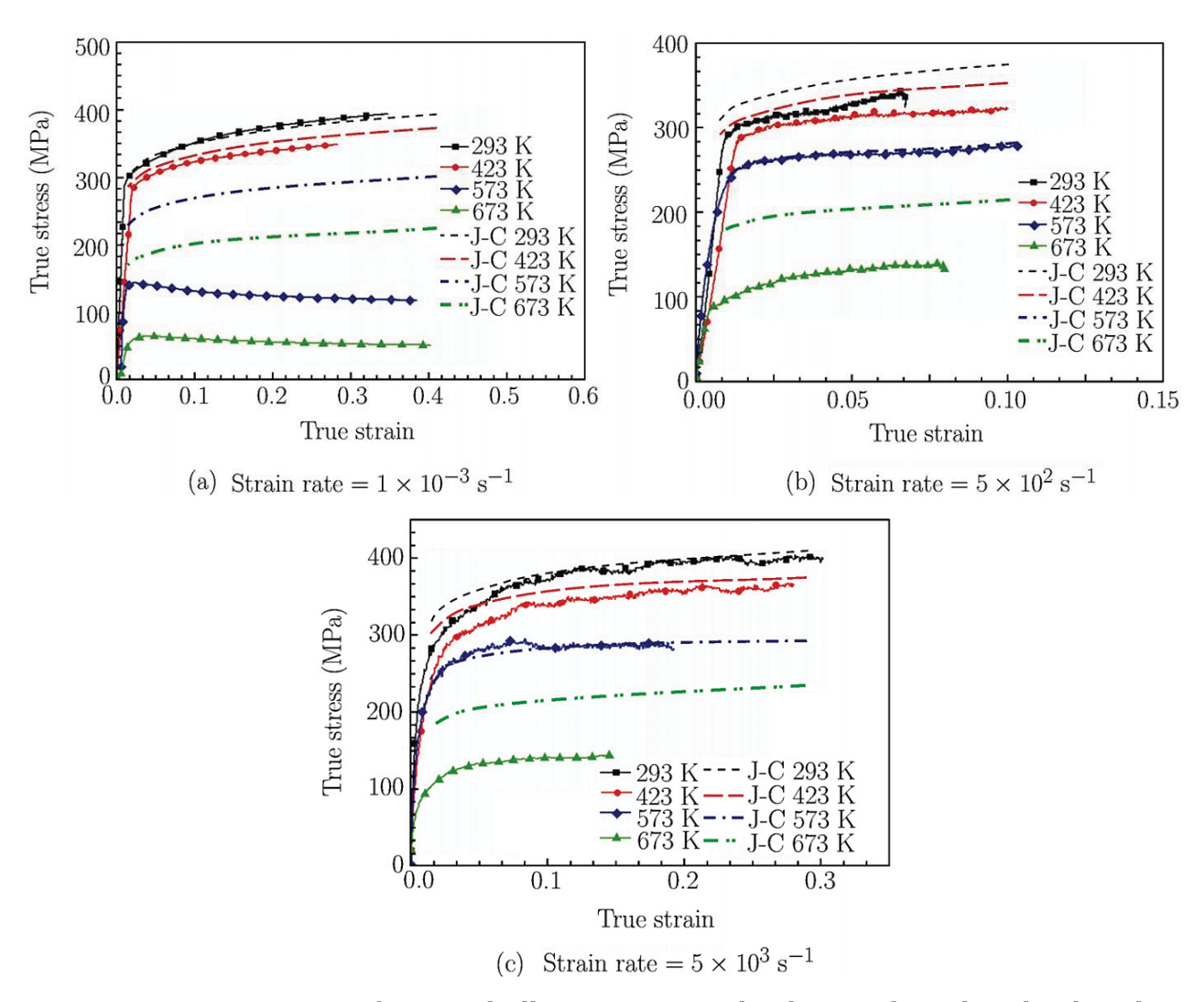


Figure 2.26. Comparison of 6061 Al alloy experimental values and predicted values by Johnson Cook equation⁵⁰

Another study concerning the use of the Johnson-Cook model vs. a physically based model by Voyiadjis-Abed to characterize the mechanical response of three grade steels in wire and bar rolling was done by Kajberg and Sundin.⁴⁷ The result of the study shows that the physically based model gave the best fit for the austenitic stainless steels while the Johnson-Cook model gave the best fit data for the high-speed steel (Figure 2.27).

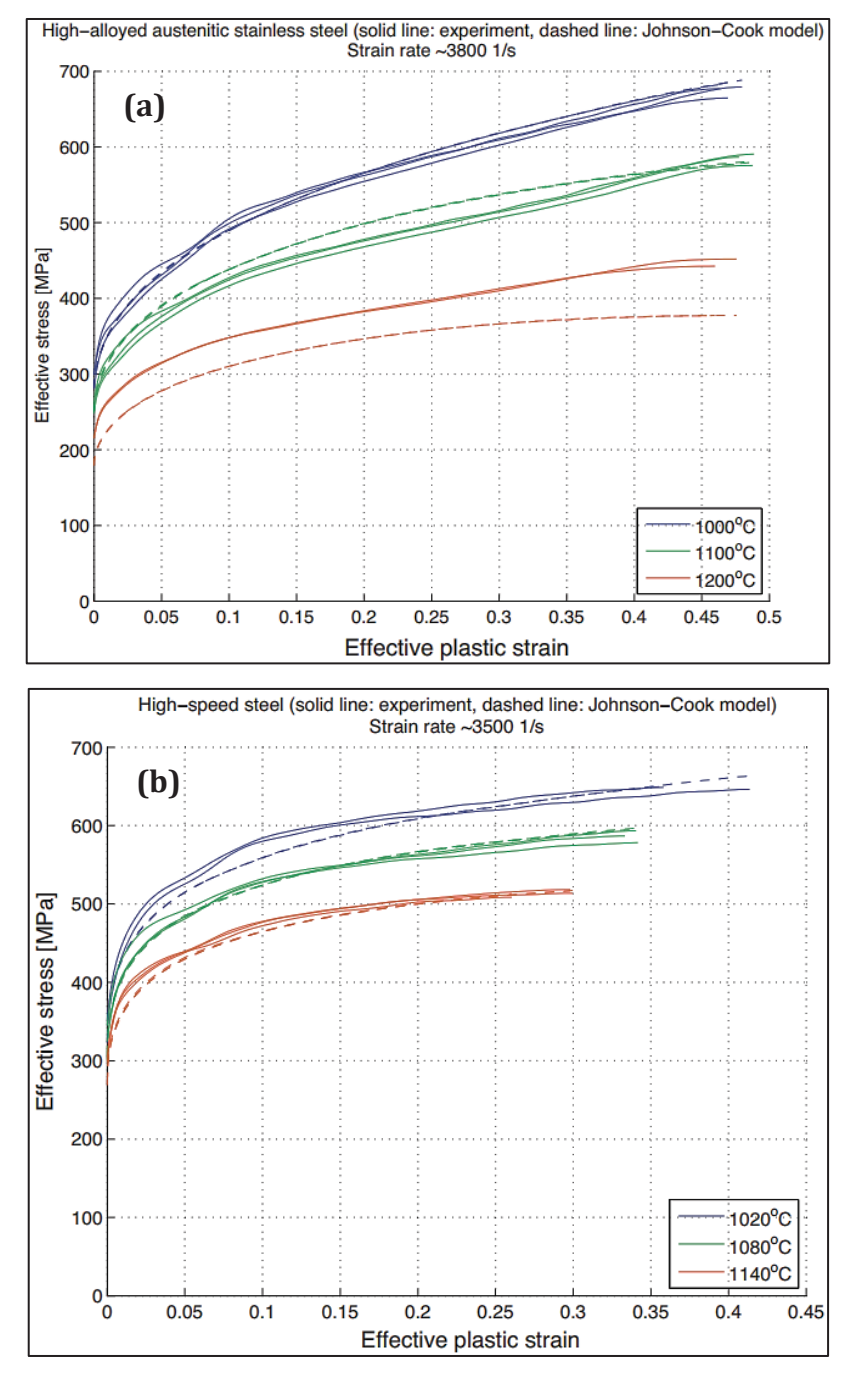


Figure 2.27. Comparison of the experimental and predicted values by Johnson-Cook model for (a) austenitic steel and (b) high-speed steel showing a better fit data for high-speed steel 47

The reason for this result when using the Johnson-Cook model may be attributed to the BCC structure of the high-speed steel which has a constant dislocation area compared to the FCC structure of the austenitic stainless steels in which the dislocation area decrease with plastic straining. Since the Johnson-Cook model does not consider the structure and dislocation density of the deformed material, an increased strain rate would only shift the stress-strain curve upwards for BCC while the work-hardening would decline for the FCC metal. The work-hardening decline for the FCC metal was not captured by the model.

Results of other studies utilizing the Johnson Cook model: Lin et al.⁷³ for the high temperature flow stress prediction of Al-Cu-Mg alloy, Xu and Huang²⁶ for the plastic behavior of 603 armor steel (Fig 2.28), and Samantaray et al.⁷⁴ for the elevated temperature flow behavior of modified 9Cr–1Mo steel all showed that the model is inadequate in describing the flow stress at high temperatures and high strain rates due to the assumption in the model that thermal softening, strain rate hardening, and strain hardening are three independent phenomena that could be isolated from each other. Therefore this model might not be able to properly model the materials studied in this work and other approaches were evaluated.

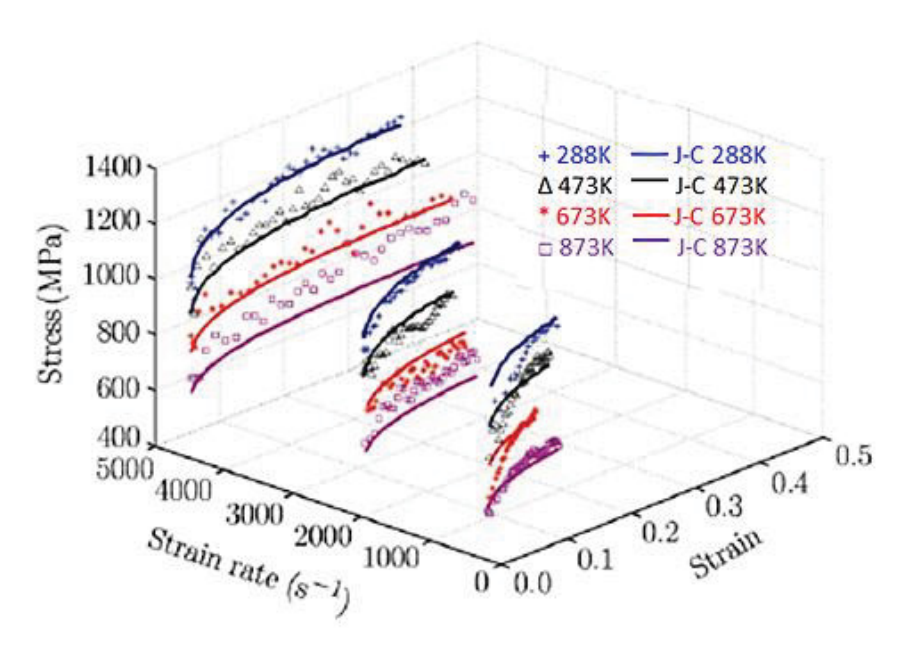


Figure 2.28. Comparison between experimental data and Johnson-Cook model for 603 armor steel under dynamic loading²⁶

2.6.2 Cowper-Symonds Model

Cowper and Symonds⁷⁵ introduced an expression for the strain rate dependency of materials to model the high strain rate behavior of mild steel. The material model couples only the strain rate with the flow stress at strain rates higher than 10^3 s⁻¹ and does not contain a thermal softening term. It takes the dynamic effects of strain rate into account by correlating the yield static stress σ_o to the yield stress obtained during dynamic loading at high strain rates.⁷⁶ The model is formulated according to the equation:

$$\frac{\sigma_d}{\sigma_o} = \left(1 + \left[\frac{\dot{\varepsilon}}{D}\right]^{\frac{1}{p}}\right) \tag{2.22}$$

where σ_d is the dynamic yield stress, $\dot{\epsilon}$ is the strain rate, and D and p are the material constants determined from experimental tests. The coefficient D is considered as the scale factor of the strain rate sensitivity and has a physical meaning interpreted as the strain rate required to amplify the dynamic flow stress equal to twice the quasi-static flow stress.⁷⁷ Due to the simplicity of the model, it is commonly used to describe the dynamic behavior of materials.

2.6.2.1 Results of Different Cowper-Symonds Model Fitting

Aside from the Johnson-Cook model, the Cowper-Symonds model is also commonly used to model the strain-rate effects in materials over a wide range of strain rates. Due to the power relation of its strain rate function, it has a higher strain rate sensitivity compared to the Johnson-Cook material. This section briefly discusses the results of simulation and curve fitting using the Cowper-Symonds model to the obtained experimental data from different mechanical testing over a wide range of strain rate conditions.

In the Cowper-Symonds model, only the yield stress is being influenced by the strain rate thus the resulting plastic curves (flow stress as a function of strain) are parallel.⁷⁸ Škrlec and Klemenc⁷⁸ determined the Cowper-Symonds parameters for the strain-rate dependent material behavior of mild steel E185. Using the determined D and p coefficients,

the stress curves at increasing strain rates were simulated. This resulted to parallel stress curves as shown in Figure 2.29.

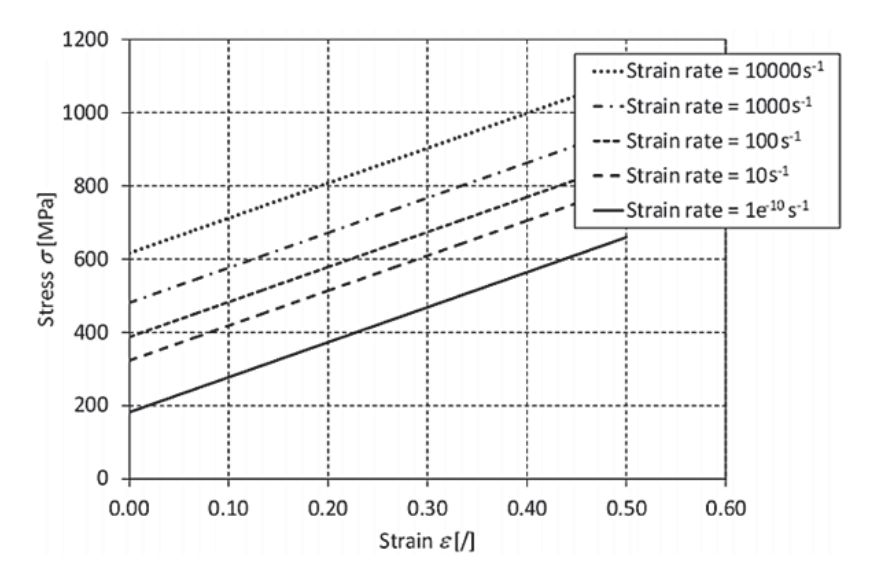


Figure 2.29 Mild steel E185 simulated plastic flow stress curves for different strain rates using the Cowper-Symonds Model⁷⁸

The comparative study of Al Salahi et al.⁷⁹ on the yield stress sensitivity to strain rates of metals showed that the Cowper-Symonds equation best fits the experimental data for copper and steel compared to the Johnson-Cook model at increasing strain rates. Figure 2.30 shows the Cowper-Symonds fit while Figure 2.31 shows the Johnson-Cook fit.

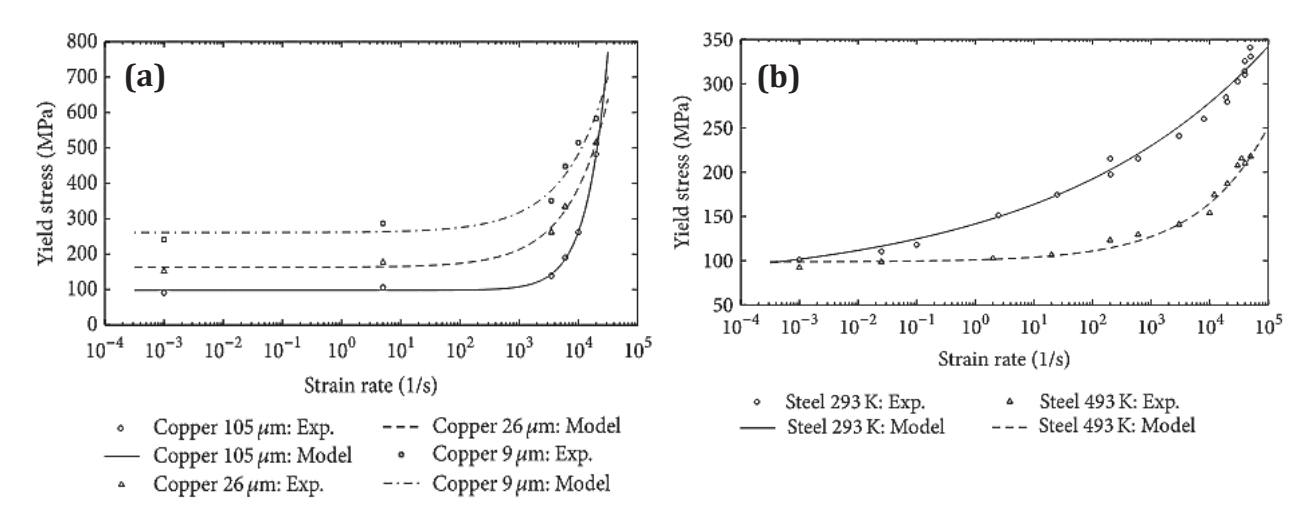


Figure 2.30 Yield stress fitting by Cowper-Symonds model at room temperature and increasing strain rates for (a) copper and (b) steel⁷⁹

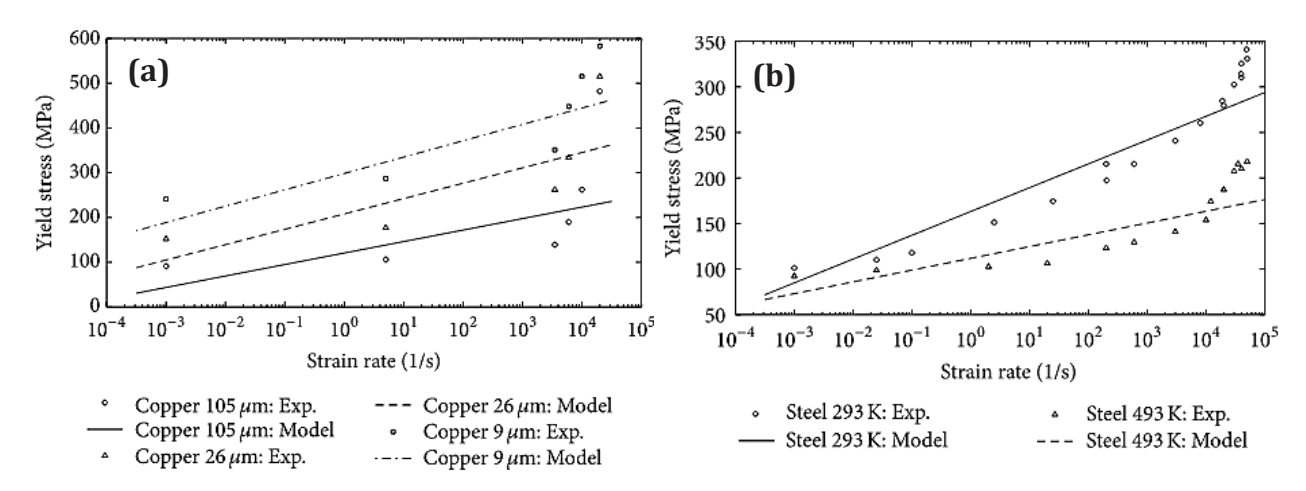
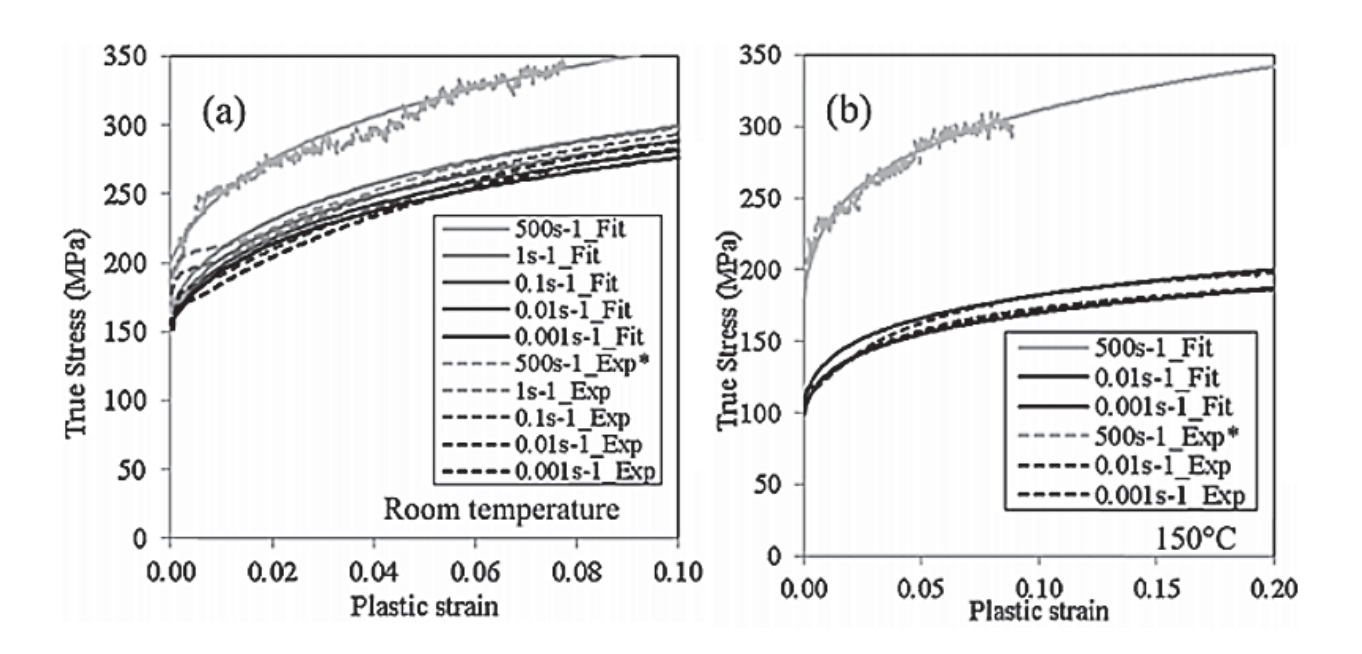


Figure 2.31 Yield stress fitting by Johnson-Cook model at room temperature and increasing strain rates for (a) copper and (b) steel⁷⁹

In the study of Tari and Worswick⁸⁰ on the elevated temperature behavior of AZ31B-0 at low to high strain rates, the rate-sensitive Cowper-Symonds strain hardening model fits the experimental stress-strain data at all temperatures (Figure 2.32). The model was able to capture the increasing effect of strain rate at elevated temperatures, especially above 150°C.



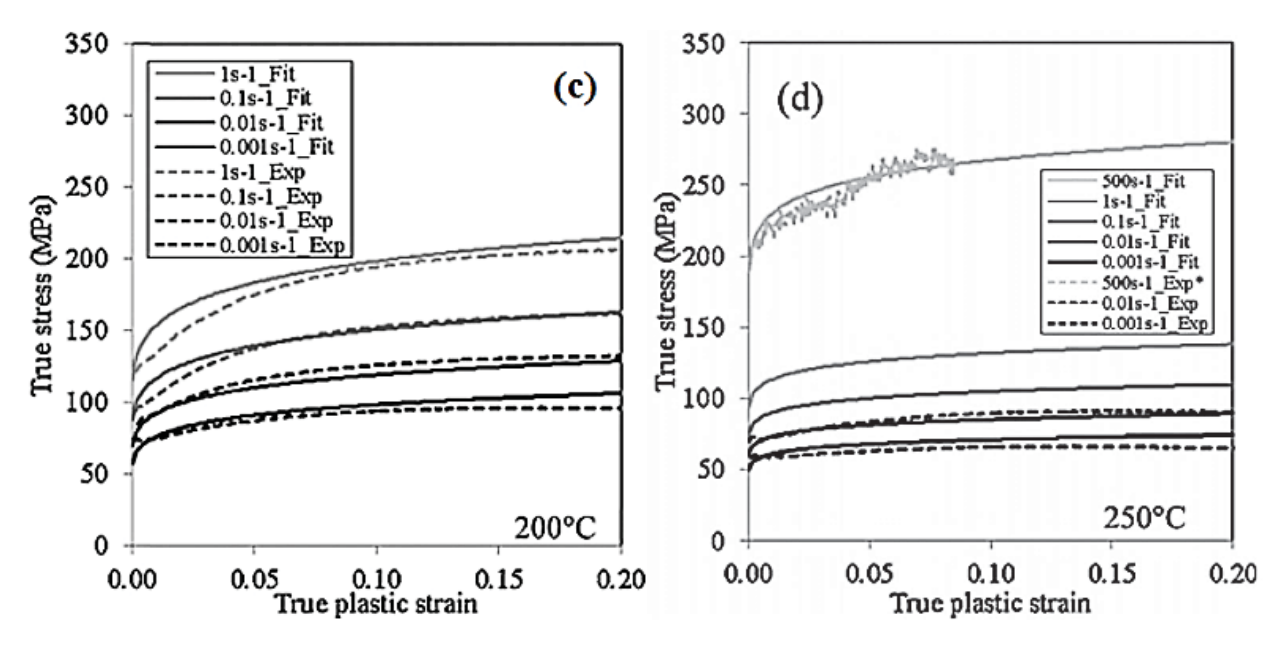


Figure 2.32 Cowper-Symonds fit on the true stress vs. true plastic strain of AZ31B-O under tension loading along the rolling direction at different strain rates and temperatures (a) room temperature, (b) 150° C, (c) 200° C, and (d) 250° C⁸⁰

2.6.3 Modified Johnson-Cook Models

Modifications of the Johnson-Cook model have been developed with simplifications to describe the dynamic behavior of materials considering the coupling effect of temperature, strain rate, and strain.

One modified Johnson-Cook model uses the Cowper-Symonds formulation to replace the strain rate effect expression.⁸¹ Instead of a log-linear relationship, the modified model considers a power law relation for the strain rate dependency of the material to capture the increase in the strain rate sensitivity as the strain rate is increased. The flow stress for the modified Johnson-Cook model is expressed as:

$$\sigma = \left[A + B(\varepsilon)^n \right] \left[1 + \left[\frac{\dot{\varepsilon}}{D} \right]^{\frac{1}{p}} \right] \left[1 - (T^*)^m \right]$$
 (2.23)

A model by Holmquist and Johnson⁸² incorporates a simple modification to the model for a better representation of the strain rate effect as an exponential function. The flow

stress can be expressed as in equation (2.23) from evidence that the strain rate influence on strength of the material is not a linear function of the natural log but rather an exponential function.

$$\sigma = [A + B(\varepsilon)^{n}][(\dot{\varepsilon}^{*})^{C}][1 - (T^{*})^{m}]$$
 (2.24)

Camacho and Ortiz⁸³ adjusted the strain rate sensitivity term C in the original Johnson Cook model to avoid unwanted effects when $\dot{\epsilon}^*$ < 1. This was used as the basis of the coupled constitutive model of viscoplasticity and ductile damage for penetration and impact proposed by Borvik et al.⁸⁴ where the flow stress is expressed as:

$$\sigma = [A + B(\varepsilon)^{n}][1 + \dot{\varepsilon}^{*}]^{C}[1 - (T^{*})^{m}]$$
 (2.25)

Lin et al.⁷³ also modified the Johnson Cook model to predict the high temperature flow stress response of Al-Cu-Mg Alloy. The strain rate constant C was expressed as the function of strain and forming temperature in the model. The coupled effects of strain rate, strain & forming temperature were also considered. There were differences observed between the fitting lines for the different strains and the values of C were shown to decrease with increasing strain. On the basis of this observation and in order to improve the prediction accuracy of the model, the flow stress can be expressed as:

$$\sigma = \left[\sigma_{p} + B(T)\epsilon^{n(T)}\right] \left[1 + C(T, \epsilon) \ln\left(\frac{\dot{\epsilon}}{\dot{\epsilon}_{0}}\right)\right]$$
(2.26)

where B(T) and n(T) are material parameters which are functions of the forming temperature, while $C(T,\epsilon)$ is also a material parameter which represents the effects of strain and forming temperature on the material flow behavior. The term σ_p is the peak stress of the material, if it has no obvious yield stage, under different forming conditions.

Another modified Johnson-Cook model was developed by Hou et al.⁸⁵ to predict the dynamic response of metal even though the current temperatures were higher or lower than the reference temperature. The model showed a good agreement with the experimental data of hot-extruded Mg-10Gd-2Y-0.5Zr under both quasi-static and

dynamic loading and wide range of temperatures. The flow stress is expressed as in equation (2.26), where λ is a material constant.

$$\sigma = (A + B\varepsilon^{n})(1 + C\ln\dot{\varepsilon}^{*})\left(1 - \lambda \frac{e^{T/T_{m}} - e^{T_{r}-T_{m}}}{e^{-e^{T_{r}-T_{m}}}}\right)$$
(2.27)

A modified model for the behavior of typical high strength alloy steel was proposed by Lin et al.⁸⁶ In this model, the yield and strain hardening portion of the original Johnson-Cook equation model were considered as well as the coupled effects of the temperature and strain rate on the flow behavior of the alloy steel. The flow stress in this model is expressed as:

$$\sigma = (A_1 + B_1 \varepsilon + B_2 \varepsilon^2)(1 + C_1 \ln \dot{\varepsilon}^*) \exp[(\lambda_1 + \lambda_2 \ln \dot{\varepsilon}^*)(T - T_r)] \quad (2.28)$$

where A_1 , B_1 , B_2 , C_1 , λ_1 , and λ_2 are the material constants. This modified equation was also utilized by Li et al.⁸⁷ to predict the hot deformation behavior in 28CrMnMoV steel and by He et al.⁶⁶ to predict the high temperature flow stress in 20CrMo alloy steel. Aside from the modified model as in equation (2.27), Lin et al.⁸⁸ also developed a combined Johnson-Cook and Zerilli-Armstrong for the deformation behaviors of high-strength alloy steel. A combination of the yield and strain hardening portion of the Johnson Cook model and the temperature and strain rate portion of the Zerilli-Armstrong model are present in this modified model to better represent the coupled behavior of the temperature and the strain rate effect. The measured average temperature rise (Δ T) is also incorporated in the model to represent the heat of deformation resulting from plastic work which raises the temperature of the specimen. The equation for this model is of the form:

$$\sigma = (A + B\epsilon^{n})\exp[-C_{3}(T + \Delta T) + C_{4}(T + \Delta T)\ln\dot{\epsilon}^{*}]$$
 (2.29)

2.6.4 Zerilli-Armstrong Model

The Zerilli-Armstrong model⁸⁹ proposed in 1987 is one of the most cited semiempirical model. This model is based on dislocation-mechanics theory where the concepts of thermal activation energy and crystal structure of materials are taken into consideration when deriving the flow behavior of a material. According to Zerilli and Armstrong, the flow stress σ_e can be divided into two components, the thermal σ_{th} and the athermal σ_a part which are additively separated.

$$\sigma_{\rm e} = \sigma_{\rm th} + \sigma_{\rm a} \tag{2.30}$$

The thermal portion of the stress σ_{th} is expressed as

$$\sigma_{th} = \frac{mG_0}{A_0b} e^{-\beta T} \tag{2.31}$$

where

$$\beta = 1/T \ln(A/A_0) - 1/T \ln(1 + C_4 \ln \dot{\epsilon})$$
 (2.32)

The different parameters in σ_{th} are the following: m represents the Taylor factor which relates the shear stress to the normal stress, G_0 is the Gibbs free energy of activation at T=0K, A is the dislocation activation area, A_0 is the corresponding area at T=0K, b is the Burgers vector and β is the parameter associated with the strain rate. From the study of Armstrong and Campbell , "the first term on the right hand side of equation (2.32) is effectively constant using the expansion $\ln(1+x) \approx x$ for small values of x". Thus the expressions for the thermal stresses for body centered cubic (BCC) and face centered cubic (FCC) can be simplified as

$$\sigma_{\text{th}} = C_1 \exp(-C_3 T + C_4 T \ln \dot{\epsilon}) \text{ (BCC metals)}$$
 (2.33)

$$\sigma_{th} = C_2 \epsilon^{1/2} \exp(-C_3 T + C_4 T \ln \dot{\epsilon}) \text{ (FCC metals)}$$
 (2.34)

The dislocation activation area A_0 is considered as constant at equations (2.31) and (2.33) and is considered proportional to $\epsilon^{1/2}$ for FCC metals.⁸⁹

The athermal component of the flow stress σ_a is given by the temperature-independent stress and the term for the contribution of the flow stress dependent on the grain size which is combined to the term C_o . The yield stress increases as the grain size decreases and this dependence can be described by the Hall-Petch equation, $\sigma = kd^{1/2}$ where d is the grain diameter and k is constant.

For BCC materials, a separate plastic strain-hardening contribution to the flow stress is also added from an assumed power law dependence on strain rate given by $\Delta \sigma_a = C_5 \epsilon^n$. The flow stress expressions for the two different crystal lattice structures are finally given by

$$\sigma_{e} = C_{o} + C_{1} \exp(-C_{3}T + C_{4}T \ln \dot{\epsilon}) + C_{5}\varepsilon^{n} (BCC)$$
(2.35)

$$\sigma_{\rm e} = C_{\rm o} + C_{\rm 2} \epsilon^{1/2} \exp(-C_{\rm 3}T + C_{\rm 4}T \ln \dot{\epsilon})$$
 (FCC) (2.36)

where T is the absolute temperature (K). The main difference between the two equations is that the plastic strain is uncoupled from strain rate and temperature for BCC metals.

2.6.4.1 Results of Different Zerilli Armstrong Model Fitting

The Zerilli-Armstrong model is commonly used to examine the interrelationship between the flow properties of a material and the deformation microstructure. This model provides a particularly intuitive description of the deformation process based from dislocation mechanics. In this section, the results of different Zerilli-Armstrong model fitting will be discussed.

Lee and Tang⁹¹ used the Zerilli-Armstrong FCC model to describe the mechanical properties of 6061-T6 Al alloy in relation to its microstructural response when impacted at elevated temperatures. A good agreement between the theoretical results using the model and experimental results were observed (Figure 2.33).

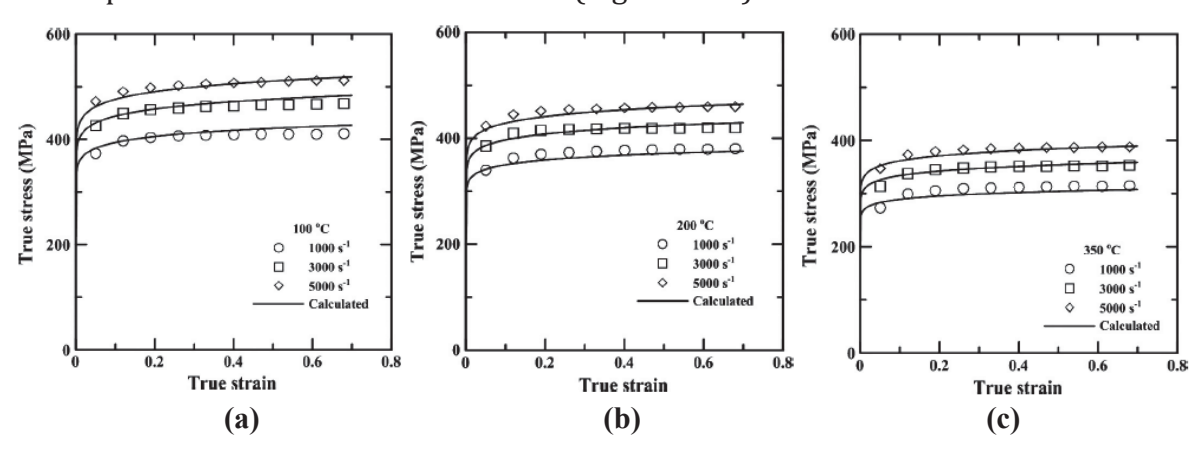


Figure 2.33. Comparison of theoretical and experimental stress-strain curves of 6061-T6 specimen at temperatures of (a) 100°C, (b) 200°C, (c) 350°C⁹¹

The good correlation of the results may be attributed to the integration of the term representing the microstructural evolution (grain size and dislocation cell) during deformation in defining the flow stress. The results from microstructure observations showed that the change in grain size and dislocation cell size is dependent on the strain rate and temperature. The grain size and dislocation cell size increase significantly with decreasing strain rate or increasing temperature and lead to a reduction in the flow stress. On the basis of this microstructural observation, it can be concluded that the flow stress of the specimen is related not only to the strain rate and temperature but also on the grain size and dislocation cell size.

The Zerilli-Armstrong model was again used by Lee and Cao 92 to determine the dynamic deformation behavior of Haynes 188 alloy subjected to high temperature and high strain loading. The model was observed to adequately describe the dynamic response of the specimen. Evidence from the variation of the square root of dislocation density and true stress with strain rate as a function of temperature (Figure 2.34) and variation of flow stress with square root of dislocation density (Figure 2.35) showed that a direct correspondence exists between the dislocation density and the flow stress. The hardening relation term, $\sigma = \sigma_0 + \alpha_1 \text{Gb} \sqrt{\rho}$ relates the flow stress and dislocation density.

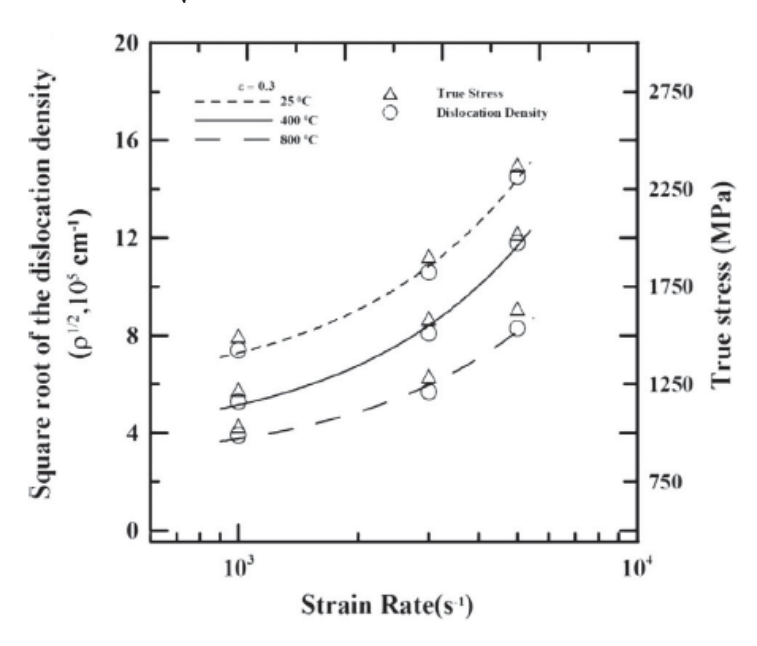


Figure 2.34. Variation of square root of dislocation density and true stress with strain rate as a function of temperature⁹²

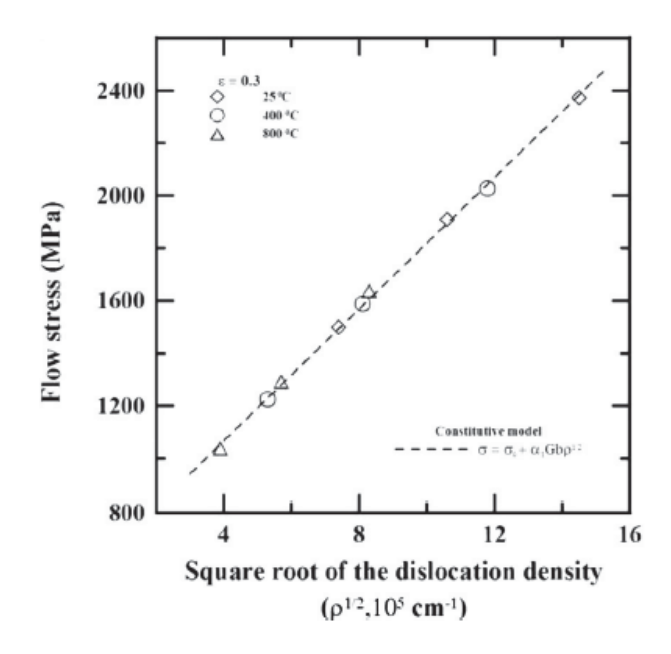


Figure 2.35. Variation of flow stress with square root of dislocation density given constant true strain of 0.3^{92}

Chiou et al.⁹³ also utilized the Zerilli-Armstrong model to determine the effects of strain rate on the dynamic impact deformation behavior of Fe-Mn-Al alloy. Errors within 5% were found after comparing the experimental result and computed results through the Zerilli-Armstrong model.

2.6.5 Modified Zerilli-Armstrong Model

A modified Zerilli-Armstrong model which considers the "effects of isotropic hardening, strain rate hardening, thermal softening, and the coupled effects of temperature and strain and of strain rate and temperature on flow stress" was developed by Samantaray et al.⁹⁴ In this model, the athermal component of the flow stress is neglected and the $C_2\epsilon^n$ component of the original model is represented as $(C_1+C_2\epsilon^n)$ where C_1 represents the yield stress at reference temperature and reference strain and C_2 and n represents the effect of work hardening. The modified Zerilli-Armstrong model for FCC metals is expressed as:

$$\sigma = (C_1 + C_2 \varepsilon^n) \exp \{-(C_3 + C_4 \varepsilon) T^* + (C_5 + C_6 T^*) \ln \dot{\varepsilon}^* \}$$
 (2.42)

In the equation of the flow stress, $T^* = (T - T_{ref})$ where T and T_{ref} are the current and reference temperatures respectively and C_1 , C_2 , C_3 , C_4 , C_5 , C_6 and n are material constants. Samantaray et al.^{74,94} utilized the modified model to predict the flow behavior of modified 9Cr-1Mo steel⁷⁴ and titanium-modified austenitic stainless steel⁹⁴ at elevated temperatures. Results showed that there is a good agreement (in terms of correlation coefficient and absolute average error) between the predicted data of the model with the experimental data over the entire ranges of strain rate, temperature, and strain.

2.7 Summary of Literature Review

IN718 and 300M steel are aerospace materials that are commonly used for high temperature and high strength applications such as in engine rotors and landing gears, respectively. These aircraft parts are manufactured via machining, specifically turning processes, wherein the workpiece material is subjected to severe loads of deformation at elevated temperatures. The review of the high strain rate and temperature properties of IN718 and 300M steel shows that the flow stress increases with increasing strain rate but decreases with increasing temperature. There is interdependence on the effect of the strain rate and temperature on the flow stress of the materials.

The Split-Hopkinson Pressure Bar (SHPB) is one of the apparatus that can perform tests at strain rates ranging from $10^2 \, \text{s}^{-1}$ to $10^4 \, \text{s}^{-1}$, thus can simulate machining conditions and measure the flow stress at dynamic conditions. The major design parameters that must be considered in a SHPB set-up are the Hopkinson bars, specimen dimension and ratio, and pulse shaper.

The literature reports showed that the dynamic behavior of the materials in terms of flow stress data is a very important input for the Finite Element simulation. Therefore, a correct stress-strain relationship must be identified and used in material modelling. It is also necessary to identify the material model that best represents the dynamic deformation characteristics of the materials. The most commonly used material constitutive models that describe the stress-strain behavior of materials at high strain rate and temperature are the

Johnson-Cook model, Cowper-Symonds model, and the Zerilli-Armstrong model. The parameters in the Johnson-Cook & Cowper-Symonds model can be determined relatively easily because the models consider the effect of each parameter (strain, strain rate, and temperature) independently and consider only the macroscopic observations to describe the flow stress. The major difference between these two models is the strain-rate effect relation which is expressed in a log-linear form in the Johnson-Cook model and in a power-law form in the Cowper-Symonds model. The Zerilli-Armstrong model on the other hand is based on the physical processes which consider the microstructural evolution (grain size) in deriving the flow behavior of the material.

The main advantage of Johnson-Cook model over the Zerilli-Armstrong model is the number of materials for which the parameters are known. On the other hand, the advantage of the Zerilli-Armstrong model over the Johnson-Cook model is it is based on physical processes taking place in the deforming material and can therefore more accurately represent the behavior of the material.

The material constitutive models are only guides to characterize the flow stress and it was shown in literature reports that there is no perfect model. The material parameters are varied for the same material thus, it is always necessary to evaluate these material parameters and optimize them to improve the flow stress characteristics which will best suit the machining conditions.

Chapter 3: Experimental Set-up and Procedures

The dynamic behavior in terms of the strain rate and temperature sensitivity of IN718 and 300M steel materials were investigated by performing high strain rate and high temperature Compressive Split-Hopkinson Pressure Bar experiments. The tests were carried out at two different sample dimensions for both the IN718 and 300M steel materials.

3.1 Materials and Experimental Conditions

3.1.1 Inconel 718 (IN718)

The IN718 material used for the tests meets the AMS Specification 5662. The chemical composition of the IN718 is presented in Table 3.1

Table 3.1 Chemical composition of IN718 from manufacturing specification (AMS 5662)

Material			Nomina	ıl Compositi	on <i>wt.%</i>		
Material	Ni	Cr	Mo	Nb	Ti	Al	Fe
IN718	54.03	17.82	2.89	5.08	1.08	0.48	18.53

Two different cylindrical dimensions of the material: 6 mm \times 6 mm and 4 mm \times 4 mm in length and diameter were utilized for the tests. The samples were machined from a 0.5" bar diameter with a hardness of 43 HRC and average grain size of 23 μ m (ASTM Grain Size 8).95

The strain rate sensitivity of the material was characterized by performing room temperature compressive SHPB tests at gas pressures ranging from 100 psi to 220 psi which resulted to strain rates from 10^2 s⁻¹ to 10^3 s⁻¹. Elevated temperature experiments from 250°C to 500°C at varying gas pressures were also performed to determine the thermal softening of the material.

A complete test matrix for room temperature and high temperature tests can be seen in Table 3.2 and Table 3.3 Respectively. Due to the limited number of samples available, only one test for some test conditions were done which is mostly for the 6 mm \times 6 mm

dimension. While at least two tests were carried out for $4 \text{ mm} \times 4 \text{ mm}$ dimension at each condition to ensure measurement repeatability.

Table 3.2 IN718 test matrix showing the number of tests done at room temperature

Sample	Gas Pressure (psi)							
Dimension	100	100 150 180 220						
6 mm × 6 mm		1 1						
4 mm × 4 mm	2	2	2	2				

Table 3.3 IN718 test matrix showing the number of tests done at elevated temperatures

Gas Pressure (ps						(psi)			
Sample Dimension		220		200		180		15	50
Difficusion	250°C	350°C	500°C	250°C	250°C	350°C	500°C	350°C	500°C
6 mm × 6 mm	1	1	2	1	1	1	1	1	1
4 mm × 4 mm		2	2		2	2	2	2	2

3.1.2 300M Steel

The 300M steel material used in this study meets the AMS Specification 6257E. The chemical composition of the 300M steel is presented in Table 3.4.

Table 3.4 Chemical composition of 300M steel from manufacturing specification (AMS 6257E)

Matarial -				Nom	inal Cor	npositi	on <i>wt.</i> 9	%			
Material -	С	Si	Mn	P	S	Cr	Mo	Ni	Cu	V	Al
300M steel	0.42	1.65	0.76	0.007	0.001	0.79	0.38	1.78	0.11	0.077	0.029

The 300M steel samples used for the tests are cylindrical with dimensions of 6 mm \times 6 mm and 4 mm \times 4 mm in length and diameter. The samples were machined from a 0.5" bar diameter with a hardness of $\sim\!55$ HRC and average grain size of 22.6 μm (ASTM Grain Size 8).96

Similar with the IN718 material, the strain rate sensitivity of the material was investigated by performing room temperature compressive SHPB tests at varying gas

pressures (100 psi to 220 psi). The thermal softening of the material was also determined by doing tests at elevated temperatures at 350°C and 500°C at varying gas pressures.

The complete test matrix can be seen in Table 3.5 for room temperature tests and in Table 3.6 for high temperature tests. The limited number of samples with 6 mm \times 6 mm dimension only allowed for one test at elevated temperatures while at least two tests were performed for the samples with 4 mm \times 4 mm dimension for all the test conditions. Also, no room temperature test was done for the 6 mm \times 6 mm sample. Preliminary tests showed that at this dimension, the deformation is insufficient to result to a valid voltage signal, even at the highest gas pressure of 220 psi.

Table 3.5 300M steel test matrix showing the number of tests done at room temperature

Sample	Gas Pressure (psi)					
Dimension	120 150 180 220					
4 mm × 4 mm	1	2	2	2		

Table 3.6 300M steel test matrix showing the number of tests done at elevated temperatures

Campla	Gas Pressure (psi)									
Sample	22	20	18	30	15	50	12	20	10	00
Dimension	350°C	500°C	350°C	500°C	350°C	500°C	350°C	500°C	350°C	500°C
6 mm × 6 mm	1	1	1	1						
4 mm × 4 mm			2		2	2	2	2	2	2

3.2 Compressive Split-Hopkinson Pressure Bar (SHPB) Test

The basic fundamentals of the Split-Hopkinson Pressure Bar were defined in Section 2.3.2. The conventional SHPB system illustrated in Figure 2.13 was utilized in this study. This section introduces the experimental set-up and procedures for room temperature and high temperature test using the Split-Hopkinson Pressure Bar (SHPB) apparatus at the Hot Deformation Laboratory in Wong Building, McGill University.

3.2.1 Room Temperature Compressive Split-Hopkinson Pressure Bar Test

The main components of the SHPB system are the striker, incident and transmitter bars that are mounted and aligned longitudinally using steel supports with bronze sleeves. The striker bar used in the set-up is 14 inches (0.36 m) in length whereas the incident and the transmitter bars are 45 inches (1.14 m) in length. All the three bars are 0.375 inches (9.6 mm) in diameter and are made of VascoMax C350 maraging steel, heat treated and aged to a hardness of 55-60 HRC. A thin disk of multipurpose Aluminum 6160 with a thickness of 0.02 inches (0.5 mm) and diameter of 0.22 inches (5.6 mm) was used as a pulse shaper material. The method of the selection of the pulse shaper material and dimension will be discussed in Chapter 4. Clay was used as a momentum trap at the end of the transmitter bar to dampen the energy and bring the bar to rest. The schematic diagram of the SHPB set-up is shown in Figure 3.1.

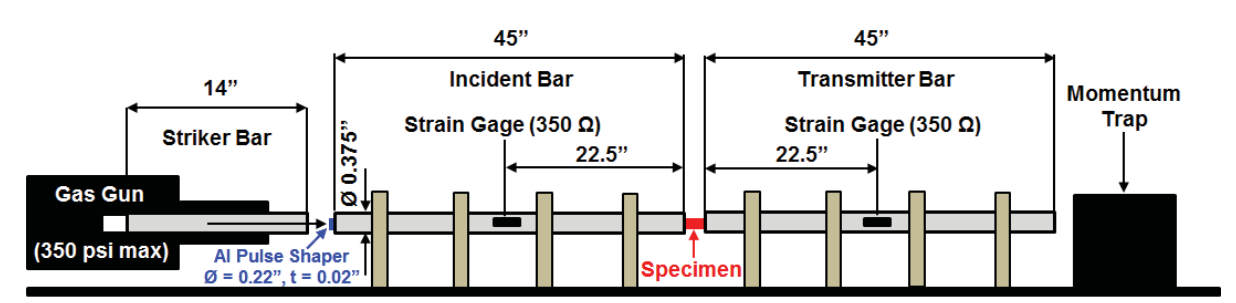


Figure 3.1. Schematic diagram of the SHPB set-up

The density, elastic modulus and uniaxial compressive yield strength of the VascoMax C350 maraging steel pressure bar material are given in Table 3.7. To ensure that the bars remain in linear elastic regime during tests, the maximum stress experienced by the bar at the highest test gas pressure of 220 psi at room temperature was calculated. The bars were tested without a sample (bars together) and a maximum stress of 0.781 GPa was calculated which is below the compressive yield strength of 2.675 GPa of the pressure bar.

1	8 8
VascoMax C350 maragir	ng steel
Density (Kg/m³)	8082.53
Elastic Modulus, E (GPa)	200

2.675

Compressive Yield Strength (GPa)

Table 3.7. Properties of VascoMax C350 maraging steel

The actual SHPB set-up is shown in Figure 3.2. The striker bar is pneumatically accelerated out of the gas gun and impacts the incident bar. Varying the pressure of the gas gun allows for the variation of the impact velocity of the striker bar. The operating gas pressure of the gas gun ranges from $10 - 230\pm 5$ psi. The impact results in the generation of an elastic compressive stress wave (incident wave), that travels through the incident bar and into the specimen. The amplitude of the incident wave is a direct function of the striker bar's impact velocity. To reduce friction and maintain uniaxial compression in the sample, Boron Nitride powder is applied on the flat sides of the specimen to lubricate the interface between the bars and the specimen.

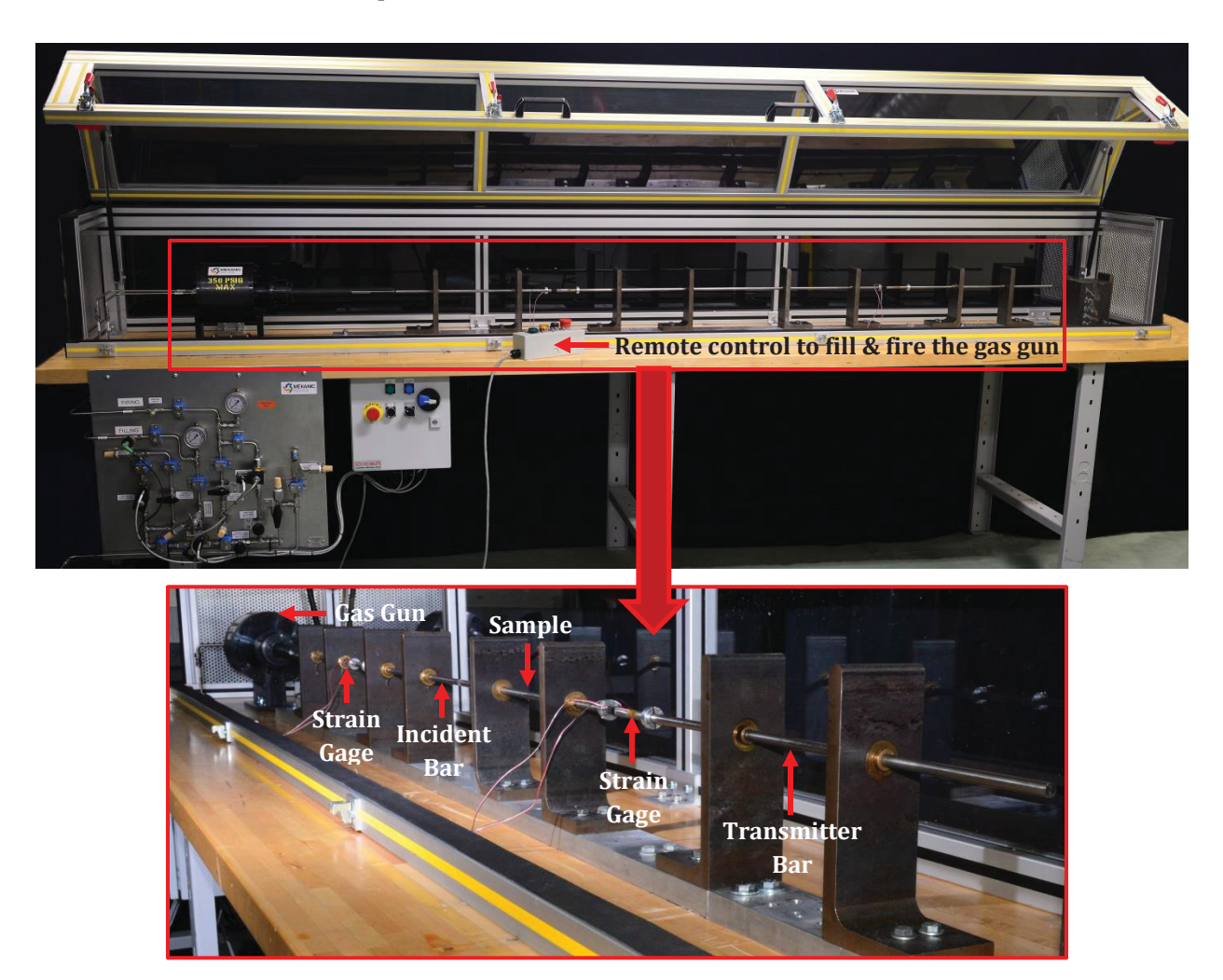


Figure 3.2. McGill Split-Hopkinson Pressure Bar apparatus set-up

The magnitude of the elastic waves propagating in the incident and transmitter bars were recorded by the strain gages attached at each of the bars. The foil strain gages used on the bars were of type EA-06-062AQ-350 LE with a resistance of 350 ohms and gage factor of 2.085 manufactured by Vishay Micro-Measurements. Two strain gages were attached diametrically opposed on the middle of each bar and are equidistant from the specimenbar interface on either side of the specimen. The strain gages were attached at a distance of 22.5 inches from the bar's end. This distance is greater than the length of the striker bar to avoid interference from the reflection signals.⁴⁴ The configuration (diametrically opposed) of the strain gages are intended to cancel out the effect of bending, should there be any. Figure 3.3 shows the position and orientation of one of the strain gages on the bar.

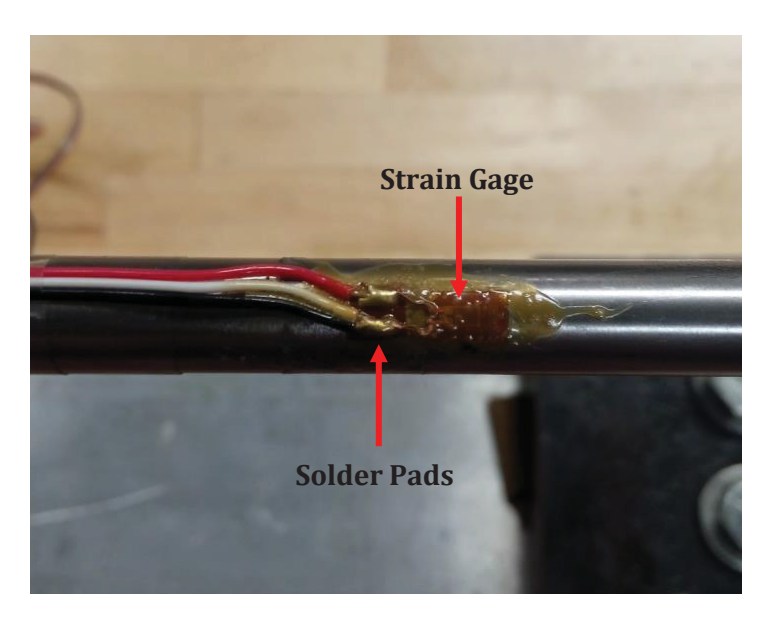


Figure 3.3. Illustration of strain gage attached on the SHPB bar

The strain gages in each of the bar are connected to a Half-Wheatstone bridge configuration as seen in Figure 3.4. The two bridges are powered by a direct current of 10V with an intensity of 0.04 amps. The bridges are connected to a four channel, 12 bit (10 mega samples per second digitizers) Nicolet Pro 40C oscilloscope on which the test result is registered in a form of a voltage history.⁹⁷

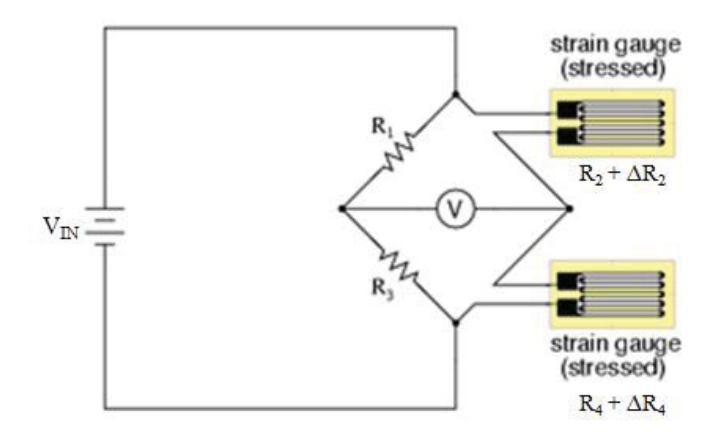


Figure 3.4. Half-Wheatstone bridge configuration in each Hopkinson bar

Figure 3.5 shows the oscilloscope set-up. It is important to note that Channels 2 and 3 on the oscilloscope each represent the incident/reflected and transmitted portions of the waves recorded respectively. The incident pulse is approximately trapezoidal in shape while the shapes of the transmitted and reflected pulses depend on the properties of the tested sample.

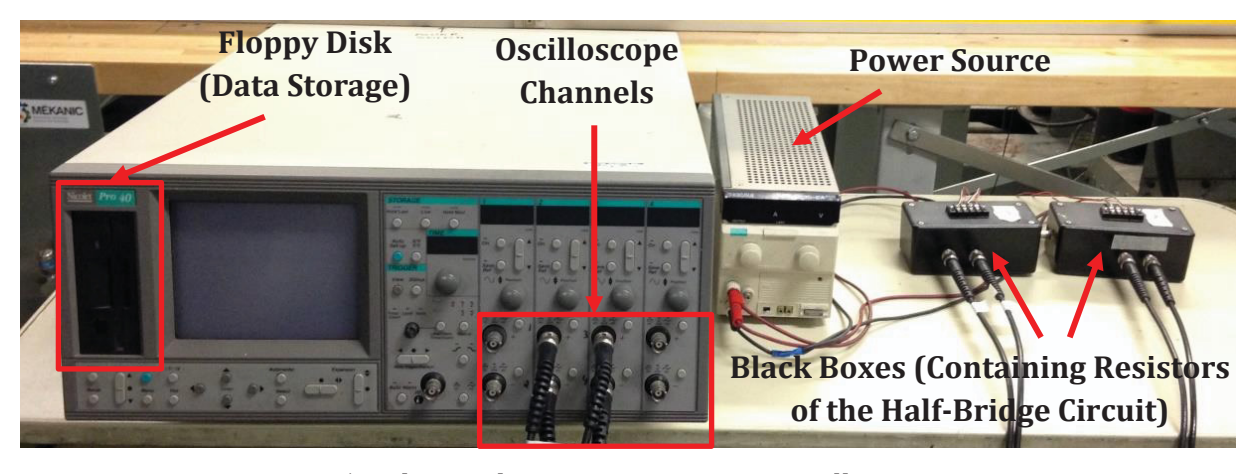


Figure 3.5. Split-Hopkinson Pressure Bar oscilloscope set-up

3.2.2 High Temperature Compressive Split-Hopkinson Pressure Bar Test

Testing the specimens at high temperatures is an essential part of the study in order to determine the effects of temperature on the plastic deformation of the materials. To heat the samples to the desired temperatures, a home-made radiation furnace was used. The

furnace has an operating temperature of up to 500°C. The furnace has four (4) halogen lamps installed on the interior of its wall. The halogen lamp is a 500 Watt Q500T3/CL/130V that is 118 mm in length and has a double ended socket.

For the high temperature test, the radiation furnace was placed at the center of the Hopkinson set-up as shown in Figure 3.6. It encloses the specimen and parts of the pressure bars. A quartz tube is also inserted in the middle of the furnace surrounding the bars and the sample. It protects the lamps from being broken once the sample flies during the impact.

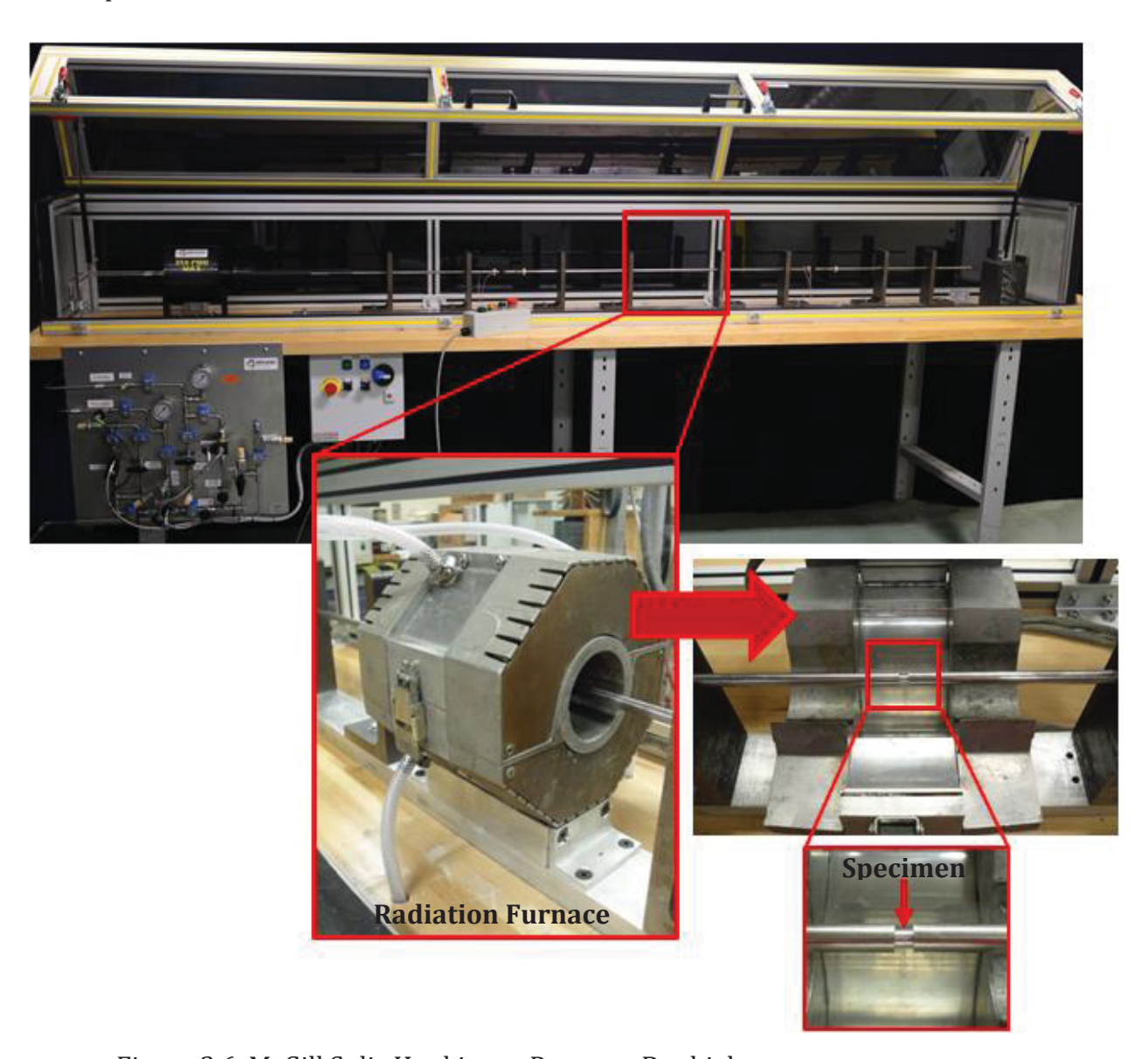


Figure 3.6. McGill Split-Hopkinson Pressure Bar high temperature test set-up

A thermocouple was placed on the sample to measure the heating temperature. As soon as the specimen reached the desired deformation temperature, the safety cover was closed and the striker bar was fired. Immediately before firing, the two Half-Wheatstone bridges are balanced to compensate for any effect of the bar temperature on the strain gages.

Due to the set-up limitation, the sample was heated while being sandwiched by the incident and transmitter bar, thus temperature gradient was produced along the length of the pressure bar. The temperature rise of the bar at varying distance from the center of the furnace was measured by placing additional thermocouples at the transmitted bar. Due to the symmetry of the set-up, the temperature rise was considered to be similar on both the incident and transmitted bars. At the highest deformation temperature of 500°C, the temperature of the bar 3.25 inches from the center of the furnace (just right at the edge of the furnace) is 114°C. The part of the bar where the strain gages are attached remained to be at room temperature (22°C). The measured thermal gradient in the bar is shown in Figure 3.7.

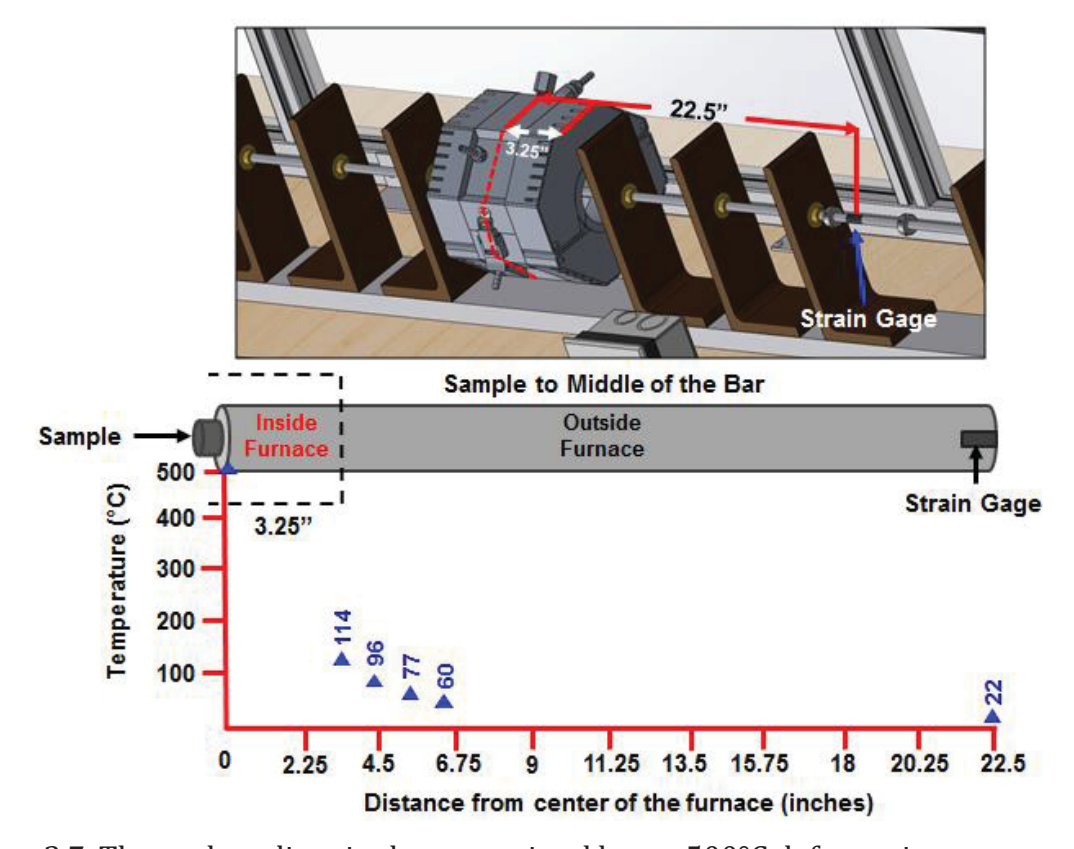


Figure 3.7. Thermal gradient in the transmitted bar at 500°C deformation temperature

The temperature rise in the bar can affect its elastic modulus, the phase velocity of the waves travelling through the bar and the resulting stress-strain data. Chiddister and Malvern⁴⁹ and Lindholm and Yeakley⁹⁸ devised a procedure on how to correct for the effects of the thermal gradient in the bar. In this study, the effects of thermal gradient on the resulting stress-strain data were not corrected as the temperature rise is not high enough to significantly decrease the elastic modulus of the bar. A 100°C temperature rise changes the elastic modulus of the C350 maraging Steel by a maximum of 2%^{99,100} which is not enough to alter the results of the test. However, the effects of thermal gradients must be numerically corrected particularly when the temperature rise is 600°C or higher in steel bars.¹⁰¹

3.2.3 Data Acquisition and Processing

A sample output data (voltage-time) from the strain gages on the Hopkinson bars in this study is shown in Figure 3.8. The time at which the waves start picking up in magnitude is not the same for the reflected and transmitted waves. A signal artifact can also be seen prior to the transmitted wave. As illustrated in Figure 3.7, the start time (time zero) of the reflected wave appeared earlier than the start time (time zero) of the transmitted wave which appeared after the signal artifact.

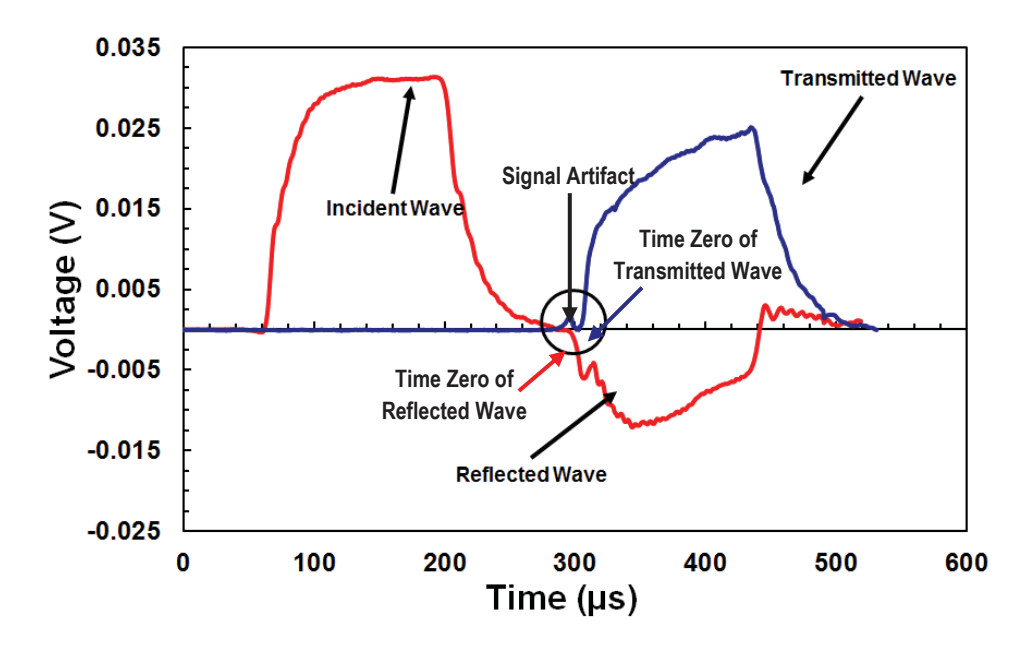


Figure 3.8. Sample output signal from compressive SHPB test

The difference in the start time is attributed to the fact that the incident wave is immediately reflected at the incident bar/specimen interface while the transmitted wave takes some time to travel to the specimen/transmitted bar interface. Thus, it is important to note that the time zero must be defined for each reflected and transmitted wave, getting rid of any signal artifacts. These two points must be chosen correctly and correlated to each other to obtain consistent and repeatable results.

The voltage-time signals captured by the oscilloscope from each bar are then converted to their respective micro-strains as in equations 3.1 to 3.3, where v_i , v_r and v_t are the recorded test voltages, v_{input} is 10V and gage factor \emptyset is 2.085. These microstrains are then used to calculate for the engineering stress, strain, and strain-rate of the sample tested as in equations 2.12 to 2.14.

$$\varepsilon_i(t) = \frac{2*v_i(t)}{v_{input}*\emptyset} \tag{3.1}$$

$$\varepsilon_r(t) = \frac{2*v_r(t)}{v_{input}*\emptyset} \tag{3.2}$$

$$\varepsilon_t(t) = \frac{2*v_t(t)}{v_{input}*\emptyset} \tag{3.3}$$

Once the engineering stress and strain are determined, the true stress and true strain can be calculated using equations 3.4 and 3.5 respectively.

$$\sigma_{true} = \sigma_{eng} (1 - \varepsilon_{eng})$$
 (3.4)

$$\varepsilon_{true} = -\ln(1 - \varepsilon_{eng}) \tag{3.5}$$

A time history plot of the stress, strain rate and strain obtained from the waves in Figure 3.8 are shown in Figures 3.9 and 3.10.

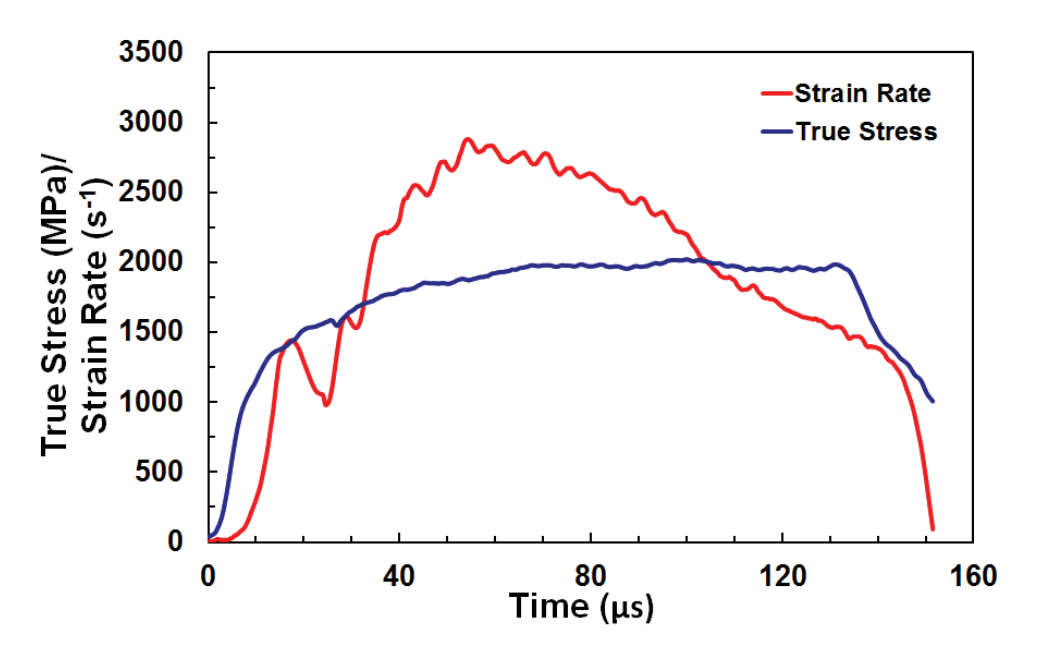


Figure 3.9. Strain rate and true stress time history of a compressive SHPB test

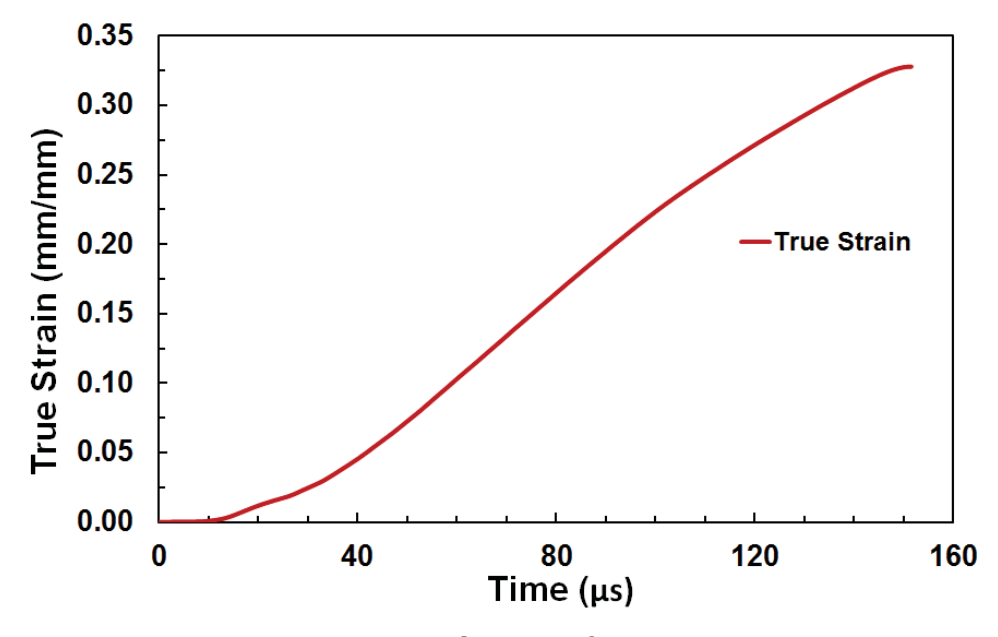


Figure 3.10. True strain time history of a compressive SHPB test

Chapter 4: Pulse Shaping Results

As mentioned in Chapter 3, Section 3.2.1, an Aluminum 6061 pulse shaper with a 5.6 mm \varnothing and 0.5 mm thickness was utilized in all the tests. The details of how this particular pulse shaper was chosen will be discussed in this chapter.

4.1 Evaluation of Pulse Shaper

The shape of the incident pulse was modified from a rectangular shape with high oscillations to a ramp shape by using a "tip material" or pulse shaper attached to the face of the incident bar where the striker bar impacts. Two (2) pulse shaper materials that are commonly used in the literature, 53,56,62 Multipurpose Aluminum 6061 and Multipurpose 110 Copper with dimensions shown in Table 4.1 were chosen and assessed.

Table 4.1 Test matrix for the Al6061 and Cu110 pulse shaper selection

Material	Diameter (mm)	Thickness (mm)	Gas Pressure (psi)	No. of Tests
		0.5	50	2
		1.0	50	2
Multipurpose	5.6	1.0	100	2
Aluminum		2.0	50	2
6061		2.0	100	2
(Al6061)		0.5		2
	3.175	1	50	2
		2		2
		0.5		2
Markinson	5.6	1	50	2
Multipurpose 110 Copper		2		2
(110Cu)		0.5		2
(1100u)	3.175	1	50	2
		2		2

The effect of the pulse shapers on the shape of the incident signal was evaluated by testing the Hopkinson bars together without a sample as illustrated in Figure 4.1. All the tests were done at a gas pressure of 50 psi with some also done at a gas pressure of 100 psi.

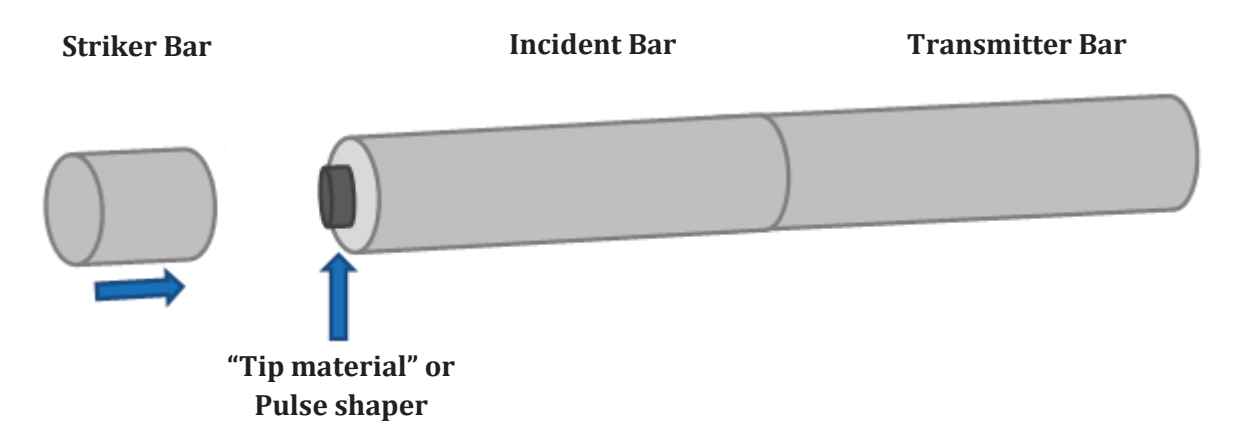


Figure 4.1. Pulse shaping technique using a "tip material" or pulse shaper

As discussed by Naghdabadi et al.⁵³ the ramp shaped incident pulse generally consists of four regions as shown in Figure 4.2. The duration of each region depends on the dimension (thickness and diameter) of the pulse shaper, the length of the striker bar and its velocity. In this study, the dimensions of the Al6061 and 110Cu pulse shaper materials were evaluated. The effects of the thickness and diameter of two pulse shaper materials on the shape of the incident pulse presented in a voltage-time plot will be discussed in this section.

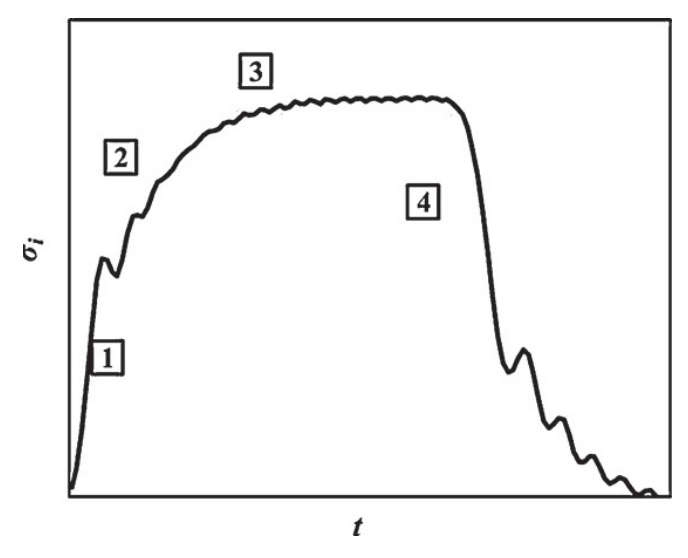


Figure 4.2. A typical ramp shaped incident pulse consisting of four regions: (1), (2), (3), and $(4)^{53}$

Four regions of a ramp shaped incident pulse⁵³:

- (1) Elastic deformation of the pulse shaper during loading
- (2) Plastic deformation of the pulse shaper during loading
- (3) Rigid mode of the pulse shaper (maximum plastic deformation of the pulse shaper)
- (4) Elastic deformation of the pulse shaper during unloading

4.1.1 Effect of Pulse Shaper Thickness

The effect of the Al6061 and 110Cu pulse shaper thickness (0.5 mm vs. 1 mm) for a diameter of 5.6 mm and 3.175 mm are shown in Figures 4.3 and 4.4 respectively. The striker bar velocity used for the tests measured using high speed camera is 12 m/s (50 psi). It can be observed that the initial high rising portion and oscillations in the incident pulse produced without using a pulse shaper were removed and minimized by using the Al6061 and 110Cu pulse shapers.

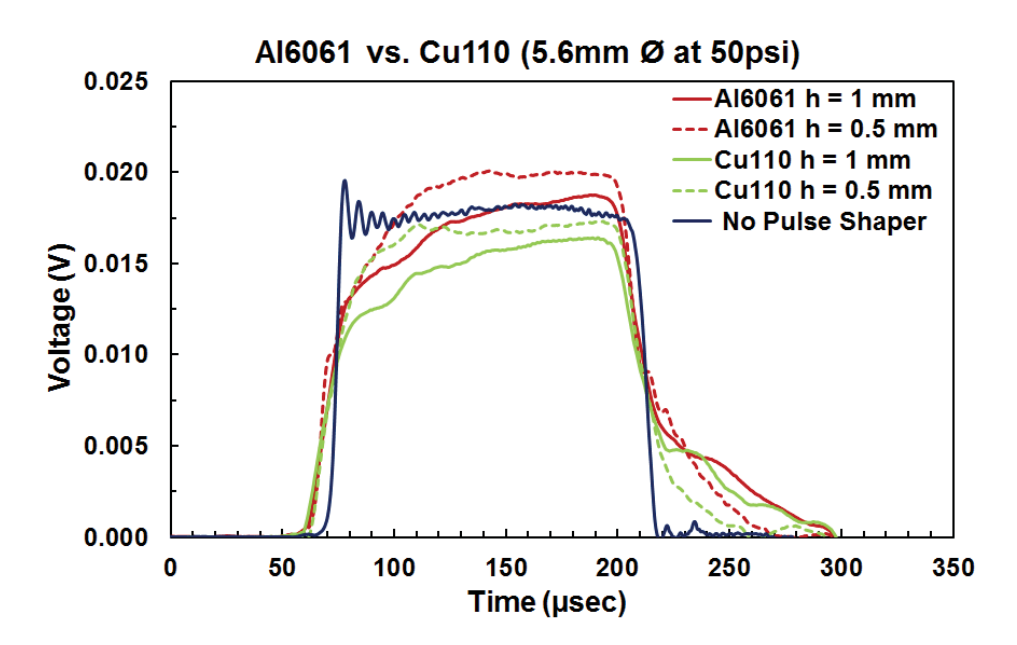


Figure 4.3. Profile of incident pulse using 5.6 mm \varnothing Al6061 and Cu110 pulse shaper with 0.5 mm and 1.00 mm thickness

For the diameter of 5.6 mm (Fig. 4.3), it can be seen that the rise time and duration of the incident pulse increased as the thickness of the pulse shaper is increased. The 1 mm thick pulse shapers have a rise time of $\sim 60~\mu s$ compared to a $\sim 40~\mu s$ rise time of for 0.5 mm thick pulse shapers. The end point of the plastic deformation (end point of region 2 illustrated in Fig. 4.2) is mostly affected by the increase in the pulse shaper thickness. The 1 mm thick pulse shaper for both materials produced a better ramp shaped incident pulse compared to the 0.5 mm thick pulse shaper. The Al6061 pulse shaper has higher incident

pulse amplitude than the 110Cu pulse shaper due to its lower compressive strength and higher deformation resulting to more compressive forces transferred into the incident bar.

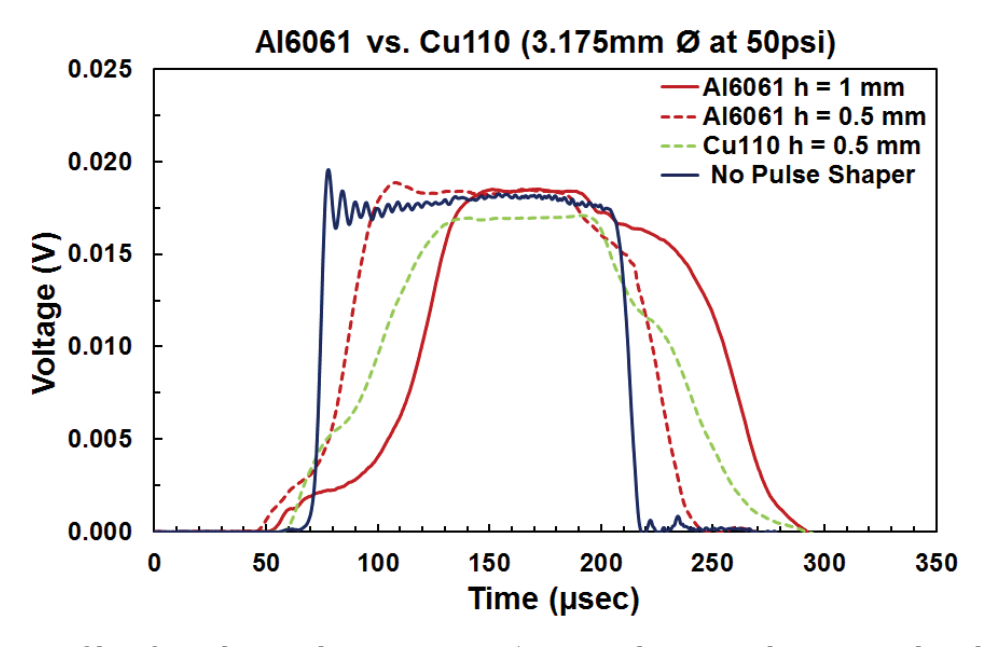


Figure 4.4. Profile of incident pulse using 3.175 mm Ø Al6061 and Cu110 pulse shaper with 0.5 mm and 1.00 mm thickness

For the diameter of 3.175 mm (Fig.4.4), no incident pulse was recorded for 1 mm thick 110Cu pulse shaper. It can also be observed that at this diameter, the incident pulse ramps down as the thickness of the pulse shaper is increased.

Also, no incident signals were recorded for 2 mm thick pulse shaper for both materials and diameters. This may be because 2 mm is thick enough to dampen and absorb the compressive forces thus none is transferred and recorded in the incident bar.

4.1.2 Effect of Pulse Shaper Diameter

The effect of the Al6061 and 110Cu pulse shaper diameters (3.175 mm vs. 5.6 mm) for a thickness of 0.5 mm and 1 mm are shown in Figures 4.5 and 4.6 respectively. The high rising portion and oscillations in the incident pulse produced without a pulse shaper were removed and minimized with the use of the Al6061 and 110Cu pulse shapers.

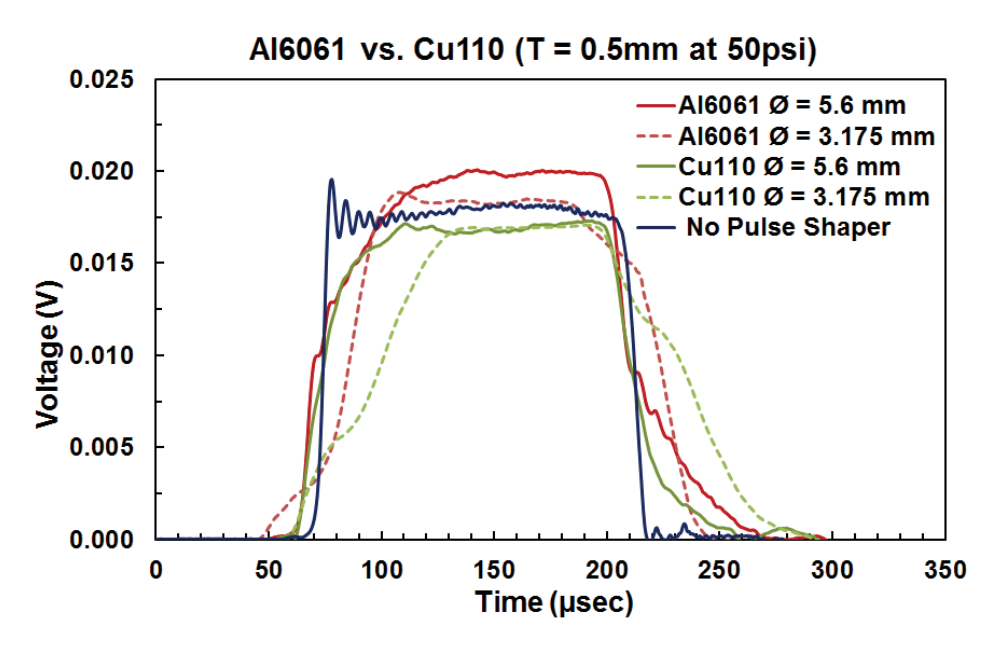


Figure 4.5. Profile of the incident pulse using 0.5 mm thick Al6061 and Cu110 pulse shaper with 5.6mm and 3.175mm \varnothing

For the thickness of 0.5 mm (Fig. 4.5), it can be seen that the rise time and duration of the incident pulse decreased as the diameter of the pulse shaper is increased. It can also be noted that the start point of the plastic deformation in the pulse shaper (start point of region 2 illustrated in Fig. 4.2) is strongly affected by the pulse shaper diameter.⁵³ Comparing the diameters at 0.5 mm thickness, the Al6061 with 5.6 mm diameter produced the best ramp shaped incident pulse.

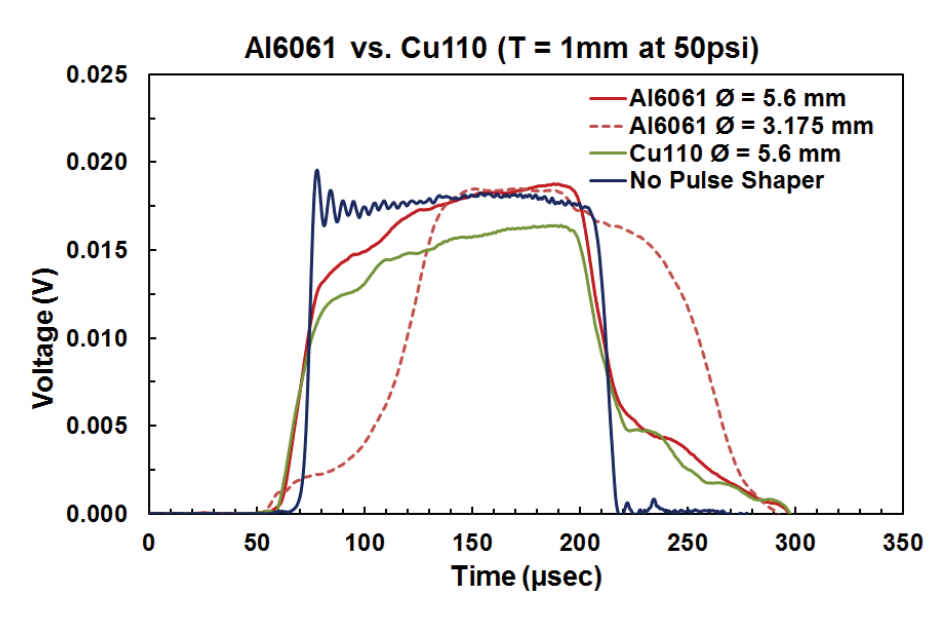


Figure 4.6. Profile of the incident pulse using 1 mm thick Al6061 and Cu110 pulse shaper with 5.6 mm and 3.175 mm \varnothing

For the thickness of 1 mm (Fig. 4.6), no incident pulse was recorded for 5.6 mm diameter 110Cu pulse shaper. Similar with the result for 0.5 mm thick pulse shaper, the start point of the plastic deformation in the pulse shaper (start point of region 2 illustrated in Fig. 4.2)⁵³ is strongly affected by the change in pulse shaper diameter which caused the incident wave for Al6061 to ramp down instead at a diameter of 3.175 mm. Comparing the diameters at 1 mm thickness, the Al6061 and 110Cu pulse shapers with 5.6 mm diameter produced the best ramp shaped incident pulse, although the Al6061 pulse shaper has higher incident pulse amplitude.

Based from the results of the pulse shaping evaluation, the Al6061 pulse shaper with a diameter of 5.6 mm ø with either 0.5 mm or 1 mm thickness resulted in a good incident pulse profile and high rise time, and thus can be either chosen as the shaper material. However in this study, the 0.5 mm thickness Al6061 was selected instead due to its higher amplitude and higher achievable strain rate. The operating gas pressure of the SHPB set-up is limited only to 250psi. In order to achieve higher strain rates, a thinner shaper that will not absorb or dampen too much of the compressive force needed for greater specimen

deformation was selected. The thinner shaper will allow the transfer of compressive force into the specimen being tested.

Chapter 5: Experimental Results and Discussion

The data generated from the room temperature and high temperature Split-Hopkinson Pressure Bar tests will be presented in this chapter. In this study, the experimental variables that can be controlled are the gas pressure of the gas gun that is used to launch the striker bar and the temperature of the specimen.

The strain rate of the tested specimen is dependent on the impact velocity of the striker bar which is controlled by the gas pressure used to launch the striker bar. A gas pressure that could produce a certain strain rate at a certain test temperature is not known. Thus, in order to determine the effect of the strain rate and temperature on the flow stress of the materials, the high strain rate experiments were performed at different gas pressures from 100 psi to 220 psi and elevated temperatures from 250°C to 500°C. The combination of the various gas pressures and temperatures yielded different strain rates. The calculation of the actual strain rate measured for each test will be discussed in this chapter.

The experimental stress-strain curves at a constant temperature with increasing strain rates were compared to evaluate the strain rate effect, while the experimental stress-strain curves at a constant strain rate with increasing temperatures were compared to evaluate the temperature effect.

5.1 Actual and Nominal Strain Rate

The actual strain rate for each test was measured based on the strain history of the flow stress and its corresponding strain rate. The actual strain rate is the average of the strain rate values, starting from the portion after the ring-up period up to the maximum strain of the flow stress before unloading (Fig. 5.1 and 5.2).

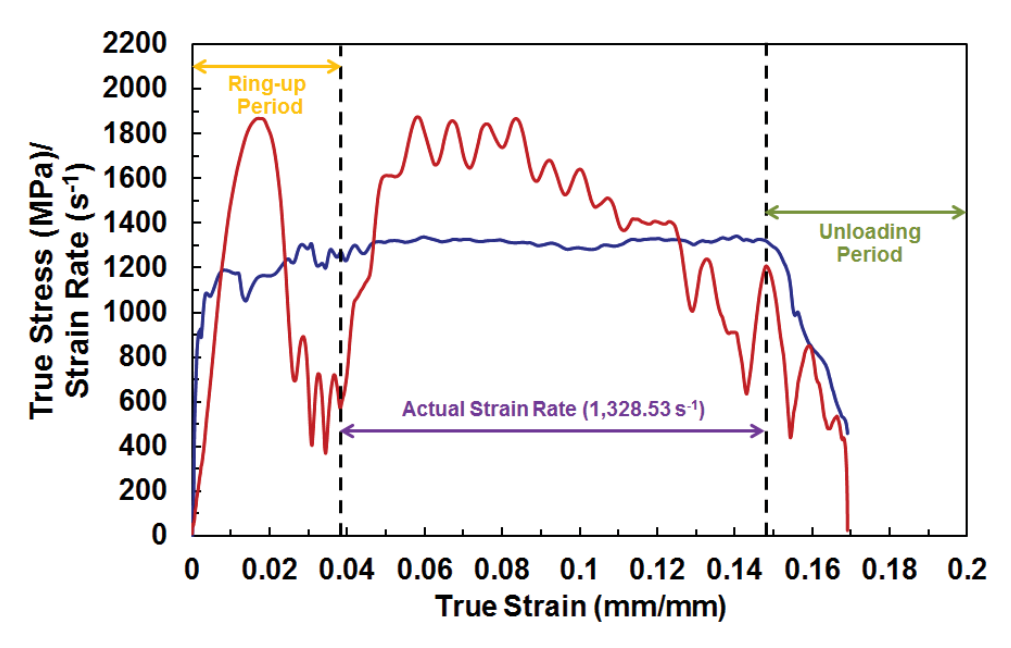


Figure 5.1. True stress and strain rate vs. true strain plot for IN718 6mm \times 6mm sample (500°C, 220 psi)

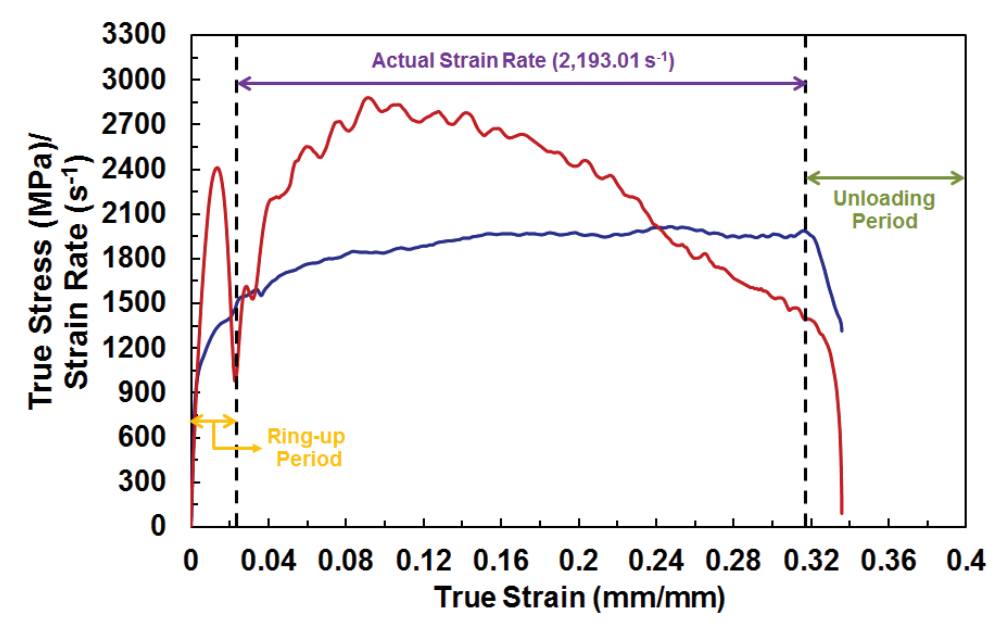


Figure 5.2. True stress and strain rate vs. true strain plot for IN718 4mm \times 4mm sample (22°C, 180 psi)

The ring-up period in the strain rate vs. strain plot is characterized by the high initial portion in the strain rate curve. This happens at the first 20-30% of the total deformation of the material for 6 mm \times 6 mm samples and 10-15% of the total material deformation for

the 4mm \times 4mm samples. The bigger sample dimension (in particular the length) has a longer ring-up period due to the longer time needed for the pulses to traverse the entire specimen and achieve a state of mechanical equilibrium. Figures 5.1 and 5.2 illustrate the portion of the strain rate curve for a representative 6 mm \times 6 mm and 4 mm \times 4 mm samples that are used to calculate the actual strain rate of the test.

The actual strain rate yielded from different gas pressures and varying temperatures were rounded to a nominal strain rate value. The actual strain rate value remains very close to the nominal one with a maximum difference of 10%.

5.2 Flow Stress of IN718

The combination of gas pressures and temperatures resulted in various strain rate values. The results for 6 mm \times 6 mm IN718 samples are shown in Table 5.1 while the results for 4 mm \times 4 mm IN718 samples are shown in Table 5.2. The smaller sample dimension was mostly used in the experiments as it resulted to more deformation and gave a signal with less ring-up period. Initial tests using the 6 mm \times 6 mm dimension showed gross ringing in the signals especially at low gas pressures. The nominal value of the strain rates that will be used to compare the flow stresses were also shown in the tables.

Table 5.1. Test condition matrix and strain rates of 6 mm × 6 mm IN718 samples

Temperature (°C)	Gas Pressure (psi)	Total No. of Tests	Actual & Nominal Strain Rate (s ⁻¹)
22	220	1	521.72 (~500)
22	180	1	327.44 (~300)
	220		878.78 (~900)
250	200	1	814.73 (~800)
	180		524.32 (~500)
	220		823.85 (~800)
350	180	1	724.93 (~700)
	150		546.63 (~500)
500	220	2	1,260.38 (~1,300)
	180	1	1,035.85 (~1,000)
	150		672.47 (~700)

Table 5.2. Test condition matrix and strain rates of 4 mm × 4 mm IN718 samples

Temperature (°C)	Gas Pressure (psi)	Total No. of Tests	Actual & Nominal Strain Rate (s ⁻¹)
	220		2,599.94 (~2,600)
22	180	2	2,193.01 (~2,200)
22	150	<u></u>	2,024.97 (~2,000)
	100		816.63 (~800)
250	180	2	2,193.39 (~2,200)
	220		3,284.06 (~3,300)
350	180	2	2,445.24 (~2,400)
	150		2,208.02 (~2,200)
500	220		3,470.78 (~3,500)
	180	2	2,775.20 (~2,800)
	150		2,214.85 (~2,200)

5.2.1 Effect of Strain Rate on the Flow Stress of IN718

The effect of strain rate on the flow stress of IN718 was investigated by plotting the stress-strain curves at a given temperature over a range of strain rates. Figures 5.3 to 5.6 show the true stress vs. true strain plots at constant temperatures of 500, 350, 250, and 22°C. The four figures only show one representative stress-strain curve for each strain rate although these tests have at least 2 repeats as shown in Tables 5.1 and 5.2.

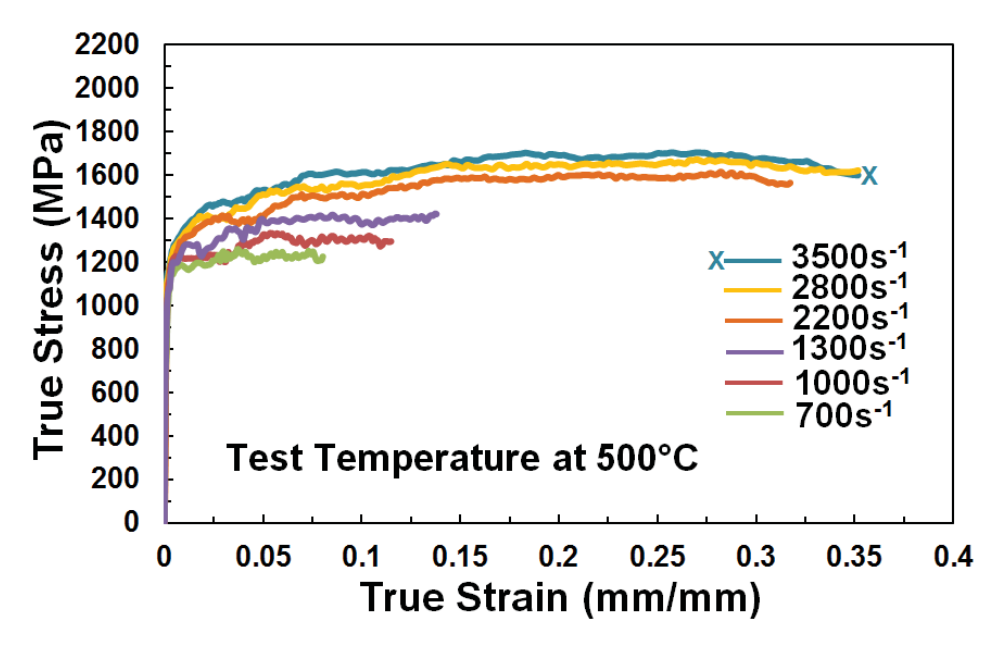


Figure 5.3. IN718 true stress vs. true strain plot at 500° C and nominal strain rates of 700, 1,000, 1,300, 2,200, 2,800, and 3,500 s⁻¹. (X mark on the stress-strain curve at 3,500 s⁻¹ denotes fractured specimen)

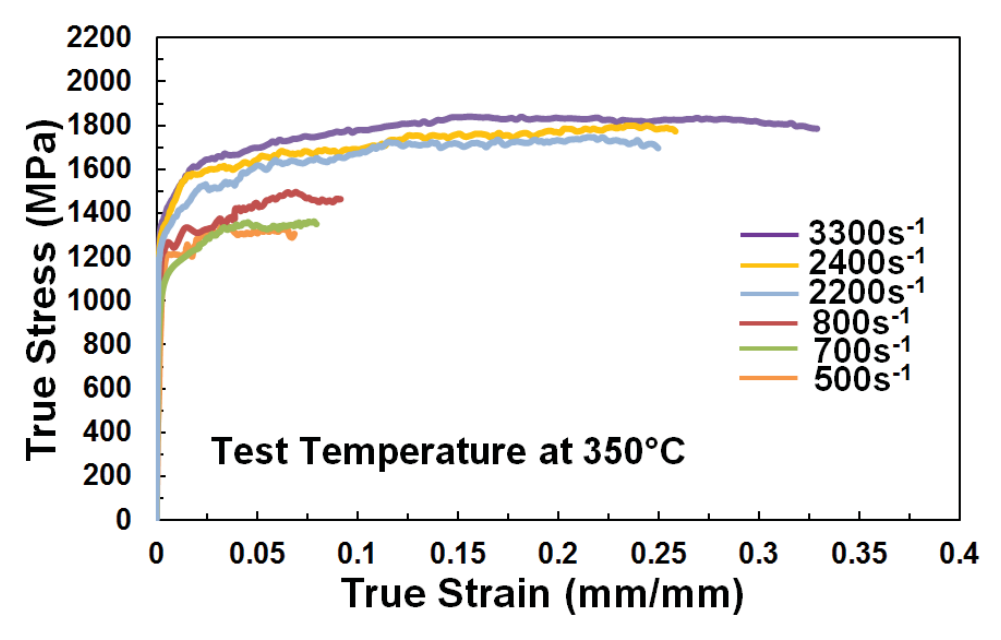


Figure 5.4. IN718 true stress vs. true strain plot at 350° C and nominal strain rates of 500, 700, 800, 2,200, 2,400, and 3,300 s⁻¹

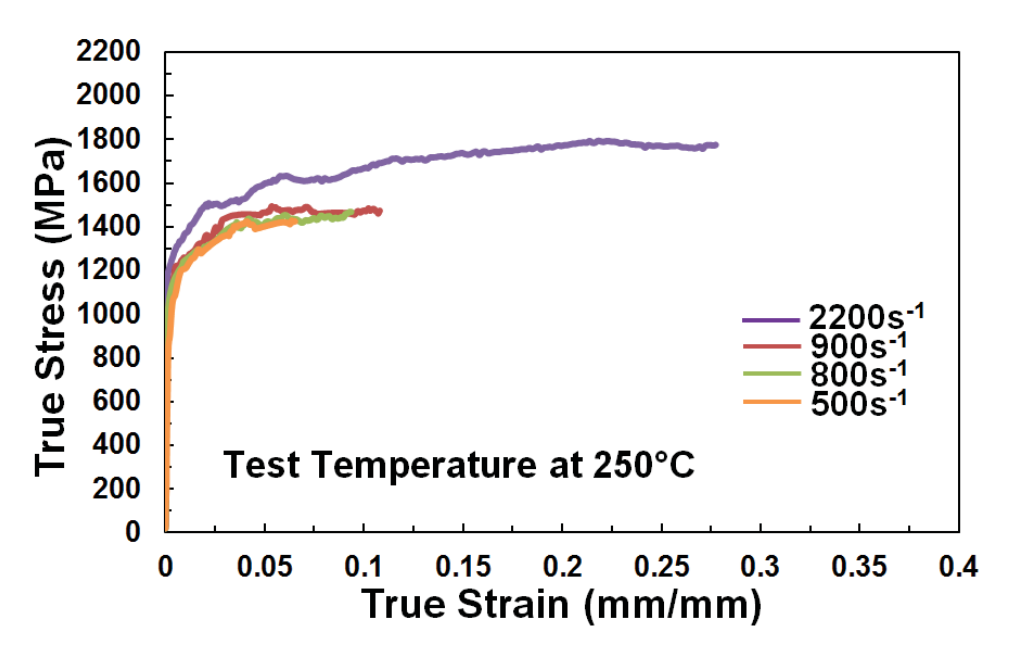


Figure 5.5. IN718 true stress vs. true strain plot at 250°C and nominal strain rates of 500, 800, 900, and $2,200 \, s^{-1}$

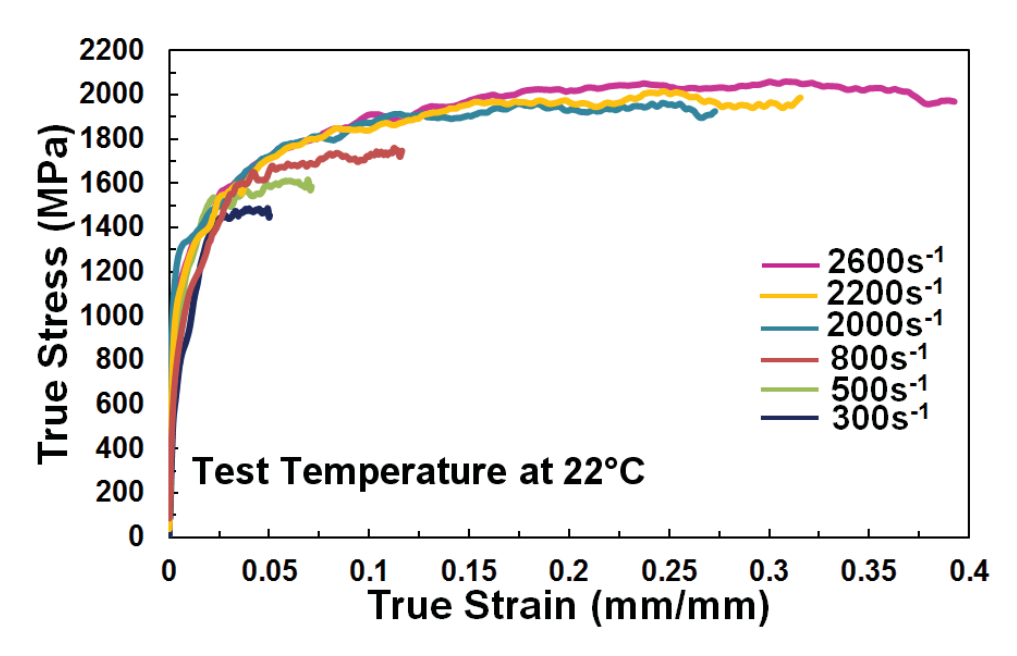


Figure 5.6. IN718 true stress vs. true strain plot at 22°C and nominal strain rates of 300, 500, 800, 2,000, 2,200, and 2,600 $\rm s^{-1}$

The Split-Hopkinson testing covered strain rates from 3×10^2 s⁻¹ to $\sim3\times10^3$ s⁻¹. The maximum strain rate of 3,500 s⁻¹ was achieved at a deformation temperature of 500°C and

this resulted to the failure of the material in shear. Deformed 4mm \times 4mm IN718 samples at the highest achieved strain rate at deformation temperatures of 22°C, 350°C, and 500°C are shown in Figure 5.7.

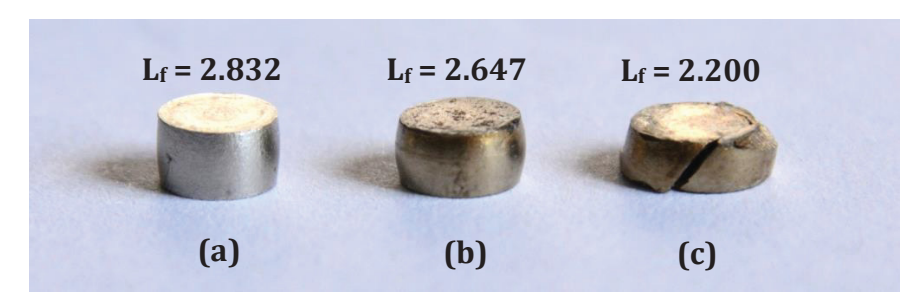


Figure 5.7. Deformed 4 mm \times 4 mm IN718 samples tested at a temperature and strain rate of (a) 22°C and 2,600 s⁻¹ (b) 350°C and 3,300 s⁻¹, and (c) 500°C and 3,500 s⁻¹

As the strain rate increases, the flow stress of IN718 also increases (Fig. 5.3 to 5.6). Previous studies have shown that this response of the material can be attributed to the increased rate of dislocation generation at the grain boundaries resulting in dislocation pile-up and entanglement,²² increased influence of dislocation drag mechanism,¹⁰³ and rapid twin structures formation¹⁰⁴ which prompts a corresponding increase in the plastic flow resistance. Similar behavior of IN718 is reported on the studies of Pereira and Lerch,¹⁰⁵ DeMange et al.⁷¹ Lee et al.²³ and Wang et al.²⁴

Each flow stress curve in the plots (Fig. 5.3 to 5.6) increases quickly at the onset of dynamic plastic deformation, but increases more slowly at larger strains. This behavior can be quantified in terms of the work hardening rate of the material by comparing the slopes of the stress-strain curves. The variation of the work hardening rate with temperature at strain rates of 500, 800, and 2,200 s⁻¹ and true strains of 0.04 and 0.07 were plotted in Figure 5.8.

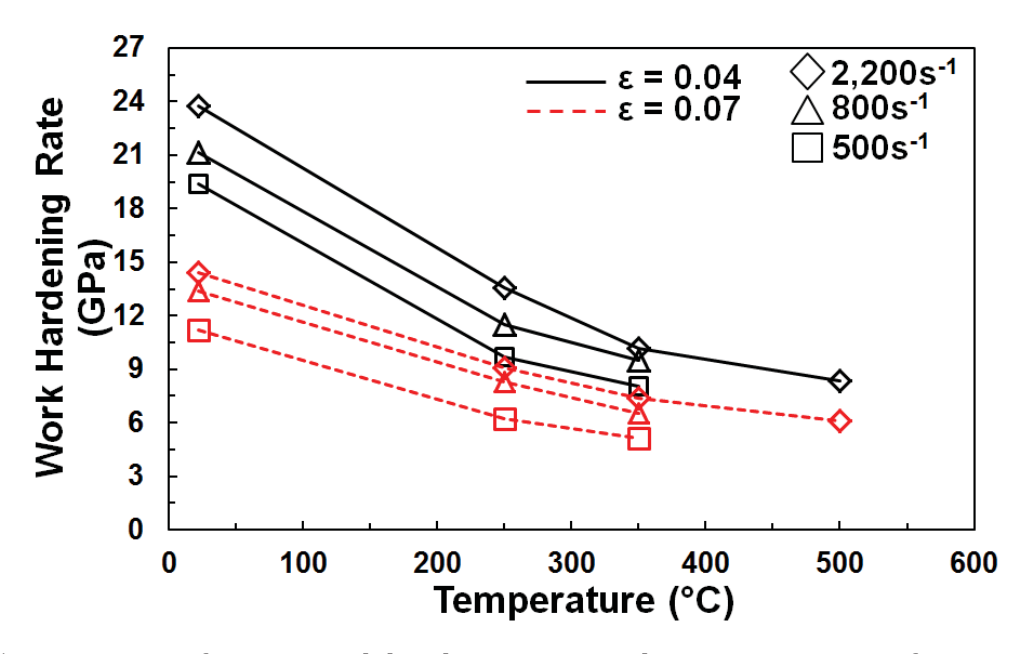


Figure 5.8. Variation of IN718 work hardening rate with temperature as a function of strain rate (500, 800 and 2,200 s⁻¹) and true strain (ϵ = 0.04 and ϵ = 0.07)

At a true strain of 0.04, the maximum work hardening occurs at the highest strain rate of 2,200 s⁻¹ at all deformation temperatures. The same trend was seen for a true strain of 0.07, although the work hardening rates are lower compared to those at 0.04 true strain. Also, the work hardening rate decreases with increasing temperature for a constant value of strain and strain rate.

In dynamic impact tests such as the ones performed in this study, the plastic work done during the deformation generates heat that causes a temperature increase in the material. This is due to the fact that the Hopkinson test is a fast deformation process wherein the heat generated has little time to dissipate to the surrounding. 106,107 consequently, the material may experience a thermal softening effect due to adiabatic heating. The deformation-induced temperature rise (ΔT) can be calculated using the integral equation 5.1 which is a function of the material's density ρ and specific heat capacity C_p , and where n is the coefficient of heat conversion ≈ 1 , σ is the stress, and d_{ε} is the strain interval.

$$\Delta T = \int_0^\varepsilon \frac{n}{\rho c_p} \sigma d_\varepsilon \tag{5.1}$$

The variation of the temperature rise, ΔT with true strain as a function of strain rate and temperature was calculated using Eq. 5.1 and plotted in Figure 5.9. The temperature rise increases with increasing strain rate and decreasing temperature. The highest temperature rise (maximum thermal softening effect) in the material occurs at the highest strain rate (2,200 s⁻¹) and lowest temperature (22°C).

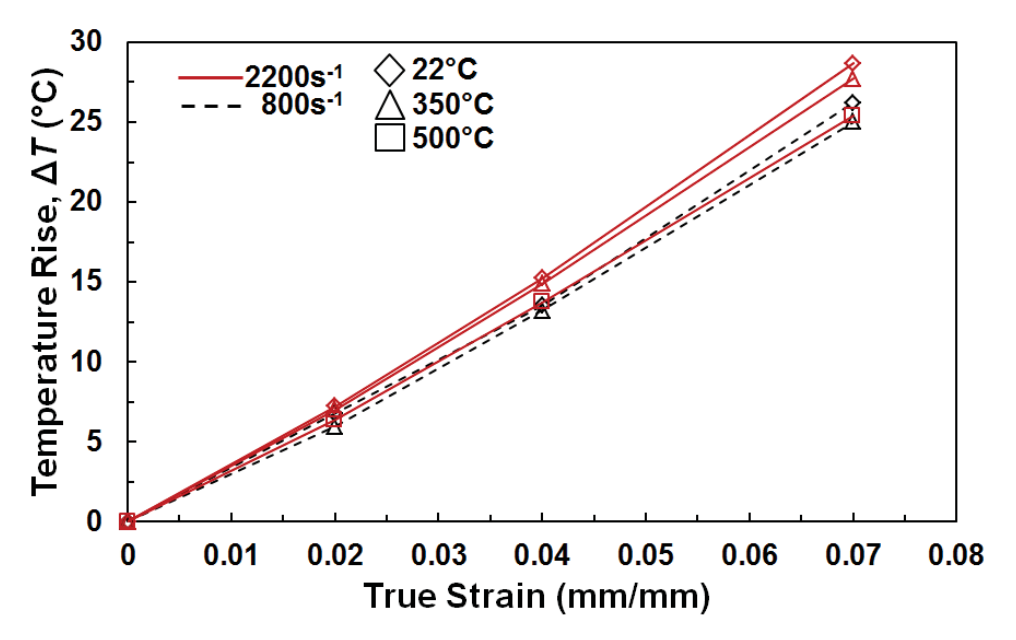


Figure 5.9. Variation of IN718 deformation-induced temperature rise ΔT with true strain as a function of strain rate (800 and 2,200 s⁻¹) and temperature (22, 350 and 500°C)

For the room temperature tests, the temperature rise at the highest strain rate of $2,600~\rm s^{-1}$ at the maximum true strain of ~ 0.40 reached 194° C. Although there was a temperature rise in the material, the dynamic work hardening rate still dominated the thermal softening effect as reflected by the positive work hardening rate for all temperatures and strain rate. The shape of the flow stress curves also does not show a drop that is indicative of the thermal softening effect as the governing the mechanism.

5.2.2 Effect of Temperature on the Flow Stress of IN718

The effect of the deformation temperature on the flow stress of IN718 is illustrated by the stress-strain curves plotted at a constant strain rate with increasing temperatures.

Figures 5.10 to 5.12 show the true stress vs. true strain plots at constant strain rates of 500, 800, and $2,200 \, \mathrm{s}^{-1}$ with deformation temperatures of 250, 350, and 500°C. It can be observed from the 3 plots that the deformation temperature has a significant effect on the dynamic behavior of IN718. The flow stress of IN718 decreases with increasing deformation temperature.

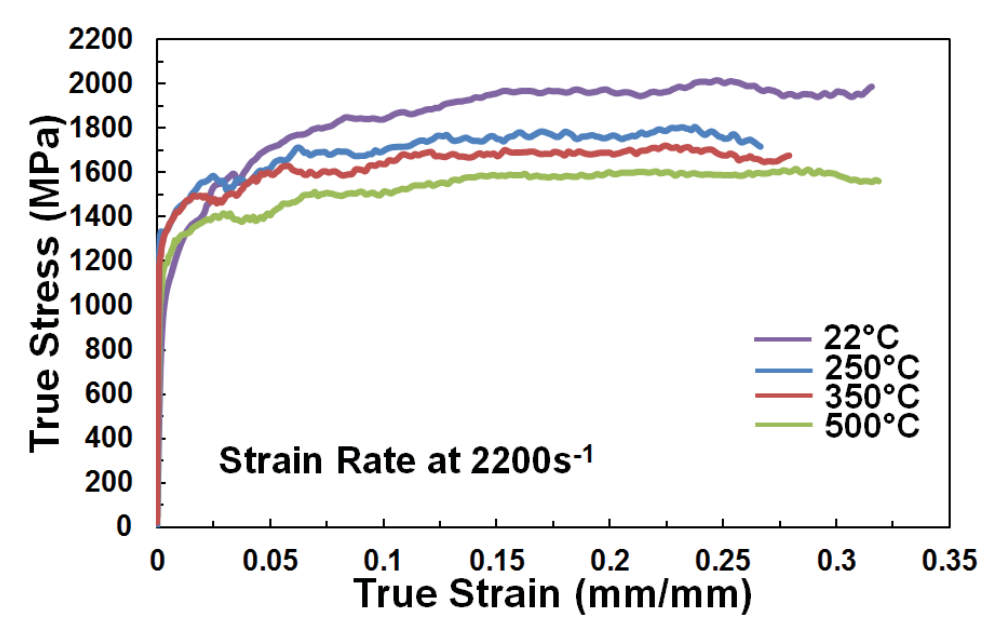


Figure 5.10. IN718 true stress vs. true strain at nominal strain rate of 2,200 s $^{-1}$ and temperatures of 22, 250, 350, and 500°C

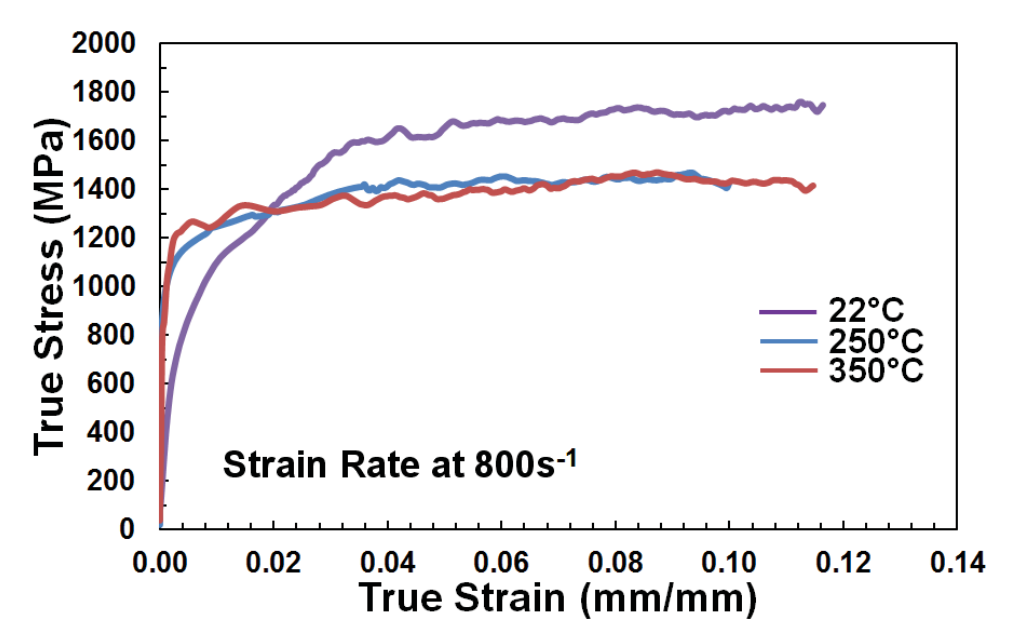


Figure 5.11. IN718 true stress vs. true strain at nominal strain rate of $800~s^{-1}$ and temperatures of 22, 250, and $350^{\circ}C$

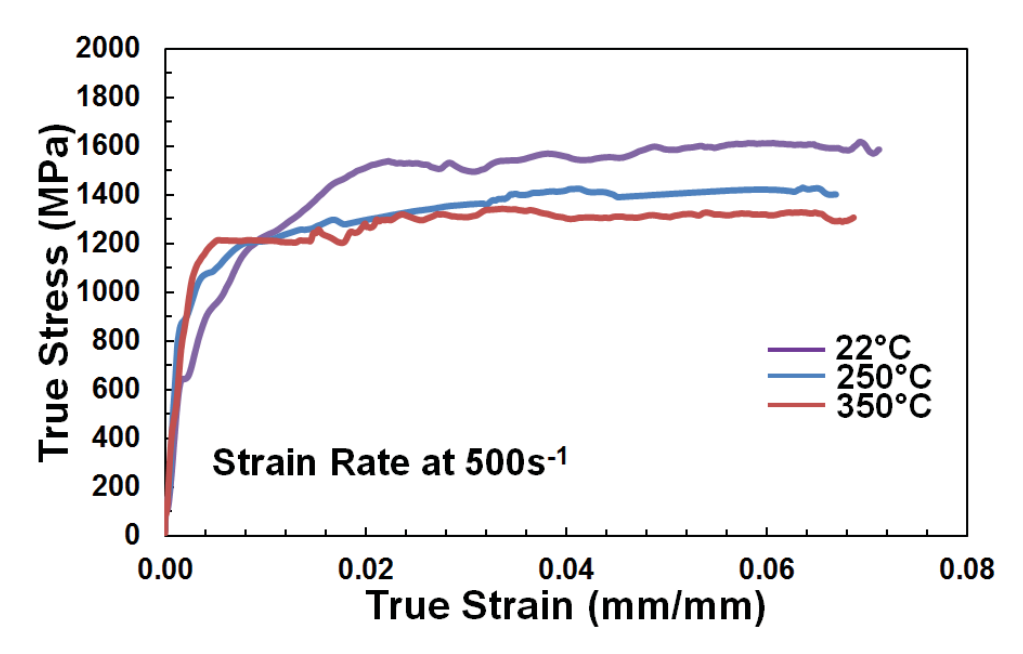


Figure 5.12. IN718 true stress vs. true strain at nominal strain rate of $500~s^{-1}$ and temperatures of 22, 250, and $350^{\circ}C$

The thermal softening effect in the material was examined by plotting the true stress with the deformation temperature as a function of the strain rate and true strain. It can be

seen in Figures 5.13 and 5.14 that at all values of true strain and strain rate, the stress decreases with increasing temperature. This phenomenon can be attributed to the increased mobility of dislocations with temperature. Also, previous study²³ on IN718 has shown that the thermal softening effect is the result of temperature-induced grain growth.

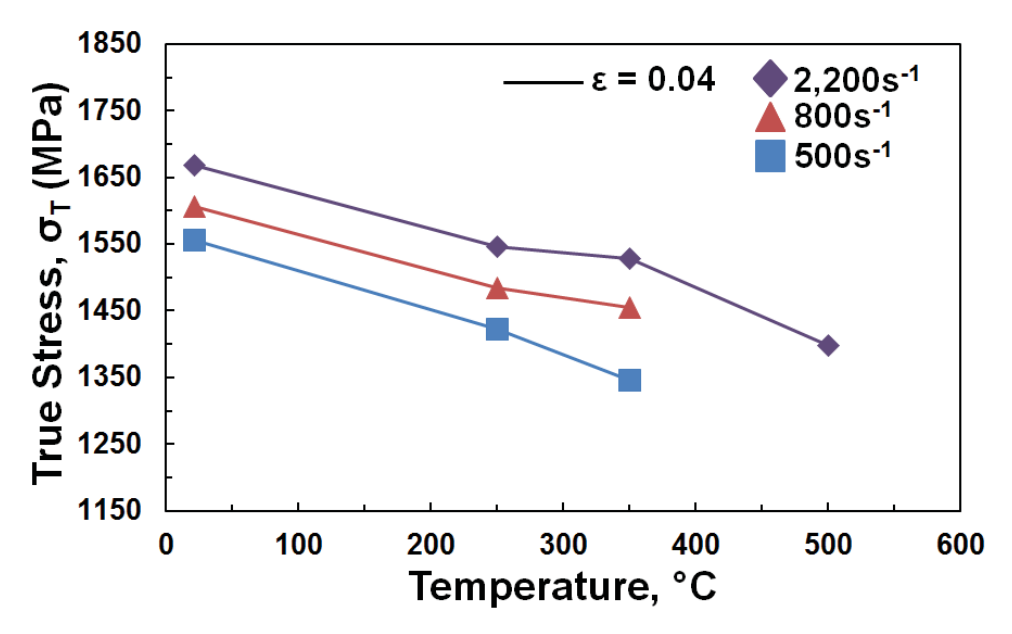


Figure 5.13. Variation of IN718 flow stress with temperature as a function of true strain (ϵ = 0.04) and strain rate (500, 800, 2,200 s⁻¹)

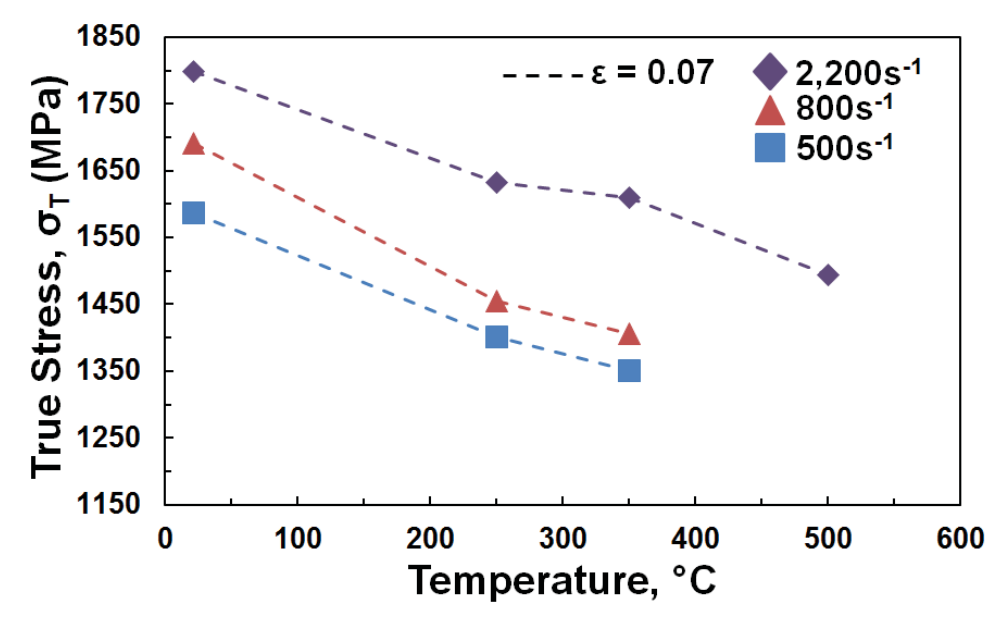


Figure 5.14. Variation of IN718 flow stress with temperature as a function of true strain (ϵ = 0.07) and strain rate (500, 800, 2,200 s⁻¹)

5.3 Flow Stress of 300M Steel

The experimental parameters, gas pressure and temperature, used for the testing of 6 mm \times 6 mm 300M steel samples and 4 mm \times 4 mm 300M steel samples are shown in Table 5.3 and Table 5.4 respectively. The resulting actual strain rates of the tests and their nominal values were also presented in the tables.

Table 5.3. Test condition matrix and strain rates of 6 mm × 6 mm 300M steel samples

Temperature (°C)	Gas Pressure (psi)	Total No. of Tests	Actual & Nominal Strain Rate (s ⁻¹)
250	220	1	371.85 (~400)
350	180	1	284.98 (~300)
F00	220	1	810.91 (~800)
500	180	1	632.88 (~600)

Table 5.4. Test condition matrix and strain rates of 4 mm × 4 mm 300M steel samples

Temperature (°C)	Gas Pressure (psi)	Total No. of Tests	Actual & Nominal Strain Rate (s ⁻¹)
	220		1,878.16 (~1,900)
22	180	2	1,301.74 (~1,300)
22	150		824.94 (~800)
	120	1	499.27 (~500)
	180		1,480.74 (~1,500)
350	150		1,338.19 (~1,300)
350	120	2	787.25 (~800)
	100		516.17 (~500)
500	150		1,876.20 (~1,900)
	120	2	1,403.38 (~1,400)
	100		1,332.95 (~1,300)

5.3.1 Effect of Strain Rate on the Flow Stress of 300M Steel

The influence of strain rate on the flow stress behavior of 300M steel was studied by conducting tests at various strain rates at three constant temperatures. The plot of the true stress vs. true strain with increasing strain rates at deformation temperatures of 500°C, 350°C, and 22°C are shown in Figures 5.15, 5.16, and 5.17 respectively. One representative

stress-strain curve for each strain rate is shown in the plots while these tests have at least 2 repeats as shown in Tables 5.3 and 5.4.

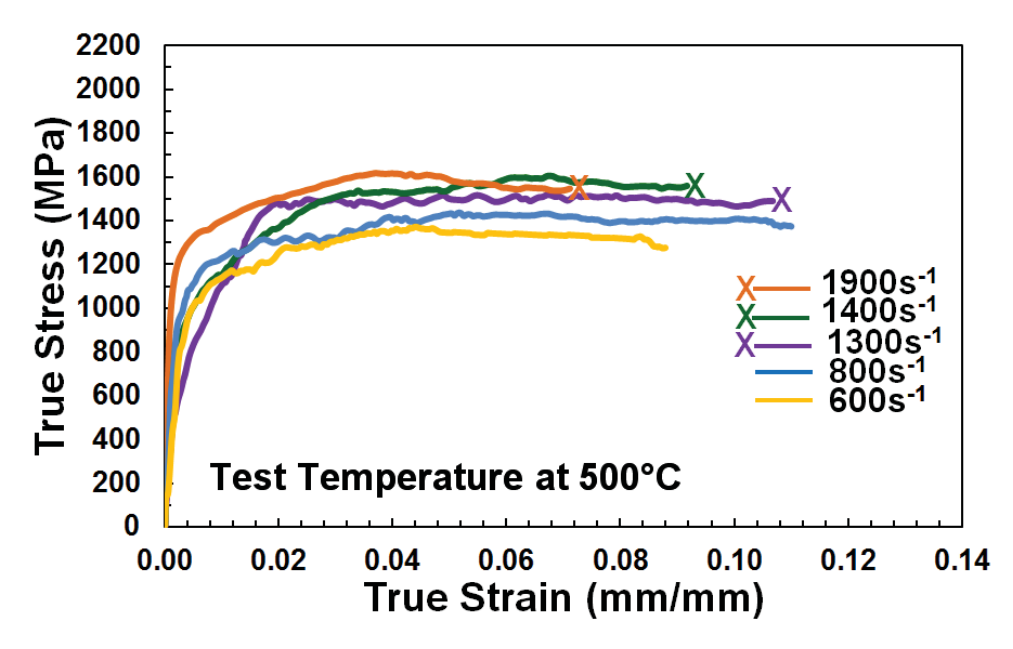


Figure 5.15. 300M steel true stress vs. true strain at 500° C and nominal strain rates of 600, 800, 1,300, 1,400, and 1,900 s⁻¹ (X mark on the stress-strain curve at 1,300, 1,400, and 1,900 s⁻¹ denotes fractured specimen)

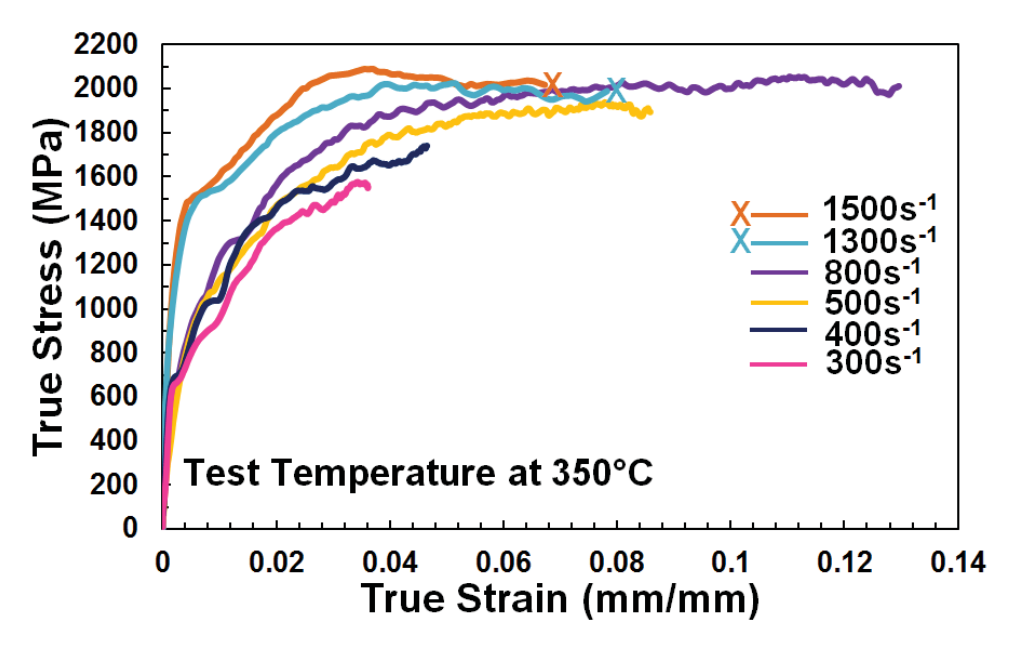


Figure 5.16. 300M steel true stress vs. true strain at 350°C and nominal strain rates of 300, 400, 500, 800, 1,300, and 1,500 s⁻¹ (X mark on the stress-strain curve at 1,300 and 1,500 s⁻¹ denotes fractured specimen)

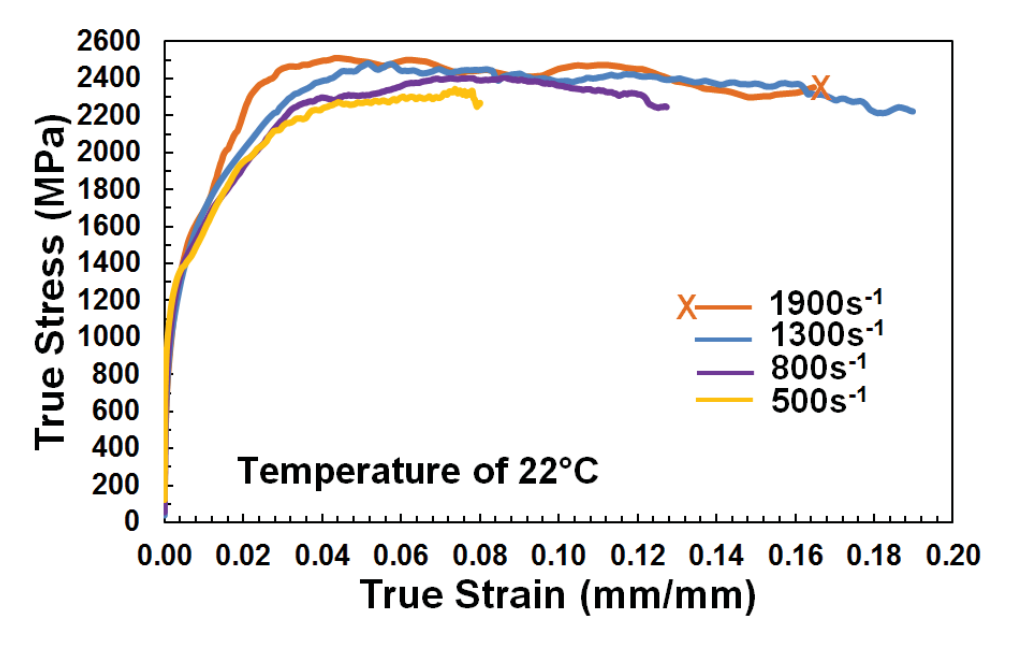


Figure 5.17. 300M steel true stress vs. true strain at 22° C and nominal strain rates of 500, 800, 1,300, and 1,900 s⁻¹ (X mark on the stress-strain curve at 1,900 s⁻¹ denotes fractured specimen)

The flow stress in all plots (Fig. 5.15 to 5.17) was observed to increase with strain rate at all deformation temperatures. Although, the material resulted in shear failure starting at a strain rate of 1,300 s⁻¹ at 500°C and 350°C and 1,900 s⁻¹ at 22°C. The failed 4mm \times 4mm samples at 22°C and 500°C are shown in Figure 5.18. The maximum strain rate achieved was 1,900 s⁻¹ at room temperature and at 500°C test. At all deformation temperatures, data suggests that the flow stress of the material saturates at approximately 1,650 MPa at 500°C, 2,100 MPa at 350°C, and 2,450 MPa at 22°C before failure, therefore attempts to obtain information at even higher strain rates weren't done.

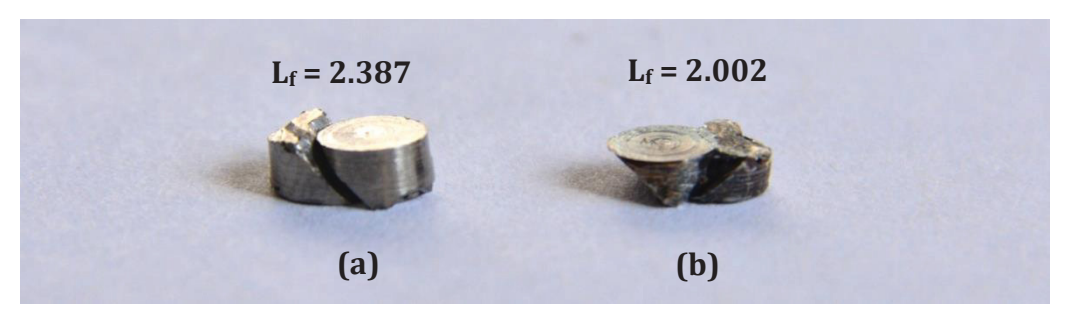


Figure 5.18. Fractured 4 mm \times 4 mm 300M steel samples tested at a temperature and strain rate of (a) 22°C and 1900 s⁻¹ and (b) 500°C and 1900 s⁻¹

The failure of the 300M steel at high strain rates can be attributed to the adiabatic heating in the material which led to the localization of the deformation and eventual failure of the material. A previous study on AISI 4340 steel, 28 a material on which 300M steel was modified from and has the same properties as 300M steel, has shown that adiabatic shear band formation is a typical localized instability phenomenon for the material under high strain rate loading conditions. Adiabatic heating is based on the fact that the Hopkinson test is an adiabatic process. During the test, there is not enough time for the heat generated due to plastic work to dissipate, thus it becomes trapped in the material resulting in a localized temperature rise. The temperature rise at the maximum strain rate of 1,900 s⁻¹ at room temperature was calculated to be 129°C.

It should also be noted that, the stress-strain curves of the material under the test conditions which resulted to failure, concaves down after reaching the maximum stress.

This suggests that thermal softening due to adiabatic heating governs at higher strain rates and overcame the effect of strain hardening. Adiabatic deformation occurs when the rate of localization equals or exceeds the strain hardening rate in the material.¹⁰⁸

5.3.2 Effect of Temperature on the Flow Stress of 300M Steel

The effect of temperature on the flow stress of 300M steel is presented on Figures 5.19 and 5.20. The true stress vs. true strain at constant strain rates of $800 \, s^{-1}$ and $1,300 \, s^{-1}$ at increasing temperatures were plotted. It is clear from the plots that the flow stress decreases with increasing temperature.

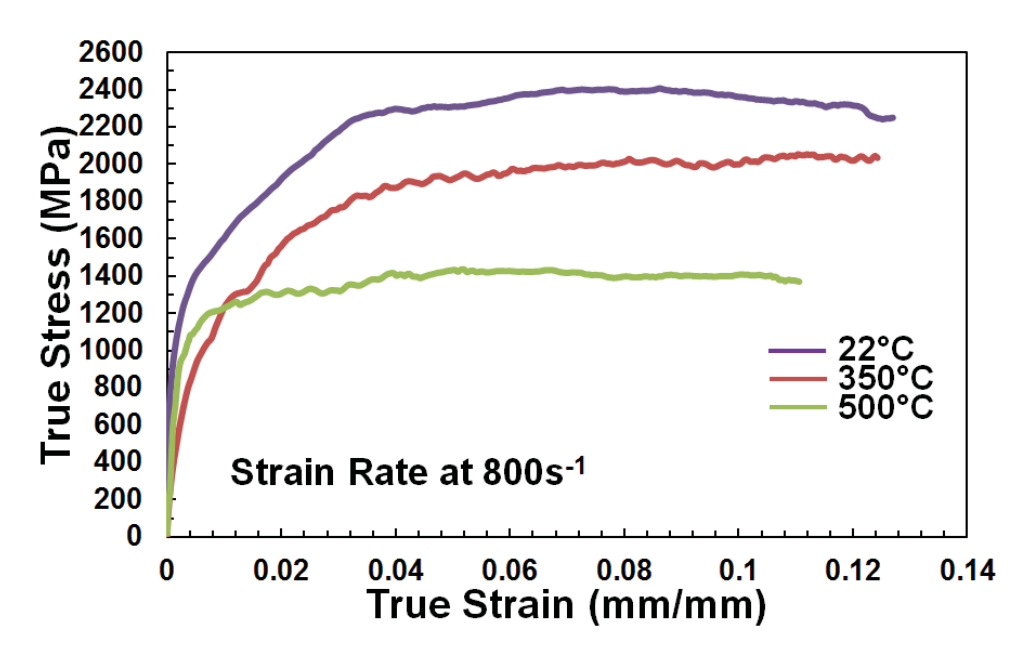


Figure 5.19. 300M steel true stress vs. true strain at a nominal strain rate of $800 \, s^{-1}$ and temperatures of 22, 350, and 500° C

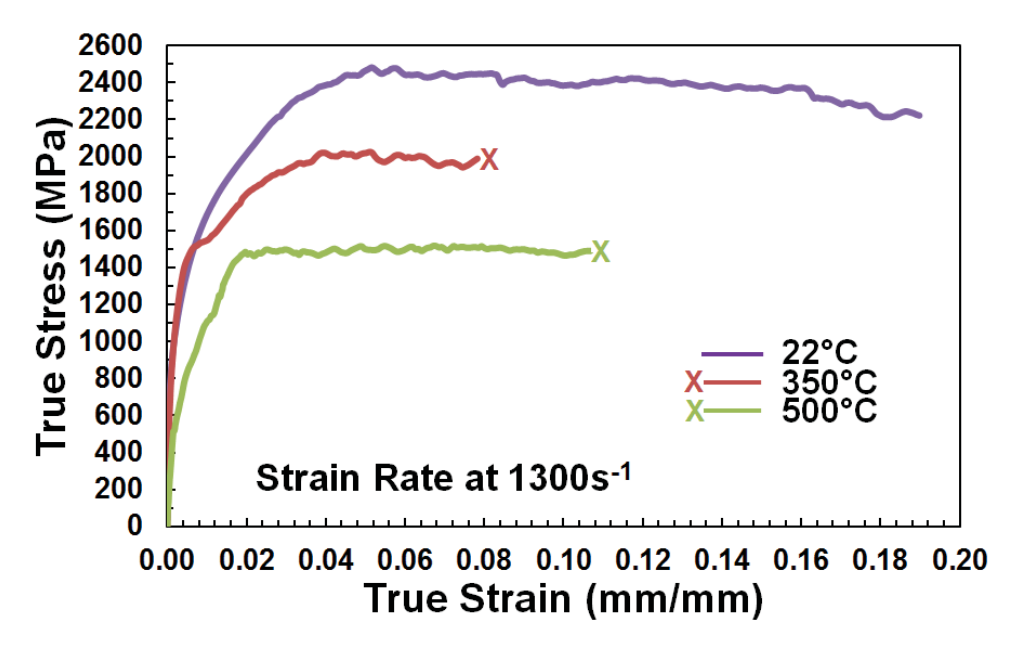


Figure 5.20. 300M steel true stress vs. true strain at a nominal strain rate of 1,300 s⁻¹ and temperatures of 22, 350, and 500°C (X mark on the stress-strain curve at 350 and 500°C denotes fractured specimen)

The thermal softening effect in the material was examined by plotting the true stress with the deformation temperature as a function of the strain rate and true strain. Figures 5.21 and 5.22 show the plot at 0.04 and 0.07 true strain wherein the stress decreases with increasing temperature for strain rates of $800 \, \text{s}^{-1}$ and $1,300 \, \text{s}^{-1}$.

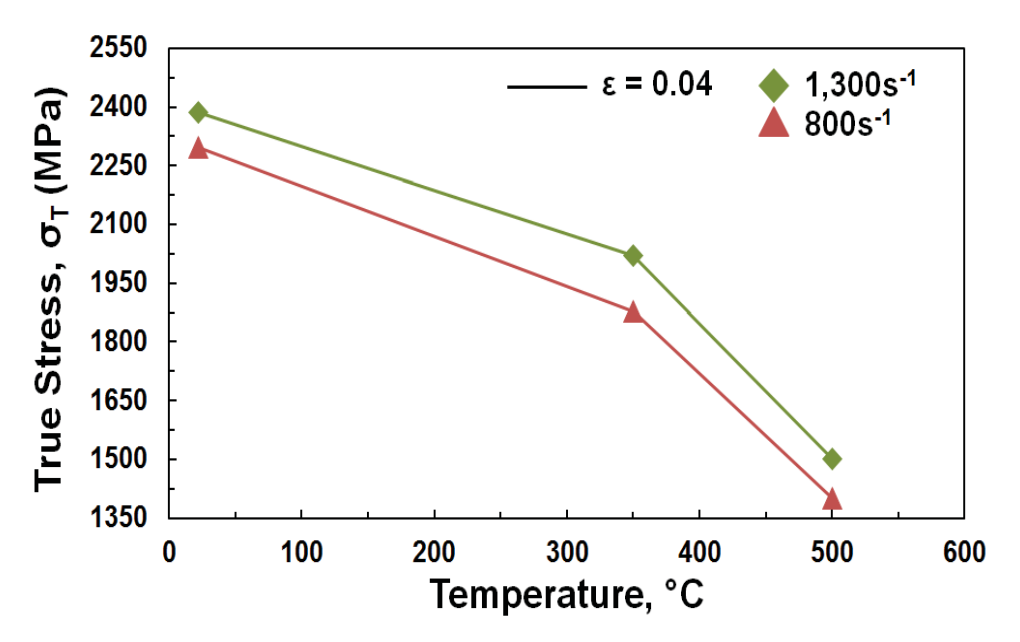


Figure 5.21. Variation of 300M steel flow stress with temperature as a function of true strain (ϵ = 0.04) and strain rate (800 and 1,300 s⁻¹)

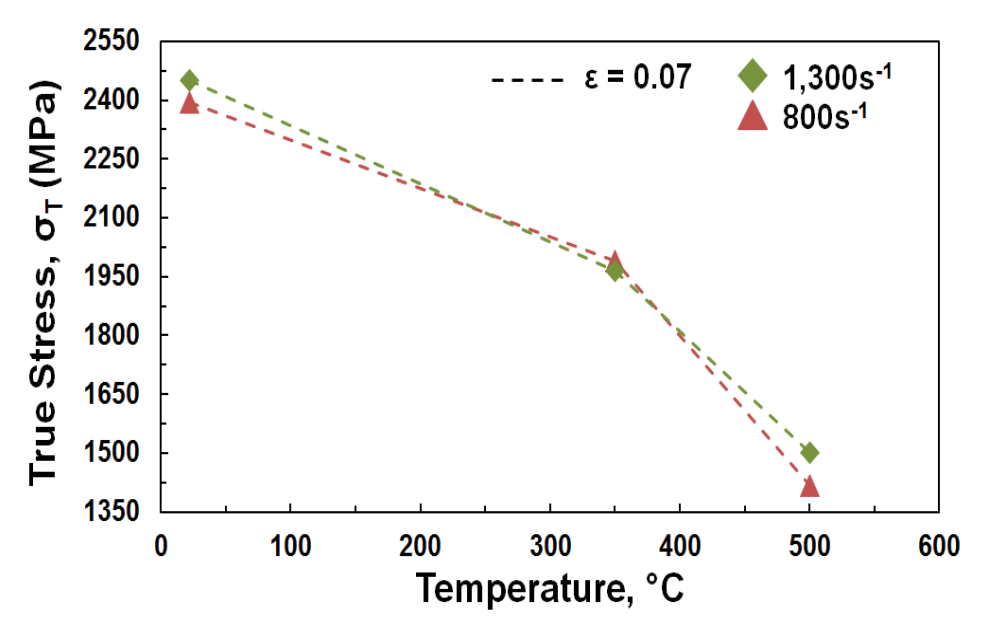


Figure 5.22. Variation of 300M steel flow stress with temperature as a function of true strain (ϵ = 0.07) and strain rate (800 and 1,300 s⁻¹)

Chapter 6: Material Constitutive Model Fitting for IN718

The obtained experimental stress-strain data discussed in Chapter 5.1 were utilized to fit and identify the material constants of the Johnson-Cook model and a modified Johnson-Cook model with a Cowper-Symonds strain rate sensitivity function for IN718. In this chapter, the steps on how each material constant of the models was identified from the experimental stress-strain results at quasi-static strain rate, high strain rates, and elevated temperatures will be discussed. The results of the fitting of the two models will also be compared.

For the simplification of the presentation of the models, the modified Johnson-Cook model with Cowper-Symonds function will be referred to as "Cowper-Symonds (modified Johnson-Cook) model" in this thesis.

6.1 Johnson-Cook Constitutive Model for IN718

The Johnson-Cook model (Eq. 2.19) is an empirical model which derives its constants from a combination of the quasi-static results at room temperature and high strain rate results at varying strain rates and temperatures. The values of the material constants A, B, n, C, and m are determined from an empirical fit of the flow stress data (as a function of strain, strain rate, and temperature) to the flow stress equation of the model.

6.1.1 Determination of the Yield A, Strain Hardening Modulus B, and Strain Hardening Exponent n

The expression on the first bracket of the Johnson-Cook model gives the strain hardening constants A, B, and n where A is the yield stress and B and n represents the effects of strain hardening. This expression gives the stress as a function of strain at room temperature, $T^* = 0$, and quasi-static condition for when the strain rate of interest ($\dot{\epsilon}$) and reference strain rate is the same ($\dot{\epsilon}_o$), $\dot{\epsilon}^* = 1$. At these conditions, the Johnson-Cook equation can be written as:

$$\sigma = [A + B(\varepsilon)^n][1 + Cln1][1 - 0^m]$$
(6.1)

$$\sigma = [A + B(\varepsilon)^n] \tag{6.2}$$

For IN718, three (3) quasi-static tensile results at room temperature and 0.003 s⁻¹ strain rate were used to obtain the A, B, and n constants of the model. To determine these material constants, two (2) methods, either linear regression analysis on equation (6.2) or non-linear regression analysis on the true stress-strain curve in the plastic zone can be used.

6.1.1.1 Linear Regression Analysis

In the linear regression analysis method, the yield stress A can be determined by analyzing the elastic region of the quasi-static stress-strain curve. It is the stress at zero plastic strain, $A = \sigma_o$. The linear slope of the elastic region was identified by applying a linear fit on the tensile results. The slope or the elastic modulus from the three tensile tests has a resulting average value of 190 GPa. To identify the yield stress, a 0.2% offset from the linear slope of the elastic region was used. A yield stress value is found from the intersection of the 0.2% offset line and the experimental stress-strain curve. The resulting average of the yield stress values from the three tensile data is 1,203 MPa. Figure 6.1 illustrates how the yield stress was determined using one of the quasi-static stress-strain data.

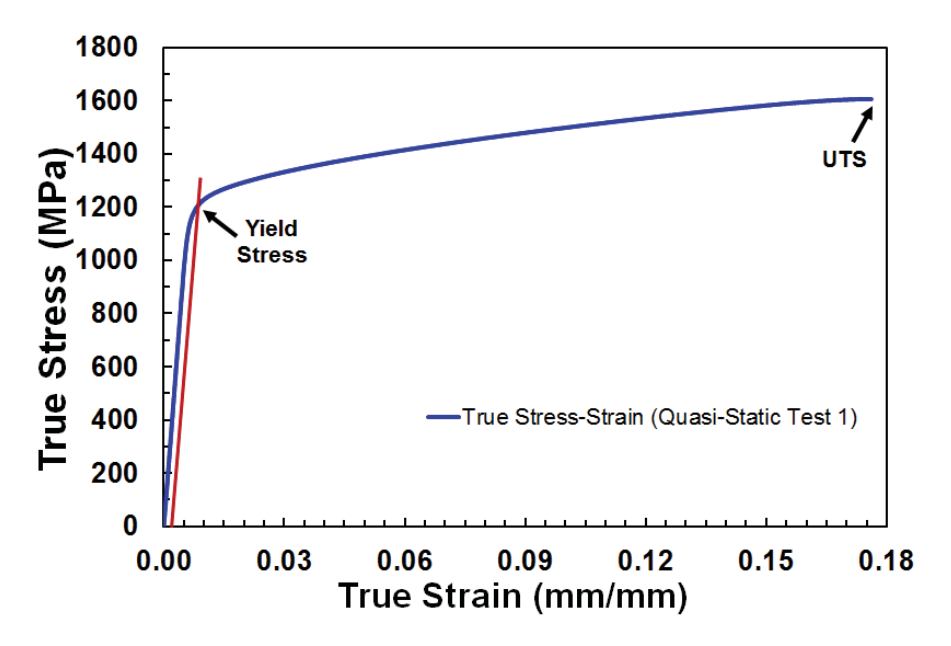


Figure 6.1. Illustration of yield stress determination for IN718 quasi-static stress-strain curve

After the material constant A was identified, the strain hardening modulus B, and strain hardening exponent n can be determined by analyzing plastic region of the quasi-static stress-strain curve defined in terms of the plastic stress and plastic strain only. This plastic region is defined by the stress obtained from subtracting the yield stress from the true stress, and strain resulting from the difference between the total strain minus the corresponding strain found for the 0.2% offset or elastic strain. Rearranging and manipulating equation (6.2) results to:

$$log(\sigma - A) = log(B) + nlog(\varepsilon)$$
(6.3)

Equation (6.3) represents a line with slope n and y-intercept of log(B). Thus, the constants B and n can be determined by applying a linear fit to the plot of the log (plastic stress) vs. log (plastic strain) as illustrated in Figure 6.2. To show the process, the same stress-strain data was used as in the determination of the yield stress A.

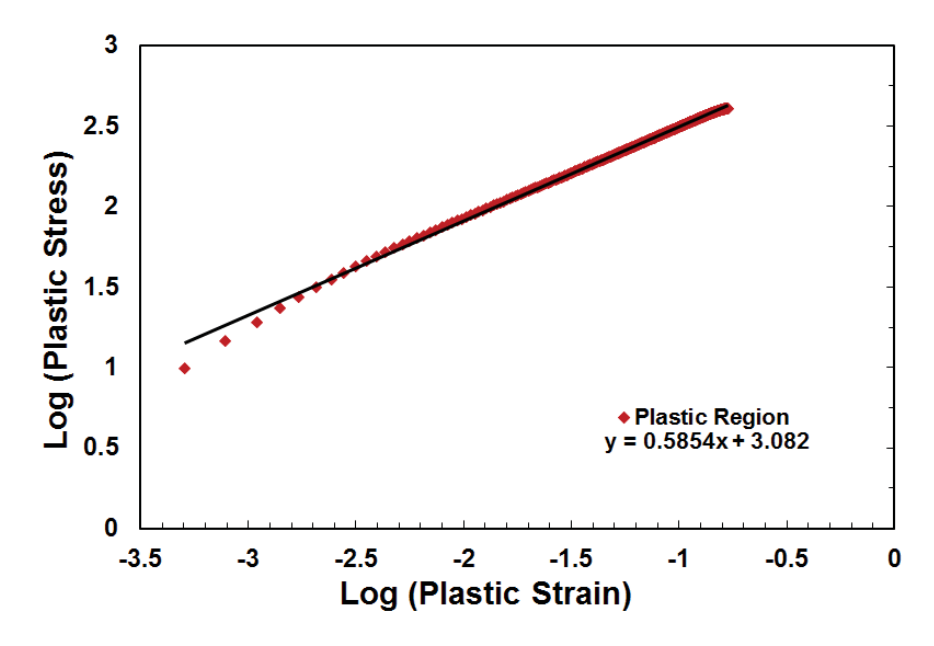


Figure 6.2. Linear fit on the plastic region of IN718

The equation for the linear fit gives the slope as the strain hardening exponent n while B is determined from 10 raised to the y-intercept. The average values of B and n from the three quasi-static tensile tests were determined to be 1242 MPa and 0.498. The summary of the constants A, B, and n for each test are presented in Table 6.1.

Table 6.1. Summary of strain hardening material constant values for IN718 (linear regression analysis)

Quasi-Static Tensile Test No.	A (Yield Stress) (MPa)	B (Strain Hardening Modulus) (MPa)	n (Strain Hardening Exponent)
1	1201	1208	0.585
2	1204	1276	0.611
3	1203	1242	0.597
Average	1203	1242	0.598

6.1.1.2 Non-Linear Regression Analysis

In the non-linear regression analysis method, the plastic zone, from the yield point to the ultimate tensile strength (UTS) of the quasi-static stress-strain curve was used. Using the OriginPro software, a non-linear curve fit in a Power Law form of $y = a + bx^c$ was applied to the plastic zone of the stress-strain curve. This form is the same as the expression in the first bracket of the Johnson-Cook equation thus, a gives the yield stress (A), b is the strain hardening modulus (B), and c is the strain hardening exponent (n) of the IN718 material. A non-linear curve fit on the plastic stress-strain data of tensile test no. 1 is illustrated in Figure 6.3.

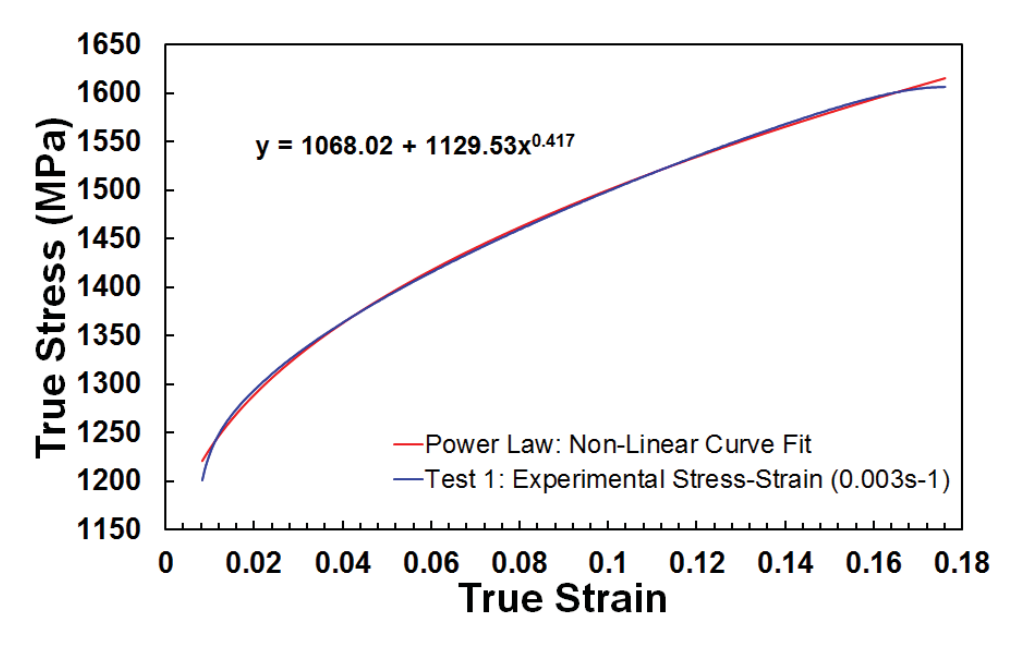


Figure 6.3. Non-linear curve fit on the plastic region of IN718

The average values of each constant from the three quasi-static tensile data using the non-linear curve fitting analysis are: A = 1067 MPa, B = 1129MPa, and n = 0.416. The summary of the constants A, B, and n for each test are presented in Table 6.2.

Table 6.2. Summary of strain hardening material constant values for IN718 (non-linear curve fitting)

Quasi-Static Tensile Test No.	A (Yield Stress) (MPa)	B (Strain Hardening Modulus) (MPa)	n (Strain Hardening Exponent)
1	1068	1130	0.417
2	1080	1146	0.440
3	1052	1110	0.392
Average	1067	1129	0.416

6.1.1.3 Comparison of Constants A, B, and n (Linear vs. Non-Linear Regression Analysis)

Both methods are acceptable processes for determining the strain hardening constants of the Johnson-Cook equation. The main difference between them is that in the linear regression analysis, a fixed value of the yield stress is used while the B and n values are being simultaneously determined. Due to this fixed yield stress value, sometimes this method requires selecting only a portion in the plastic stress-strain curve to be analyzed so as not to skew the values of the B and n constants away from fitting the experimental data.

In the non-linear curve fitting on the other hand, the yield stress value is allowed to vary so that the values of the resulting constants would give a minimized difference between the experimental quasi-static stress-strain values in the plastic zone vs. the Johnson-Cook approximated quasi-static stress-strain curve using the identified A, B, and n constants.

The first bracket of the Johnson-Cook equation represents the approximation to the plastic region of the quasi-static stress-strain curve without the effects of strain rate hardening and thermal softening, thus B and n constants must be calculated so that it represents the best fit of the plastic region of the stress-strain curve.

Using the average value of the constants A, B, and n determined from both the linear regression method and non-liner curve fitting method, the Johnson-Cook approximated stress in the plastic zone is plotted against the experimental quasi-static stress-strain curve as shown in Figure 6.4.

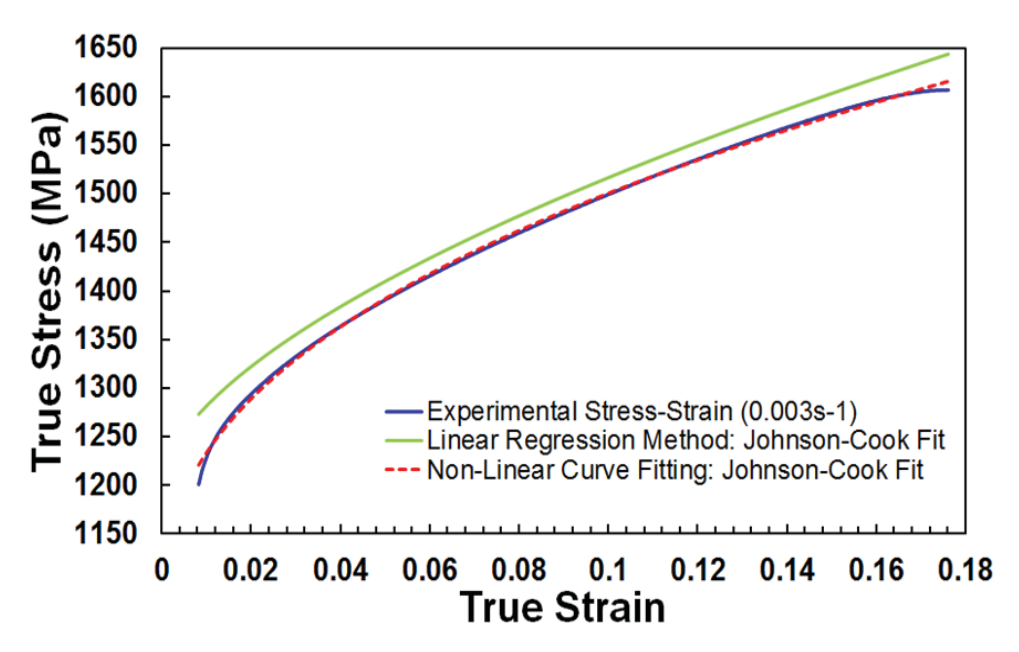


Figure 6.4. IN718 experimental vs. Johnson-Cook approximated stress-strain curves using linear vs. non-linear regression analysis method

It can be observed from Figure 6.3 that using the A, B, and n constants determined using the non-linear curve fitting method better fits the plastic region of the experimental stress-strain curve. Therefore in this study, the constant values (A = 1067 ± 3.75 MPa, B = 1129 ± 2.91 MPa, n = 0.416 ± 0.005) from the non-linear curve fitting method will be utilized.

6.1.2 Determination of the Strain Rate Sensitivity Parameter C

The strain rate sensitivity parameter C corresponds to the strain rate effect. This parameter can be identified from the analysis of the expression in the second bracket of the Johnson-Cook equation and from the results of high strain rate tests conducted at room temperature and varying strain rates.

In order to identify the C parameter, a static strain value must be defined first. The static strain is the strain value that gives a minimum difference, sometimes an intersection, between the Johnson-Cook approximated stress using the identified A, B, and n constants and the experimental quasi-static stress in the stress-strain curve. The corresponding

stress value of the static strain is defined as the static stress. The static strain relates the stress data at high strain rates to the quasi-static stress-strain data.

The minimum stress difference between the curve fit using the A, B, and n constants and the experimental quasi-static stress-strain curve as shown in Figure 6.5 has a value of 0.009 MPa at a strain of 0.1653. This strain was not considered as the static strain as it appears very close to the UTS and does not represent the area in the stress-strain curve that would exhibit the strain rate effect. The second next minimum stress difference has a value of 0.016MPa and occurs at a strain of 0.0426. This was chosen as the static strain.

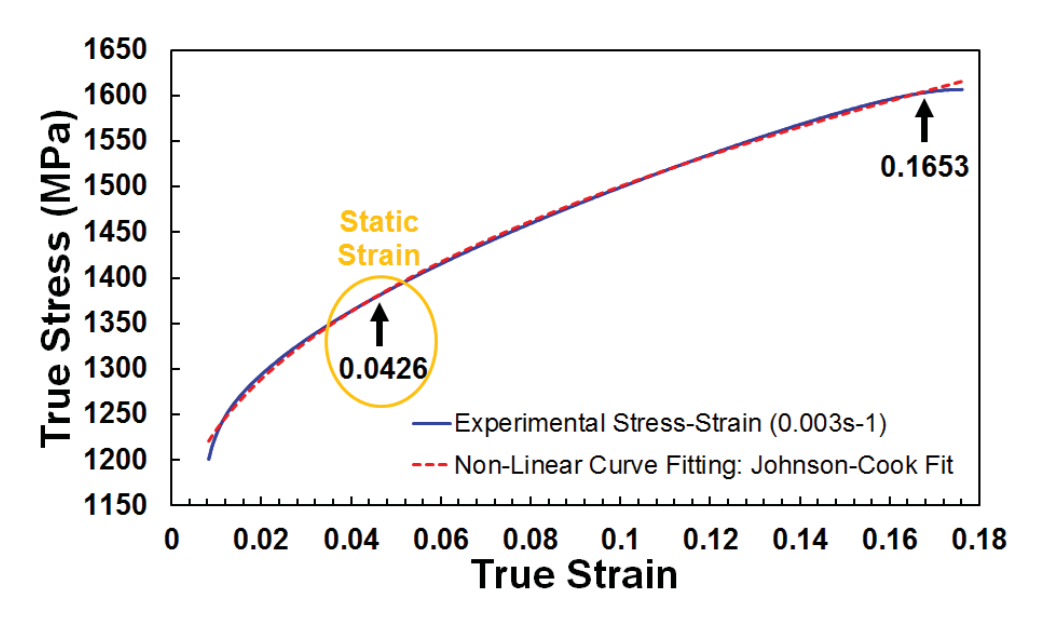


Figure 6.5. Illustration of static strain determination from the Johnson-Cook fit curve vs. the experimental quasi-static stress-strain curve

The average value of the static strain and static stress determined from the three quasi-static stress-strain data is tabulated in Table 6.3. The value 0.0426 was chosen as the static strain and this would define the value of flow stress for the determination of both the strain sensitivity parameter C and thermal softening coefficient m. The corresponding static stress value was determined to be 1371 MPa.

Quasi-Static Tensile Test No.	Static Strain	Static Stress (MPa)
1	0.0426	1371
2	0.0460	1376
3	0.0393	1365
Average	0.0426	1371

Table 6.3. Summary of the static strain and static stress values for IN718

At room temperature (neglecting the effect of thermal softening) and constant strain (static strain), the expression in the second bracket of the Johnson-Cook equation can be written as:

$$\sigma = \left[\sigma_{static}\right] \left[1 + C \ln \frac{\dot{\varepsilon}}{\dot{\varepsilon}_o}\right] \left[1 - 0^m\right] \tag{6.4}$$

$$\sigma = \left[\sigma_{static}\right] \left[1 + C \ln \frac{\dot{\varepsilon}}{\dot{\varepsilon}_o}\right] \tag{6.5}$$

The parameter $\dot{\epsilon}$ is the test strain rate while $\dot{\epsilon}_o$ is the reference strain rate (0.003 s⁻¹) where A, B, and n constants were identified. Conventionally, the $\dot{\epsilon}_o$ value is chosen to be 1 s⁻¹ for convenience so that the term $\frac{\dot{\epsilon}}{\dot{\epsilon}_o}$ in equation 6.5 would only be equal to the test strain rate. The important point in selecting this parameter from values from 0.001 s⁻¹ to 1 s⁻¹ is to note the consistency with the choice of the strain hardening parameters A, B, and n. If these strain hardening parameters are determined from the quasi-static stresses vs. plastic strain, the parameter $\dot{\epsilon}_o$ should be set to the value of the plastic strain-rate used in the quasi-static test.⁸¹

Rearranging equation 6.5 results to equation 6.6 which represents an equation of a line where $y=\frac{\sigma}{\sigma_{static}}$, slope m is the strain rate sensitivity parameter C and where the y-intercept is set to 1. The constant C can then be determined from the plot of $\frac{\sigma}{\sigma_{static}}$ vs. $\frac{\dot{\epsilon}}{\dot{\epsilon}_o}$, where σ is the dynamic stress at a static strain of 0.0426 identified from the stress-strain result of the SHPB tests at varying strain rates.

$$\frac{\sigma}{\sigma_{static}} = \left[1 + C \ln \frac{\dot{\varepsilon}}{\dot{\varepsilon}_o}\right] \tag{6.6}$$

Results from six (6) varying high strain rate tests (300, 500, 800, 2,000, 2,200, and 2,600 s⁻¹) at room temperature were utilized to determine the constant C. Each dynamic stress value is an average from two (2) high strain rate tests. Figure 6.6 shows the plot of the dynamic stress/static stress vs. $ln \frac{\dot{\varepsilon}}{\dot{\varepsilon}_o}$. The slope of the least fit square gives the strain rate sensitivity parameter C a value of 0.0138 ± 0.0014.

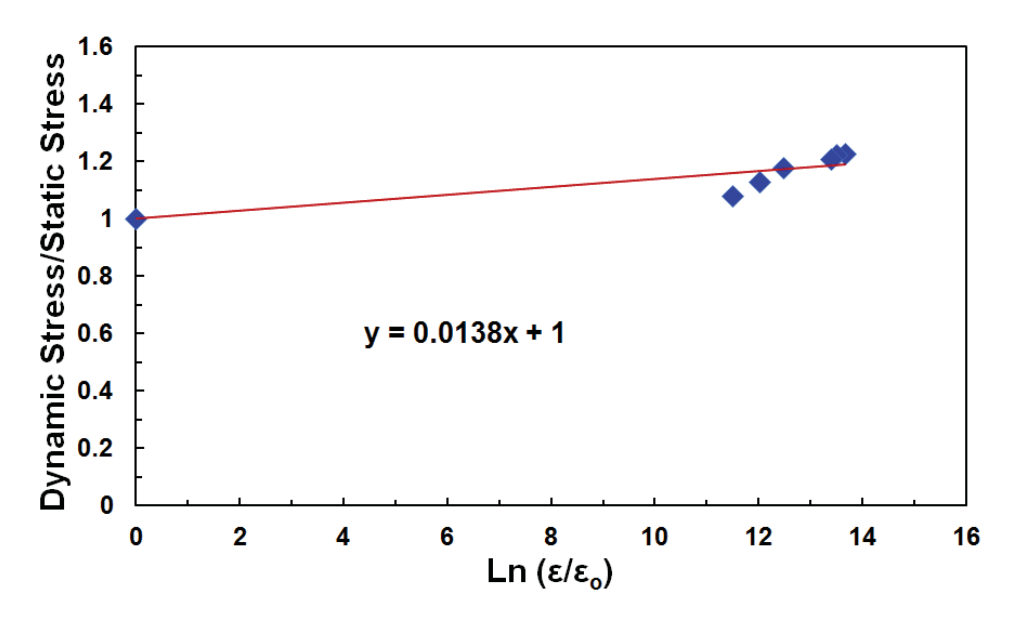


Figure 6.6. IN718 plot of dynamic to static stress ratio vs. ln ($\dot{\epsilon}/\dot{\epsilon}_o$)

It can be observed from Figure 6.6 that the ratio of the dynamic stress to static stress is greater than one. This reflects the fact that the dynamic stress is always greater than the static stress.

6.1.3 Determination of the Thermal Softening Coefficient m

The thermal softening coefficient m corresponds to the effect of temperature on the dynamic response of IN718 as represented by the expression on the third bracket of the Johnson-Cook equation. This coefficient can be determined from the stress-temperature

response of the material and is taken from experiments conducted at specific strain rates with varying temperatures.

At a constant strain (0.0426) and strain rate, the expression in the third bracket of the Johnson-Cook equation can be written as:

$$\sigma = \left[\sigma_{dynamic(RT)}\right] \left[1 + Cln1\right] \left[1 - \left(\frac{T - T_r}{T_m - T_r}\right)^m\right]$$
(6.7)

$$\sigma = \left[\sigma_{dynamic(RT)}\right] \left[1 - \left(\frac{T - T_r}{T_m - T_r}\right)^m\right] \tag{6.8}$$

$$\sigma = [\sigma_{dynamic(RT)}][1 - (T^*)^m]$$
(6.9)

The parameter $\sigma_{dynamic(RT)}$ is the stress at room temperature for the specific strain rate where the effect of temperature is being examined, while the parameter σ on the other hand is the dynamic stress at the test temperature. The homologous temperature T^* is a function of the reference temperature $T_r = 22$ °C, melting temperature of IN718 material $T_m = 1336$ °C, and test temperature T which varies. Rearranging and manipulating equation 6.9 result to:

$$log\left(1 - \left(\sigma/\sigma_{dynamic(RT)}\right)\right) = mlog(T^*)$$
(6.10)

The plot of $log\left(1-\left(\sigma/\sigma_{dynamic(RT)}\right)\right)$ vs. $log(T^*)$ results to points that correlates to the coefficient m. By applying a least fit square on the data points where the y-intercept is set to 0, the slope value gives the coefficient m.

The results at a strain rate of 2,200 s⁻¹ were utilized to identify the thermal softening coefficient m. Only this strain rate value was attained at all deformation temperatures of 250, 350, and 500°C while the strain rates of 500 s⁻¹ and 800 s⁻¹ were achieved at only two deformation temperatures of 250 and 350°C. Figure 6.7 illustrates the determination of

coefficient m for strain rate of 2,200 s $^{-1}$. A thermal softening coefficient m value of 1.71 \pm 0.09 was determined from the plot.

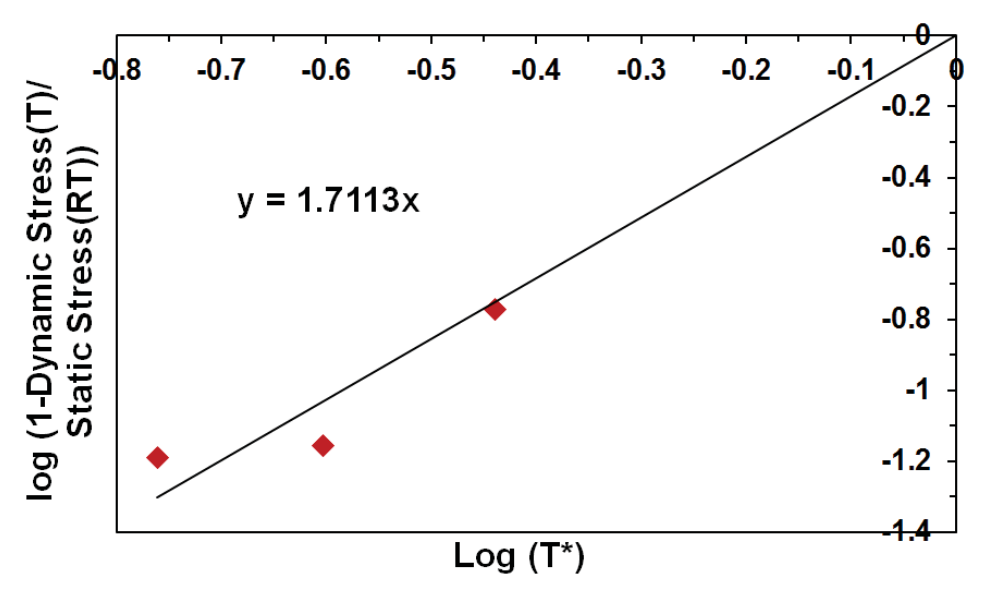


Figure 6.7. IN718 plot of $\log\left(1-\left(\sigma/\sigma_{dynamic(RT)}\right)\right)$ vs. $\log(T^*)$ for 2200 s⁻¹

The Johnson-Cook material parameters for IN718 determined in this study are shown in Table 6.4.

Table 6.4 Summary of Johnson-Cook parameters for IN718

Johnson-Cook Parameters for IN718						
A (MPa) B (MPa) n C m						
1067 ± 3.75	1129 ± 2.91	0.416 ± 0.005	0.0138 ± 0.0014	1.71 ± 0.09		

6.2 Cowper-Symonds (Modified Johnson-Cook) Model for IN718

The modified Johnson-Cook model with Cowper-Symonds strain rate form is shown in equation 6.11. It has the same form as that of the Johnson-Cook model (Eq. 2.19) but with a strain rate function expressed as a two parameter exponential.⁸¹

$$\sigma = \left[A + B \left(\varepsilon^{n} \right) \right] \left[1 + \left(\frac{\dot{\varepsilon}}{D} \right)^{1/p} \right] \left[1 - \left(\frac{T - T_{o}}{T_{m} - T_{o}} \right)^{m} \right]$$
 (6.11)

The only difference between the two models is the equation in the second bracket which corresponds to the strain rate sensitivity function of the model. In the Cowper-Symonds (modified Johnson-Cook) model, the strain rate dependency of the material is expressed in a power law relation instead of a log-linear relation.

Since only the expression in the second bracket was modified between the two models, the method of identifying the material constants A, B, n, and m in the first and third brackets follows the same procedure with that in the Johnson-Cook model as discussed in Sections 6.1.1 and 6.1.3, and thus has the same values.

6.2.1 Determination of the Cowper-Symonds Coefficients D and p

The Cowper-Symonds coefficients D (scale factor of the strain rate sensitivity) and p are determined from the results of high strain rate tests at room temperature with varying strain rates. At room temperature and constant strain (static strain), the Cowper-Symonds (modified Johnson-Cook) equation can be written as:

$$\sigma = \left[\sigma_{static}\right] \left[1 + \left(\frac{\dot{\varepsilon}}{D}\right)^{1/p}\right] \left[1 - 0^{m}\right] \tag{6.12}$$

$$\sigma = \left[\sigma_{static}\right] \left[1 + \left(\frac{\dot{\varepsilon}}{D}\right)^{1/p}\right] \tag{6.13}$$

where $\dot{\epsilon}$ is the test strain rate, σ is the dynamic stress and σ_{static} is the static stress. Similar with the Johnson-Cook model discussed in Section 6.1.2, the corresponding static stress at quasi-static strain rate and dynamic stresses at high strain rates are determined at a static strain value of 0.0426.

Re-arranging equation 6.13 results to equation 6.14 which has the two coefficients D and p as unknowns.

$$\frac{\sigma}{\sigma_{static}} = \left[1 + \left(\frac{\dot{\varepsilon}}{D}\right)^{1/p}\right] \tag{6.14}$$

With the value of the expression $\frac{\sigma}{\sigma_{static}}$ known for each strain rate, initial values of the D and p coefficients in the lower and upper strain rate ranges were determined by substituting two sets of strain rate values into equation 6.14. For the lower strain rate range, 300 s⁻¹ and 800 s⁻¹ values were used while 800 s⁻¹ and 2600 s⁻¹ values were used for the upper strain rate range. The coefficients for the lower and upper strain rate ranges were then determined by solving a system of equations with two variables via substitution. This method was adapted from and discussed in detail in the work of M. Di Sciuva et al. ¹⁰⁹ The values of the coefficients D and p identified for the two strain rate ranges are shown in Table 6.5.

Table 6.5 IN718 Cowper-Symonds coefficients D and p at strain rate ranges of 300-800 s⁻¹ and 800-2,600 s⁻¹

Strain Rate (s ⁻¹)	D (s ⁻¹)	р
300-800	6032	1.17
800-2600	3,641,358	4.88

The Cowper-Symonds coefficients determined for 300-800 s⁻¹ and 800-2,600 s⁻¹ ranges were evaluated by calculating the dynamic stress/static stress value using the determined D and p coefficients and plotting it against the strain rate. The plots of the resulting dynamic stress/static stress value vs. strain rate alongside the experimental data are shown in Figure 6.8.

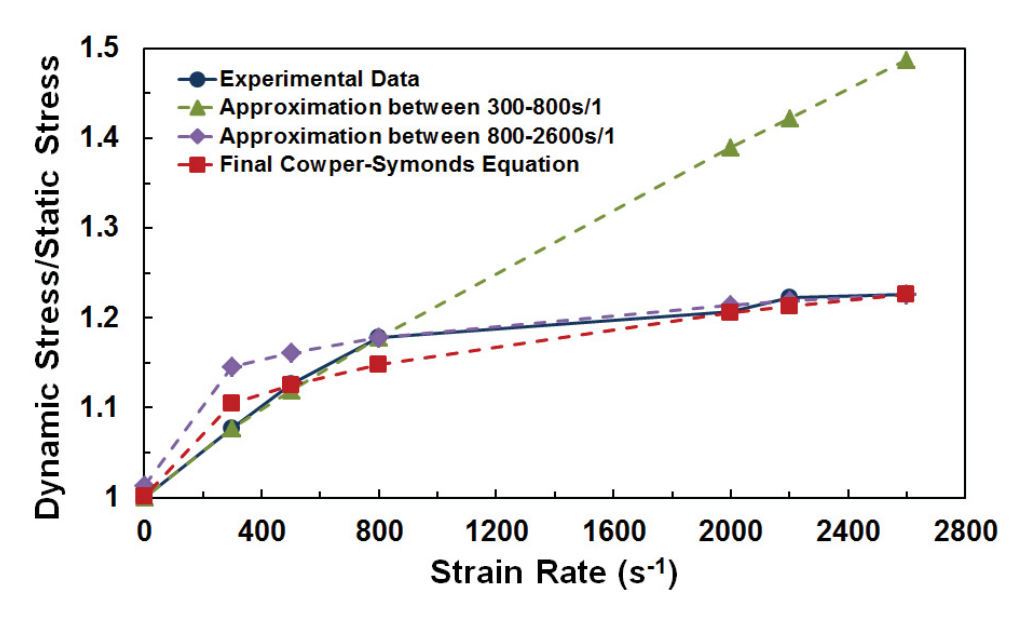


Figure 6.8. Evaluation of the initial (lower and upper strain rate ranges) and final Cowper-Symonds coefficients of IN718

The final Cowper-Symonds coefficients for the entire strain rate range (300-2,600 s⁻¹) were found by trial and error and by performing a few iterations using the Excel program. The plot of the dynamic stress/static stress value vs. strain rate using the final coefficients is also shown in Figure 6.7. The final Cowper-Symonds coefficients have a value of D = 169,876 and p = 2.82.

6.3 Comparison of the Constitutive Model Fits for IN718

The experimental data obtained at high strain rates and elevated temperatures were used to fit both the Johnson-Cook and Cowper-Symonds (modified Johnson-Cook) models. The parameters of the models used for the fitting are shown in Tables 6.6 and 6.7.

Table 6.6 Identified Johnson-Cook model parameters for IN718

Parameter	Estimate	95% LCL	95% UCL
A (MPa)	1.067×10^3	1.060×10^3	1.074×10^3
B (MPa)	1.128×10^3	1.123×10^3	1.134×10^3
n	0.416	0.407	0.425
С	0.0138	0.0103	0.0172
m	1.711	1.421	2.002

Table 6.7 Identified Cowper-Symonds (modified Johnson-Cook) model parameters for IN718

Parameter	Estimate	95% LCL	95% UCL
A (MPa)	1.067×10^3	1.060×10^3	1.074×10^3
B (MPa)	1.128×10^{3}	1.123×10^3	1.134×10^3
n	0.416	0.407	0.425
D (s ⁻¹)	169,876	-	-
p	2.82	-	-
m	1.711	1.421	2.002

The strain rate and temperature sensitivity of the models and how well they fit the experimental data will be investigated in this section. The general trend of the fitted flow curve will also be discussed.

6.3.1 Strain Rate Sensitivity of the Johnson-Cook vs. Cowper-Symonds (Modified Johnson-Cook) Model for IN718

The predicted curves using the Johnson-Cook model for increasing strain rates at room temperature is shown in Figure 6.9. The predicted flow stress curves showed no sensitivity to the increase in strain rates from $10^2 \, \text{s}^{-1}$ to $10^3 \, \text{s}^{-1}$ range. There are no distinct separations between the curves at strain rate ranges of $10^2 \, \text{s}^{-1}$ and $10^3 \, \text{s}^{-1}$.

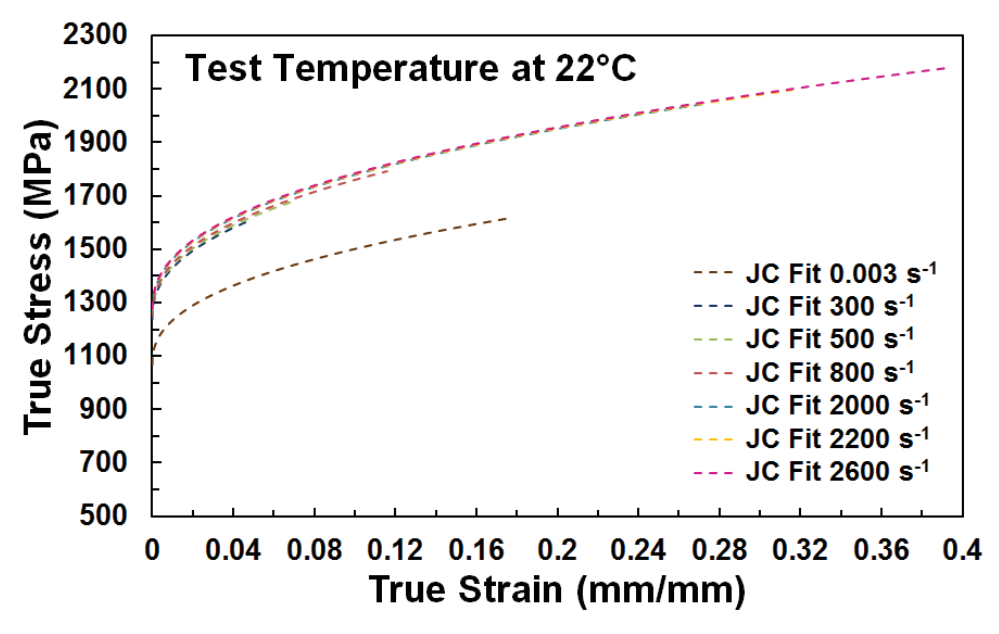


Figure 6.9. Predicted curves for IN718 at room temperature with increasing strain rates using the Johnson-Cook model

The comparisons of the experimental data with the predicted curves using the Johnson-Cook model are shown in Figure 6.10. The model does not fit all the experimental data very well. It has a good fit for the quasi-static result at $0.003~\rm s^{-1}$ and strain rates at $10^2~\rm s^{-1}$ range specifically at $800~\rm s^{-1}$. However, it underestimates the flow stress at $10^3~\rm s^{-1}$ strain rates and overestimates the flow stress at strain rates lower than $800~\rm s^{-1}$. A closer look of the fit at $10^2~\rm s^{-1}$ strain rates starting at a true stress of $1350~\rm MPa$ can be seen in Figure 6.11.

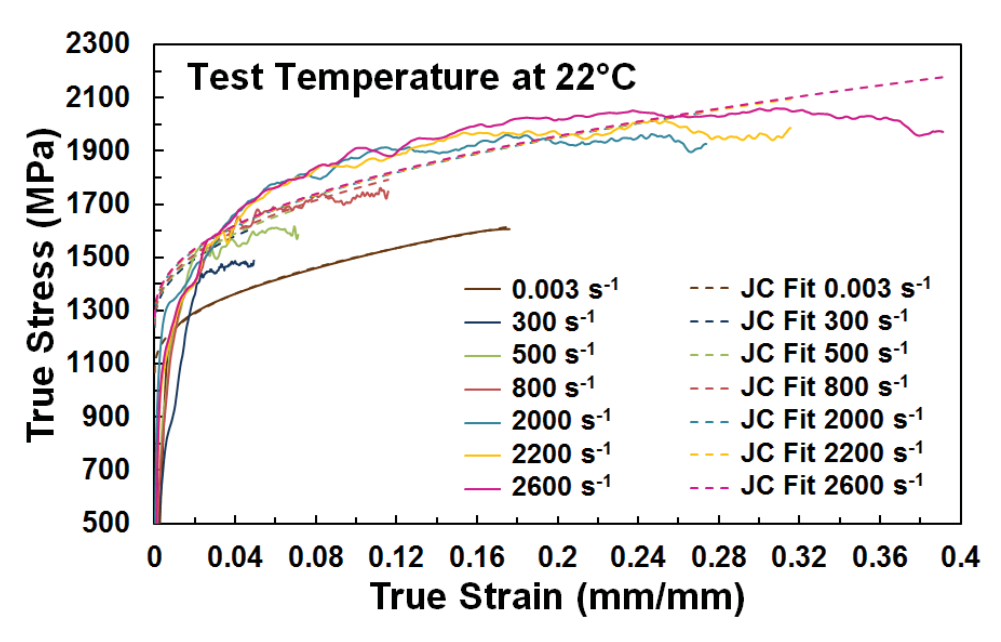


Figure 6.10. Comparison of experimental and Johnson-Cook model predicted flow stress curves of IN718 at room temperature with increasing strain rate

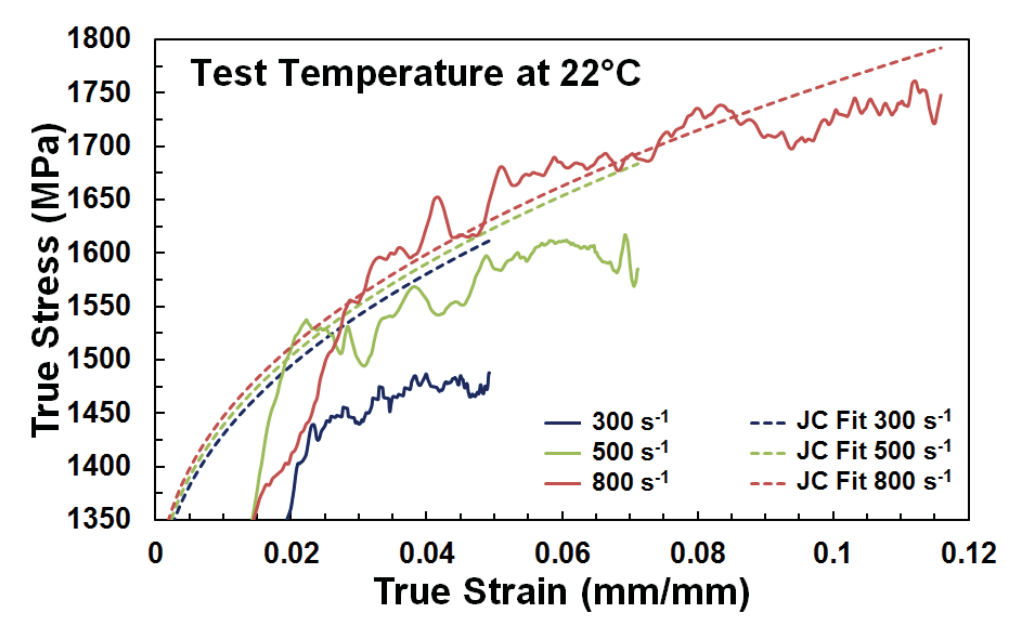


Figure 6.11. Johnson-Cook fit on the experimental data of IN718 at strain rates of 10^2 s⁻¹ (300, 500, and 800 s⁻¹) at room temperature

The lack of fit using the Johnson-Cook model is due to the change and difference in the strain rate sensitivity that occurs in the material at strain rates between $10^2 \, \text{s}^{-1}$ and $10^3 \, \text{s}^{-1}$ as illustrated in Figure 6.10. There is a distinct jump and characteristic change in the

flow stress between these strain rate ranges which was not captured by the model. The log-linear strain rate relation in the model is rarely observed for most metal and alloys. Two regions of strain rate hardening behavior are usually evident as shown in Figure 6.12 with a transition between them at strain rates in the range of $10^2 \, \text{s}^{-1}$ to $10^3 \, \text{s}^{-1}$.

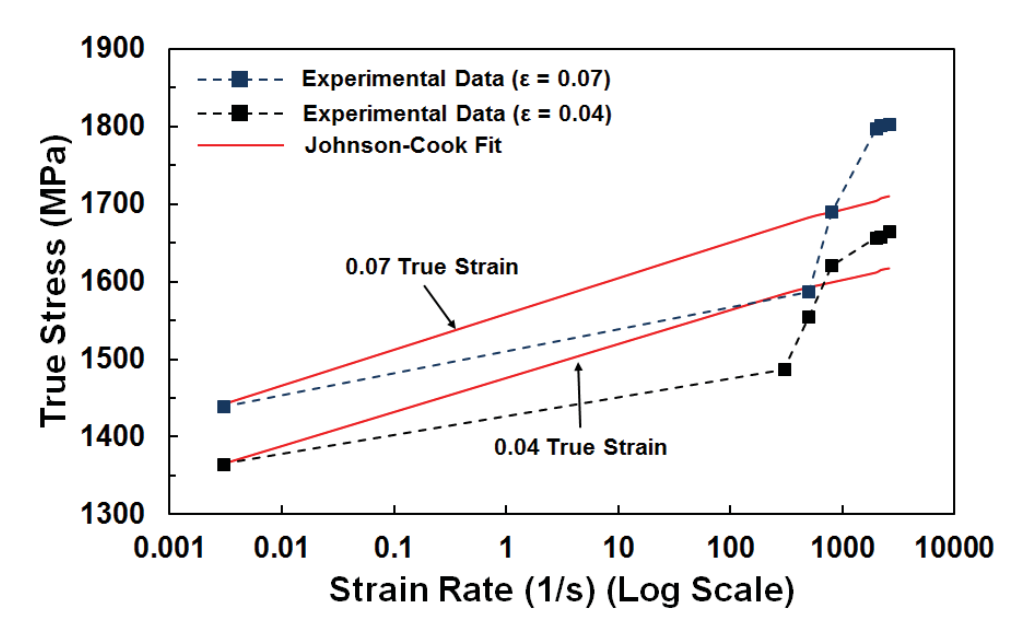


Figure 6.12. Strain rate sensitivity of Johnson-Cook model for IN718 at room temperature (true stress vs. log strain rate plot at 0.04 and 0.07 strain)

This can be observed not only at room temperature but also at higher deformation temperatures as demonstrated by the flow stress curves in Figures 5.1 and 5.2. The difference in the flow stress ($\sim 100 \text{MPa}$) is greater between strain rates at 10^2 s^{-1} range compared to the difference ($\leq 50 \text{MPa}$) between strain rates at 10^3 s^{-1} range. The strain rate sensitivity of the material appears to decrease at 10^3 s^{-1} strain rate. The Johnson-Cook model assumes a constant log-linear strain rate sensitivity which does not represent the behavior of the material.

The Cowper-Symonds (modified Johnson-Cook) model has a better strain rate sensitivity compared to the Johnson-Cook model as shown in Figure 6.13.

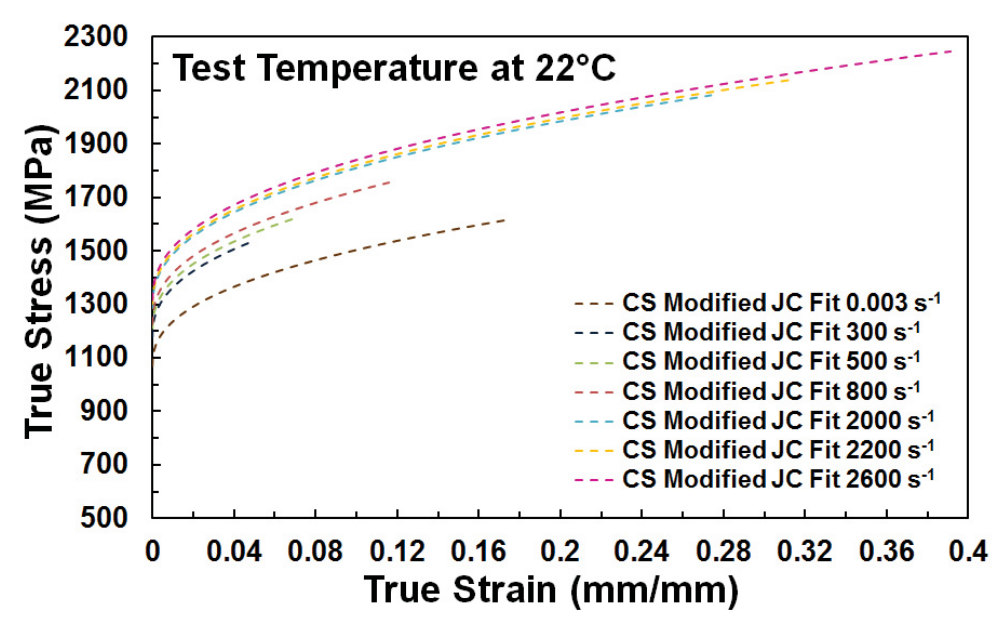


Figure 6.13. Predicted curves for IN718 at room temperature with increasing strain rates using Cowper-Symonds (modified Johnson-Cook) model

The predicted curves at room temperature with increasing strain rates showed distinct separations as the strain rate level increased. Defined curve separations at different strain rate ranges of $0.003~s^{-1}$, $10^2~s^{-1}$, and $10^3~s^{-1}$ can be observed.

Also, a better fit of the predicted curve to the experimental data is observed as shown in Figure 6.14. The model fits all the experimental data well at quasi-static and high strain rates. It captured the change of and difference in the strain rate sensitivity at increasing strain rates as shown in Figure 6.15.

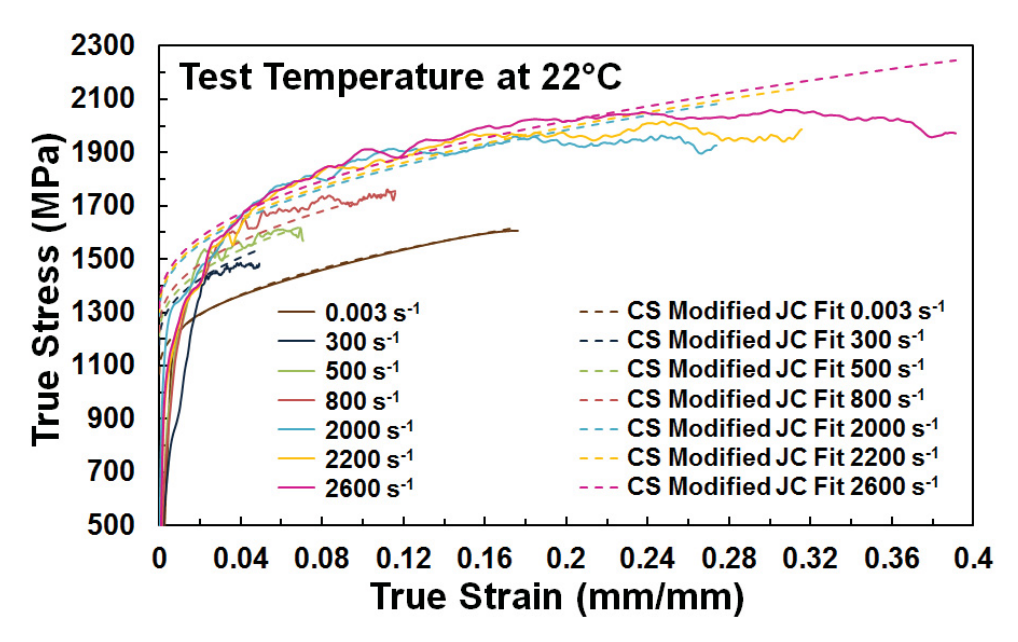


Figure 6.14. Comparison of experimental and Cowper-Symonds (modified Johnson-Cook) model predicted flow stress curves of IN718 at room temperature with increasing strain rate

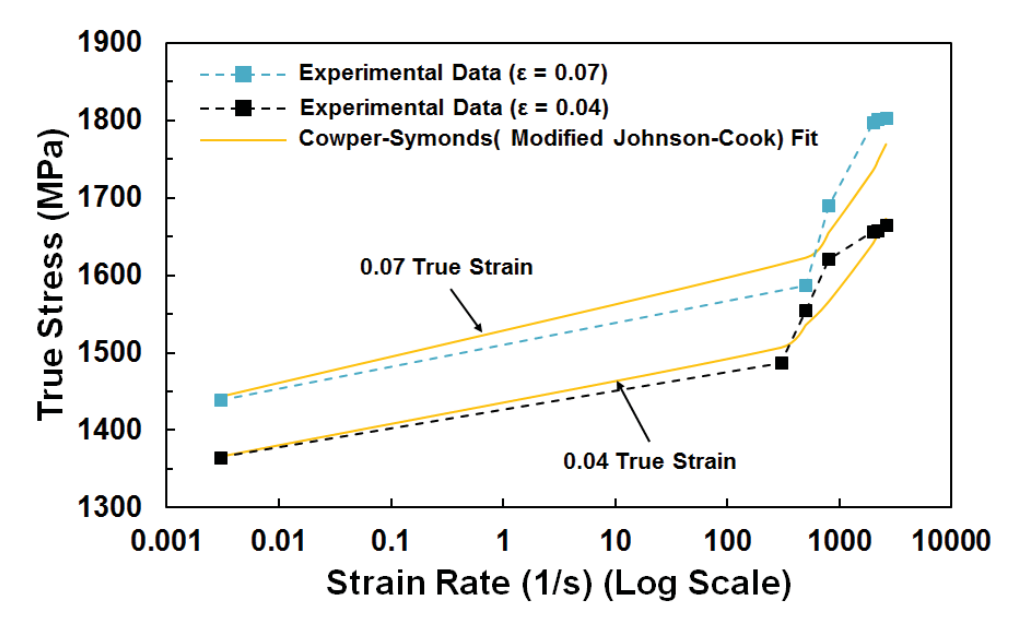


Figure 6.15. Strain rate sensitivity of Cowper-Symonds (modified Johnson-Cook) model for IN718 at room temperature (true stress vs. log strain rate plot at 0.04 and 0.07 strain)

In order to quantify how well each model fits the experimental data and how one model is better than the other in fitting the experimental data, statistical parameters such

as the Residual Sum of Squares (RSS), R² of Non-Linear Regression, and Standard Error of Regression (SER) were calculated to measure the goodness of fit of the models. The values of the statistical parameters for both models (Johnson-Cook (JC) and Cowper-Symonds (modified Johnson-Cook) (CS (modified JC)) are shown in Table 6.8.

Table 6.8 Summary of the statistical parameters representing the goodness of fit of the models to IN718 experimental data at room temperature and varying strain rates

Strain	Residual Sum of Squares Strain (RSS)			of Nonlinear egression		Standard Error of Regression (SER)	
Rates	JC	CS (modified JC)	JC	CS (modified JC)	JC	CS (modified JC)	
0.003	1.00×10^{8}	1.01×10 ⁸	0.25	0.25	439.23	440.36	
300	3.71×10^7	3.03×10^7	-0.01	0.17	391.33	353.75	
500	2.78×10^{7}	2.44×10^{7}	0.26	0.35	328.47	307.78	
800	1.98×10^{7}	1.85×10 ⁷	0.43	0.47	278.36	269.12	
2000	1.52×10^{7}	1.61×10^7	0.62	0.59	242.50	249.70	
2200	1.66×10^{7}	1.82×10^7	0.61	0.57	252.55	264.16	
2600	2.09×10^{7}	2.35×10^{7}	0.61	0.56	280.76	298.01	

At the quasi-static strain rate of 0.003 s⁻¹, both models have the same values for the RSS, R², and SER indicating that they fit the quasi-static data similarly. At the strain rate level of 10² s⁻¹ (300, 500, and 800 s⁻¹), the Cowper-Symonds (modified Johnson-Cook) model has a better goodness of fit compared to the Johnson-Cook model as shown by its lower RSS and SER values and higher R² values. A smaller RSS value indicates a tighter fit of the model to the data and a smaller value of SER indicates a closer distance of the data points to the fitted line. This result reflects the strain rate sensitivity of the Cowper-Symonds (modified Johnson-Cook) model at 10² s⁻¹ which was not observed in the Johnson-Cook model.

The strain rate sensitivity of each model was compared in Figure 6.16 by plotting the true stress vs. log of strain rate curves at a constant strain of 0.04. Due to the power-law relation in the Cowper-Symonds (modified Johnson-Cook) model, it captured the strain rate sensitivity better than Johnson-Cook model, especially in the 10² s⁻¹ strain rate range.

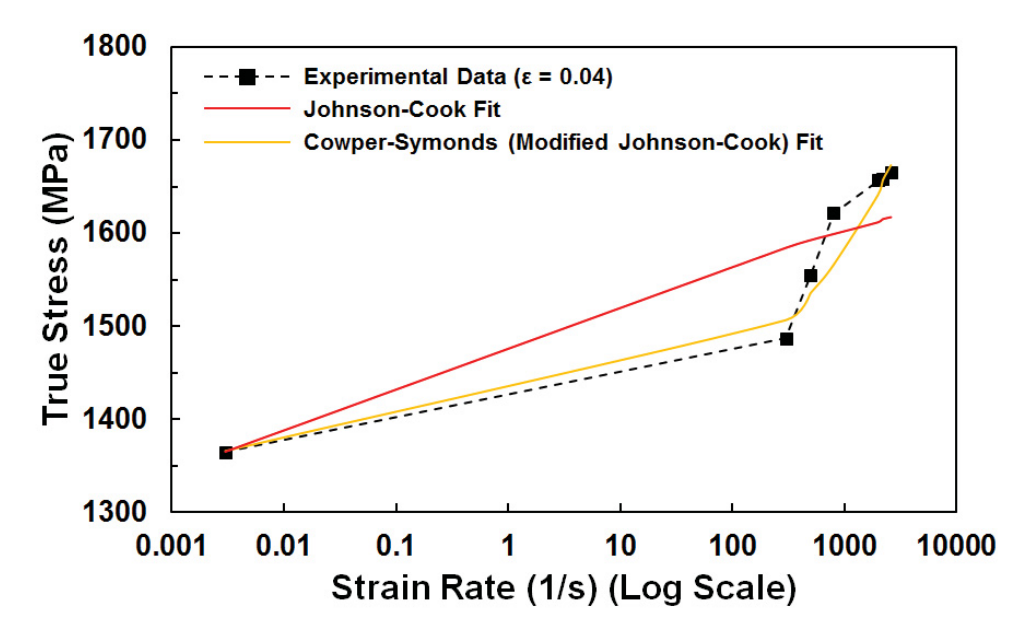


Figure 6.16. Comparison of the strain rate sensitivity of the constitutive fits of Johnson-Cook vs. Cowper-Symonds (modified Johnson-Cook) model for IN718 at 0.04 strain at room temperature

The predicted curves at strain rates of 2,000-2,600 s⁻¹ using the Johnson-Cook and Cowper-Symonds model (Fig. 6.9 and 6.13) were observed to continuously increase with strain while the experimental stress-strain data were shown to flatten due to the thermal softening via adiabatic heating. The predicted curves can be corrected by identifying and including the strain localization at the peak load along the curve. The study of Kobayashi¹¹⁰ discussed the process of this correction which requires monitoring the strain distribution across the specimen's dimension via fiducial measurements from the specimen's images and videos during the deformation test. This process is not a standard method in Johnson-Cook and Cowper-Symonds modelling and is beyond the scope of this study.

6.3.2 Temperature Sensitivity of the Johnson-Cook vs. Cowper-Symonds (Modified Johnson-Cook) Model for IN718

The temperature sensitivities of both the models were evaluated by plotting the experimental data vs. model fit at varying temperatures. The fit using the Johnson-Cook

model are shown in Figures 6.17 to 6.19 while the fit using the Cowper-Symonds (modified Johnson-Cook) model are shown in Figures 6.20 to 6.22.

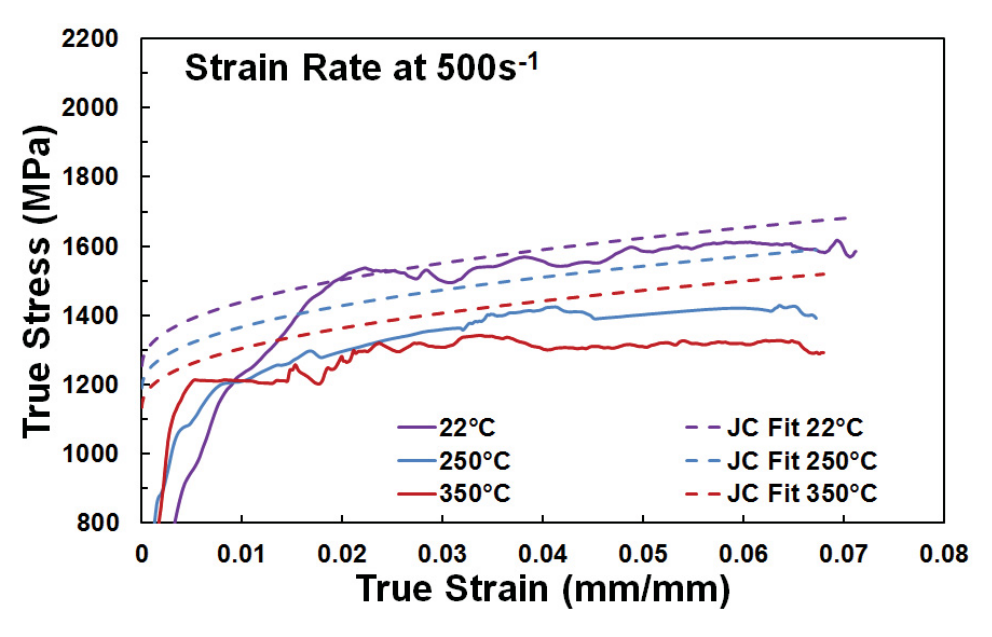


Figure 6.17. Johnson-Cook fit on the experimental data of IN718 at 500 s⁻¹ with increasing temperatures of 22°C, 250°C, and 350°C

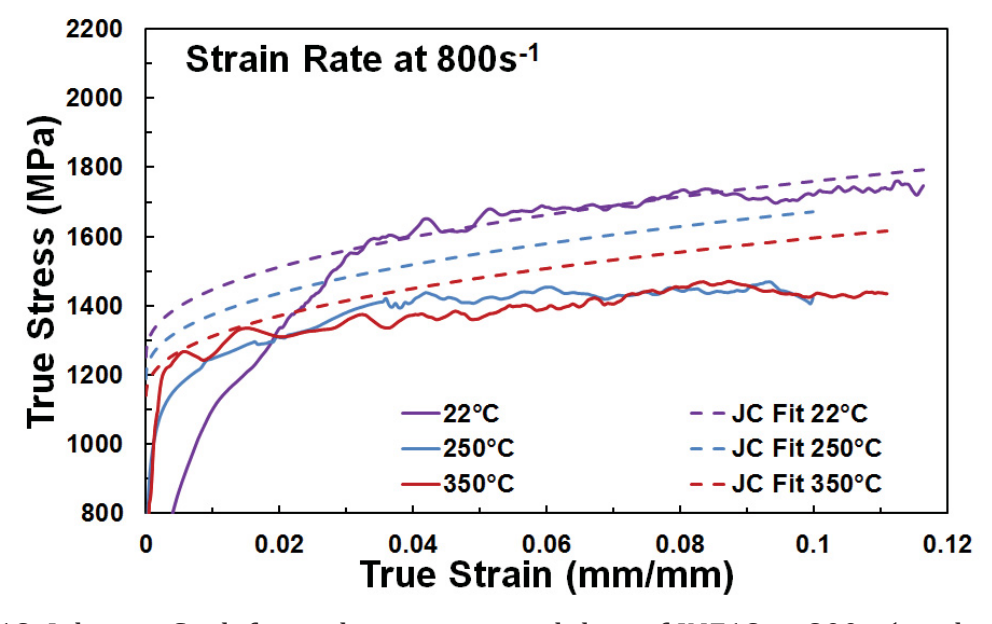


Figure 6.18. Johnson-Cook fit on the experimental data of IN718 at 800 s $^{\text{-}1}$ with increasing temperatures of 22°C, 250°C, and 350°C

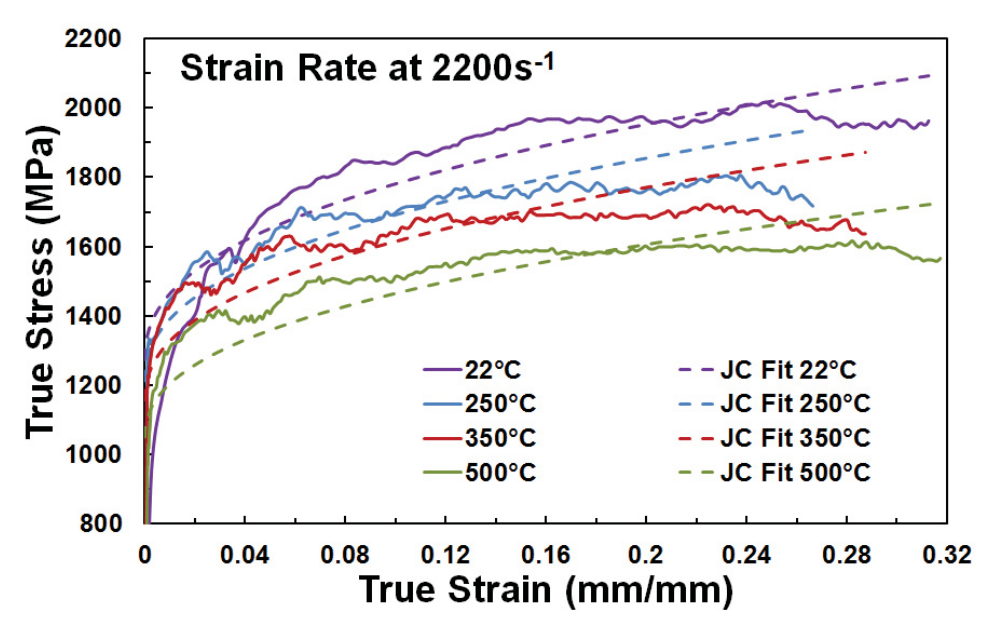


Figure 6.19. Johnson-Cook fit on the experimental data of IN718 at 2200 s $^{-1}$ with increasing temperatures of 22°C, 250°C, 350°C, and 500°C

The temperature sensitivity of the material is captured by the model. The model best fits the experimental data at all deformation temperatures at 2,200 s⁻¹. At lower strain rates of 500 s⁻¹ and 800 s⁻¹, the model overestimates the experimental data at 250 and 350°C. This is due to the fact that the thermal softening coefficient m was calibrated only at 2,200 s⁻¹ strain rate as explained in section 6.3. The lack of data at 500°C for strain rates of 500 s⁻¹ and 800 s⁻¹ made it not possible to use these strain rates in determining the m coefficient. A better temperature sensitivity of the model can be achieved if more deformation temperatures were used to calibrate the model.

The Cowper-Symonds (modified Johnson-Cook) model also captured the temperature sensitivity of the IN718 material as shown in Figures 6.20 to 6.22. Similar with the Johnson-Cook model, the best fit at all deformation temperatures can be seen at the strain rate of $2200 \, \text{s}^{-1}$ (Fig. 6.22).

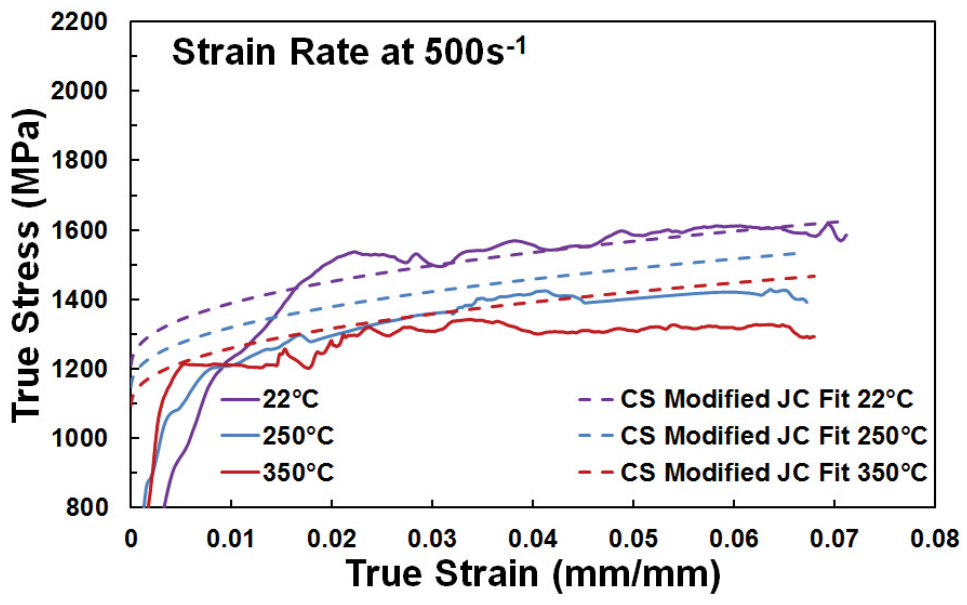


Figure 6.20. Cowper-Symonds (modified Johnson-Cook) fit on the experimental data of IN718 at $500 \, \text{s}^{-1}$ with increasing temperatures of 22° C, 250° C, and 350° C

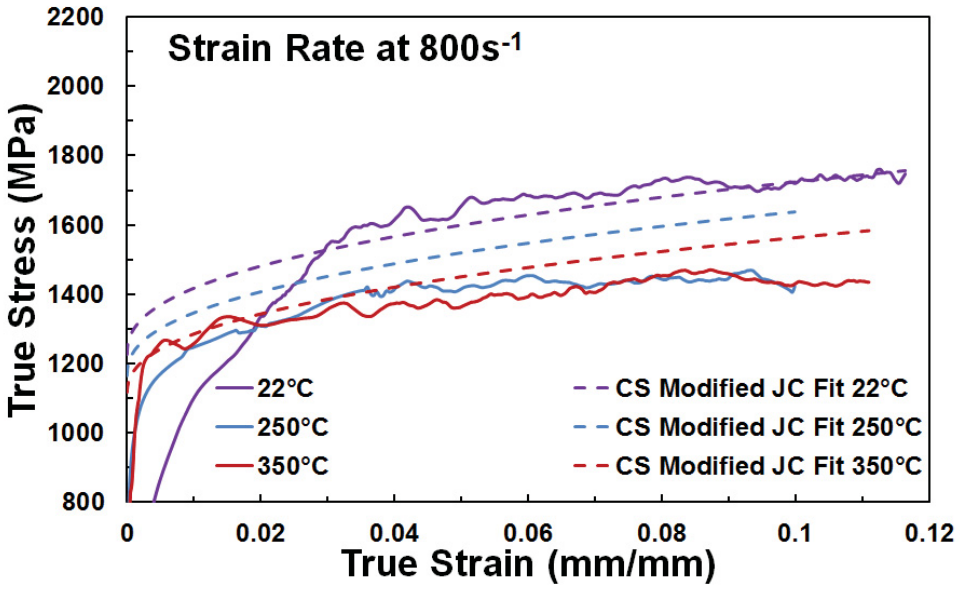


Figure 6.21. Cowper-Symonds (modified Johnson-Cook) fit on the experimental data of IN718 at $800 \, s^{-1}$ with increasing temperatures of 22° C, 250° C, and 350° C

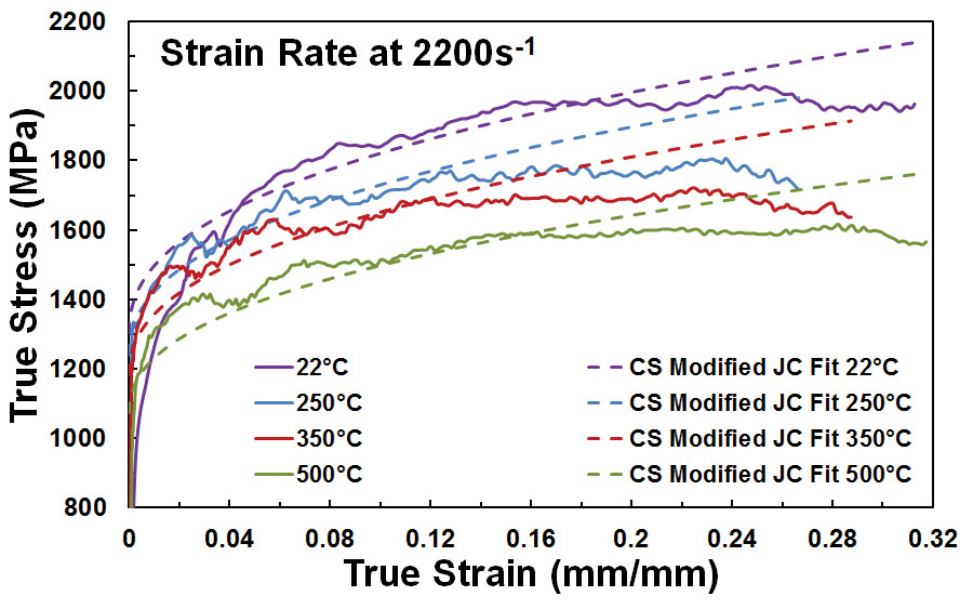


Figure 6.22. Cowper-Symonds (modified Johnson-Cook) fit on the experimental data of IN718 at 2200 s⁻¹ with increasing temperatures of 22°C, 250°C, 350°C, and 500°C

The goodness of fit of the two models at constant strain rates and increasing temperatures were compared in terms of statistical parameters. The calculated Residual Sum of Squares (RSS), R² of Non-Linear Regression, and Standard Error of Regression (SER) for each model at varying parameters are tabulated in Tables 6.9 to 6.11.

Table 6.9 Summary of parameters representing the goodness of fit of the models to IN718 experimental data at $500 \, \text{s}^{-1}$ and increasing temperature

(At 500 s ⁻¹) Temperature	Residual Sum of Squares (RSS)		R ² of Nonlinear Regression		Standard Error of Regression (SER)	
remperature	JC	CS (modified JC)	JC	CS (modified JC)	JC	CS (modified JC)
22°C	2.78×10 ⁷	2.44×10 ⁷	0.26	0.35	328.47	307.78
250°C	3.03×10^{7}	2.53×10 ⁷	0.02	0.18	341.52	312.12
350°C	2.98×10^{7}	2.52×10 ⁷	-0.03	0.13	338.36	311.02

Table 6.10 Summary of parameters representing the goodness of fit of the models to IN718 experimental data at $800 \, s^{-1}$ and increasing temperature

(At 800 s ⁻¹)	Residual Sum of Squares (RSS)		R ² of Nonlinear Regression		Standard Error of Regression (SER)	
Temperature	JC	CS	JC	CS (CS)	JC	CS
	,	(modified JC)		(modified JC)	ŕ	(modified JC)
22°C	1.98×10^{7}	1.85×10^{7}	0.43	0.47	278.36	269.12
250°C	2.57×10^7	2.25×10^{7}	0.06	0.17	314.10	294.14
350°C	1.54×10^{7}	1.34×10^{7}	0.24	0.34	254.72	237.73

Table 6.11 Summary of parameters representing the goodness of fit of the models to IN718 experimental data at 2,200 s⁻¹ and increasing temperature

	Residual Sum of Squares		\mathbb{R}^2 o	f Nonlinear	Standard Error of		
Temperature	((RSS)	R	Regression		Regression (SER)	
(At 2200 s ⁻¹)	IC	CS	IC	CS	IC	CS	
	JC	(modified JC)	JC	(modified JC)	JC	(modified JC)	
22°C	1.66×10^7	1.82×10^{7}	0.61	0.57	252.55	264.16	
250°C	1.91×10^7	2.08×10^{7}	0.51	0.46	276.19	288.49	
350°C	1.38×10^7	1.53×10^7	0.53	0.47	227.82	240.07	
500°C	1.70×10^7	1.81×10^{7}	0.54	0.51	255.33	263.95	

Statistical results representing the goodness of fit of the models tabulated in Tables 6.8 to 6.10 show that at $500 \, \text{s}^{-1}$ and $800 \, \text{s}^{-1}$, the Cowper-Symonds (modified Johnson-Cook) model fit the experimental data better than the Johnson-Cook model. The RSS and SER values are lower while the R^2 values are higher for the Cowper-Symonds (modified Johnson-Cook) model fit which suggest that this model has a tighter fit to the experimental data.

At a strain rate of 2,200 s⁻¹, the Johnson-Cook model has a slightly better fit than the Cowper-Symonds (modified Johnson-Cook) model as shown by its slightly lower RSS and SER values and slightly higher R² values. This is because the Cowper-Symonds (modified Johnson-Cook) model overestimates the stress starting at 0.12 strain as shown in Figure 6.21.

6.4 Comparison with IN718 Johnson-Cook Model Parameters in Literature

The parameters of the Johnson-Cook model for the IN718 material published in literature are summarized in Table 6.12. The high strain rate and elevated temperature conditions used in each of the studies are on the range of $10^2 \, \rm s^{-1}$ to $10^4 \, \rm s^{-1}$ and 100° C to 1000° C, respectively. Different values and combinations of strain rates and temperatures were used in each of the studies.

Table 6.12 Johnson-Cook parameters of IN718 published in the literature

Researcher	A (MPa)	B (MPa)	n	С	m	έ (s ⁻¹)	Material Condition/Heat Treatment
Wang (23)	963	937	0.333	Varies at different strain rate & temperature	1.3	0.001	Solution and Aging Treated
Demange (71)	1290	895	0.5260	0.016	1.55	0.03	Annealed+718°C/8h (vacuum), cool at 38°C/h to 621°C, hold at 621°C/8h, quick cool
Pereira (105)	1350	1139	0.6522	0.0134	1.55	1.0	AMS5596 (Annealed+718°C/8h (vacuum), cool at 38°C/h to 621°C, hold at 621°C/8 h, quick cool)
Kobayashi (110)	980	1370	0.164	0.02	1.03	1	-
Zhou (111)	900	1200	0.6	0.0092	1.27	1.0	-
Brar (112)	1138	1324	0.5	0.0092	1.27	1.0	-
This Study	1067	1128	0.416	0.0138	1.71	0.003	AMS5662M (Vac Age at 718°C/8h, cool at 38°C/h to 621°C, hold at 621°C/8h, vac argon quench)

It is shown in Table 6.11 that each study resulted to different values of the Johnson-Cook parameters. The parameters identified in this thesis are within the range of the values in the literature. The differences in the values are due to the following three main reasons: the IN718 materials have dissimilar specifications and heat treatment conditions, a slightly higher or lower reference strain rate was used, and the region of the curve used for fitting was chosen selectively.

The Johnson-Cook parameters identified by other researchers such as Wang,²⁴ Demange⁷¹ and Pereira¹⁰⁵ were used to simulate the flow stress curves at high strain rates and room and high temperature. The parameters from the works of the mentioned researchers were chosen since their studies have a similar specification/heat treatment of the IN718 material or a value of the reference strain rate close to that in this study. To evaluate how the parameters identified by other researchers will fit the experimental data from this thesis, the predicted Johnson-Cook curves and experimental stress-strain data are plotted in Figures 6.23 and 6.24.

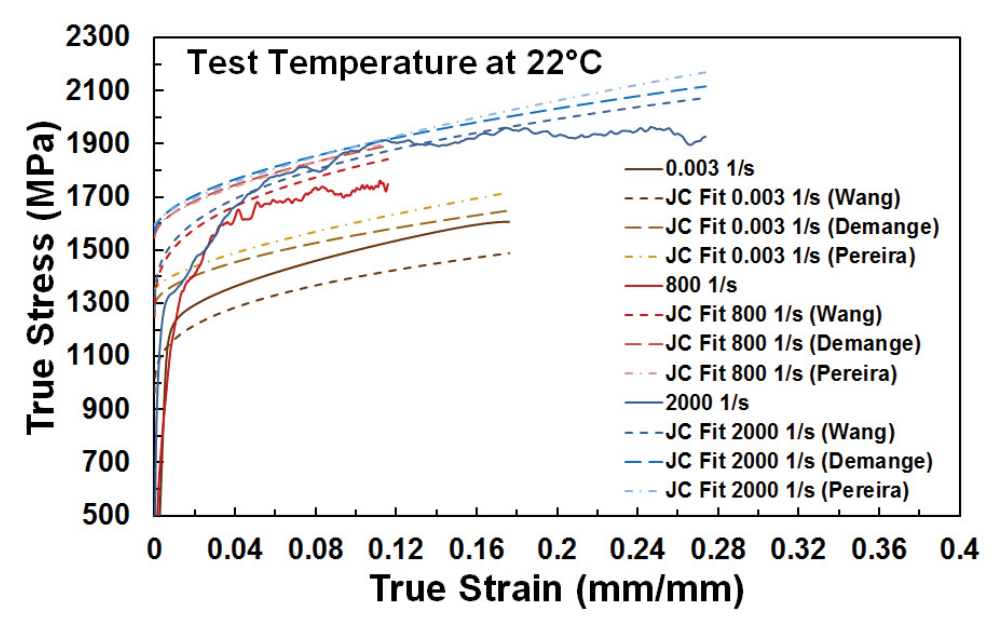


Figure 6.23. Experimental stress-strain curves vs. predicted stress-strain curves using Wang's 24 , Demange's 71 , and Pereira's 105 Johnson-Cook parameters at room temperature and 0.003, 800, and 2,200 s $^{-1}$ strain rates

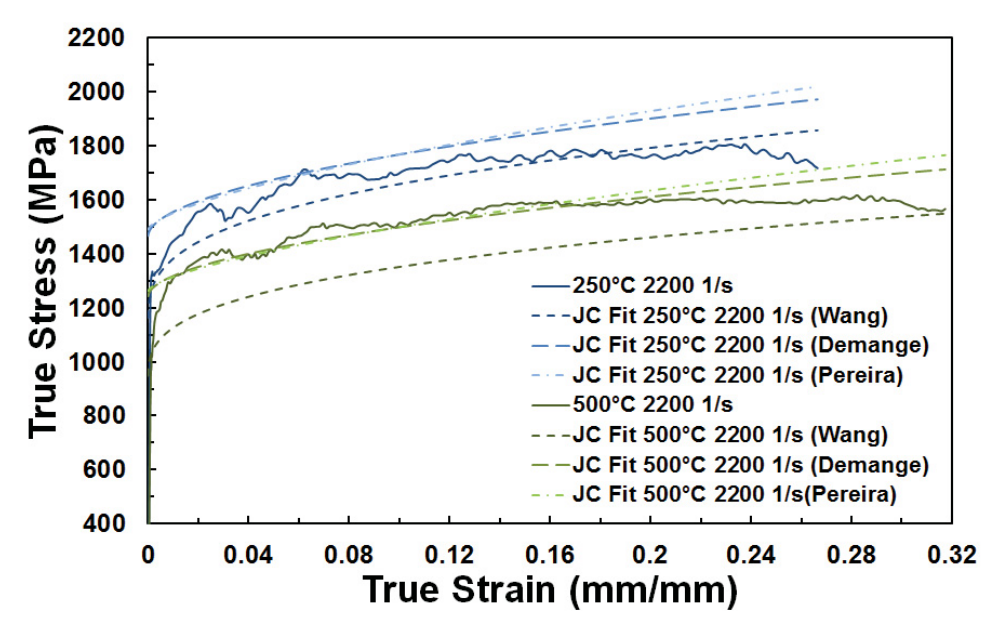


Figure 6.24. Experimental stress-strain curves vs. predicted stress-strain curves using Wang's²⁴, Demange's⁷¹, and Pereira's¹⁰⁵ Johnson-Cook parameters at 2,200 s⁻¹ and 250 and 500°C temperatures

Figure 6.23 shows that Wang's²⁴ parameters underestimate the experimental data at 0.003 s⁻¹ but has a better fit to the data at 800 and 2,200 s⁻¹ compared to Demange's⁷¹ and Pereira's¹⁰⁵ parameters. On the other hand, Demange's⁷¹ and Pereira's¹⁰⁵ parameters overestimate the data at all strain rates. Figure 6.24 shows that at higher deformation temperature, Demange's⁷¹ and Pereira's¹⁰⁵ parameters better fit the data compared to Wang's. ²⁴ Based from these observations, it can be concluded that there is a challenge when using the published IN718 parameters when fitting experimental data if the material conditions and test conditions are different.

Chapter 7: Material Constitutive Model Fitting for 300M Steel

The obtained experimental stress-strain data discussed in Chapter 5.2 were utilized to identify the material constants of the Johnson-Cook model and Cowper-Symonds (modified Johnson-Cook) model for 300M steel. In this chapter, the steps on how each material constant was identified from the experimental stress-strain results at quasi-static strain rate, high strain rates, and elevated temperatures will be discussed. The goodness of fit of the predicted curves on the experimental data using the two models will also be compared and discussed.

7.1 Johnson-Cook Constitutive Model for 300M Steel

7.1.1 Determination of the Yield A, Strain Hardening Modulus B, and Strain Hardening Exponent n

A similar process outlined in Chapter 6.1 for IN718 was used to determine the strain hardening constants A, B, and n for 300M steel. Results from three (3) quasi-static tensile tests (ASTM E8) at room temperature and strain rate of $8.3 \times 10^{-5} \, \text{s}^{-1}$ were analyzed to obtain the constants. Both linear and non-linear regression analysis methods were executed.

7.1.1.1 Linear Regression Analysis

The average yield stress determined from a 0.2% offset from the linear slope of the elastic region of the stress-strain curve was 1,712 MPa. The linear fit on one of the plot of the quasi-static plastic region of 300M steel is shown in Figure 7.1. The average B and n values determined from the three quasi-static tensile results are 3,890 MPa and 0.603. The summary of the constant values for each test is tabulated in Table 7.1.

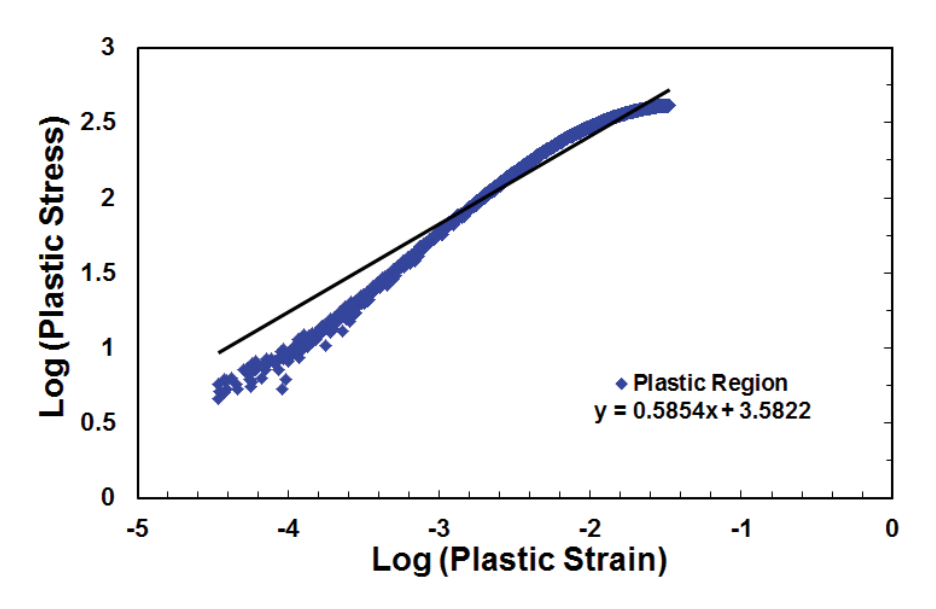


Figure 7.1. Linear fit on the plastic region of 300M steel

Table 7.1 Summary of strain hardening material constant values for 300M steel (linear regression analysis)

Quasi-Static Tensile Test No.	A (Yield Stress) (MPa)	B (Strain Hardening Modulus) (MPa)	n (Strain Hardening Exponent)
1	1708	4572	0.637
2	1727	3296	0.586
3	1702	3801	0.585
Average	1712	3890	0.603

7.1.1.2 Non-Linear Regression Analysis

A non-linear curve fit on the plastic region of one quasi-static tensile test result is shown in Figure 7.2. After applying a non-linear curve fit on the plastic region of each of the stress-strain curves, the average values of the strain hardening constants are found to be: A = 1542 MPa, B = 1531 MPa, and n = 0.326. The summary of the constants A, B, and n for each test are presented in Table 7.2.

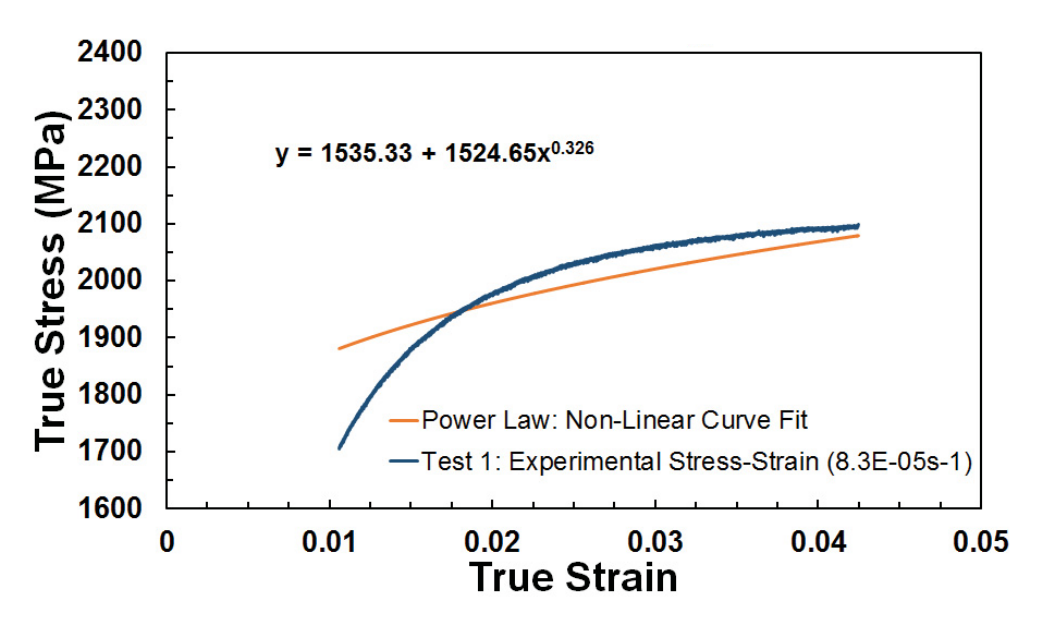


Figure 7.2 Non-linear curve fit on the plastic zone of 300M steel

Table 7.2. Summary of strain hardening material constant values for 300M steel (non-linear curve fitting)

Quasi-Static Tensile Test No.	A (Yield Stress) (MPa)	B (Strain Hardening Modulus) (MPa)	n (Strain Hardening Exponent)
1	1535	1525	0.326
2	1541	1530	0.326
3	1549	1538	0.327
Average	1542	1531	0.326

7.1.1.3 Comparison of Constants A, B & n (Linear vs. Non-Linear Regression Analysis)

Using the average value of the constants A, B, and n determined from both the linear regression method and non-liner curve fitting method, the plot of the Johnson-Cook approximated stress in the plastic zone is compared to the experimental quasi-static stress-strain curve as shown in Figure 7.3. It is clearly shown in the plot that the constants determined using the non-linear curve fitting method approximates the plastic zone better.

Therefore, the strain hardening constant values that will be adapted in this study is A = 1542 ± 0.46 MPa, B = 1531 ± 1.55 MPa, and n = $0.326 \pm 2.77 \times 10^{-4}$.

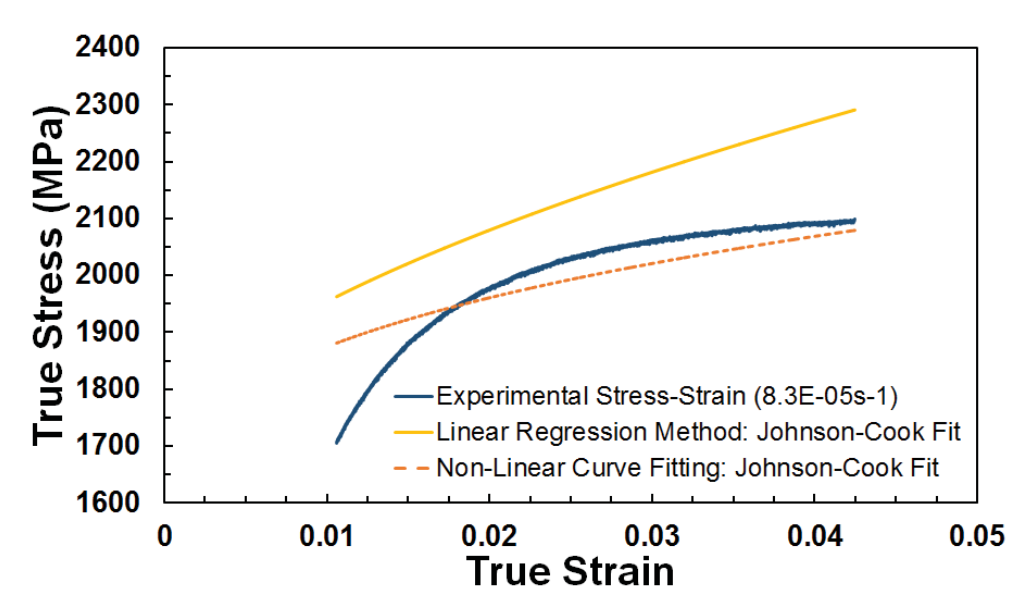


Figure 7.3. 300M steel experimental vs. Johnson-Cook approximated stress-strain curves using linear vs. non-linear regression analysis method

7.1.2 Determination of the Strain Rate Sensitivity Parameter C

The static strain value that would be used to relate the quasi-static stress to the high strain rate and high temperature stress, and consequently to identify the strain sensitivity parameter C and thermal softening coefficient m was easily determined from the intersection of the experimental quasi-static stress-strain curve and Johnson-Cook approximated curve using the constants from the non-linear curve fitting method in Figure 7.2. The average static strain from the three quasi-static tests has a value of 0.0179 with a corresponding average static stress of 1953 MPa. This strain is about 20% of the total plastic strain. Examining the plot of the quasi-static vs. dynamic stress curves in Figure 7.4, it can be observed that at 0.0179 strain, the quasi-static stress is greater than the dynamic stresses at 600, 900, and 1300 s⁻¹ strain rates. This phenomenon can be attributed to the "ring-up" period during the Hopkinson test which greatly impacts the first portion of the stress curve until 20% strain of the material.

Using the value of 0.0179 as the static strain would result to a negative slope which gives an incorrect behavior as the material's deformation resistance will appear to reduce with strain rate which is not the case as displayed by the increase in the flow stress with strain rate at higher strain values. Therefore, a static strain value of 0.025 with a corresponding static stress of 2036 MPa was used instead. This strain corresponds to 30% of the total deformation of the material at the lowest dynamic strain rate of 600 s⁻¹.

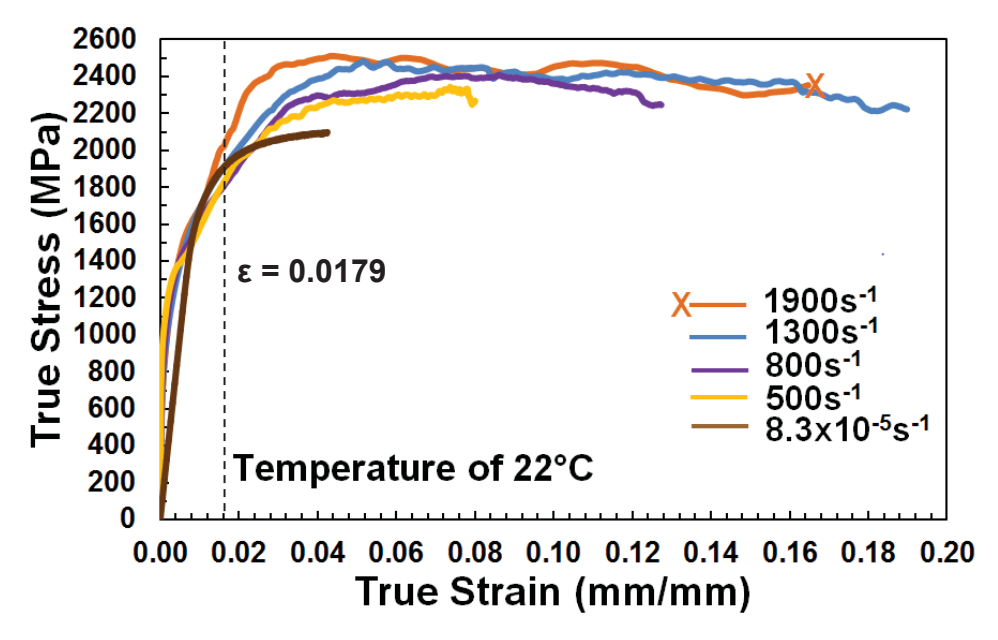


Figure 7.4. Plot of 300M steel quasi-static stress vs. dynamic stress at room temperature showing the strain of 0.0179

Following the same procedure in Chapter 6.2, results from six (4) varying high strain rate tests (500, 800, 1,300, 1,900 s⁻¹) at room temperature were utilized to determine the constant C. The plot of the dynamic stress/static stress vs. $\ln\frac{\dot{\varepsilon}}{\dot{\varepsilon}_o}$ from four varying high strain rate tests at room temperature is shown in Figure 7.5. Each dynamic stress value used in the plot is an average of two (2) high strain rate tests. The slope of the least fit square gives the strain rate sensitivity parameter C a value of 0.0036 ± 0.0016.

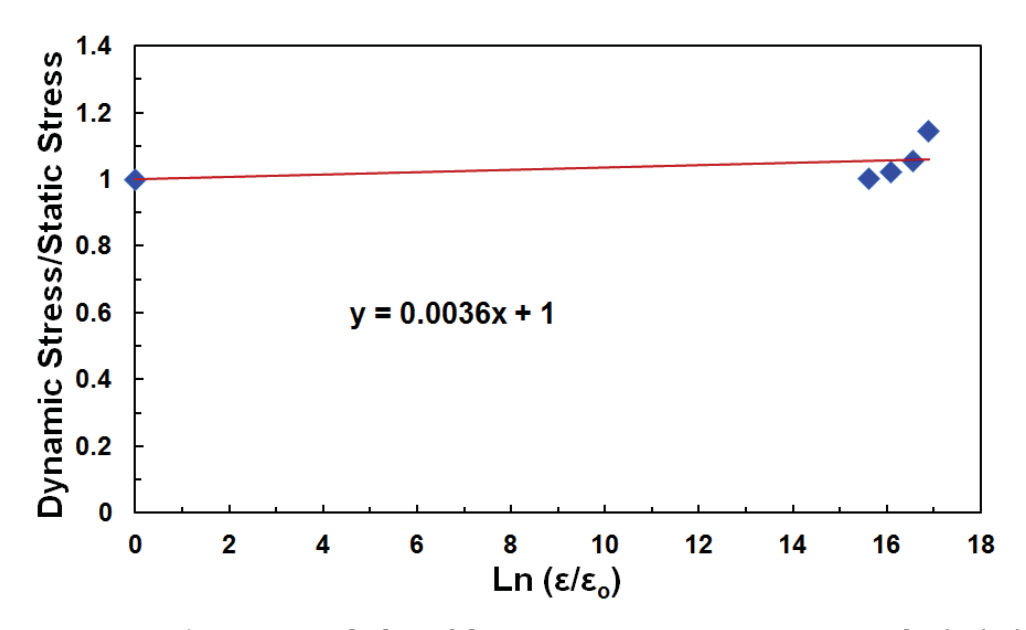


Figure 7.5. 300M steel plot of dynamic to static stress ratio vs. ln ($\dot{\epsilon}/\dot{\epsilon}_{o}$)

7.1.3 Determination of the Thermal Softening Coefficient m

Similar procedure discussed in Section 6.3 for IN718 was followed to determine the thermal softening coefficient of the 300M steel material. Experimental results at two constant strain rates of 800 s⁻¹ and 1,300 s⁻¹ with increasing deformation temperatures were used. The flow stress curves were related to each other using the same static strain value of 0.025 as in the determination of the strain rate sensitivity parameter C. The homologous temperature T* was calculated using reference temperature T_r = 22°C, melting temperature of 300M steel material $T_m = 1421$ °C, and test temperature T which varies.

The plot of the log (1-Dynamic Stress (T)/Static Stress (RT)) vs. log (T*) for strain rates of 800 s⁻¹ and 1,300 s⁻¹ are shown in Figures 7.6 and 7.7 respectively. Only two deformation temperatures (350 and 500°C) were used to determine the m coefficient. The average m coefficient from the plots of the two strain rates resulted to a value of 1.191 \pm 0.085.

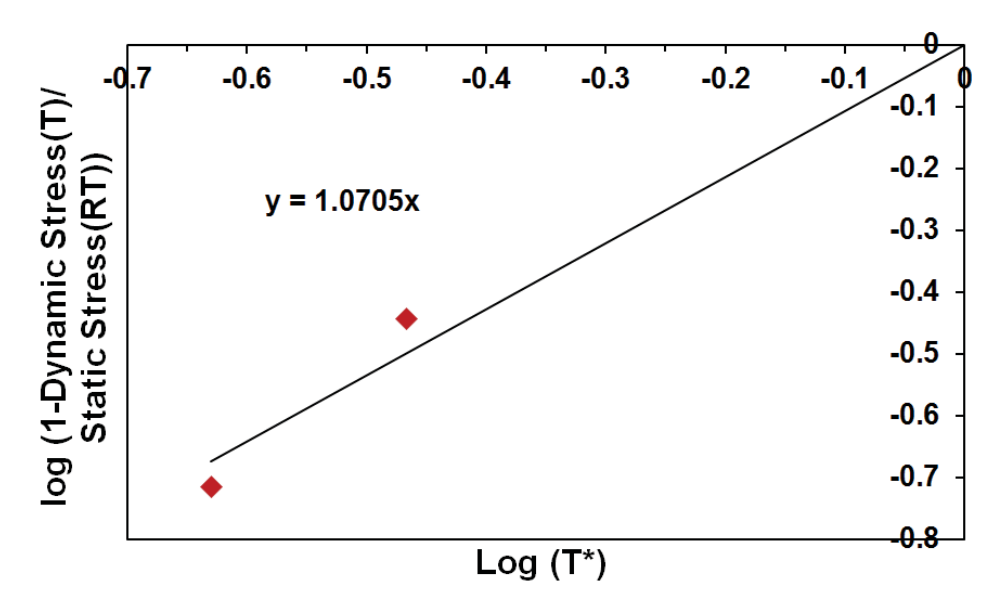


Figure 7.6. 300M steel plot of $\log\left(1-\left(\sigma/\sigma_{dynamic(RT)}\right)\right)$ vs. $\log(T^*)$ for 800 s⁻¹

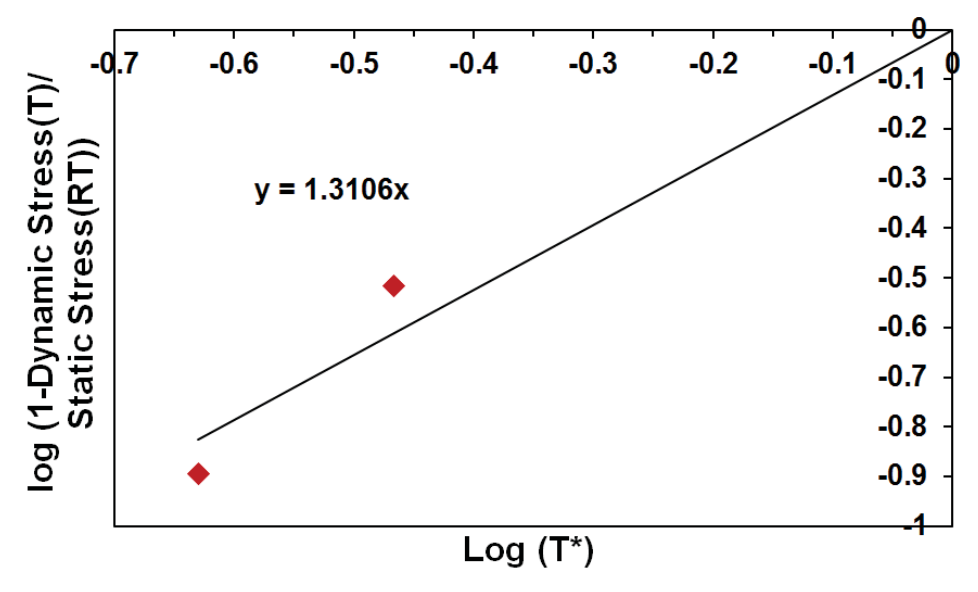


Figure 7.7. 300M steel plot of $\log\left(1-\left(\sigma/\sigma_{dynamic(RT)}\right)\right)$ vs. $\log(T^*)$ for 1300 s⁻¹

The Johnson-Cook material parameters for 300M steel determined in this study are shown in Table 7.3.

Table 7.3 Summary of Johnson-Cook parameters for 300M steel

Johnson-Cook parameters for 300M steel						
A (MPa) B (MPa) n C m						
1542 ± 0.46	1531 ± 1.55	$0.326 \pm 2.77 \times 10^{-4}$	0.0036 ± 0.0016	1.191 ± 0.085		

7.2 Cowper-Symonds (Modified Johnson-Cook) Model for 300M Steel

The Cowper-Symonds (modified Johnson-Cook) model (Eq. 6.11) used in the constitutive fitting of IN718 was also utilized to model the flow stress of 300M steel. In this section, the steps on how the Cowper-Symonds coefficients D and q were identified for the 300M steel material will be discussed.

7.2.1 Determination of the Cowper-Symonds Coefficients D and p

A similar procedure discussed in Section 6.2.1 for determining the D and p coefficient of IN718 was followed to identify the same coefficients for the 300M steel material. The static strain value of 0.025 used to determine the Strain Rate Sensitivity Parameter c (Section 7.1.2) and Thermal Softening Coefficient m (Section 7.1.3) of the Johnson-Cook model was also utilized to determine the D and q coefficients of the Cowper-Symonds equation for 300M steel.

Using the re-arranged Cowper-Symonds equation at room temperature (Eq. 6.14), the values of the dynamic stress, σ and static stress, σ_{static} at 0.025 strain were substituted into the equation. Strain rate values of 500 s⁻¹ and 800 s⁻¹ were used to identify the initial coefficients at the lower strain rate range, while strain rate values of 800 s⁻¹ and 1900 s⁻¹ were used to identify the coefficients at the higher strain rate range. By the method of substitution, the two variables (D and q) in the system of equations for the lower and upper strain rate range were solved for. The values of the D and p coefficients identified for the two strain rate ranges are shown in Table 7.4.

Table 7.4 300M steel Cowper-Symonds coefficients D and p at strain rate ranges of 500-800 s^{-1} and 800-1,900 s^{-1}

Strain Rate (s ⁻¹)	D (s ⁻¹)	р
500-800	1949	0.24
800-1900	4240	0.44

The Cowper-Symonds coefficients determined for the lower (500-800 s⁻¹) and upper (800-1,900 s⁻¹) strain rate ranges were evaluated by plotting the dynamic stress/static stress values calculated using the determined D and p coefficients vs. the strain rate. The plots of the computed dynamic stress/static stress value vs. strain rate alongside the experimental data are shown in Figure 7.8.

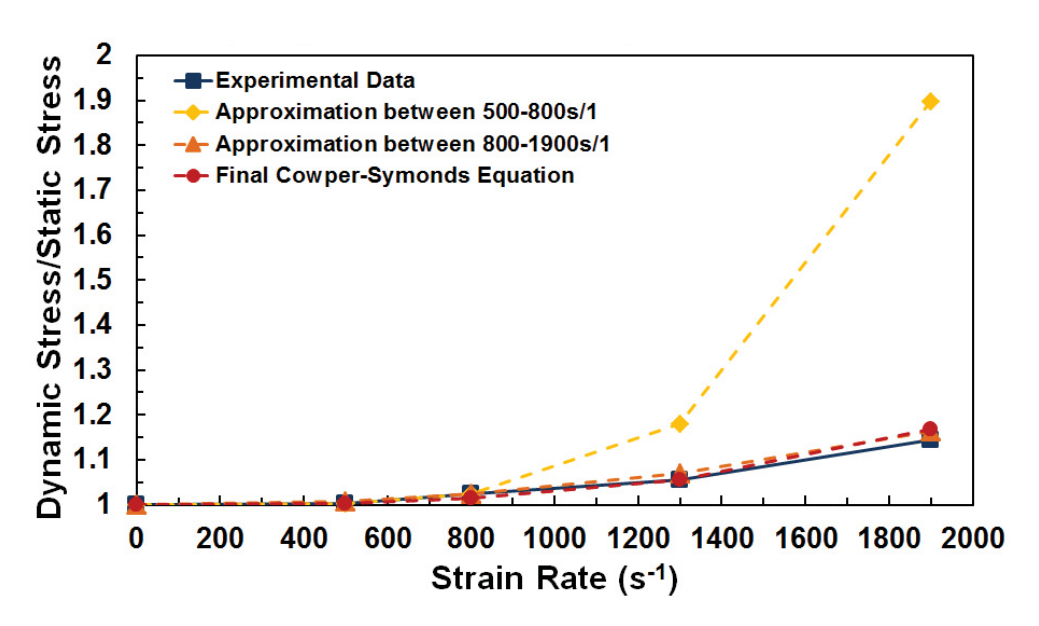


Figure 7.8. Evaluation of the initial (lower and upper strain rate ranges) and final Cowper-Symonds coefficients of 300M steel

The final Cowper-Symonds coefficients for the entire strain rate range (500-1,900 s⁻¹) were found by trial and error and by performing a few iterations using the Excel program. The plot of the dynamic stress/static stress value vs. strain rate using the final coefficients is also shown in Figure 7.8. The final Cowper-Symonds coefficients have a value of D = 3529 and p = 0.35.

The method described for determining the D and p coefficients of the Cowper-Symonds equation was adapted from the work of M. Di Sciuva et al. 109

7.3 Comparison of the Constitutive Model Fits for 300M Steel

The experimental data of the 300M steel material were fitted using the Johnson-Cook and Cowper Symonds (modified Johnson-Cook) model using the identified parameters shown in Tables 7.5 and 7.6.

Table 7.5 Identified Johnson-Cook model parameters for 300M steel

Parameter	Estimate	95% LCL	95% UCL
A (MPa)	1.542×10^3	1.539×10^3	1.544×10^3
B (MPa)	1.531×10^3	1.526×10^3	1.536×10^3
n	0.326	0.325	0.327
С	0.0036	-8.965×10 ⁻⁴	0.0080
m	1.191	0.827	1.554

Table 7.6 Identified Cowper-Symonds (modified Johnson-Cook) model parameters for 300M steel

Parameter	Estimate	95% LCL	95% UCL
A (MPa)	1.542×10^3	1.539×10^3	1.544×10^{3}
B (MPa)	1.531×10^{3}	1.526×10^3	1.536×10^3
n	0.326	0.325	0.327
D (s ⁻¹)	3.529×10^{3}	-	-
p	0.35	-	-
m	1.191	0.827	1.554

The results of the constitutive fits and sensitivity of each of the models to strain rate and temperature will be presented in this section.

7.3.1 Strain Rate Sensitivity of the Johnson-Cook vs. Cowper-Symonds (Modified Johnson-Cook) Model for 300M Steel

The Johnson-Cook predicted curves for 300M steel at room temperature with increasing strain rates are shown in Figure 7.9. The model did not reflect any sensitivity to strain rate. The predicted curves at 10^2 s⁻¹ and 10^3 s⁻¹ range were concentrated at one stress level with no distinct separation between the curves. Only the flow stress curve at the quasi-static strain rate of 8.3×10^{-5} s⁻¹ can be clearly distinguished from the other curves at higher strain rates.

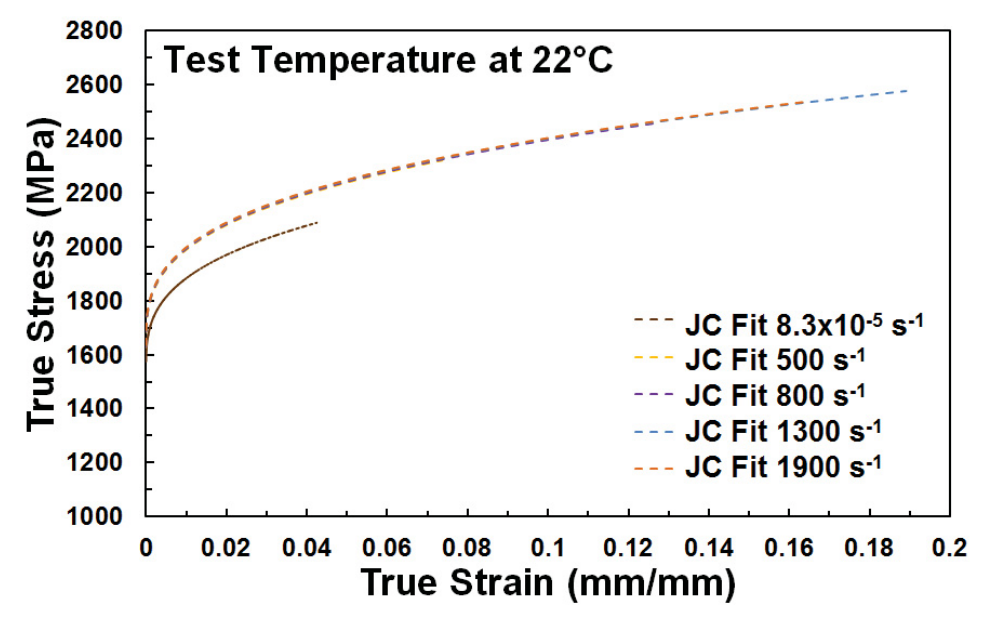


Figure 7.9. Predicted curves for 300M steel at room temperature with increasing strain rates using the Johnson-Cook model

The comparison of the Johnson-Cook Fit predicted curves to the experimental data at room temperature and increasing strain rates is shown in Figure 7.10 with a zoom in of the plot starting at 2000 MPa shown in Figure 7.11. It can be seen from the plot that the model captured the plastic portion of the quasi-static curve and the curve at 500 s⁻¹ relatively well but clearly underestimates the data higher strain rates.

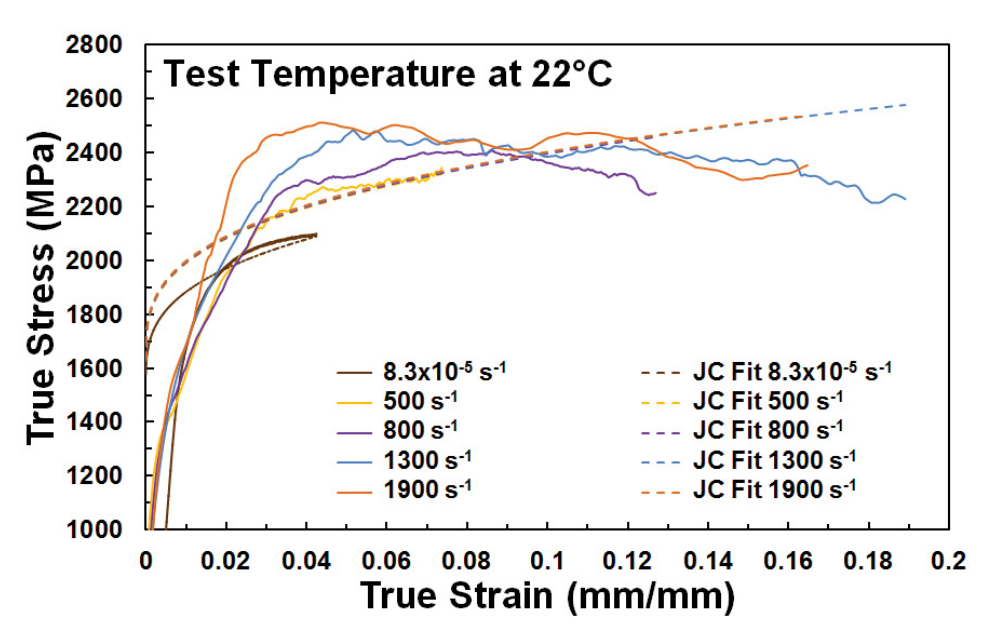


Figure 7.10. Comparison of experimental and Johnson-Cook model predicted flow stress curves of 300M steel at room temperature with increasing strain rate

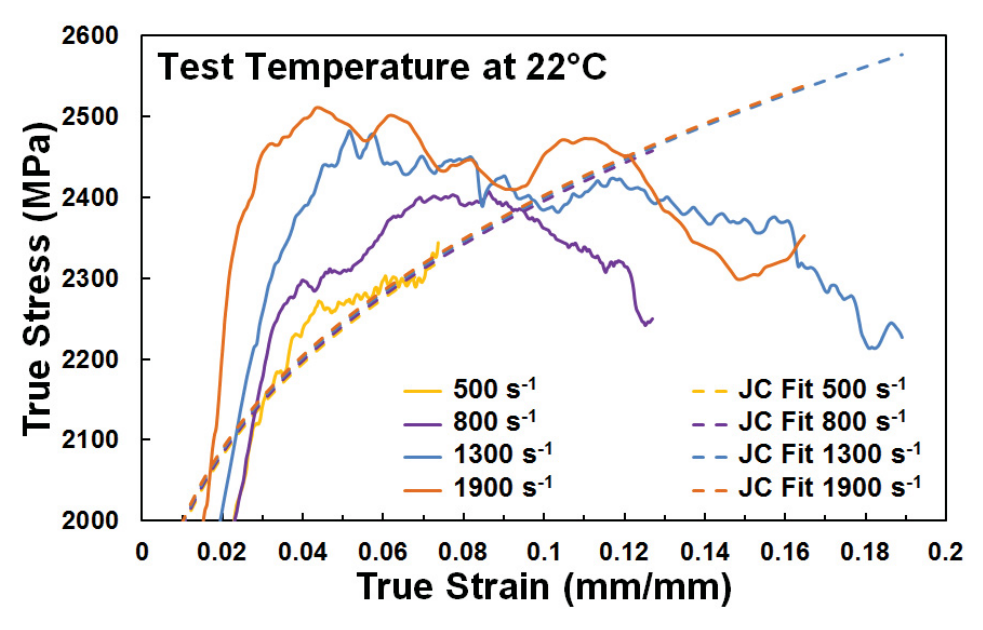


Figure 7.11. Zoom-in of Johnson-Cook fit for 300M steel at room temperature starting at a true stress 2000 MPa

The lack of fit as illustrated in Figure 7.12 is due to the simple-log linear strain rate expression in the Johnson-Cook model which does not apply to the dynamic behavior of the

material. The strain rate sensitivity as the strain rate increases, e.g. strain rates higher than 500 s⁻¹, and flow stress saturation occurring at >1300 s⁻¹ (10^3 s⁻¹ range) cannot be captured by the Johnson-Cook model.

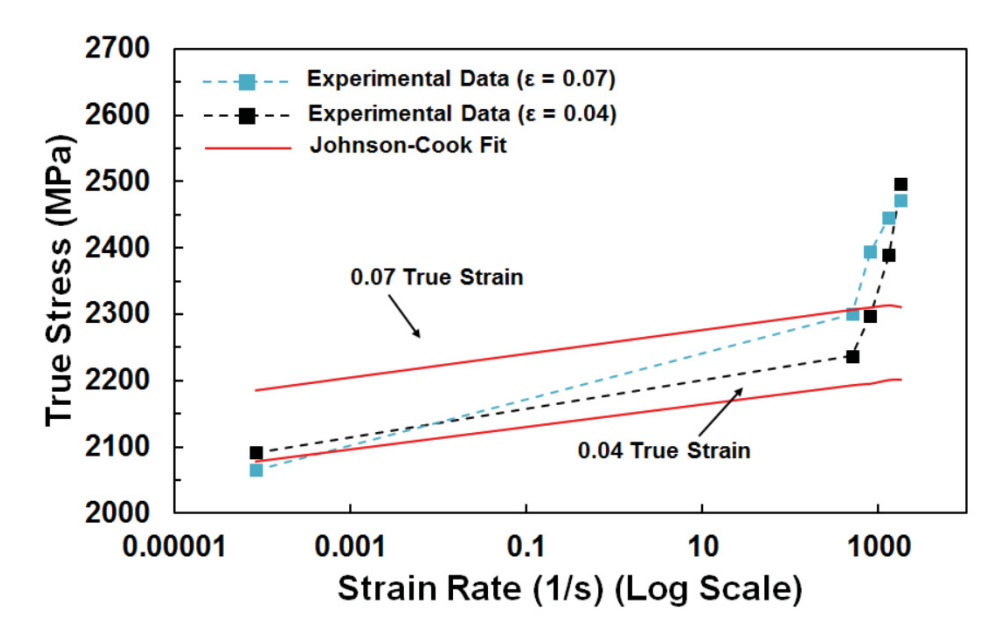


Figure 7.12. Strain rate sensitivity of Johnson-Cook fit for 300M steel at room temperature

Another reason for the lack of fit is that the adiabatic heating phenomenon which is very evident in the 300M steel material and which caused the decrease of flow stress and failure of the material is not incorporated in any functions in the model.

The predicted curves using the Cowper-Symonds (modified Johnson-Cook) model for room temperature and increasing strain rates are shown in Figure 7. 13. In this figure, a better sensitivity of the model can be observed as illustrated by the flow stress curve separation as the strain rate is increased. The flow stress curve for a specific strain rate can be easily identified.

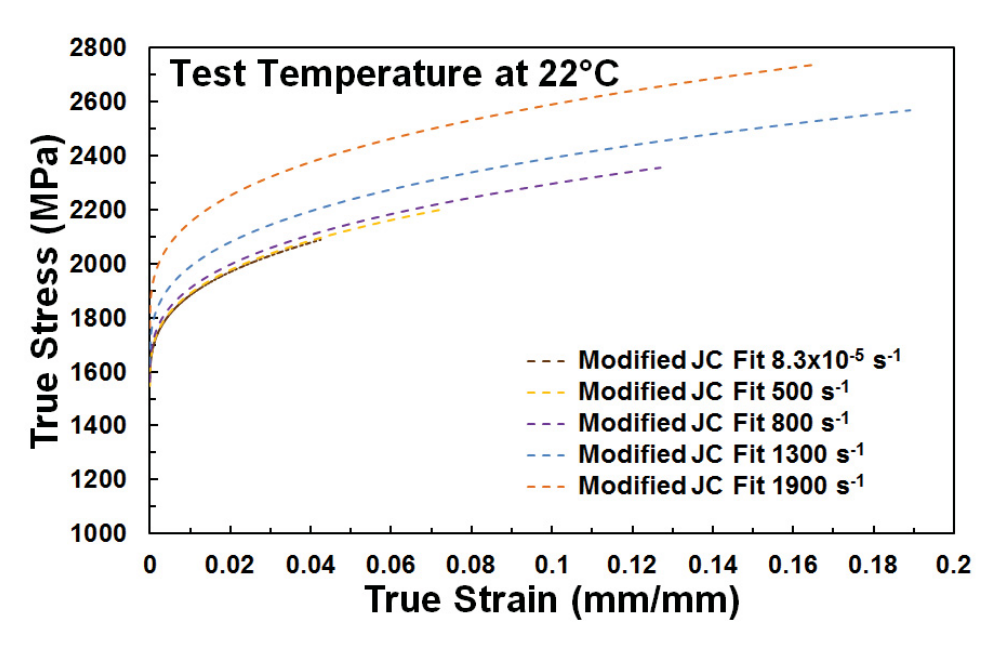


Figure 7.13 Predicted curves for IN718 at room temperature with increasing strain rates using Cowper-Symonds (modified Johnson-Cook) model

Although a better strain rate sensitivity was observed by using the Cowper-Symonds (modified Johnson-Cook) model, the model still did not fit the experimental data very well as shown in Figure 7.14. Similar with the Johnson-Cook model, it did not capture the flow stress saturation and thermal softening due to adiabatic heating at $10^3 \, \text{s}^{-1}$ strain rate range. The predicted curves using the model showed a continuous increase in the flow stress with strain for all strain rates while experimental data showed a drop on the flow stress starting at a strain of 0.085 for 900 s⁻¹, 0.055 for 1,300 s⁻¹, and 0.045 for 1,900 s⁻¹. There are no added functions in the Cowper-Symonds (modified Johnson-Cook) Model that represents these phenomena since only the relation for the strain rate function was changed.

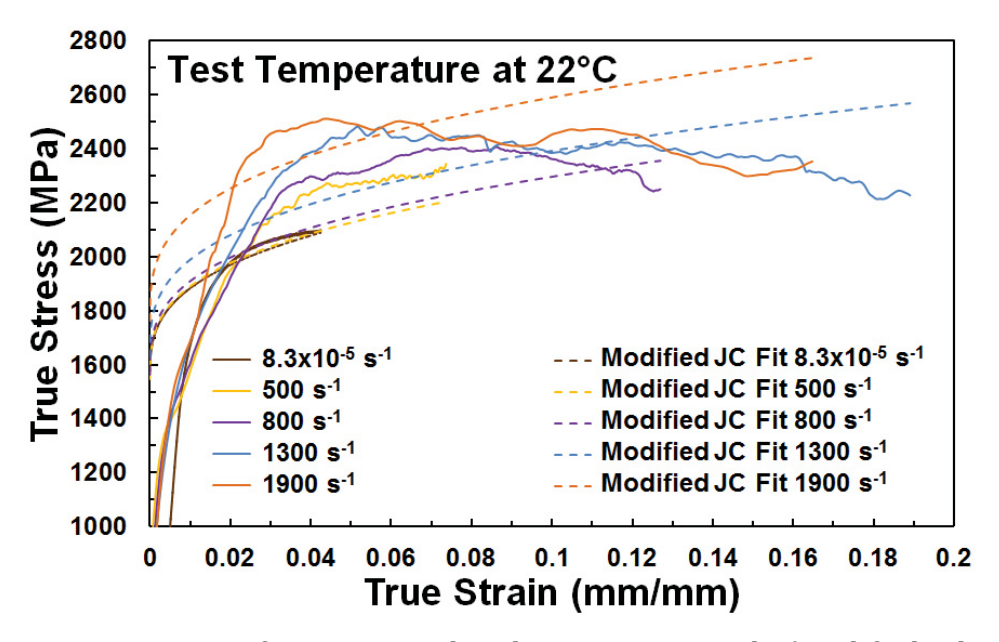


Figure 7.14. Comparison of experimental and Cowper-Symonds (modified Johnson-Cook) model flow stress curves of 300M steel at room temperature with increasing strain rate

The sensitivity of the model at 10^3 s⁻¹ strain rates was observed to be very high compared to what the experimental data displayed. Also, although the sensitivity at 10^2 s⁻¹ strain rates well represented the experimental data, the model still underestimated the data at all strain rates as illustrated in Figure 7.15.

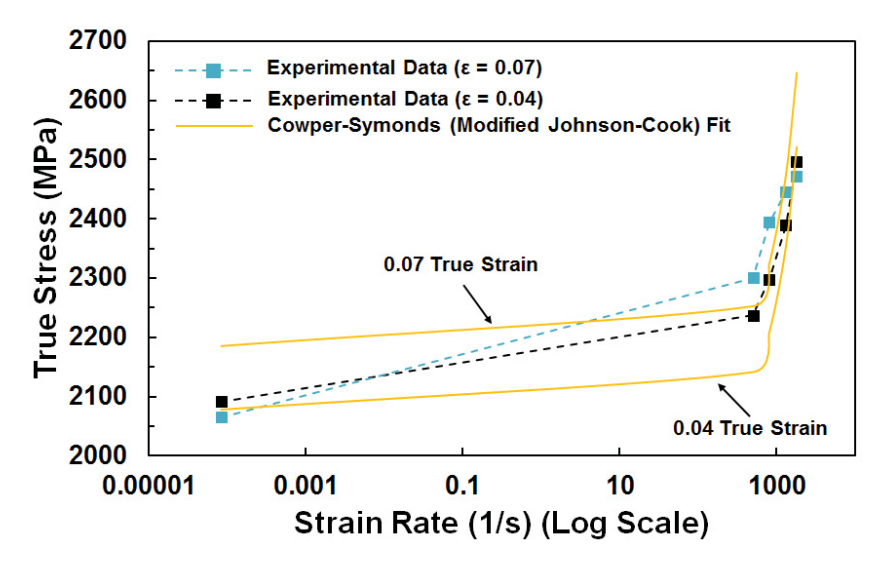


Figure 7.15. Strain rate sensitivity of Cowper Symonds (modified Johnson-Cook) model for 300M steel at room temperature (true stress vs. log strain rate plot at 0.04 and 0.07 strain)

The goodness of fit of the Johnson-Cook and Cowper Symonds (modified Johnson-Cook) models to the experimental data were compared in terms of statistical parameters. The Residual Sum of Squares (RSS), R² of Nonlinear Regression, and Standard Error of Regression (SER) were calculated to asses which model has a tighter fit to the experimental data. Table 7.7 tabulates the summary of the calculated value for each of the statistical parameters for the two models.

Table 7.7 Summary of the statistical parameters representing the goodness of fit of the models to 300M steel experimental data at room temperature and varying strain rates

Strain	Residual Sum of rain Squares (RSS)		_	f Nonlinear egression	Standard Error of Regression (SER)	
Rates	JC	CS (modified JC)	JC	CS (modified JC)	JC	CS (modified JC)
8.3×10 ⁻⁵	1.17×10 ⁷	1.17×10 ⁷	-0.14	-0.14	686.04	686.044
500	2.77×10^{7}	2.45×01 ⁷	0.46	0.52	364.66	343.03
800	3.47×10^{7}	3.16×10^7	0.48	0.53	366.99	349.93
1300	4.01×10^{7}	3.96×10^7	0.45	0.45	392.64	390.39
1900	3.86×10^{7}	4.92×10^7	0.45	0.30	469.85	530.08

At the quasi-static strain rate of 8.3×10^{-5} s⁻¹, the two models similarly do not fit the experimental data as shown by their negative R² values and same values of their RSS and SER. At strain rates of 500 and 800 s⁻¹, the Cowper-Symonds (modified Johnson-Cook) model has a lower RSS and SER, and higher R² value which indicate that this model has a relatively better fit of the experimental data than the Johnson-Cook model. Likewise, the Cowper-Symonds (modified Johnson-Cook) model has a slightly better fit at 1300 s⁻¹.

Figure 7.16 shows the comparison of the strain rate sensitivity of each model by plotting the true stress vs. log of strain rate curves at a constant strain of 0.04. Although the Cowper-Symonds (modified Johnson-Cook) model underestimated the data at all strain rates, it followed the same trend of the strain rate hardening behavior of the 300M steel material better than the Johnson-Cook model.

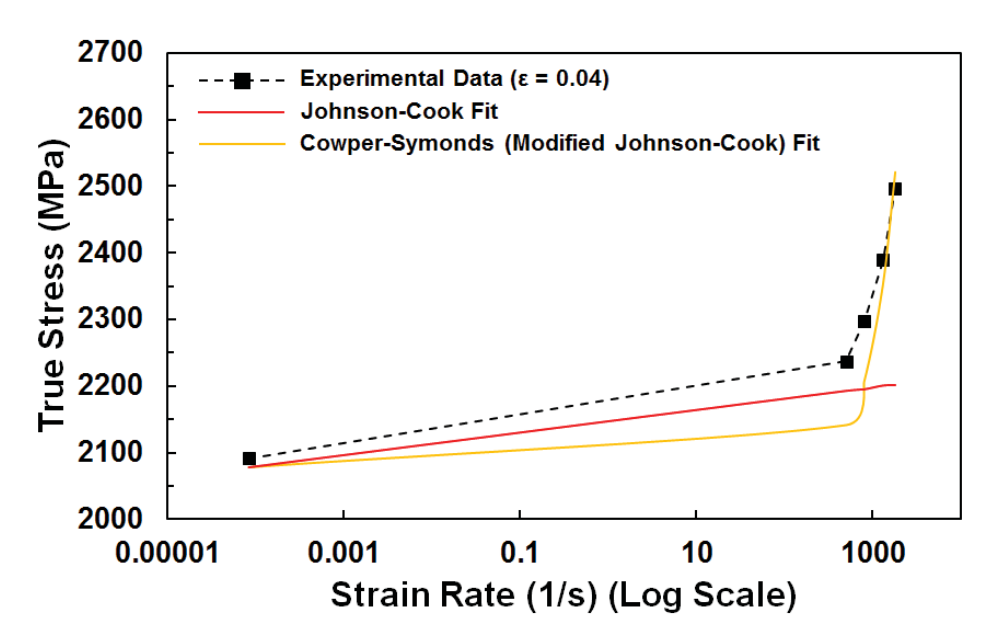


Figure 7.16. Comparison of the strain rate sensitivity of the constitutive fits of Johnson-Cook vs. Cowper-Symonds (modified Johnson-Cook) model for 300M steel at 0.04 strain at room temperature

7.3.2 Temperature Sensitivity of the Johnson-Cook vs. Cowper-Symonds (Modified Johnson-Cook) Model for 300M Steel

The thermal softening behavior of the material due to the applied deformation temperatures at two constant strain rates of 800 s⁻¹ and 1,300 s⁻¹ are shown in Figures 7.17 and 7.18. The predicted curves using the Johnson-Cook model are also shown in the plots. Generally, the model does not fit and capture the elevated temperature flow stress trend of the material.

At 800 s⁻¹ (Fig. 7.17), the model fits the experimental curve at 350°C starting at 0.03 true strain but overestimates it at 500°C. As the strain rate is increased to 1300 s⁻¹ (Fig. 7.18), it can be seen that the fit at 500°C becomes better while the underestimation of the fit at 350°C becomes greater.

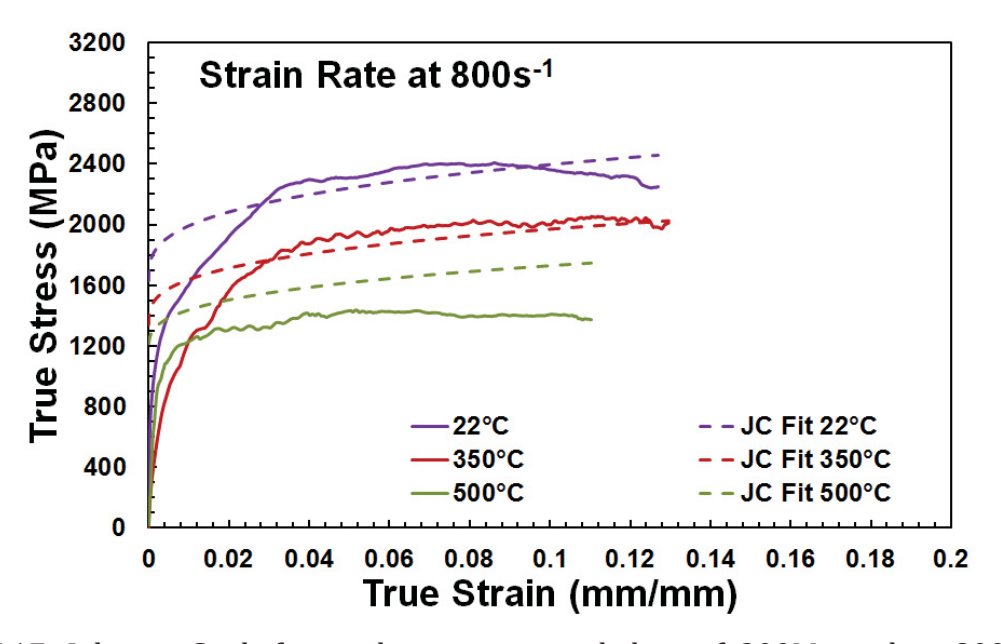


Figure 7.17. Johnson-Cook fit on the experimental data of 300M steel at 800 s $^{-1}$ with increasing temperatures of 22°C, 350°C, and 500°C

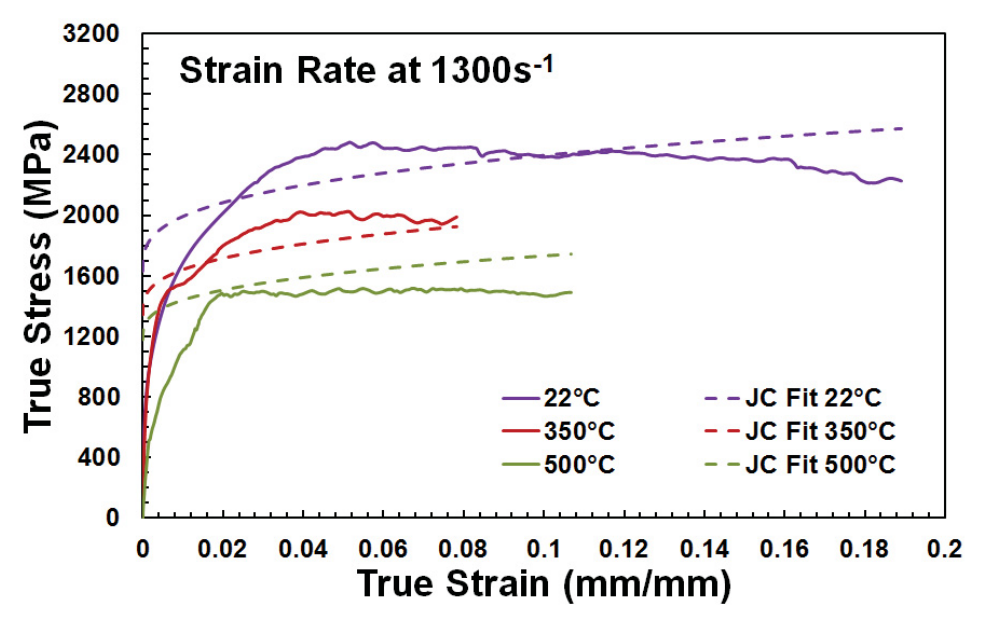


Figure 7.18. Johnson-Cook fit on the experimental data of 300M steel at 1300 s⁻¹ with increasing temperatures of 22°C, 350°C, and 500°C

The plots of the experimental flow stress curves at constant strain rates of 800 s^{-1} and 1300 s^{-1} with increasing temperature vs. the predicted Cowper-Symonds (modified Johnson-Cook) curves are shown in Figures 7.19 and 7.20.

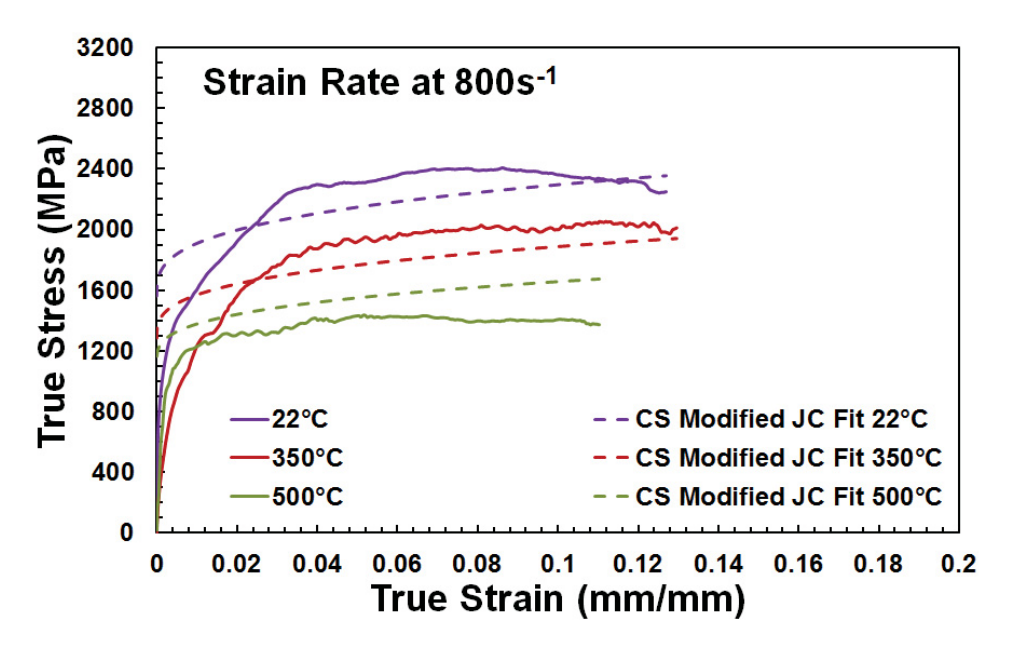


Figure 7.19. Cowper-Symonds (modified Johnson-Cook) fit on the experimental data of 300M steel at 800 s⁻¹ with increasing temperatures of 22°C, 350°C, and 500°C

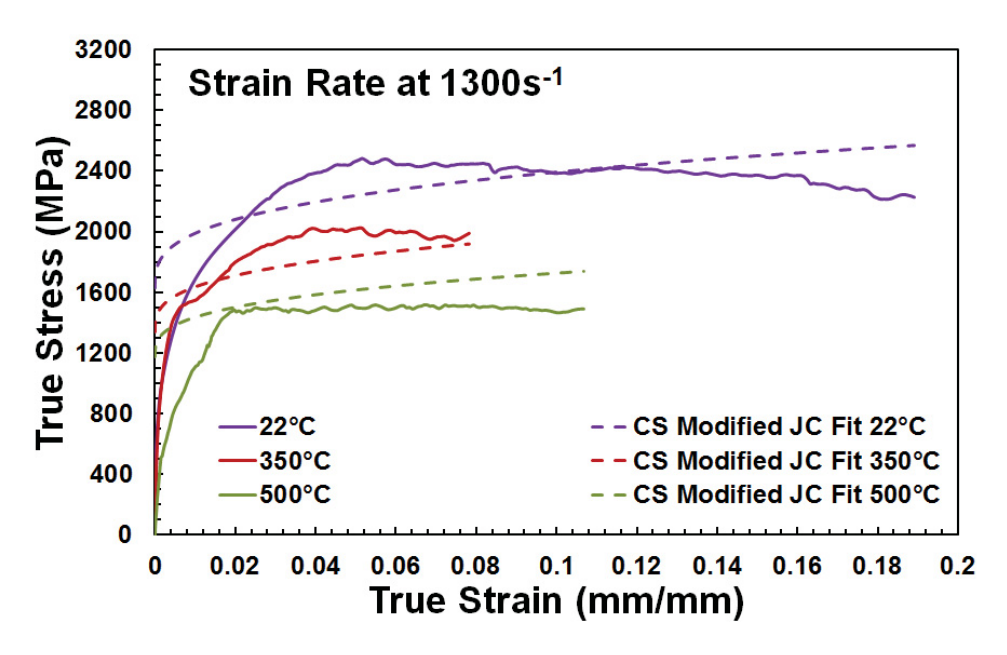


Figure 7.20. Cowper-Symonds (modified Johnson-Cook) fit on the experimental data of 300M steel at 1300 s⁻¹ with increasing temperatures of 22°C, 350°C, and 500°C

A similar trend with that of the Johnson-Cook predicted curves was observed. At both strain rates, the Cowper-Symonds (modified Johnson-Cook) model underestimated the curve at 350°C and overestimated it at 500°C.

One reason that may have had contributed to the overestimation or underestimation of the fit is that only two deformation temperatures were considered in identifying the thermal softening coefficient m. Using more deformation temperatures (below 350°C and above 500°C) would have helped the calibration of the m parameter as more data for fitting would be available.

Also, the physical state (i.e. grain size, dislocation density, etc.) of the material during deformation was not incorporated in the functions of the Johnson-Cook and Cowper-Symonds (modified Johnson-Cook) models thus the flow stress predictions were merely based on the mechanical behavior of the material.

The statistical parameters representing the goodness of fit of the two models to the experimental flow stress curves at 800 s⁻¹ and 1300 s⁻¹ with increasing deformation temperature are summarized in Tables 7.8 and Table 7.9 respectively.

Table 7.8 Summary of parameters representing the goodness of fit of the models to 300M steel experimental data at $800 \, s^{-1}$ and increasing temperature

(At 800 s ⁻¹) Temperature	Residual Sum of Squares (RSS)		R ² of Nonlinear Regression		Standard Error of Regression (SER)	
	JC	CS (modified JC)	JC	CS (modified JC)	JC	CS (modified JC)
22°C	3.47×10 ⁷	3.16×10 ⁷	0.48	0.53	366.99	349.93
350°C	3.24×10^{7}	3.14×10^7	0.47	0.49	350.57	344.91
500°C	3.96×10^{7}	2.99×10^{7}	-0.47	-0.11	387.92	337.26

Table 7.9 Summary of parameters representing the goodness of fit of the models to 300M steel experimental data at $1,300 \, s^{-1}$ and increasing temperature

(At 1300 s ⁻¹) Temperature	Residual Sum of Squares (RSS)		R ² of Nonlinear Regression		Standard Error of Regression (SER)	
remperature	JC	CS (modified JC)	JC	CS (modified JC)	JC	CS (modified JC)
22°C	4.01×10 ⁷	3.96×10 ⁷	0.45	0.45	392.64	390.39
350°C	1.27×10^{7}	1.27×10^7	0.47	0.47	332.53	332.56
500°C	3.76×10^7	3.71×10^7	0.01	0.03	455.53	452.47

In general, the predicted curves using the identified material parameters for both the Johnson-Cook and modified Johnson-Cook model with Cowper-Symonds strain sensitivity function did not fit the experimental data well. Both models were not able to capture the behavior of the 300M material in terms of its strain rate sensitivity with increasing strain rate, stress saturation at strain rates $>1,300 \, \text{s}^{-1}$, and thermal softening due to the applied deformation temperature and adiabatic heating.

Chapter 8: Conclusions and Future Work

8.1 Conclusions

The purpose of this study was to investigate and provide an understanding of the high strain rate and elevated temperature behavior of IN718 and 300M steel through compressive Split-Hopkinson Pressure Bar tests. The plastic deformation of IN718 and 300M steel had to be explained quantifiably by a material constitutive model through fitting of the various stress-strain relationships at different strain rates and temperatures.

The Johnson-Cook model and modified Johnson-Cook model with Cowper-Symonds function were chosen as the material models to describe the dynamic behavior of the materials. These models were selected due to their simple form, ease of use, and straight forward approach of identifying the material constants from the experimental data.

The main conclusions that can be drawn from the experimental results of the study are the following:

- (1) The IN718 material presents positive strain rate sensitivity over the range of strain rates (10^2 s⁻¹ 10^3 s⁻¹) and temperature (22° C 500° C).
- (2) The strain hardening behavior of IN718 varied with the change in strain rate. At the quasi-static strain rate (0.003 s⁻¹) up to 10^2 s⁻¹ strain rates, the strain hardening is greater as reflected by the difference in flow stress of ~100MPa, compared to the higher strain rates (10^3 s⁻¹) with only ≤ 50 MPa difference in the flow stress.
- (3) The IN718 material exhibits a thermal softening effect at constant strain rate conditions with deformation temperatures of 250°C, 350°C, and 500°C. The flow stress at 0.04 and 0.07 strain decreases with increasing temperature and less strain hardening of the material is observed at higher temperatures.
- (4) The 300M steel material displays positive strain rate sensitivity only up to a certain strain rate value (1900 s⁻¹ at 22°C and 1300 s⁻¹ at 350°C and 500°C).
- (5) The flow stress of the 300M steel saturates at approximately at 1,650 MPa at 500°C, 2,100 MPa at 350°C, and 2,450 MPa at 22°C before failure. The failure can

- be attributed to the thermal softening response at high strain rates due to adiabatic heating.
- (6) The 300M steel material exhibits increased thermal softening effect at increasing deformation temperature. At 0.04 strain, a flow stress decrease of ∼400MPa was found at temperatures from 22°C to 350°C, while a decrease of ∼500MPa was found at temperatures from 350°C to 500°C.

The conclusions drawn from the Johnson-Cook model and modified Johnson-Cook model with Cowper-Symonds function evaluations and fittings for both the IN718 and 300M steel materials are the following:

For the IN718 material:

(1) The values of the Johnson-Cook model (Eq. 2.19) material constants for IN718 were determined to be:

Johnson-Cook parameters for IN718						
A (MPa) B (MPa) n C m						
1067 ± 3.75	1129 ± 2.91	0.416 ± 0.005	0.0138 ± 0.0014	1.71 ± 0.09		

- (2) The Johnson-Cook model fits the experimental data well in the quasi-static and $10^2 \, \text{s}^{-1}$ strain rate specifically at 800 s⁻¹. However, the model does not capture the change in the strain hardening behavior occurring at transition strain rates between $10^2 \, \text{s}^{-1}$ and $10^3 \, \text{s}^{-1}$ due to its linear function of the logarithm of the normalized strain rate.
- (3) The Johnson-Cook model fits the experimental data well for the temperature effects at high strain rates (10^3 s⁻¹). Although at lower strain rates, the model predicts flow stresses that are higher than the ones observed experimentally.
- (4) The values of the modified Johnson-Cook model with Cowper-Symonds function (Eq. 6.11) material constants for IN718 were determined to be:

Modified Johnson-Cook with Cowper-Symonds function parameters for IN718					
A (MPa) B (MPa) n D p m					
1067 ± 3.75	1129 ± 2.91	0.416 ± 0.005	169,876	2.82	1.71± 0.09

- (5) The modified Johnson-Cook model with Cowper-Symonds function has high strain rate sensitivity and was able to fit the experimental data better especially at a strain rate of $10^2 \, \text{s}^{-1}$.
- (6) The modified Johnson-Cook model with Cowper-Symonds function is a better model that represents the dynamic behavior of the IN718 material. It has a power law relation for the effect of the strain rate on the flow stress of the material. However, it still considers the effects of strain rate and temperature on the material independently rather than coupled.

For 300M steel material:

(1) The values of the Johnson-Cook model (Eq. 2.19) material constants for 300M steel were determined to be:

Johnson-Cook parameters for 300M steel						
A (MPa) B (MPa) n C m						
1542 ± 0.46	1531 ± 1.55	$0.326 \pm 2.77 \times 10^{-4}$	0.0036 ± 0.0016	1.191 ± 0.085		

- (2) The Johnson-Cook model predicted curves did not fit the experimental data at both room and elevated temperatures. The model has low strain rate sensitivity and was not able to capture the increase in flow stress with strain rate.
- (3) The Johnson-Cook model does not incorporate in its functions the thermal softening of the material due to adiabatic heating. Thus it was not able to predict the flow stress saturation at high strain rates and thermal softening.
- (4) The values of the modified Johnson-Cook model with Cowper-Symonds function (Eq. 6.11) material constants for 300M steel were determined to be:

Modified Johnson-Cook with Cowper-Symonds function parameters for 300M steel						
A (MPa) B (MPa) n D p m					m	
1542 ± 0.46	1531 ± 1.55	$0.326 \pm 2.77 \times 10^{-4}$	3,529	0.35	1.72	

(5) Similar with the Johnson-Cook model, the modified Johnson-Cook model with Cowper-Symonds function did not fit the experimental data. Although relative to the Johnson-Cook model, it has a slightly better approximation to the experimental curves.

8.2 Future Work

The work presented in this study provided some insights into the use of the Split-Hopkinson Pressure bar to achieve high strain rates and into the dynamic behavior of IN718 and 300M steel over a range of strain rates and temperatures.

In order to improve the results of the SHPB tests, the following work should be considered in the future:

- (1) Other pulse shaper materials and dimensions should be investigated to further decrease the "ring-up period" in the tests.
- (2) Correction for wave dispersion via Fast Fourier Transform (curve fitting/smoothening) could be applied on the experimental stress-strain curves to further reduce the oscillation in the curves.

In order to gain a better understanding of the mechanical behavior and governing mechanisms on the dynamic deformation of the materials, the following work should be pursued in the future:

- (1) Dynamic experiments at strain rates intermediate to those presented in the current study (from 10 s⁻¹ to 100 s⁻¹) should be performed to determine the degree of the strain rate sensitivity of the materials at this range. Data points from these experiments can be used in identifying the material parameters.
- (2) Dynamic experiments at strain rates exceeding those achieved in the current study (>3,500 s⁻¹) should be performed to gain an understanding of the behavior of the materials in those regimes.
- (3) Microstructure evolution under different strain rate regimes should be investigated to determine the effect of strain rate on the grain size growth, dislocation density, and presence of adiabatic shear bands. These may help explain the deformation mechanism governing at each strain rate regime.
- (4) Modified versions of the Johnson-Cook model such as the Ozel¹¹³, Calamaz¹¹⁴ or Lurdos¹¹⁵ model which accounts for the thermal and strain softening phenomena in the material should be evaluated.

(5) Other material models such as the Zerilli-Armstrong⁸⁹ model which considers the physical state of the material (i.e. grain size, dislocation density etc.) should be evaluated to describe the dynamic behavior of the materials.

Chapter 9: References

- 1. A. Bouvet, N. Gill, and S. Nadkarni, The changing face of aerospace & defense industry: A review and key segments and emerging trends, Cappemini Consulting, (France, 2011).
- 2. A. Weber, Assembly automation takes off in aerospace industry, WWW Document (http://www.assemblymag.com/articles/92790-assembly-automation-takes-off-in-aerospace-industry).
- 3. Boeing, Commercial Airplanes Fact Sheet, WWW Document (http://investors.boeing.com/investors/fact-sheets/default.aspx).
- 4. W.D. Klopp, *Aerospace Structural Metals Handbook*. (Purdue Research Foundation, West Lafayette, IN, 1995), Code 4103, pp. 1-19.
- 5. T.M. Pollock and S. Tin, Nickel-Based Superalloys for Advanced Turbine Engines: Chemistry, Microstructure and Properties, Journal of Propulsion and Power, **22** (2), 361-374 (2006).
- 6. J.R. Kattus, *Aerospace Structural Metals Handbook*. (Purdue Research Foundation, West Lafayette, IN, 1999), Code 4218, pp. 1-6.
- 7. K. Runesson, Constitutive Modeling of Engineering Materials Theory and Computation Lecture Notes, Chalmers University of Technology, Department of Applied Mechanics, (Gotherburg, Sweden, 2006).
- 8. J. Shi and C.R. Liu, The Influence of Material Models on Finite Element Simulation of Machining, Journal of Manufacturing Science and Engineering, **126**, 849-857 (2004).
- 9. J.D Campbell, and W.G. Ferguson, The temperature and strain-rate dependence of the shear strength of mild steel, Philosophical Magazine A, **21** (169), 63-82 (1970).
- 10. M.A. Meyers, *Dynamic behavior of materials*. (John Wiley & Sons, Inc., New York, 1994).
- 11. W. Frank, Thermally activated dislocation motion in a solid containing a multiple spectrum of dislocation obstacles, Physica Status Solidi B, **26** (1), 197-206 (1968).
- 12. M.A Meyers, D.J. Benson, O. Vohringer, B.K. Kad, Q. Xue, and H.H. Fu, Constitutive description of dynamic deformation: physically-based mechanisms, Materials Science and Engineering A, **322** (1), 194-216 (2002).
- 13. R. W. Armstrong, W. Arnold, F.J. Zerilli, Dislocation mechanics of shock-induced plasticity, Metallurgical and Materials Transactions A, **38** (11), 2605-2610 (2007).
- 14. ASM Handbook, Vol. 8, Mechanical testing and evaluation, (Materials Park OH, 2000).
- 15. P.F. Bariani, G. Berti, and S. Corazza, Enhancing performances of SHPB for determination of flow curves, CIRP Annals Manufacturing Technology, **50** (1), 153-156 (2001).

- 16. H. Kolsky, An investigation of the mechanical properties of materials at very high rates of loading, Proceedings of the Physical Society of London, Section B, **62** (II-B), 676–700 (1949).
- 17. C.T. Sims and W. Hagel, *The Superalloys*. (Wiley, New York, 1972).
- 18. D.V.V. Satyanarayana and N. Eswara Prasad, in *Aerospace materials and material technologies*. (Springer, Singapore, 2017), pp. 199-228.
- 19. H.L. Eiselstein. Age-hardenable nickel alloy. U.S. patent 3046108, 1962.
- 20. E. Akca and A. Gursel, A review on superalloys and IN718 Nickel-based INCONEL Superalloy, Periodicals of Engineering and Natural Sciences, **3** (1), 15-27 (2015).
- 21. C.T. Sims, N.S. Stoloff, and W.C. Hagel, *Superalloys II: High-temperature materials for aerospace and industrial power*. (John Wiley and Sons Inc., 1987).
- 22. P.S. Follansbee and U.F. Kocks, A constitutive description of the deformation of copper based on the use of the mechanical threshold stress as an internal state variable, Acta Metallurgica et Materialia, **36**, 81-93 (1988).
- 23. W.S. Lee, C.F. Lin, T.H. Chen, and H.W. Chen, Dynamic impact response of Inconel 718 alloy under low and high temperatures, Materials Transactions, **52** (9), 1734-1740 (2011).
- 24. X. Wang, C. Huang, B. Zou, H. Liu, and J. Wang, Dynamic behavior and a modified Johnson-Cook constitutive model of Inconel 718 at high strain rate and elevated temperature, Materials Science and Engineering A, **580**, 385-390 (2013).
- 25. W.S. Lee, C.F. Lin, T.S. Chen, and H.W. Chen, Dynamic mechanical behaviour and dislocation substructure evolution of Inconel 718 over wide temperature range, Materials Science and Engineering A, **528**, 6279-6286 (2011).
- 26. Z. Xu and F. Huang, Plastic behavior and constitutive modeling of armor steel over wide temperature and strain rate ranges, Acta Mechanica Solida Sinica, **25** (6), 598-608 (2012).
- 27. *ASM Handbook*, Vol. 1, Properties and selection: Irons, steels, and high-performance alloys, 10th Ed. (Materials Park OH, 1990).
- 28. W.S. Lee and G.W. Yeh, The plastic deformation behaviour of AISI 4340 alloy steel subjected to high temperature and high strain rate loading conditions, Journal of Materials Processing Technology, **71**, 224-234 (1997).
- 29. M.P. Groover, Fundamentals of modern manufacturing: materials, processes, and system. (Wiley, USA, 2010).
- 30. H. Ernst and M.E. Merchant, Chip formation, friction and high quality machined surfaces, Transactions of the American Society for Metals, **29**, 299 (1941).
- 31. J.R. Walker and Bob Dixon, *Machining fundamentals*. Ninth ed., (Goodheart-Willcox Publisher, Tinley Park IL, 2013).
- 32. E.G. Ng, T.I. El-Wardany, M. Dumitrescu, and M.A. Elbestawi, Physics-based simulation on high-speed machining, Machining Science and Technology, **6** (3), 301 (2002).
- 33. J.P. Davim and C. Maranhão, A study of plastic strain and plastic strain rate in machining of steel AISI 1045 using FEM analysis, Materials & Design, **30**, 160-165 (2009).

- 34. B. Hopkinson, A method of measuring the pressure produced in the detonation of high explosive or by the impact of bullets, Philosophical Transactions of the Royal Society of London A, **213**, 437–456 (1914).
- 35. R.M. Davies, A critical study of the Hopkinson pressure bar, Philosophical Transactions of the Royal Society of London A, **240** (821), 375–457 (1948).
- 36. K.D. Roberston, S.C. Chou, and J.H. Rainey, Design and operating characteristics of a Split-Hopkinson Pressure Bar apparatus, Army Material and Mechanics Research Center, (Watertown, MA, 1971).
- 37. K.T. Ramesh, *Springer Handbook of Experimental Solid Mechanics*. (Germany, 2008), pp. 929-960.
- 38. Y. Li, Y. Guo, H. Hu, and Q. Wei, A critical assessment of high-temperature dynamic mechanical testing of materials, International Journal of Impact Engineering, **36**, 177-184 (2009).
- 39. A.M. Lennon and K.T. Ramesh, A technique for measuring the dynamic behavior of materials at high temperature, International Journal of Plasticity, **14** (12), 1279-1292 (1998).
- 40. J.M. Lifshitz and H. Leber, Data processing in the Split-Hopkinson Pressure Bar tests, International Journal of Impact Engineering, **15** (6), 723-733 (1994).
- 41. U.S. Lindholm, Some experiments with the Split-Hopkinson Pressure Bar, Journal of the Mechanics and Physics of Solids, **12**, 317-335 (1964).
- 42. B.A. Gama, S.L. Lopatnikov, and J.W. Gillespie, Hopkinson bar experimental technique: A critical review, Applied Mechanics Reviews, **57** (4), 223-250 (2004).
- 43. W. Chen and B. Song, *Split-Hopkinson (Kolsky) Bar: Design, Testing and Applications.* (Springer, NY, 2011).
- 44. M.M. Al-Mousawi, S.R. Reid, and W.F. Deans, The use of the Split-Hopkinson Pressure Bar techniques in high strain rate materials testing, Proceedings of the Institution of Mechanical Engineers Part C, **211** (4), 273-292 (1997).
- 45. A. Trautmann, C.R. Siviour, and S.M. Walley, Lubrication of polycarbonate at cryogenic temperatures in the Split-Hopkinson Pressure Bar, International Journal of Impact Engineering, **31** (5), 523-544 (2004).
- 46. W.S. Lee, W.C. Sue, and C.F. Lin, The effects of temperature and strain rate on the properties of carbon-fiber-reinforced 7075 aluminum alloy metal-matrix composite, Composites Science and Technology, **60** (10), 1975-1983 (2000).
- 47. J. Kajberg and K.G. Sundin, Material characterisation using high-temperature Split-Hopkinson Pressure Bar, Journal of Materials Processing Technology, **213**, 522-531 (2013).
- 48. W.S. Lee and C.F. Lin, Plastic deformation and fracture behaviour of Ti-6Al-4V alloy loaded with high strain rate under various temperatures, Materials Science and Engineering A, **241** (1-2), 48-59 (1998).
- 49. J.L. Chiddister and L.E. Malvern, Compression-impact testing of aluminum at elevated temperatures, Experimental Mechanics, **3**, 80-90 (1963).

- 50. X. Fan, T. Suo, Q. Sun and T. Wang, Dynamic mechanical behavior of 6061 al alloy at elevated temperatures and different strain rates, Acta Mechanica Solida Sinica, **26** (2), 111-120 (2013).
- 51. Gray III GT, Classic Split-Hopkinson Pressure Bar testing. (Materials Park OH, 2000).
- 52. K. Xia and W, Yao, Dynamic rock tests using Split-Hopkinson (Kolsky) bar system, Journal of Rock Mechanics and Geotechnical Engineering, **7**, 27-59 (2015).
- 53. R. Naghdabadi, M.J. Ashrafi, and J. Arghavani, Experimental and numerical investigation of pulse-shaped Split-Hopkinson Pressure Bar test, Materials Science and Engineering A, **539**, 285-293 (2012).
- 54. E.D.H. Davies and S.C. Hunter, The dynamic compression testing of solids by the method of the Split-Hopkinson Pressure Bar, Journal of Mechanics and Physics of Solids, **11** (3), 155-179 (1963).
- 55. R.J. Christensen, S.R. Swanson, W.S. Brown, Split-Hopkinson bar tests on rock under confining pressure, Experimental Mechanics, **12** (11), 508-513 (1972).
- 56. C.E. Frantz, P.S. Follansbee, and W.J. Wright, New experimental techniques with the Split-Hopkinson Pressure Bar, 8th International Conference on High Energy Rate Fabrication. (San Antonio, Texas, USA, 1984). pp. 17-21.
- 57. X.B. Li, T.S. Lok, J. Zhao, J. Zhao, and P.J. Zhao, Oscillation elimination in the Hopkinson bar apparatus and resultant complete dynamic stress-strain curves for rocks, International Journal of Rock Mechanics and Mining Sciences, **37** (7), 1055-60 (2000).
- 58. Y.X. Zhou, K. Xia, X.B. Li, H.B. Li, G.W. Ma, J. Zhao, Z.L. Zhou, and F. Dai, Suggested methods for determining the dynamic strength parameters and mode-I fracture toughness of rock materials, International Journal of Rock Mechanics and Mining Sciences, 49, 105-12 (2012).
- 59. S. Ellwood, L.J. Griffith, D.J. Parry, Materials testing at high constant strain rates, Journal of Physics E: Scientific Instruments, **15** (3), 280 (1982).
- 60. D.J. Parry, A.G. Walker, and P.R. Dixon, Hopkinson bar pulse smoothing, Measurement Science and Technology, **6**, 443 (1995).
- 61. K. Xia, Status of characterization of strength and fracture properties of rocks under dynamic loading, 10th International Symposium on Rock Fragmentation by Blasting. (New Delhi, India, 2012) pp. 41-51.
- 62. D.J Frew, M.J. Forrestal, and W. Chen, Pulse shaping techniques for testing elastic-plastic materials with a Split-Hopkinson Pressure Bar, Experimental Mechanics, **45**, 186-195 (2005).
- 63. W.D. Callister, *Materials Science and Engineering: An Introduction*. Seventh ed., (Wiley, NY, 2007).
- 64. F. Barlat, *Advanced method in material forming*. (Springer Berlin Heidelberg, Germany, 2007).
- 65. K.J. William, Constitutive models for engineering materials, Encyclopedia of Physical Science and Technology, **3**, 603-633 (2002).
- 66. A. Hor, F. Morel, J.L. Lebrun, and G. Germain, Modelling, identification and application of phenomenological constitutive laws over a large strain rate and temperature range, Mechanics of Materials, **64**, 91-110 (2013).
- 67. Z. Gronostajski, The constitutive equations for FEM analysis, Journal of Materials Processing Technology, **106**, 40-44 (2000).

- 68. B. Shi and M.H. Attia, Evaluation criteria of the constitutive law formulation for the metal-cutting process, Proceedings of the Institution of Mechanical Engineers, Part B: Journal of Engineering Manufacture, **224**, 1313-1328 (2009).
- 69. G.R. Johnson and W.H. Cook, A constitutive model and data for metals subjected to large strains, High rates and high temperatures, Proceedings of the Seventh International Symposium on Ballistics. (Hague, Netherlands 1983), pp. 541-547.
- 70. G.R. Johnson and W.H. Cook, Fracture characteristics of three metals subjected to various strains, strain rates, temperatures and pressures, Engineering Fracture Mechanics, **21** (1), 31-48 (1985).
- 71. J.J. DeMange, V. Prakash, and J.M. Pereira, Effects of material microstructure on blunt projectile penetration of a nickel-based super alloy, International Journal of Impact Engineering, **36**, 1027-1043 (2009).
- 72. A. He, G. Xie, H. Zhang, and X. Wang, A comparative study on Johnson–Cook, modified Johnson–Cook and Arrhenius-type constitutive models to predict the high temperature flow stress in 20CrMo alloy steel, Materials & Design, **52**, 677-685 (2013).
- 73. C. Lin, Q.F. Li, Y.C. Xia and L.T. Li, A phenomenological constitutive model for high temperature flow stress prediction of Al-Cu-Mg alloy, Materials Science and Engineering, **534**, 654-662 (2012).
- 74. D.P. Samantaray, S. Mandal and A.K. Bhaduri, A comparative study on Johnson Cook, modified Zerilli–Armstrong and Arrhenius-type constitutive models to predict elevated temperature flow behaviour in modified 9Cr–1Mo steel, Computational Materials Science, 47, 568-576 (2009).
- 75. G. Cowper and P. Symonds, Strain hardening and strain-rate effects in the impact loading of cantilever beams Technical report, Division of Applied Mathematics, Brown University, (Providence, RI, USA, 1952).
- 76. M. Di Sciuva, C. Frola and S. Salvano, Low and high velocity impact on Inconel 718 casting plates: Ballistic limit and numerical correlation, International Journal of Impact Engineering, **28** (8), 849-876 (2003).
- 77. J. Choung, W. Nam, and J.Y. Lee, Dynamic hardening behaviors of various marine structural steels considering dependencies on strain rate and temperature, Marine Structures, **32**, 49–67 (2013).
- 78. A. Škrlec and J. Klemenc, Estimating the strain-rate-dependent parameters of the Cowper-Symonds and Johnson-Cook material models using taguchi arrays, Journal of Mechanical Engineering, **62**(4), 220-230 (2016).
- 79. A.A. Al Salahi and R. Othman, Constitutive equations of yield stress sensitivity to strain rate of metals: A comparative study, Journal of Engineering, **2016**, 1-7 (2016).
- 80. D. Ghaffari and M.J. Worswick, Elevated temperature constitutive behavior and simulation of warm forming of AZ31B, Journal of Materials Processing Technology, **221**, 40–55 (2015).
- 81. L. Schwer. Optional strain-rate forms for the Johnson-Cook constitutive model and the role of the parameter epsilon_0¹, (LS-DYNA, Anwenderforum, Frankenthal 2007).
- 82. T.J. Holmquist and G.R. Johnson, Determination of constants and comparison of results for various constitutive models, Journal de Physique III, **1**, 853-860 (1991).

- 83. G.T. Camacho and M. Ortiz, Adaptive Lagrangian modelling of ballistic penetration of metallic targets, Computational Methods Applied Mechanics and Engineering, **142**, 269-301 (1997).
- 84. T. Borvik, O.S. Hopperstad, T. Berstad, and M. Langseth, A computational model of viscoplasticity and ductile damage for impact and penetration, European Journal of Mechanics –A/Solids, **20** (5), 685-712 (2001).
- 85. Q.Y. Hou and J.T. Wang, A modified Johnson-Cook constitutive model for Mg-Gd-Y alloy extended to a wide range of temperature, Computational Materials Science, **50** (1), 147-152 (2010).
- 86. Y.C. Lin, X.M. Chen and G. Liu, A modified Johnson-Cook model for tensile behaviors of typical high-strength alloy steel, Materials Science and Engineering A, **527** (26), 6980-6986 (2010).
- 87. H.Y. Li, Y.H. Li, X.F. Wang, J.J. Liu, and Y. Wu, A comparative study on modified Johnson Cook, modified Zerilli-Armstrong and Arrhenius-type constitutive models to predict the hot deformation behavior in 28CrMnMoV, Materials & Design, **49**, 493-501 (2013).
- 88. Y.C. Lin and X.M. Chen, A combined Johnson-Cook and Zerilli-Armstrong model for hot compressed typical high-strength alloy steel, Computational Materials Science, **49** (3), 628-633 (2010).
- 89. F.J. Zerilli and R.W. Armstrong, Dislocation-mechanics based constitutive relations for material dynamics calculations, Journal of Applied Physics, **61** (5), 1816-1825 (1987).
- 90. R.W. Armstrong and J.D. Campbell, The microstructure and design of alloys, Proceedings of 3rd International Conference on the Strength of Metals and Alloys, Vol.1, (Cambridge, England, 1973).
- 91. W.S. Lee and Z.C. Tang, Relationship between mechanical properties and microstructural response of 6061-T6 aluminum alloy impacted at elevated temperatures, Materials & Design, **58**, 116-124 (2014).
- 92. W.S. Lee and H.C. Kao, High temperature deformation behavior of Haynes 188 alloy subjected to high strain rate loading, Materials Science and Engineering A, **594**, 292-301 (2014).
- 93. S.T. Chiou, W.C. Cheng and W.S. Lee, Strain rate effects on the mechanical properties of a Fe-Mn-Al alloy under dynamic impact deformations, Materials Science and Engineering A, **392**, 156-162 (2005).
- 94. D.P. Samantaray, S. Mandal, U. Borah, A.K. Bhaduri, and P.V. Sivaprasad, A thermoviscoplastic constitutive model to predict elevated-temperature flow behaviour in a titanium-modified austenitic stainless steel, Materials Science and Engineering A, **526**, 1-6 (2009).
- 95. H. Javadi, (Private Communication).
- 96. J. Ajaja (Private Communication).
- 97. Split-Hopkinson Pressure Bar (SHPB) Standard Operating Procedure, McGill University (Montreal, Canada, 2014).
- 98. U.S. Lindholm and L.M. Yeakley, High Strain rate Testing: Tension and compression, Experimental Mechanics. **8**, 1–9 (1968).
- 99. ATI Vascomax C350 Technical Data Sheet, (Monroe, NC, USA, 2010).

- 100. ASME B31.1-2001, Power Piping, (The American Society of Mechanical Engineers, USA, 2001).
- 101. B. Song, B.R. Antoun, X. Nie, and W. Chen, High-rate characterization of 304L stainless steel at elevated temperatures for recrystallization investigation, Experimental Mechanics, **50** (4), 553-560 (2010).
- 102. D.R. Drodge, D.M. Williamson, and W.G. Proud, Split-Hopkinson Pressure Bar techniques for the estimation of a high-strain rate elastic modulus, Proceedings of the 11th International Congress and Exposition, Society for Experimental Mechanics Inc., (Orlando, Florida, 2008).
- 103. F.J. Zerilli and R.W. Armstrong, The effect of dislocation drag on the stress-strain behavior of F.C.C. Metals, Acta Metallurgica et Materialia, **40** (8), 1803-1808 (1992).
- 104. W.S. Lee and C.F. Lin, Comparative study of the impact response and microstructure of 304L stainless steel with and without prestrain, Metallurgical and Materials Transaction A, **33** (9), 2801-2810 (2002).
- 105. J.M. Pereira and B.A. Lerch, Effects of heat treatment on the ballistic impact properties of Inconel 718 for jet engine fan containment applications, International Journal of Impact Engineering, **25**, 715-733 (2001).
- 106. M. C. Mataya and V. E. Sackschewsky, Effect of internal heating during hot compression on the stress-strain behavior of alloy 304L, Metallurgical and Materials Transaction A, **25**, 2737–2752 (1994).
- 107. R. Kapoor and S. Nemat-Nasser, Determination of temperature rise during high strain rate deformation, Mechanics of Materials, **27**, 1–12 (1998).
- 108. Y. Tirupataiah and G. Sundararajan, A dynamic indentation technique for the characterization of the high strain rate plastic flow behaviour of ductile metals and alloys, Journal of the Mechanics and Physics of Solids, **39** (2), 243-271 (1991).
- 109. M. Di Sciuva, C. Frola and S. Salvano, Low and high velocity impact on Inconel 718 casting plates: Ballistic limit and numerical correlation, International Journal of Impact Engineering, **28** (8), 849-876 (2003).
- 110. T. Kobayashi, J.W. Simons, C.S. Brown, and D.A. Shockey, Plastic flow behavior of Inconel 718 under dynamic shear loads, International Journal of Impact Engineering, **35**, 389-396 (2008).
- 111. Z. Zhou, A.S. Gill, D. Qian, and V. Vasudevan, A finite element study of thermal relaxation of residual stress in laser shock peened IN718 superalloy, International Journal of Impact Engineering. **38** (7), 590-596 (2011).
- 112. N.S Brar, O. Sawas, and H. Hilfi, Johnson-Cook strength model parameters for Inconel-718, University of Dayton, (Dayton, OH, 1996).
- 113. T. Ozel, I. Lanos, J. Soriano, and P.J. Arrazola, 3D Finite element modelling of chip formation process for machining Inconel 718: comparison of FE software predictions, Machining Science & Technology. **15**, 21-46 (2011).

- 114. M. Calamaz, D. Coupard, and F. Girot, Numerical simulation of Titanium alloy dry machining with strain softening constitutive law, Machining Science & Technology. **14**, 244-257 (2010).
- 115. O. Kurdos, F. Montheillet, and G. Damamme, Empirical and physically based flow rules relevant to high speed processing of 304L steel, International Journal of Material Forming. **1**, 1431-1434 (2008).